TECHNICAL PHYSICS VOLUME 44, NUMBER 1 JANUARY 1999

On the theory of the acceleration of plasma electrons during stimulated scattering of an intense laser wave

N. S. Ginzburg, I. V. Zotova, and A. V. Kuritsyn

Institute of Applied Physics, Russian Academy of Sciences, 603600 Nizhniĭ Novgorod, Russia

(Submitted October 6, 1997)
Zh. Tekh. Fiz. **69**, 3–8 (January 1999)

The mechanism of electron acceleration in the stimulated Raman forward scattering of a monochromatic laser wave in a cold plasma is investigated theoretically. It is shown that as a result of the stochastic interaction of the electrons with the ponderomotive wave and with plasma waves excited in the scattering process, some of the electrons are accelerated to relativistic energies. © *1999 American Institute of Physics.* [S1063-7842(99)00101-4]

The electric fields in existing accelerators are limited to 100 MV/m by the rf breakdown of the metallic cavities. For this reason the acceleration of electrons to high energies requires long and costly structures. The construction of more-compact accelerators is contingent on the possibility of generating higher electric fields. One solution of this problem may be to use high-power lasers, in which the transverse electric fields can easily reach 100 GV/m. However, these transverse fields cannot be used directly for efficient acceleration of particles. However, plasmas can be used to convert transverse fields into longitudinal fields, which are capable of accelerating particles to relativistic energies. In an electron plasma wave the electric field accompanying charge separation can be very high. For a suitably chosen wavelength the phase velocity of such a wave can be close to the speed of light, and an electron accelerated to relativistic energies and injected into a traveling wave will be in phase with the accelerating field over long distances.

Traditionally, two mechanisms of excitation of relativistic plasma waves have been studied: excitation by kilowatt fields, and excitation by beat waves.[1–5] The method of acceleration by beat waves originated from the proposal of Gaponov and Miller[1] to accelerate charged particles by the averaged ponderomotive force arising as a result of the interference of two monochromatic waves with nearly equal frequencies. Later Tajima and Dawson[2] proposed to use this ponderomotive force to excite a plasma wave which would then accelerate the particles. When the difference frequency $\delta\omega=\omega_1-\omega_2$ is close to the electron plasma frequency ω_p, a resonance excitation of plasma waves by the wave of the averaged ponderomotive potential occurs, and the electric field can reach a very large amplitude. It was assumed in those papers that the two waves with frequencies ω_1 and ω_2 are created by external sources. It has recently become clear that one of the waves can arise as a result of stimulated Raman forward scattering of the pump wave.[6–8] This principle of acceleration was confirmed experimentally in Refs. 9 and 10. The maximum energy acquired by the electrons reached 44 MeV.

In the present paper we use a one-dimensional model to investigate theoretically the mechanics of electron acceleration during stimulated Raman scattering of a laser wave. It is assumed that the external laser pump wave and the scattered wave propagate in the same direction. Their interference gives rise to a ponderomotive wave with a phase velocity close to the speed of light. This ponderomotive wave excites a longitudinal plasma wave with a phase velocity which is also close to the speed of light. Numerical modeling shows that the stochastic interaction of electrons with the ponderomotive and plasma waves causes some of the electrons of the initially cold plasma to be accelerated to relativistic energies.

MODEL AND BASIC EQUATIONS

Suppose that a circularly polarized pump wave specified by the vector potential

$$\mathbf{A}_i=\mathrm{Re}[a_i(t)(\mathbf{x}_0-i\mathbf{y}_0)\exp(i(\omega_i t-h_i z))], \tag{1}$$

where ω_i and $h_i=\omega_i/c$ are the frequency and wave number of the pump wave, is incident on a cold plasma. We consider a one-dimensional model, i.e., we assume that there is no dependence on the transverse coordinates x and y. We also assume that the scattered wave is radiated in the same direction as the incident wave and is described by the vector potential

$$\mathbf{A}_s=\mathrm{Re}[a_s(t)(\mathbf{x}_0-i\mathbf{y}_0)\exp(i(\omega_s t-h_s z))], \tag{2}$$

where ω_s and $\hbar_s=\omega_s/c$ are the velocity and wave number of the scattered wave.

The motion of the electrons in the fields of the incident (1) and scattered (2) waves is the sum of a rapidly oscillatory transverse motion with velocity

$$V_+=V_x+iV_y=\frac{e}{mc\gamma}[a_i\exp(i(\omega_i t-h_i z)) + a_s\exp(i(\omega_s t-h_s z))] \tag{3}$$

and a slow longitudinal drift motion under the influence of the averaged relativistic ponderomotive force[11,12]

$$F_z^p=\frac{e^2 h_c}{mc^2\gamma}\mathrm{Re}[ia_i a_s^*\exp(i\Theta_c)], \tag{4}$$

1063-7842/99/44(1)/5/$15.00

where $\Theta_c = \omega_c t - h_c z$ is the phase of the combination (beat) wave, with frequency $\omega_c = \omega_i - \omega_s$ and wave number $\hbar_c = h_i - h_s$.

In the field of a synchronous combination wave there arises a modulation of the volume density of electrons, with temporal and spatial periods of $2\pi/\omega_c$ and $2\pi/h_c$, respectively. As a result, the electron charge density can be written in the form

$$\rho_e = \rho_{e0}\left(1 + \mathrm{Re}\left[\sum_{n=1}^{\infty} \rho_n \exp(in\Theta_c)\right]\right), \tag{5}$$

where $\rho_n = 1/\pi \int_0^{2\pi} \exp(-in\Theta_c) dZ_0$ is the amplitude of the nth harmonic of the charge density, ρ_{e0} is the unperturbed electron charge density, which is compensated by an immobile ionic background with charge density ρ_{i0}, and $Z_0 = h_c z_0$ is the initial coordinate of the electrons.

The modulation of the electron density leads to excitation of an additional longitudinal Coulomb field (the field of plasma waves), which can be obtained from the Poisson equation

$$\frac{\partial E_z}{\partial z} = 4\pi(\rho_{i0} - \rho_e). \tag{6}$$

Substituting (5) into (6), we obtain an expression for the force exerted on the electrons by the Coulomb field:

$$F_z^q = \frac{4\pi\rho_0 e}{h_c} \mathrm{Re}\left[i \sum_{n=1}^{\infty} \rho_n \exp(in\Theta_c)\right]. \tag{7}$$

The averaged longitudinal motion of the electrons in the field of the synchronous combination wave (4) and the Coulomb self-field (7) is described by the equations

$$\frac{d\Theta_c}{d\tau} = \Delta\left(1 - \frac{p}{\gamma}\right), \tag{8}$$

$$\frac{dp}{d\tau} = \Delta \frac{1}{\gamma} \mathrm{Re}[i\tilde{a}_i \tilde{a}_s^* \exp(i\Theta_c)] + \frac{1}{\Delta} \mathrm{Re}\left[i \sum_{n=1}^{\infty} \rho_n \exp(in\Theta_c)\right], \tag{9}$$

where $\gamma = (1 + p^2 + |\tilde{a}_i|^2 + |\tilde{a}_s|^2 + 2\mathrm{Re}[\tilde{a}_i \tilde{a}_s^* \exp(i\Theta_c)])^{1/2}$ is the relativistic mass factor, $\tilde{a}_i = (e/mc^2) a_i$ and $\tilde{a}_s^* = (e/mc^2) a_s^*$ are the normalized amplitudes of the vector potentials of the incident and scattered waves, $p = p_z/mc$ is the normalized longitudinal momentum of the electrons, $\tau = t\omega_p$ is the normalized time, $\omega_p = (4\pi\rho_0 e/m)^{1/2}$ is the plasma frequency, and $\Delta = ch_c/\omega_p = (\omega_i - \omega_s)/\omega_p$ is the detuning parameter.

The equation of excitation for the slowly varying amplitude a_s of the scattered wave is obtained from the wave equation with the transverse component of the current at frequency ω_s written in the form

$$j_+^s = j_x^s + i j_y^s = \hat{j}_s \exp(i(\omega_s t - h_s z)).$$

Using relation (3) and going over to an integral over the initial coordinates of the particles with allowance for charge conservation, we obtain for the current amplitude

$$\hat{j}_s = 1/\pi \int_0^{2\pi} \rho V_+ \exp(-i(\omega_s t - h_s z))\, d(h_c z) = -\frac{\rho_0 e}{2mc} \tilde{j}^* a_i,$$

where $\tilde{j} = 1/\pi \int_0^{2\pi} \exp(-i\Theta_c)/\gamma dZ_0$.

The expression for the current amplitude at frequency ω_i can be written in an analogous form:

$$\hat{j}_i = 1/\pi \int_0^{2\pi} \rho V_+ \exp(-i(\omega_i t - h_i z))\, d(h_c z) = -\frac{\rho_0 e}{2mc} \tilde{j} a_s.$$

As a result, the time evolution of the amplitudes of the incident and scattered waves is described by the equations

$$\frac{d\tilde{a}_s^*}{d\tau} = -iI\tilde{j}\tilde{a}_i^*, \tag{10}$$

$$\frac{d\tilde{a}_i}{d\tau} = \frac{i}{4\Delta + 1/I} \tilde{j}\tilde{a}_s, \tag{11}$$

where $I = \omega_p/4\omega_s \ll 1$.

The fact that the parameter I is small allows us in the derivation of equations (8)–(11) to neglect the influence of the plasma on the phase velocities of the waves and to assume that they are equal to the speed of light. Equations (8)–(11) form a self-consistent system of equations describing the scattering of the pump wave and the acceleration of the electrons. In the general case the initial conditions can be written in the form

$$p|_{\tau=0} = p_0, \quad \tilde{a}_i|_{\tau=0} = a_i^0, \quad \tilde{a}_s|_{\tau=0} = a_s^0,$$

$$\Theta_c^0 = \Theta_0 + r\cos\Theta_0, \quad \Theta_0 \in [0, 2\pi],$$

where p_0 is the initial momentum of the electrons and r is a parameter describing the perturbation of the plasma density.

Equations (10) and (11) imply conservation of the number of incident and scattered photons:

$$\frac{|\tilde{a}_s|^2}{I} + \left(4\Delta + \frac{1}{I}\right)|\tilde{a}_i|^2 = \mathrm{const},$$

and Eqs. (9)–(11) imply conservation of longitudinal momentum in the system comprising the particle and electromagnetic field:

$$\langle p \rangle_{\Theta_0} + \frac{\Delta}{8}\left(4\Delta + \frac{1}{I}\right)|\tilde{a}_i|^2 - \frac{\Delta}{8I}|\tilde{a}_s|^2 = \mathrm{const}.$$

MODELING THE ELECTRON ACCELERATION PROCESS

In the linear stage of the interaction, at a low scattered wave amplitude $\tilde{a}_s \ll 1$, we write the phases of the electrons in the form $\Theta_c = \Theta_c|_{\tau=0} + \Delta\tau + \vartheta$, where $\vartheta \ll 1$, and after linearizing the equations of motion we arrive at the system of equations

$$\frac{d\overline{\vartheta}}{d\tau} = -\frac{\Delta}{\gamma_0}\overline{p}, \quad \frac{dp}{d\tau} = \frac{i\Delta}{2\gamma_0}\overline{a_s^*} + \frac{\overline{\vartheta}}{\Delta},$$

$$\frac{d\overline{a_s^*}}{d\tau} - i\Delta\overline{a_s^*} = -\frac{2I}{\gamma_0}\overline{\vartheta} + \frac{i\tilde{I}}{\gamma_0^3}\overline{a_s^*}, \tag{12}$$

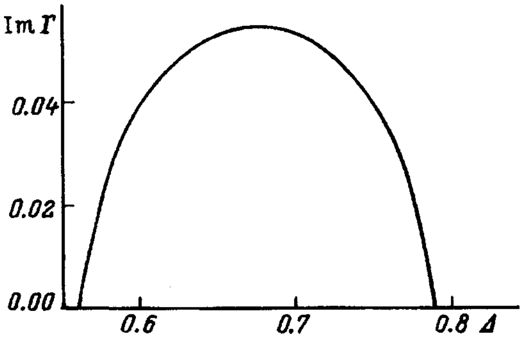

FIG. 1. Dependence of the instability growth rate on the detuning parameter Δ for $I=0.025$ and $|\tilde{a}_i^0|^2=4$.

where $\overline{\vartheta}, p=1/2\pi\int_0^{2\pi}\vartheta, p\exp(-i\Theta_c^0)dZ_0$, $\overline{a_s^*}=\tilde{a}_s^* a_i^0 \times\exp(i\Delta\tau)$, $\tilde{I}=I|a_i^0|^2$, and $\gamma_0=(1+|a_i^0|^2)^{1/2}$.

Assuming that the quantities $\overline{\vartheta}$, $\overline{p}$, and $\overline{a}_s$ vary as $\exp(i\Gamma\tau)$, we obtain the dispersion relation

$$(1-\hat{\Gamma}^2)(\hat{\Gamma}+\hat{\Delta}+\hat{I})=-\hat{\Delta}^2\hat{I}, \tag{13}$$

where $\hat{\Delta}=\gamma_0^{1/2}\Delta$, $\hat{I}=I/\gamma_0^{5/2}$, and $\hat{\Gamma}=(\gamma_0)^{1/2}\Gamma$.

It follows from Fig. 1, which shows the dependence of the instability growth rate on the detuning parameter Δ for $I=0.025$, $|\hat{a}_i|^2=4$, the maximum growth rate of the scattered wave is reached at $\Delta\approx 0.67$, i.e., at $\omega_i-\omega_s\approx 0.67\omega_p$.

We note that if relativistic effects are not taken into account, i.e., if it is assumed that the change in electron energy is small, the equations of motion (8) and (9) of the electrons reduce to the form

$$\frac{d\Theta_c}{d\tau}=\Delta(1-p), \tag{14}$$

$$\frac{dp}{d\tau}=\Delta\,\mathrm{Re}[i\hat{a}_i\hat{a}_s^*\exp(i\Theta_c)]+\frac{1}{\Delta}\mathrm{Re}\left[i\sum_{n=1}^{\infty}\rho_n\exp(in\Theta_c)\right]. \tag{15}$$

The stimulated scattering of a monochromatic wave was investigated under these assumptions in Ref. 13. Here there is no effective acceleration of the electrons. Indeed, as we see from Fig. 2, which shows the results of a numerical modeling of the system of equations (14), (15), (10), (11), the longitudinal momentum and the energy of the particles oscillate, and the maximum energy of the electrons does not exceed 2 MeV for the same pump intensity and plasma density as in the calculations presented below, in which the full system of equations (8)–(11) were used.

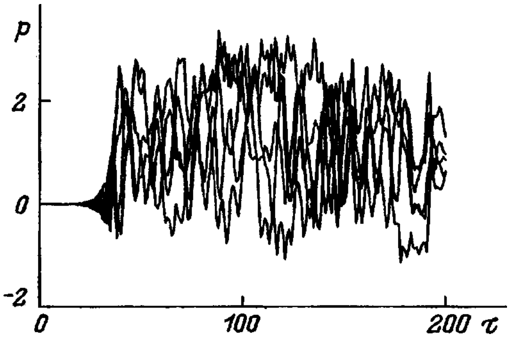

FIG. 2. Time evolution of the normalized electron energy γ if relativistic effects are neglected; $\Delta=1.05$, $I=0.025$, and $|\tilde{a}_i^0|^2=4$.

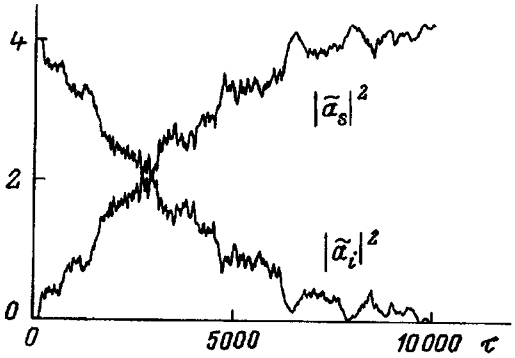

FIG. 3. Time dependence of the square amplitudes $|\tilde{a}_i|^2$ and $|\tilde{a}_s|^2$ of the incident and scattered waves, respectively, when relativistic effects are taken into account; $\Delta=0.67$, $I=0.025$, $|\tilde{a}_i|^2=4$.

The importance of taking relativistic effects into account stems from the fact that as an electron acquires energy, its translational velocity approaches the speed of light and becomes close to the phase velocity of the combination wave. As a result, a relativistic electron is accelerated for a long time at the same phase (according to Eq. (8), $d\Theta_c/\delta\tau\to 0$ as $p_z/\gamma\to 1$; Fig. 5d). At the same time there is no such autoresonance when the equations for the phase are written in the form (14).

The nonlinear stage of the interaction with relativistic effects taken into account was investigated by a numerical modeling of the self-consistent system of equations (8)–(11) by the particle-in-cell (macroparticle) method. It was assumed that the pump wave is incident on an initially cold plasma in which small fluctuations of the electron density exist, i.e., the initial conditions have the form

$$p_0=0,\quad \tilde{a}_i^0=2,\quad \tilde{a}_s^0=0,$$

$$\Theta_c^0=\Theta_0+r\cos\Theta_0,\quad r=0.001. \tag{16}$$

The results of the modeling of the system of equations (8)–(11) with initial conditions (16) and parameter values $\Delta=0.67$ and $I=0.025$ are given in Figs. 3, 4, and 5. In the calculations only the first terms in the series in Eq. (9) was

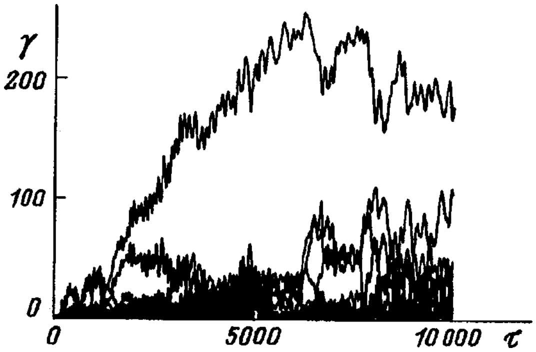

FIG. 4. Time evolution of the normalized electron energy γ.

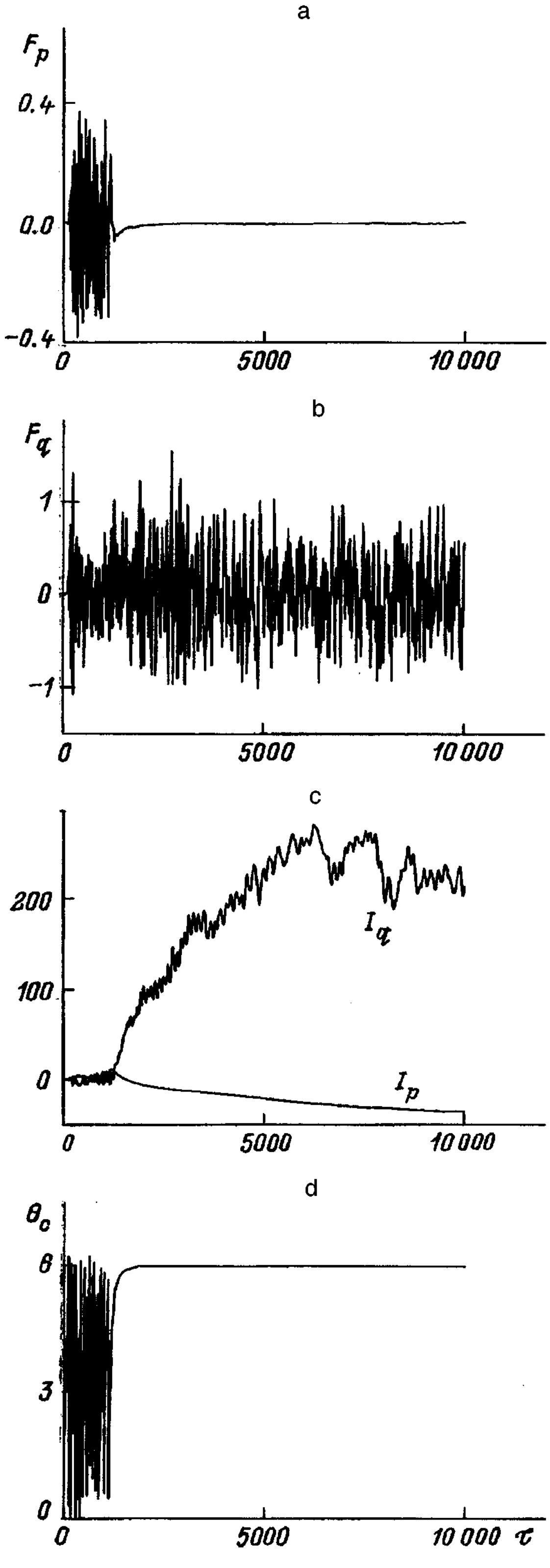

FIG. 5. Time dependence of the ponderomotive force F_p (a) and Coulomb force F_q (b) acting on the accelerated electron fraction, of the integrals I_p and I_q of these forces (c), and of the phase Θ_c of the electron relative to the combination wave (d).

kept, since a numerical modeling showed that taking the higher harmonics of the field into account does not lead to any qualitative changes in the character of the scattering or electron acceleration.

The time dependence of the square amplitudes of the incident and scattered waves are shown in Fig. 3. The stage of exponential growth of the signal amplitude $\hat{a}_s$ is in good agreement with the growth rate determined by Eq. (13). As a result of the scattering process, for $\tau<\tau_1\approx 8000$ there is almost complete transfer of the energy of the incident wave into the scattered wave. Analysis of the time dependence of the energies of all the electron fractions in units of the electron rest energy $m_ec^2=0.511\,\mathrm{MeV}$ (Fig. 4) shows that two stages can be distinguished in the acceleration process. In the first stage, for $\tau<\tau_0\approx 1500$, there is an increase in the energy of all the electron fractions, i.e., there is in fact a heating of the electrons, the maximum energy of which does not exceed 20 MeV ($\gamma<40$). In the second stage, for $\tau_0<\tau<\tau_1$, when the most efficient scattering of the pump wave occurs, a small fraction of the electrons is accelerated to an energy of 120 MeV ($\gamma=240$), while the energies of the remaining electron fractions remain practically the same as in the first stage.

The mechanism of acceleration of the electron fraction can be traced in Fig. 5a–d. It is clear that the cause of the acceleration is the stochastic interaction of the electrons with the ponderomotive and plasma waves, the phase velocity of which in the given model is equal to the speed of light. In the first stage ($\tau<\tau_0$) the ponderomotive force F_p (Fig. 5a) and the Coulomb force F_q (Fig. 5b) acting on the accelerated electron fraction are of the same order, and acceleration occurs under the influence of both forces. As the electrons are accelerated and their mass increases, the ponderomotive force acting on them decreases, with the result that for $\tau>\tau_0$ the acceleration occurs predominantly under the influence of the longitudinal plasma waves. Indeed, as can be seen from Fig. 5c, the value of the time integral I_q of the Coulomb force is much larger than the corresponding integral I_p of the ponderomotive force.

Numerical estimates show that when laser radiation of intensity $W=5\times10^{18}\,\mathrm{W/cm^2}$ ($\tilde{a}_i^0=2$) and wavelength $\lambda=1.054\,\mu\mathrm{m}$ ($I=0.025$) acts on a plasma of density $n_e=10^{19}\,\mathrm{cm^{-3}}$ ($\omega_p=1.78\times10^{14}\,\mathrm{s^{-1}}$), electrons are accelerated to an energy of 100 MeV over a time $t\approx 25\,\mathrm{ps}$, and the maximum amplitude of the plasma waves reaches $E_q\approx 10^{11}\,\mathrm{V/m}$.

The acceleration occurs most efficiently if the scattering of laser wave occurs not on a cold plasma but on a beam of electrons with an initial longitudinal velocity close to the speed of light. For comparison, Fig. 6 shows the acceleration of particles in the case of an initial electron energy of 1.6 MeV. It is seen that at the same values of the pump intensity and wavelength the energy of one of the fractions reaches 350 MeV; in that case the time of energy acquisition is shortened substantially. Thus for the investigated acceleration mechanism the optimal situation is for the scattering to occur in a dense plasma into which is injected a beam of electrons with an energy of the order of a few MeV.

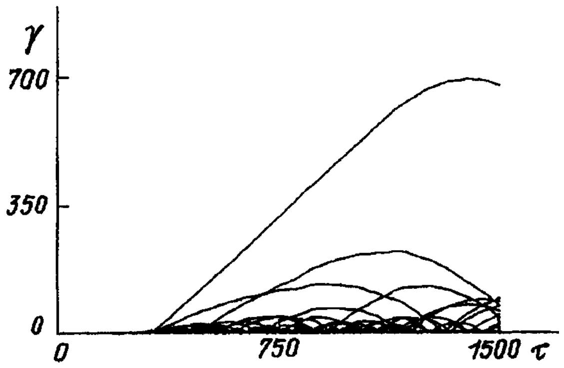

FIG. 6. Time dependence of the normalized electron energy in the scattering of a wave on an electron beam; $p_0=3$, $\Delta=1.6$, $I=0.025$, and $|\tilde{a}_i^0|^2=4$.

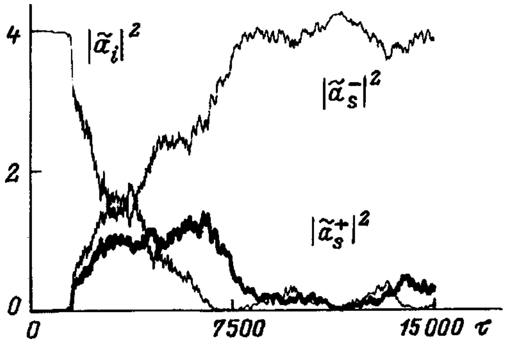

FIG. 7. Time evolution of the square amplitude $|\tilde{a}_i|^2$ of the incident wave field and of the Stokes $|\tilde{a}_s^-|^2$ and anti-Stokes $|\tilde{a}_s^+|^2$ components of the scattered wave for $\Delta=0.71$, $I=0.025$, and $|\tilde{a}_i^0|^2=4$.

EXCITATION OF THE ANTI-STOKES COMPONENT

Excitation of the anti-Stokes component of the field of the scattered radiation was observed in the experiments described in Refs. 9 and 10. That process can also be taken into account in the model investigated here.

Suppose that there exist two scattered waves $\mathbf{A}_s^+$ and $\mathbf{A}_s^-$ of circular polarization, with frequencies $\omega_s^+=\omega_i+\Delta\omega_p$ and $\omega_s^-=\omega_i-\Delta\omega_p$, respectively, i.e., the detuning from the frequency of the incident wave is the same for the two waves. In this case, using the same normalization as for equations (8)–(11), we have the self-consistent system of equations

$$\frac{d\Theta_c}{d\tau}=\Delta\left(1-\frac{p}{\gamma}\right), \tag{17}$$

$$\frac{dp}{d\tau}=\frac{\Delta}{\gamma}\mathrm{Re}[i\tilde{a}_s^+\tilde{a}_i^*\exp(i\Theta_c)-i\tilde{a}_s^-\tilde{a}_i^*\exp(-i\Theta_c)$$
$$+2i\tilde{a}_s^+(\tilde{a}_s^-)^*\exp(2i\Theta_c)]+\frac{1}{\Delta}\mathrm{Re}\left[i\sum_{n=1}^{\infty}\rho_n\exp(in\Theta_c)\right], \tag{18}$$

$$\frac{d\tilde{a}_s^-}{d\tau}=\frac{i}{1/I-4\Delta}(\tilde{j}_1^*\tilde{a}_i+\tilde{j}_2^*\tilde{a}_s^+),$$

$$\frac{d\tilde{a}_s^+}{d\tau}=\frac{i}{1/I+4\Delta}(\tilde{j}_1\tilde{a}_i+\tilde{j}_2\tilde{a}_s^-), \tag{19}$$

$$\frac{d\tilde{a}_i}{d\tau}=iI(\tilde{j}_1\tilde{a}_s^-+\tilde{j}_1^*\tilde{a}_s^+), \tag{20}$$

where $\gamma=(1+p^2+|\tilde{a}_i|^2+|\tilde{a}_s^-|^2+|\tilde{a}_s^+|^2+2\mathrm{Re}[\tilde{a}_s^+(\tilde{a}_s^-)^*\times\exp(2i\Theta_c)+\tilde{a}_s^+\tilde{a}_i^*\exp(i\Theta_c)+\tilde{a}_s^-\tilde{a}_i^*\exp(-i\Theta_c)])^{1/2}$.

The results of a numerical modeling of this system with initial conditions (16) and the parameter values $\Delta=0.71$ and $I=0.025$ show that excitation of the anti-Stokes component is indeed observed during the acceleration of the electrons (Fig. 7).

It should be noted that excitation of the anti-Stokes component can occur only together with the Stokes, since it follows from a solution of the dispersion relation (13) under the condition $\Delta<0$ that the growth rate for a scattered wave with a frequency higher than that of the incident wave is equal to zero. If, however, both scattered waves are taken into account, then, since the growth rate for the Stokes component is greater than zero, plasma waves are excited which initiate the excitation of the anti-Stokes component.

The authors thank V. A. Mironov, M. D. Tokman, and G. M. Fraĭman for a helpful discussion.

[1] A. V. Gaponov and M. A. Miller, Zh. Éksp. Teor. Fiz. **34**, 242 (1958) [Sov. Phys. JETP **7**, 168 (1958)].
[2] T. Tajima and J. M. Dawson, Phys. Rev. Lett. **43**, 267 (1979).
[3] F. Amiranoff, A. Antonetti, P. Audebert *et al.*, Plasma Phys. Controlled Fusion **38**, 295 (1996).
[4] Ya. B. Faĭnberg, Fiz. Plazmy **13**, 607 (1987) [Sov. J. Plasma Phys. **13**, 350 (1987)].
[5] Ya. B. Faĭnberg, A. K. Berezin, V. A. Balakirev *et al.*, Relyativistskaya vysokochastotnaya élektronika. Nizhniĭ Novgorod, No. 7, 104–134 (1992).
[6] P. Sprangle, E. Esarey, J. Krall *et al.*, Phys. Rev. Lett. **69**, 2200 (1992).
[7] T. M. Antonsen and P. Mora, Phys. Rev. Lett. **69**, 2204 (1992).
[8] W. B. Mori, C. D. Decker, D. E. Hinkel *et al.*, Phys. Rev. Lett. **72**, 1482 (1994).
[9] A. Modena, A. E. Dangor, Z. Najmudin *et al.*, Nature (London) **377**, 606 (1995).
[10] A. Modena, A. E. Dangor, Z. Najmudin *et al.*, IEEE Trans. Plasma Sci. **PS-24**, 289 (1996).
[11] V. A. Kozlov, A. G. Litvak, and E. V. Suvorov, Zh. Éksp. Teor. Fiz. **76**, 147 (1979) [Sov. Phys. JETP **49**, 75 (1979)].
[12] V. L. Bratman, N. S. Ginzburg, and M. I. Petelin, Zh. Éksp. Teor. Fiz. **76**, 930 (1979) [Sov. Phys. JETP **49**, 469 (1979)].
[13] A. G. Litvak, V. I. Petrukhina, and V. Yu. Trakhtengerts, JETP Lett. **18**, 111 (1973).

Translated by Steve Torstveit

BRIEF COMMUNICATIONS

Steady-state thermonuclear plasma as a source of nuclear-physics data

V. G. Kiptilyĭ and V. O. Naĭdenov

A. F. Ioffe Physicotechnical Institute, Russian Academy of Sciences, 194021 St. Petersburg, Russia

(Submitted July 10, 1997)
Zh. Tekh. Fiz. **69**, 114–118 (January 1999)

Measurements of cross sections of nuclear reactions of charged particles in the kiloelectron-volt range present a difficult experimental problem because of their small size. At the same time, the need for accuracy in the determination of such cross sections continues to grow in connection with the active development of such branches of science as controlled thermonuclear fusion, astrophysics, cosmology, and nuclear physics itself. The present communication discusses the motivation for performing experiments in this energy range and the difficulties such experiments involve, and proposes a new experimental approach to measuring the cross sections of such reactions using the steady-state plasmas available in thermonuclear facilities. © *1999 American Institute of Physics.* [S1063-7842(99)01901-7]

INTRODUCTION

Nuclear physics has made it possible to place the solution of many problems of cosmology, astrophysics, and plasma physics on a quantitative basis. In turn, the development of these sciences poses new problems for nuclear physics, the prospects for solution of which depend on the level of knowledge and experimental database of nuclear physics. A striking example of this interaction is provided by ongoing research on the problem of solar neutrinos. The nuclear-physics approach to the solution of this problem[1] is to examine peculiarities of the mechanisms of low-energy nuclear reactions. This is not the only example of this kind, and for this reason it is of interest to consider a number of basic problems whose solution requires a knowledge of cross section data on the nuclear reactions of light nuclei at astrophysical energies. We did not set it as our goal in Sec. 1 to provide an exhaustive review, rather this paper should be viewed as an attempt to highlight what in our opinion are the most important directions in this field. Section 2 discusses the difficulties of experimentally examining low-energy nuclear reactions, and also problems of analysis and interpretation of data. Section 3 provides a description of a new experimental approach to obtaining information about nuclear cross sections and represents an attempt to put it on a solid basis. It is proposed to use a thermonuclear plasma like those existing in tokamaks as a source of low-energy nuclear reactions.

1. SOME LOW-ENERGY NUCLEAR-PHYSICS PROBLEMS

a) *Liberation of heat in stars.* Self-consisting stellar models which yield observable characteristics (brightness, size, mass, temperature, etc.) are based on the assumption of the thermonuclear nature of the liberated energy as a result of an entire train of exothermic nuclear reactions. For example, static nucleosynthesis in stars of the main sequence such as the Sun pass through the hydrogen ($p-p$) and the carbon–nitrogen (CNO) cycle. At the same time, the cross section of the main reaction of the $p-p$ cycle $p+p\rightarrow d+e^{+}+\nu$ and of an entire train of others in this chain have either not been measured or have been measured with insufficient accuracy, e.g., the reaction $^{7}\mathrm{Be}+p\rightarrow{}^{8}\mathrm{B}+\gamma$. None of the cross sections of the reactions of the $p-p$ cycle have been measured at energies of the order of 1.5 keV, corresponding to the temperature at the center of the Sun. At present, physical conclusions are based on cross sections extrapolated from values measured at higher energies.

To solve the problem of solar neutrinos, additional data on cross sections of the reactions $^{3}\mathrm{He}+{}^{3}\mathrm{He}\rightarrow{}^{4}\mathrm{He}+2p$, $^{3}\mathrm{He}+{}^{4}\mathrm{He}\rightarrow{}^{7}\mathrm{Be}+\gamma$, $^{7}\mathrm{Be}+p\rightarrow{}^{8}\mathrm{B}+\gamma$, and $^{15}\mathrm{N}+p\rightarrow{}^{16}\mathrm{O}+\gamma$ can be of great significance.

Stars at later stages of the evolution of ''hot matter'' contain the heavier elements ^{4}He, ^{12}C, ^{14}N, ^{16}O, etc. And although the temperature in the interiors of such stars is higher than for the Sun, the higher Coulomb barrier significantly lowers the probability of nucleosynthesis. Here the situation with the experimental data is even more dramatic. Thus, the authors of Ref. 2, for example, use the most recent nuclear data, which differ from the data published earlier in the review of Ref. 3 — by a factor of 1.7 in the case of the reaction $^{12}\mathrm{C}(\alpha,\gamma)^{16}\mathrm{O}$, and by two to three orders of magnitude for the reactions $^{17}\mathrm{O}(p,\gamma)^{18}\mathrm{F}$ and $^{17}\mathrm{O}(p,\alpha)^{14}\mathrm{N}$.

b) *Nucleosynthesis.* The problem of nucleosynthesis can be divided into two parts: synthesis of primordial elements and synthesis of elements in subsequent stages of the evolution of the Universe. The first direction, if we retain the model of a hot Universe, does not touch directly upon the problem discussed in the present paper, since the process of formation of primordial elements occurs at relatively high energies (0.1–1 MeV) and the necessary reactions are quite well known. Problems still arise here, associated with experimental difficulties of absolute measurements. Thus one can discern a clear pattern over the last 20 years in which papers have periodically appeared which do not address the fundamentals of the theory but rather apply new, refined cross-section data.[4]

The abundance of primordial elements such as H, D, ^{3}He, ^{4}He, and ^{7}Li, serves as a starting point for models of the chemical evolution of stars, galaxies, interstellar matter, etc. The most sensitive to the parameters of the evolutionary models are D, ^{3}He, and ^{7}Li. In this regard, the deuterium content, in contrast to ^{3}He and ^{7}Li, during the evolution of a star can only decrease relative to the content of a primordial element. Comparison of calculations with experiment is hindered as a result of the large spread of data in the elemental content of various objects of the Universe. Thus, the deuterium content of the protosolar matter, if we identify the latter with the atmospheres of Saturn, Jupiter, Uranus, and Neptune, varies from $(1.6\pm1.3)\times10^{-5}$ (Ref. 5) to $(3.6\pm1.4)\times10^{-5}$ (Ref. 6), given as the D/H ratio. Evolutionary models[7] predict a decrease of the D/H ratio by a factor of 2–2.5 between the primordial state and the present state of the Universe. At the same time, the first measurements of the primordial deuterium content[8,9] in the direction of the quasar $Q0014+813$ $(z=3.32)$ gave $\mathrm{D/H}=2\times10^{-4}$. If direct measurements of primordial deuterium are confirmed, then it will become necessary to reconsider the evolutionary model of the Universe and introduce into consideration as-yet unknown processes of rapid burnup of deuterium.

An analogous situation arises in the case of ^{3}He; the evolutionary models[7] predict values $5-7$ times greater than the values corresponding to the time of formation of the Sun, and 5–20 times greater than the values corresponding to the *HII* galactic regions (compact blue galaxies with low heavy-element content, which are identified with the smallest chemical evolution. Calculations by the authors of Ref. 7 show that the problem can be eliminated if there exists a hypothetical energy resonance below 10 keV in the nuclear reaction $^3\mathrm{He}+{}^3\mathrm{He}\rightarrow{}^4\mathrm{He}+2p$. The existence of this resonance was first proposed to solve the solar neutrino problem.[10,11] In fact, a special accelerator was built just to study this reaction at low energies (Project LUNA) under ultralow background conditions.[12]

c) *Controlled thermonuclear fusion (CTF).* Most thermonuclear facilities of tokamak type use DD plasma at temperatures of $0.5-15$ keV. For additional high-frequency heating, small amounts of H and ^{3}He are added to the plasma. Recent experiments with DT plasma at the large JET and TFTR thermonuclear facilities have shown that self-sustained burning can now be achieved in an experimental thermonuclear reactor. Obviously, the accuracy requirements on the cross section data on the nuclear reactions taking place in the plasma increase with the approach of the practical use of thermonuclear energy.

There is another aspect to the problem of nuclear reactions in CTF, namely the search for ''cleaner'' fuels and final products (in the sense of their radioactivity) $^6\mathrm{Li}+\mathrm{H}\rightarrow{}^3\mathrm{He}+{}^4\mathrm{He}$, $^{11}\mathrm{B}+\mathrm{H}\rightarrow3{}^4\mathrm{He}$, and $^{10}\mathrm{B}+\mathrm{H}\rightarrow{}^7\mathrm{Be}+{}^4\mathrm{He}$. The lowest energy at which the last reaction was studied was 18.7 keV (Ref. 13). The results indicate that a resonance can be expected at 10 keV, which corresponds to a plasma temperature around 4.9×10^6 K. A study of this problem would be incomplete without a parallel study of the competing channel of the reaction $^{10}\mathrm{B}+\mathrm{H}\rightarrow{}^{11}\mathrm{C}+\gamma$.

d) *Nuclear-physics problems.* A study of nuclear interactions of small-nucleon systems and especially reactions of radiative capture occupies a special place in nuclear physics since in some cases it allows one to calculate the contributions of different reaction channels. As was already noted, problems of low-energy resonances are very important.

In this sense, the reaction $\mathrm{D}(d,\gamma)^4\mathrm{He}$ is of special interest since a study of this reaction can provide information about the structure of the wave functions of a system of two deuterons in the region of the continuum and the ground state of ^{4}He. Cross sections of the reaction $\mathrm{D}(p,\gamma)^3\mathrm{He}$ at low energies are needed to investigate scattering in $n-d$ and $p-d$ three-nucleon systems and also capture of p and s protons with subsequent transition to the ground state $2S_{1/2}$ of the ^{3}He nucleus via $E1$ and $M1$ transitions. The authors of Ref. 14 calculated the contributions of $E1$ and $M1$ amplitudes to the total cross section of the reaction $\mathrm{D}(p,\gamma)^3\mathrm{He}$. They showed that their ratio varies quite noticeably as a function of the reaction energy: $E1{:}M1=3{:}2$ for 1.2 MeV and $E1{:}M1=1{:}9$ for 12 keV. It may be expected that this effect is manifested in the excitation function of the reaction at low energies. Analogous problems arise in the analysis of the reaction $^7\mathrm{Li}(p,\gamma)^8\mathrm{Be}$ (Ref. 15).

2. EXPERIMENTAL PROBLEMS OF CROSS-SECTION MEASUREMENTS

The small value of the cross sections is the main difficulty in experiments performed in the kilovolt energy range. Thus, the cross section of the above-mentioned reaction $^3\mathrm{He}+{}^3\mathrm{He}\rightarrow{}^4\mathrm{He}+2p$ at 25 keV is $(7\pm2)\times10^{-12}b$ (Ref. 16). To measure such cross sections, it is necessary to undertake special measures such as have been undertaken in the German–Italian Project LUNA (Laboratory for Underground Nuclear Astrophysics).[12] A special 50-keV accelerator has been assembled in an underground laboratory (Gran Sasso), where the background level in the case of the reaction $^3\mathrm{He}+{}^3\mathrm{He}\rightarrow{}^4\mathrm{He}+2p$ is of the order of one event per day. Nevertheless, sufficient statistical accuracy at 15 keV is achieved for an exposure of around six months.

In the traditional experimental setup for measuring cross sections of low-energy nuclear reactions there is one more problem, connected with electron screening of the nucleus. This question has been worked out in plasma physics[17] and examined for the case of an astrophysical plasma at various densities and temperatures.[18,19] In the thermonuclear plasma contained in tokamak-type setups, this effect is negligibly small. However, for solid-state and gaseous targets the problem of taking this effect into account has still not been solved. Experiments provide clear evidence of the influence of atomic-shell electrons on the cross section of the nuclear reaction.[12,13]

Screening lowers the Coulomb barrier for the bombarding particle and thus increases the yield of the reaction. The penetrability of the Coulomb barrier at an energy E in the center-of-mass system enters into the expression for the

TABLE I.

Main thermonuclear reactions		Reactions with main impurities		Reactions with other light impurities	
$D(p,\gamma)^3He$,	γ5.5	$^9Be(p,\gamma)^{10}B$,	γ6.6	$^6Li(d,\gamma)^8Be$,	γ22.3
$T(p,\gamma)^4He$,	γ19.8	$^9Be(d,\gamma)^{11}B$,	γ16.8	$^6Li(t,\gamma)^9Be$,	γ17.7
$D(d,\gamma)^4He$,	γ23.8	$^9Be(^3He,\gamma)^{12}C$,	γ26.3	$^7Li(d,\gamma)^9Be$,	γ16.7
$T(d,\gamma)^5He$,	γ16.7	$^{12}C(d,\gamma)^{14}N$,	γ10.3	$^7Li(t,\gamma)^{10}B$,	γ17.3
$^3He(d,\gamma)^5Li$,	γ16.4	$^{12}C(t,\gamma)^{15}N$,	γ14.8	$^{10}B(d,\gamma)^{12}C$,	γ25.2
$T(t,\gamma)^6He$,	γ12.3	$^{14}N(d,\gamma)^{16}O$,	γ20.7	$^{10}B(t,\gamma)^{13}C$,	γ23.9
$^6Li(p,\gamma)^7Be$,	γ5.6,5.2	$^{14}N(t,\gamma)^{17}O$,	γ18.6	$^{11}B(p,\gamma)^{12}C$,	γ16.0
$^7Li(p,\gamma)^8Be$,	γ17.3			$^{11}B(d,\gamma)^{13}C$,	γ18.7
				$^{19}F(p,\gamma)^{20}Ne$,	γ12.8

reaction cross section in the form of the factor $(1/E)\times\exp(-B/\sqrt{E})$, where $B=\pi Z_1 Z_2(e^2/\hbar c)(2\mu c^2)^{1/2}$; $\mu=m_1 m_2/(m_1+m_2)$ is the reduced mass of the reacting particles, and Z_1 and Z_2 are their charges. To achieve a quantitative description of electron screening, an effective potential U is introduced. This is equivalent to the situation in which the bombarding particle penetrates the Coulomb barrier of the ''bare'' target nucleus which is now not at the energy E, but at the effective energy $E+U$. The change in the cross section resulting from screening is expressed by the coefficient

$$f(E)=\frac{\sigma(E+U)}{\sigma(E)}=\exp\left(\frac{U}{2E}\,\frac{B}{\sqrt{E}}\right). \tag{1}$$

It should be noted that the potential U depends on the model and, what is more, as was noted in Ref. 12, in a number of cases there is a significant discrepancy between experiment and the model calculations. In all of the investigated reactions the measured increase in the cross sections is greater than the increase calculated on the basis of current atomic models. An exception is the reaction $^3He+^3He\to^4He+2p$, for which, according to the calculations, $f(E)=1.2$ for $E=25$ keV, and electron screening is not observed experimentally.

The experimental and theoretical difficulties in the determination of the low-energy cross sections have motivated a search for new approaches to the setup of the experiments. One such approach, the basis for which is expounded in Ref. 20, is developed below.

3. STEADY-STATE THERMONUCLEAR PLASMA AS A SOURCE OF NUCLEAR-PHYSICS DATA

a) *Basic principles.* The advances that have been achieved to date with CTF in tokamaks open up definite possibilities for obtaining nuclear data at low energies. This pertains, first of all, to the main thermonuclear reactions D+H, D+D, D+T, D+^{3}He, T+H, and T+T, but does not exclude the possibility of investigating reactions involving the light impurity nuclei which are present in the plasma or are intentionally injected into it in order to carry out the experiment. It should be noted that because of problems connected with the detection of the reaction products, only channels with a neutron or gamma-ray yield allow one to carry out measurements in plasma experiments. Table I lists the main reactions accompanied by the emission of gamma rays.

Such experiments require neutron and gamma-ray spectrometers. This makes it possible to obtain sufficiently accurate relative—and in a number of cases, absolute—measurements. It is not the aim of the present paper to analyze this entire set of reactions; as an example, in the following Section we describe a project that is in preparation.[20]

In a tokamak with small radius of the plasma column a the ion temperature and density varies as a function of the distance r from the center of the plasma as $T(r)=T(0)(1-r^2/a^2)$ and $n(r)=n(0)(1-r^2/a^2)^{1/2}$. The rate of the reaction in the plasma is given by

$$R(r)=\frac{n_1(r)n_2(r)}{1+\delta_{12}}\langle\sigma v\rangle, \tag{2}$$

where $n_1(r)$ and $n_2(r)$ are the radial concentrations of the reacting particles, δ_{12} is the Kronecker delta, and $\langle\sigma v\rangle$ is the rate parameter, which is equal to the reaction cross section averaged over the Maxwell distribution of the particles.

Tokamak measurement complexes have a number of independent diagnostics for determining $T(r)$ and $n(r)$. This makes it possible to use data obtained on such complexes to accurately calculate the reaction rates. The strong dependence of the reaction rates on the ion temperature and density implies that the main contribution to the reaction yield comes from the central part of the plasma. Performing measurements in different operating regimes of the tokamak makes it possible to determine the parameter $\langle\sigma v\rangle$ as a function of temperature. This dependence can also be measured in one temperature regime, but with the help of of several collimated spectrometers observing the plasma along different chords of the plasma column.

As a result of fusion of the main components of the plasma, light charged particles with megavolt energies are formed. For example, in the reaction $D+T\to^4He+n$ alpha particles with energy 3.5 MeV are created. They then thermalize, forming a distinct velocity distribution different from Maxwellian. Nuclear reactions produced by such particles can also be the object of research provided the distribution function is well known, or they can be used for plasma diagnostics.[21]

The proposed approach undoubtedly has limited application, but even so it has great significance for low-energy studies, as it has a number of advantages over the standard experiments. Below we consider some possible means of realizing it.

b) *Measurement of radiation-capture cross sections in a* H/D/T tokamak plasma. The reactions $D+H \rightarrow {}^3He+\gamma$, $D+D \rightarrow {}^4He+\gamma$, and $D+T \rightarrow {}^5He+\gamma$ have been examined in accelerators at energies up to $15-25$ keV (Refs. 22–24), which corresponds to plasma temperatures of 5–10 keV. This energy range is interesting because anomalous behavior of the reaction cross sections has been predicted here.

The idea of the proposed tokamak experiment is to simultaneously measure the 2.45-MeV neutron yield of the reaction $D+D \rightarrow {}^3He+n$ and the yields of the 23.8 and 5.5-MeV gamma rays formed in the reactions $D+D \rightarrow {}^4He+\gamma$ and $D+H \rightarrow {}^3He+\gamma$, and thereby determine the relative reaction parameters. In the case of a DT plasma it is necessary to detect 14.1-MeV neutrons and and 16.7-MeV gamma rays. This kind of experiment requires larger tokamaks of the type T-15, JT-60U, JET, and TFTR.

The neutron and gamma-ray spectrometers should be placed in a collimator in order to view the central part of the plasma and lower the background. As a spectrometer for the 2.45-MeV neutrons it is possible to use an NE213 liquid scintillator. To record gamma radiation it is necessary to have a detector with high sensitivity to energetic photons, e.g., a multicrystal GAMMACELL spectrometer,[25] which is a total-energy gamma-ray absorption detector.

In the case of the reactions $D+T \rightarrow {}^5He+\gamma$ and $D+T \rightarrow {}^4He+n$, it is possible to use one detector to record 14.1-MeV neutrons and 16.7-MeV gamma rays, selecting the events by the shape of their signals. The relatively high rates of these reactions makes it possible to perform some unique measurements—two-dimensional $n\gamma$-tomography of a DT tokamak plasma using two detecting setups of the pinhole-camera type. Such an experiment does not give temperature-integrated information, but rather differential information about the ratio of reaction cross sections.

One of the main difficulties of tokamak experiments has to do with the fact that the existence time of a steady-state Maxwellian plasma is still limited to several seconds, i.e., the problem of a statistically significant experiment arises. Speed-of-light estimates made with a GAMMACELL spectrometer in Ref. 25 show that limiting plasma temperatures at which the measurement results of the experiments will be reliable correspond to an energy range that is essentially unattainable for accelerator experiments.

Diagnostic measurements of gamma radiation in tokamak experiments show that the gamma-ray spectra extend to energies of 10–12 MeV, and their intensity depends on the rate of the thermonuclear reaction. Estimates of the background level for the geometry of a T-15 tokamak showed that at a plasma temperature of 10 keV the signal exceeds the background in the gamma-ray spectrum by a factor of 2–4 for an energy of 5.5 MeV. This ratio varies only slightly when the temperature is lowered.

CONCLUSION

The proposed approach to measurement of the cross sections of nuclear reactions using a tokamak plasma can substantially extend the energy range (1–10 keV) of the experimental data of important reactions for astrophysics, nuclear physics, and plasma physics. In contrast to accelerator measurements, this approach does not require one to take account of model corrections to the electron screening. A comparison of measurement results obtained by different experimental methods would make it possible to estimate the adequacy of the implemented models.

[1] J. N. Bahcall, *Neutrino Astrophysics* (Cambridge University Press, New York, 1989).

[2] O. Aubert, N. Prantos, and I. Baraffe, Astron. Astrophys. **312**, 845 (1996).

[3] G. Caughlan and W. A. Fowler, At. Data Nucl. Data Tables **40**, 291 (1988).

[4] T. P. Walker, G. Steigman, D. N. Schramm *et al.*, Fermilab-Pub-91/36-A (1991).

[5] R. Courtin, D. Gautier *et al.*, Astrophys. J. **287**, 899 (1984).

[6] V. G. Kunde *et al.*, Astrophys. J. **263**, 443 (1982).

[7] D. Galli, F. Palla *et al.*, Astrophys. J. **443**, 536 (1995).

[8] A. Songaila, L. L. Cowie *et al.*, Nature (London) **368**, 599 (1994).

[9] R. F. Carswell, M. Rauch *et al.*, MNRAS, Vol. 268, p. L1 (1994).

[10] V. N. Fetisov and Y. S. Kopysov, Phys. Lett. B **40**, 602 (1972).

[11] W. A. Fowler, Nature (London) **238**, 23 (1972).

[12] G. Fiorentini, R. W. Kavanagh, and C. Rolfs, Z. Phys. A **350**, 289 (1995).

[13] C. Angula, S. Engstler *et al.*, Z. Phys. A **345**, 231 (1993).

[14] J. L. Ballot, A. M. Eiro, and F. D. Santos, in *Nuclei in the Cosmos*, edited by H. Oberhummer, Vienna, 1990, pp. 157–162.

[15] R. M. Chasteler, H. R. Weller *et al.*, Phys. Rev. Lett. **72**, 3949 (1994).

[16] A. Krauss, H. W. Becker *et al.*, Nucl. Phys. A **467**, 273 (1987).

[17] E. E. Sulpeter, Austr. J. Phys. **7**, 373 (1954).

[18] Setsuo Ichimaru, Rev. Mod. Phys. **65**, 255 (1993).

[19] H. Dzitko, Tureck-Chieze *et al.*, Austr. J. Phys. **447**, 428 (1995).

[20] V. G. Kiptily, V. O. Naidenov, I. A. Polunovsky, Pis'ma Zh. Tekh. Fiz. **20**(10), 33 (1994) [Tech. Phys. Lett. **20**, 400 (1994)].

[21] V. G. Kiptily, A. S. Mishin, V. O. Naidenov *et al.*, EPA, Vol. 14B, Pt. 4, pp. 1688–1692 (1990).

[22] C. M. Griffits *et al.*, Can. J. Phys. **41**, 724 (1963).

[23] F. J. Wilkinson and F. E. Cecil, Phys. Rev. C **31**, 2036 (1985).

[24] F. E. Cecil and F. J. Wilkinson, Phys. Rev. Lett. **53**, 767 (1984).

[25] V. G. Kiptily *et al.*, in *Diagnostics for Experimental Thermonuclear Fusion Reactors*, edited by P. E. Stott, G. Gorini, and E. Sindoni (Plenum Press, New York, 1996), pp. 463–466.

Translated by Paul F. Schippnick

TECHNICAL PHYSICS VOLUME 44, NUMBER 1 JANUARY 1999

Radio-frequency power compressor

V. I. Ivannikov, Yu. D. Chernousov, and I. V. Shebolaev

Institute of Chemical Kinetics and Combustion, Siberian Branch of the Russian Academy of Sciences, 630090 Novosibirsk, Russia

(Submitted August 18, 1997)
Zh. Tekh. Fiz. **69**, 119–120 (January 1999)

An rf power compressor is proposed which contains two standing-wave cavities mounted to the side wall of the waveguide to form amplified rf pulses. © *1999 American Institute of Physics.* [S1063-7842(99)02001-2]

Radio-frequency power pulses can be produced with rapid extraction of the accumulated energy from compressors — systems containing high-Q storage cavities and input–output devices.[1] The SLED system,[2] in which the compressor contains two storage cavities and a three-decibel coupler (bridge), has obtained wide practical use. Storage of rf energy in the compressor takes place when the generator connected to the system is switched on, and output takes place upon rapid phase reversal of the generator. Since this compressor scheme was first proposed it has been applied in unmodified form, which is explained by its simplicity and functionality. To decrease the electric field strength in the coupling aperture of the cavity with the waveguide, it has been proposed to increase the number of coupling apertures to two.[3] The device can also be set up without a bridge by using a traveling-wave cavity (VPM system[4]); however, this is unacceptable in the ten-centimeter range due to the absence of sufficiently compact high-Q cavities of this type.

Connecting the cavities to the side wall of the waveguide (using the scheme of ''parallel coupling'' of the cavities with a reflection compensation line[5]), it is possible to set up the compressor without a bridge using standing-wave cavities. A diagram of such a device is shown in Fig. 1. Cavities *A* and *B*, which could be cavities for the $H_{102}(A)$ and $H_{101}(B)$ modes, for example, are coupled along the narrow wall with the waveguide (*4,5*) by coupling apertures *1–3*, where apertures *1* and *2* are identical. We assume that the resonant frequencies of the cavities are identical and equal to the frequency of the exciting signal ω. The distance between coupling apertures *1* and *2* is equal to $\lambda_g/2$, and between *1* and *3*, to $\lambda_g/4$, where λ_g is the wavelength in the waveguide, i.e., coupling apertures *1* and *2* are arranged symmetrically relative to aperture *3*. With the aid of such a device it is possible to form amplified rf power pulses analogous to the scheme in Ref. 2. To get a better picture of the operation of this device, consider transient processes in the system. Let a wave with amplitude a enter the system at its input end *4* during times $t \geqslant 0$; as a result the wave a_{out} is formed at its output *5*. At any time t, each of the coupling apertures emits a symmetrical wave in toward the two ends of the waveguide *4, 5*. The emitted waves interfere with each other and with the incident wave. For the stored energy in the cavities W_1 and W_2 we can write[6]

$$dW_1/dt = P_{41} - P_{14} - P_{13} + P_{31} + P_{32} - P_{23} - P_{25} - P_{11},$$

$$dW_2/dt = P_{13} - P_{31} + P_{23} - P_{32} - P_{22}, \tag{1}$$

where $P_{41} = a^2/2$ is the power of the signal incident on the input *4*, $P_{14} = (2T_1a_1 - T_2a_2)^2/2$, $P_{13} = (a - T_1a_1)^2/2$, $P_{31} = (T_2a_2 - T_1a_1)^2/2$, $P_{32} = (a - T_1a_1 - T_2a_2)^2/2$, $P_{23} = T_1^2a_1^2/2$, $P_{25} = (a - 2T_1a_1 - T_2a_2)^2/2 = a_{\text{out}}^2/2$ is the power of the signal that has passed aperture *2* and been emitted from the output *5*, $P_{11} = \omega W_1/Q_1$ and $P_{22} = \omega W_2/Q_2$ are the power losses in the cavities, a_1 and a_2 are the amplitudes of the waves in the first and second cavities, T_1 and T_2 are the transfer coefficients of apertures *1* and *2* and of aperture *3*, respectively; and Q_1 and Q_2 are the intrinsic Q factors of the two cavities.

Introducing the notation $V_1^2/2 = W_1$ and $V_2^2/2 = W_2$, it can be shown that $2T_1a_1 = V_1(\omega k_1/2Q_1)^{1/2}$ and $T_2a_2 = V_2(\omega k_2/2Q_2)^{1/2}$, where k_1 and k_2 are the coupling coefficients of cavities *A* and *B*, respectively with the waveguide *4, 5*. Substituting these relations into Eqs. (1) we obtain for V_1 and V_2

$$dV_1/dt = a(\omega k_1/2Q_1)^{1/2} - (1 + k_1)\omega V_1/2Q_1,$$

$$dV_2/dt = a(\omega k_2/2Q_2)^{1/2} - (1 + k_2)\omega V_2/2Q_2. \tag{2}$$

The variables separate and the solutions for V_1 and V_2 are independent

$$V_1 = a(2Q_1k_1/\omega)^{1/2}(1 - \exp(-t/\tau_1))/(1 + k_1),$$

$$\tau_1 = 2Q_1/\omega(1 + k_1),$$

$$V_2 = a(2Q_2k_2/\omega)^{1/2}(1 - \exp(-t/\tau_2))/(1 + k_2),$$

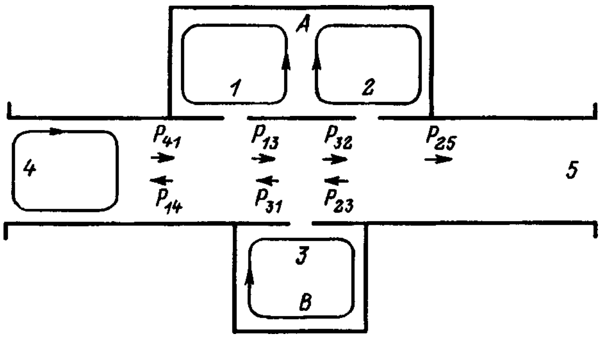

FIG. 1.

$\tau_2 = 2Q_2/\omega(1+k_2)$.

There is no coupling between the cavities since for the chosen symmetrical geometry of the coupling apertures the waves emitted from apertures *1* and *2* of cavity *A* arrive at aperture *3* of cavity *B* with opposite phase and cavity *B* is therefore not excited by these waves. Correspondingly, cavity *A* is not excited by waves emitted by cavity *B*. Therefore, oscillations are set up in each cavity independently and the phase shift between them is determined only by the distance between coupling apertures *1* and *3* and is equal to $\pi/2$.

Let $k_1 = k_2 = k$, $Q_1 = Q_2 = Q$, $\tau_1 = \tau_2 = \tau = 2Q/\omega(1+k)$. In this case, the compressor does not reflect in the transient or steady-state regime and the transmitted wave a_{out} is given by $a_{\mathrm{out}} = a(1-\exp(-t/\tau))(1-k)/(1+k)$. For $k=1$ the condition of critical coupling of the entire compressor with the line is realized in the steady-state regime: the system does not reflect and $a_{\mathrm{out}}=0$. Here each cavity is also critically coupled with the waveguide. For $k \gg 1$ in the steady-state regime, similar to the situation in Ref. 2, $a_{\mathrm{out}} \approx -a$ (a characteristic feature of compressors of SLED type — the phase of the transmitted wave at the output of the system is opposite to that of the incident wave). If the phase of the generator is shifted by π (the output regime of Ref. 2) after completion of the energy storage process, then the transmitted wave $a_{\mathrm{out}} = -a[1+(2k/(1+k))\exp(-t/\tau)]$. Here $t=0$ corresponds to initiation of output. For large k, as in Ref. 2, the wave $a_{\mathrm{out}} \approx -3a$ at the initiation of output.

Operation of the scheme was tested at the frequency $f = 2856$ MHz at a low power level. The cavities were constructed from a standard rectangular waveguide of cross section 72×34 mm. The characteristic tuning points were checked for the coupling coefficients of the coupling of the cavities with the line equal to $k=1$ and 4.5. For a single cavity connected to the side wall of the cavity, the relation between the standing-wave coefficient ρ in the line and the coupling coefficient k is given by $\rho = 2k+1$. Each cavity was tuned separately and their frequencies coincided. The band characteristic of the signal transmitted by the tuned system has the form of a curve with one minimum symmetric about the frequency f for any k. For $k=1$ at the frequency f the power is almost completely absorbed in the cavities. For $k=4.5$ the level of the transmitted signal for a matched pair was -4 dB (the calculated value is -3.9 dB). The dependence of ρ on frequency (the band characteristic of the reflected signal of the pair of cavities) in this case because of the different intrinsic Q factor has the form of a two-humped curve (Fig. 2) with its minimum at f ($\rho = 1.08$). AT the reflection maxima $\rho \approx 1.3$. Pulsed measurements were performed during the operation of an rf generator in the continuous regime; phase reversal occurred at 1 kHz. The measured gain coefficient for $k=1$ was 5.5 dB (calculated value 6 dB), and for $k=4.5-7.6$ dB (8.4 dB). The measurements showed that for $k=1$ and 4.5 the qualitative and quantitative parameters of the system were close to the calculated values. Differences between the experimental and calculated values were due to inaccuracies in the construction and tuning of the system, measurement errors, and also radiative losses from the cavities during phase reversal of the generator.

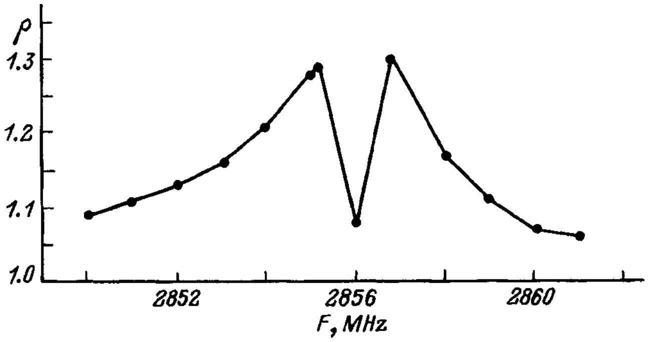

FIG. 2.

The considered pulsed rf power compressor has all the positive features of a SLED system, plus the advantage of no bridge. Such a design can be used in upgrades of compression systems. Note that the possibility of coupling an H_{015} cavity with a waveguide shorted out at one end with the coupling realized by two apertures shifted by $\lambda_g/2$ was tested in Ref. 3. In the proposed device this was realized for a traveling wave in the waveguide and with a H_{102} cavity. Since the field structure in the region of the coupling apertures coincides for H_{102} and H_{015} cavities, the results of the present study also apply to cavities of H_{015} type.

[1] A. N. Didenko and Yu. G. Yushkov, *High-Power Microwave Pulses of Nanosecond Duration* [in Russian], Energoatomizdat, Moscow, 1984.
[2] Z. D. Farkas *et al.*, in *Proceedings of the Ninth Conference on High Energy Accelerators*, 1974, pp. 576–582.
[3] H. Matsumoto *et al.*, Nucl. Instrum. Methods Phys. Res. A **330**, 1 (1993).
[4] V. E. Balakin and I. V. Syrachev, in *Proceedings of the Third International European Particle Accelerator Conference*, 1992, p. 1173.
[5] V. I. Ivannikov, Yu. D. Chernousov, and I. V. Shebolaev, Zh. Tekh. Fiz. **56**, 2407 (1986) [Sov. Phys. Tech. Phys. **31**, 1441 (1986)].
[6] V. I. Ivannikov, Yu. D. Chernousov, and I. V. Shebolaev, Zh. Tekh. Fiz. **66**(5), 162 (1996) [Tech. Phys. **41**, 493 (1996)].

Translated by Paul F. Schippnick

TECHNICAL PHYSICS VOLUME 44, NUMBER 1 JANUARY 1999

Characteristics of the formation of radiation defects in silicon structures

Sh. Makhkamov, N. A. Tursunov, M. Ashurov, R. P. Saidov, and S. V. Martynchenko

Institute of Nuclear Physics, Academy of Sciences of Uzbekistan, 702132 Tashkent, Uzbekistan

(Submitted November 24, 1997)
Zh. Tekh. Fiz. **69**, 121–123 (January 1999)

The method of deep-level transient spectroscopy is used to investigate aspects of the formation of radiation defects in silicon p^+-n diffusion structures when bombarded by accelerated electrons. It is shown that for base thicknesses of the p^+-n structures in the range 0.2–0.6 mm a substantial change in the concentration of the radiation defects formed in this way is observed, having a maximum at 0.25 mm. Below 0.2 mm and above 0.6 mm the concentration of radiation defects exhibits a weak dependence on base thickness. The observed effect is explained by variation of the relative concentrations of vacancies and interstitial silicon atoms in the base during formation of p^+-n pairs. *© 1999 American Institute of Physics.* [S1063-7842(99)02101-7]

An extensive amount of information has accumulated on the formation of radiation defects in silicon and silicon structures.[1–11] Primary attention has been given to the nature and parameters of the bombarding nuclear particles,[1–6] the conditions of irradiation,[1–10] and the degree of perfection and impurity composition of the initial material,[2,6,8,11] but the effect of the production regimes and means of preparation of p^+-n structures, peculiarities of design and geometrical dimensions of the bases on the formation of radiation defects has not been identified although these data would allow a deeper understanding of the process of formation of various defect complexes in p^+-n structures and could be a decisive factor in any improvement in the quality and characteristics of silicon devices that could be achieved using radiation technology.

The present paper presents results of an experimental study of the effect of the base thickness on the efficiency of introduction of radiation defects into silicon diffusion structures during bombardment by accelerated electrons and considers a possible mechanism of their formation.

The object of study was *n*-type silicon with a resistivity of $4-20\,\Omega\cdot\mathrm{cm}$; p^+-n structures were prepared by boron diffusion at temperatures of 1050–1100 °C. The depth of the p^+ layer was $27-30\,\mu\mathrm{m}$. The based thickness was varied from 0.1 to 2.0 mm. The area of the $p-n$ junctions was the same for all the investigated structures and was equal to 9 mm.

The structures were bombarded by accelerated electrons with energy 6 MeV in the fluence interval $10^{14}-3\times10^{15}\,\mathrm{cm}^2$. The concentration of the formed radiation defects was measured by deep-level transient spectroscopy. The measurements showed that upon bombardment, regardless of the base thickness, radiation defects formed in the investigated structures, primarily with levels $E_c=0.17$ and 0.44 eV belonging to vacancy–oxygen complexes (*A* centers) and vacancy–phosphorus atom complexes (*E* centers), respectively, and also with levels $E_c=0.23$ and 0.39 eV corresponding to various charge states of the divacancy (Fig. 1).

The concentration of all levels increases with increase of the fluence of electron bombardment, which is in good agreement with the data in the literature.[2,9] Comparison of the concentration of detected levels shows that the main fraction of the radiation defects consists of *A* centers.

Figure 2 plots the variation of the concentration of radiation-defect levels as a function of the base thickness of the p^+-n structures after bombardment by electrons with a fluence of $1.5\times10^{15}\,\mathrm{cm}^{-2}$. As can be seen, the efficiency of introduction of the detected radiation defects has an anomalous character and depends on the base thickness.

For the investigated p^+-n structures a noticeable variation in the concentration of radiation defects is observed at base thicknesses in the interval 0.2–0.6 mm, with a maximum at 0.25 mm. As the base thickness is decreased below 0.2 mm or increased above 0.6 mm their concentration exhibits a weak dependence and remains nearly constant. Data on the presence of a maximum in the dependence of the radiation-defect concentration on the base thickness of p^+-n structures are absent in the literature. The observed maximum cannot be explained within the framework of the existing range–absorption mechanism for accelerated electrons at the energy of the bombarding particles,[2,3] since for the investigated thicknesses 6-MeV electrons pass through with minimum losses, generating radiation defects uniformly throughout the volume of the silicon sample. The presence of a substantial dependence of the concentration of radiation defects on the base thickness of the structures in the interval 0.2–0.6 mm with maximum at 0.25 mm can be explained by a change in the relative concentrations of vacancies and interstitial silicon atoms in the base of the structures as a result of various physical–chemical events taking place in the silicon and at the Si–SiO$_x$ interface during preparation of the p^+-n structures.

Many authors[12,13] think that the Si–SiO$_2$ interface arising during thermal oxidation of silicon should be treated as a transitional layer with variable chemical composition. They suggest that a monolayer of nonstoichiometric SiO$_x$ ($1<x<2$) is formed on the single-crystal silicon boundary, consisting of incompletely oxidized silicon. This is followed by

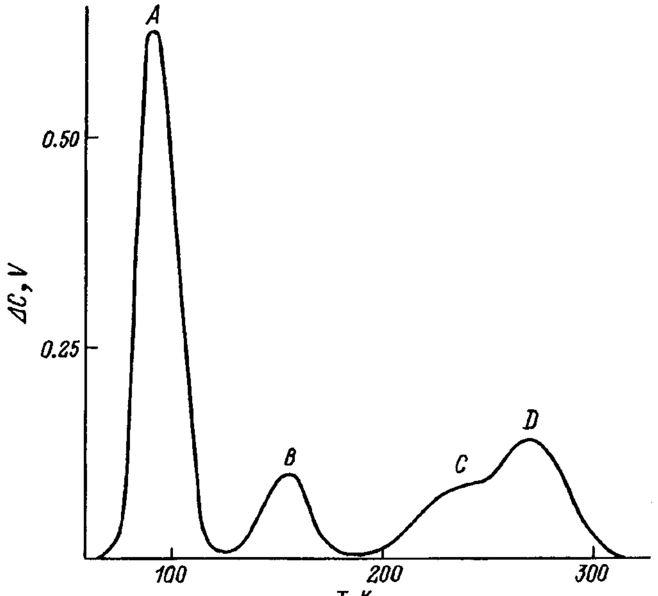

FIG. 1. Deep-levels spectrum of radiation defects in a p^+-n structure with base thickness 0.3 mm, irradiated by electrons with fluence $1.5\times10^{15}\,\mathrm{cm}^{-3}$: $E_c-E_i=0.17$ (*A*), 0.23 (*B*), 0.39 (*C*), 0.44 eV (*D*).

an intermediate layer of SiO_2 with large internal mechanical strains, which is then followed by the usual unstrained, stoichiometric amorphous SiO_2.

Later it was shown[14] that oxidation of silicon is a complex process and the conditions of heat treatment play a substantial role in the generation and annihilation of vacancies and interstitial silicon atoms, where the latter are a primary component of SiO_x.

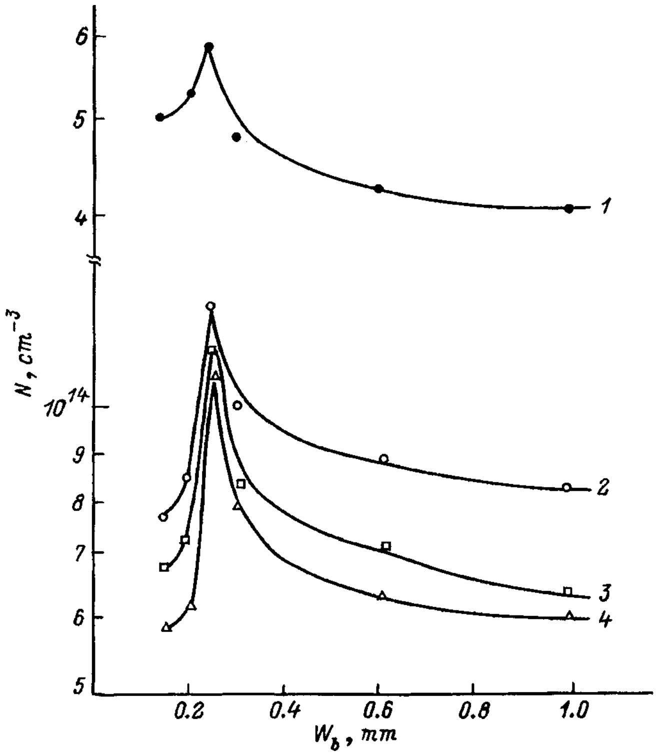

FIG. 2. Dependence of the change in the concentration of radiation defect levels on the base thickness of p^+-n structures for irradiation by electrons with a fluence of $1.5\times10^{15}\,\mathrm{cm}^{-2}$: $E_c-E_i=0.17$ (*1*), 0.44 (*2*), 0.23 (*3*), 0.39 eV (*4*).

In our study of the effect of heat treatment on the generation of native point defects we unambiguously established that thermal diffusion of group-III and V dopant elements is accompanied by the formation in the base and at the silicon–silicon oxide interface of vacancies and interstitial silicon atoms.

The degree of supersaturation of the silicon with native point defects during formation of the $p-n$ junction is determined by the condition of heat treatment, and the process can be described by the following reactions:

$$\mathrm{Si}+\mathrm{O}_2\rightarrow\mathrm{SiO}_2, \tag{1}$$

$$\mathrm{SiO}_2+\mathrm{Si}\rightarrow2\,\mathrm{SiO}, \tag{2}$$

$$B_i+\mathrm{Si}_s\rightleftarrows B_s+\mathrm{Si}_i, \tag{3}$$

where i and s indicate that the boron or silicon atom is located at an interstial position or lattice site, respectively.

Reactions (1) and (2) are accompanied primarily by generation and supersaturation of the near-surface region and Si–SiO_x interfaces with native interstitial atoms, and reaction (3) is accompanied by saturation of the bulk of the silicon primarily with vacancies and interstitial atoms up to the onset of thermodynamic equilibrium. An increase in the boron concentration in the silicon due to the difference in their atomic radii can give rise to a compressive or dilatative stress in the lattice, which can also alter the ratio of interstitial silicon atoms and vacancies in the near-boundary region of p^+-n structures. When one takes into account that the areas of the crystal and the $p-n$ junction, the conditions of heat treatment, and the production processes involved in the preparation of the p^+-n structures are identical and that the probability of migration of a vacancy is large, and also taking into account the physico-chemical processes based on reactions (2) and (3), it may be surmised that the degree of saturation of the silicon with vacancies is determined mainly by the base thickness, where a decrease of the latter leads to an increase in the degree of saturation of the silicon with vacancies, and for certain thicknesses supersaturation of the crystal with vacancies is reached. Under these conditions, the equilibrium state is established — the concentration of vacancies diffusing into the volume becomes equal to the concentration of vacancies escaping to sinks. Such a situation is more probable for structures with base thickness ~0.25 mm. It is obvious that, depending on the degree of saturation of the base with vacancies the silicon crystals will exist in various metastable states. Subsequent irradiation of such crystals by penetrating radiation leads to destruction of the metastable state due to irradiation-induced generation of additional vacancies and interstitial silicon atoms. As they migrate around the crystal, the radiation-generated nonequilibrium vacancies and interstitial silicon atoms interact with each other and with impurities and self defects created during heat treatment in the fabrication of the p^+-n structures, forming radiation defects with various levels. A comparison of the absolute values of the concentrations of the different radiation-defect levels in the region of the maximum (Fig. 2) shows that their rate of formation does not depend on the type of radiation defect that is formed but does depend on the base thickness. Such a variation of the level concentrations can be explained by the fact that one of the components of the radiation defects formed is a vacancy,[1–5] which forms not only upon irradiation but also during heat treatment in the fabrication of the p^+-n structure,[14] i.e., irradiation of silicon supersaturated with vacancies during heat treatment produces the maximum concentration of radiation defects.

The lowering the concentration of radiation defects in diodes with a thinner base ($d<0.25$ mm) may have to do with a change in the ratio of vacancy generation to annihilation in the volume of the crystal during formation of p^+-n structures due to a change in the degree of saturation of the Si–SiO_2 interface by native interstitial atoms. In this case, with decrease of the base thickness the probability of supersaturation of the Si–SiO_2 interface with native interstitial atoms grows and a ''free volume'' is formed at the interface,[14] caused by the difference between the mean distance between the silicon atoms in the oxide and in the lattice. The magnitude of the deformation field varies while relaxation of the arising strain is accompanied by diffusion of excess silicon atoms from the interface into the volume of the base, i.e., the process of annihilation of vacancies with interstitial silicon atoms starts to predominate over processes of their generation and the concentration of vacancies in the base of the diode begins to fall precipitously. Subsequent irradiation of such diodes shows that the rate of formation of radiation defects drops dramatically with decrease of the base thickness (<0.25 mm) and stabilizes for $d\leqslant 0.15$ mm. Thus, a difference in the number of vacancies in the base of p^+-n structures before radiation treatment leads to a change in the rate of formation of radiation defects upon irradiation. A confirmation of the mechanism of formation of radiation defects in diffusion p^+-n structures proposed above is the absence of a maximum in the dependences of the concentration of radiation defects on the base thickness in alloyed diodes.

This aspect of the behavior of radiation-defect centers can also be the reason why in many studies of radiation defect formation in silicon diode structures no difference was observed in the efficiencies of introduction of defect centers.[2,10,12]

On the basis of the present study we may conclude that an examination of the effect of geometrical and design peculiarities of p^+-n structures on the formation of radiation defects can provide important information about their nature, and that data on increasing the efficiency of formation of radiation defects as a function of the base thickness along with the presence of a maximum at 0.25 mm make it possible to optimize the radiation-production process and predict the design peculiarities of fabrication of devices with the help of radiation technology.

[1] *Physical Processes in Irradiated Semiconductors* [in Russian], edited by L. S. Smirnov (Nauka, Novosibirsk, 1977).

[2] *Questions of the Radiation Technology of Semiconductors* [in Russian], edited by L. S. Smirnov (Nauka, Novosibirsk, 1980).

[3] V. S. Vavilov and N. A. Ukhin, *Radiation Defects in Semiconductors and Semiconductor Devices* [in Russian], Atomizdat, Moscow, 1969.

[4] *Action of Penetrating Radiation on the Products of Electronics Technology* [in Russian], edited by E. A. Ladygin (Sov. Radio, Moscow, 1980).

[5] F. P. Korshunov, G. V. Gatal'skiĭ, and G. M. Ivanov, *Radiation Effects in Semiconductor Devices* [in Russian], Nauka i Tekhnika, Minsk, 1976.

[6] L. S. Berman and A. A. Lebedev, *Deep-Level Transient Spectroscopy in Semiconductors* [in Russian], Nauka, Leningrad, 1981.

[7] V. S. Vavilov, V. B. Glazman, N. U. Isaev, B. N. Mukashev, and A. V. Spitsyn, Fiz. Tekh. Poluprovodn. **8**, 471 (1974) [Sov. Phys. Semicond. **8**, 303 (1974)].

[8] A. A. Zolotukhin and L. S. Milevskiĭ, Fiz. Tekh. Poluprovodn. **6**, 2240 (1972) [Sov. Phys. Semicond. **6**, 1886 (1972)].

[9] Yu. M. Dobrovinskiĭ, Sh. Makhkamov, A. Mirzaev *et al.*, Fiz. Tekh. Poluprovodn. **25**, 523 (1991) [Sov. Phys. Semicond. **25**, 316 (1991)].

[10] A. A. Zolotukhin, A. K. Kovalenko, G. M. Meshcheryakova, *et al.*, Fiz. Tekh. Poluprovodn. **9**, 1201 (1975) [Sov. Phys. Semicond. **9**, 800 (1975)].

[11] Sh. Makhkamov, M. Mamanova, Yu. V. Pakharukov, and N. A. Tursunov, Pis'ma Zh. Tekh. Fiz. **18**(24), 44 (1992) [Tech. Phys. Lett. **18**, 811 (1992)].

[12] N. N. Gerasimenko, A. V. Dvurechenskiĭ, V. I. Panov, and L. S. Smirnov, Fiz. Tekh. Poluprovodn. **5**, 1644 (1971) [Sov. Phys. Semicond. **5**, 1439 (1971)].

[13] E. N. Nicollian and J. R. Brews, *MOS Physics and Technology* (Wiley, New York, 1982).

[14] Yu. V. Vyzhigin, N. A. Sobolev, B. P. Gresserov, and E. I. Shek, Fiz. Tekh. Poluprovodn. **25**, 1324 (1991) [Sov. Phys. Semicond. **25**, 799 (1991)].

Translated by Paul F. Schippnick

TECHNICAL PHYSICS VOLUME 44, NUMBER 1 JANUARY 1999

A method of reducing diffusion losses in a drift spectrometer

E. V. Krylov

Technical Design Institute of Geophysical and Environmental Instrumentation, Siberian Branch of the Russian Academy of Sciences, 630090 Novosibirsk, Russia

(Submitted December 8, 1997)
Zh. Tekh. Fiz. **69**, 124–127 (January 1999)

A method is considered which reduces diffusion losses during analysis of the ions of heavy molecules passed together with a carrier gas through a separation system at atmospheric pressure. Separation takes place under the action of a transverse variable electric field in a way similar to the case of quadrupole mass spectrometers. Instead of the usual uniform-field planar capacitor, it is proposed to employ a cylindrical capacitor with a nonuniform field. It is shown experimentally that a severalfold increase in the output signal is achieved. © *1999 American Institute of Physics.* [S1063-7842(99)02201-1]

This paper addresses a new method of separating ions in a dense, air-based medium on the basis of the nonlinear dependence of the ion mobility on the electric field strength. References 1–5 described a new method for separating ions in a gas on the basis of the dependence of the mobility coefficient on the electric field strength as well as a device for realizing it. The essence of this method consists in the following. For a constant density N of the drift gas the dependence of the mobility coefficient K on the electric field strength E can be represented in the form

$$K(E)=K_0(1+\alpha(E)), \tag{1}$$

where K_0 is the value of the mobility coefficient in a weak field and $\alpha(E)$ is a normalized function describing the dependence of the mobility on the field.

From the requirement of isotropy of the ion drift space it follows that the dependence $\alpha(E)$ can only be an even function of E. We write the series expansion of the function $\alpha(E)$ in even powers of E in explicit form

$$\alpha(E)=\sum_{n=1}^{\infty} \alpha_{2n}\cdot E^{2n}. \tag{2}$$

The constant expansion coefficients α_{2n} depend only on the form of the ion–molecule interaction potential.

The operation of a drift spectrometer (Fig. 1) is based on the dependence of the ion mobility coefficient K on the electric field strength E. The presence of a nonzero dependence $\alpha(E)$ leads to the result that under the action of a periodic electric field $E(t)$, asymmetric in the polarity and satisfying the conditions

$$\int_0^T E(t)dt=\langle E(t)\rangle=0, \quad \langle E^{2n+1}(t)\rangle\neq 0, \tag{3}$$

where T is the period of the field, n is an integer greater than 1, the ions will complete rapid oscillations with period T and move slowly along the force lines of the field with a velocity V that is characteristic for the given type of ion. The difference in the velocities V for different types of ions is used to separate them.

Separation takes place in a chamber formed by two electrodes, between which a stream of ionized gas is pumped. A voltage is applied to the electrodes, as a result of which the ions in the chamber are acted on by an electric field

$$E(t)=E_s(t)+E_c=E_s\cdot f(t)+E_c, \tag{4}$$

where $E_s(t)$ satisfies condition (3), $E_s=\max|E_s(t)|$, $E_c \ll E_s$, and $f(t)$ is a unit-normalized function describing the shape of the field.

Under the action of such a field an ion drifts transverse to the stream of drift gas with its own characteristic velocity $V=\langle K(E)E(t)\rangle$. Reaching the electrode, the ion loses its charge and is not recorded. If E_c is such that for some type of ion the compensation condition $V=0$ is fulfilled, then these ions move through the separation chamber with the stream of drift gas and are recorded at the output of the

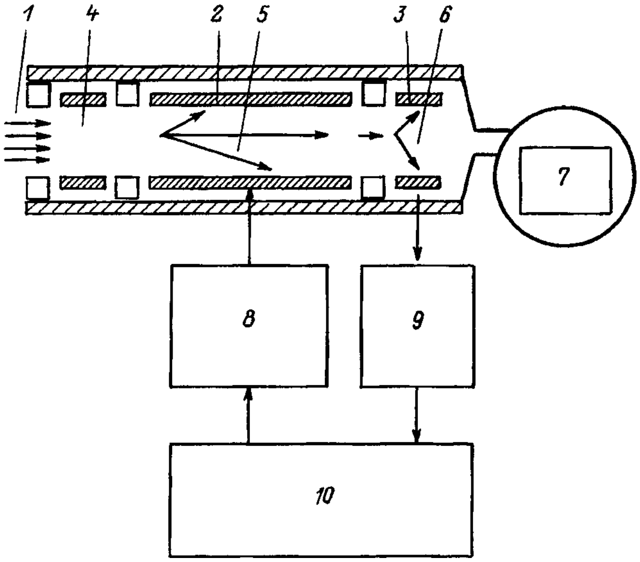

FIG. 1. Drift spectrometer: *1* — gas being analyzed, *2* — separation chamber, *3* — polarized electrode, *4* — ionization chamber, *5* — ion trajectories, *6* — recording chamber, *7* — gas pump, *8* — generator of separating voltage, *9* — electrometer, *10* — control and data processing system.

electrometer. We call this value E_c the output field strength of the given type of ion. Reference 1 derives the dependence of E_c on E_s and the function $\alpha(E)$

$$E_c=\frac{\langle \alpha\cdot E_s\rangle}{1+\langle\alpha\rangle+\left\langle\frac{\partial\alpha}{\partial E}\cdot E_s\right\rangle}. \tag{5}$$

Taking expansion (2) into account, this formula takes the form

$$E_c=\frac{\sum_{n=1}^{\infty}\alpha_{2n}E_s^{2n+1}\langle f^{2n+1}(t)\rangle}{1+\sum_{n=1}^{\infty}(2n+1)\alpha_{2n}E_s^{2n}\langle f^{2n}(t)\rangle}. \tag{5a}$$

RESULTS AND DISCUSSION

When the compensation condition is satisfied for some type of ion, the main reason for ion losses in the analysis channel is ion diffusion to the walls of the separation chamber. In the case of the experimental setup described in Ref. 1, ion diffusion to the walls of the separation chamber leads to a three to fivefold decrease of the useful signal. A method for dealing with diffusion losses is proposed.

The essence of this method consists in the following. Ion separation leads to a spatially nonuniform (e.g., radial) electric field. The field gradient points in the same direction as the vector of the compensating field E_c. The presence of an electric field gradient leads to the result that a restoring force acts on the ions diffusing from their equilibrium position, at which the compensation condition is fulfilled. A compression of the ion cloud arises, leading to a decrease of ion diffusion losses.

Before turning to a calculation of the ion separation process in a spatially nonuniform field $E_c+E_sf(t)$, I introduce the following notation: $\mathbf{r}_0$ is the position vector of the point at which the compensation condition $\langle V(r_0)\rangle=0$ is fulfilled; $E_c(E_s)$ is the dependence of the compensating field strength on the amplitude of the separating field for the given type of ion. This dependence is assumed to be known from experiment or is calculated from formula (5); $p(\mathbf{r})=E(\mathbf{r})/E(\mathbf{r}_0)$ is a function describing the spatial dependence of the field strength.

We fix some nonzero value of E_s and the corresponding output field strength $E_c(E_s)$ for some type of ion and consider the motion of an ion in the vicinity of the point $\mathbf{r}_0$. The separating field $E_sp(\mathbf{r})$ and the compensating field $E_cp(\mathbf{r})$ will act on it. The condition of compensation for $\mathbf{r}\neq\mathbf{r}_0$ is, generally speaking, not fulfilled since the action of the separating field $E_sp(\mathbf{r})$ is compensated by the constant field $E_c(E_sp(\mathbf{r}))\neq E_cp(\mathbf{r})$. Consequently, the action of the fields on the ion at the point $\mathbf{r}$ will be equivalent to the action of a constant field with field strength

$$E_{ef}=E_c(E_sp(r))-E_cp(r). \tag{6}$$

The solution of the ion diffusion equation $\mathbf{J}=nK\mathbf{E}_{ef}=D\nabla\mathbf{n}$ describes the motion of the cloud of ions in the spatially nonuniform field $E_c+E_sf(t)$.

Under the assumption of smallness of the displacement of the ion from the point r_0, the diffusion equation can be solved in explicit form. The expansion of the function E_{ef} in the small parameter $\Delta r/r_0=(r-r_0)/r_0$ at the point $\mathbf{r}_0$ has the form

$$E_{ef}=\left(E_c-\frac{\partial E_c}{\partial E_s}E_s\right)\cdot\nabla p(r_0)\cdot\Delta r\equiv\gamma\Delta r, \tag{7}$$

where $\nabla p(\mathbf{r})$ is the spatial gradient of the field and $\gamma\Delta r$ is the scalar value of the function E_{ef} in the chosen direction.

If the value of γ is negative and not equal to zero, then the diffusion equation has a stationary solution. The steady-state distribution of the ion density has a Gaussian shape with characteristic width $\sqrt{2D/K\gamma}$ and center at the point $\mathbf{r}_0$.

We will obtain estimates for a coaxial separation chamber consisting of a coaxially arranged cylinder and rod, between which a separating field is created. In this case, the field strength and the function $p(r)$ in cylindrical coordinates are given by

$$E(r)=\frac{U}{\ln\left(\frac{r_1}{r_2}\right)\cdot r};\quad p(r)=\frac{r_0}{r}, \tag{8}$$

where U is the voltage applied to the plates, and r_1 and r_2 are the inner and outer radius, respectively, of the separation chamber.

We assume that the compensation condition is fulfilled at the point $r_0=(r_1+r_2)/2$, and we estimate the effect for diffusion drift of the ions in the radial direction, i.e., toward the walls of the coaxial chamber. The purpose of the estimate will be to calculate the minimum separation between the electrodes $d=r_1-r_2$ for which diffusion losses of the ions will be negligibly small. To estimate the dependence $E_c(E_s)$, we use formula (5a), taking into account only the first term of the expansion (2) of the dependence $\alpha(E)$. Substituting $\alpha(E)=\alpha_2E^2$ in Eq. (5) and restricting the expression to zero-order terms, we obtain

$$E_c=\alpha_2\langle f^3\rangle\cdot E_s^3. \tag{9}$$

Elementary calculations give the value of γ for radial ion drift

$$\gamma=\frac{2E_c}{r_0}\approx\frac{2U_c}{r_0\cdot d}, \tag{10}$$

where U_c is the compensation voltage.

The assumption of smallness of Δr made above gives us the right to use instead of the exact value (8) for E_c the approximate value $E_c\approx U_0/d$. The negative sign of γ is ensured by the condition of codirectionality of E_c and ∇p (for positive ions). In the opposite case, the effect of compression of the ion cloud is replaced by one of repulsion, which will lead to the loss of ions to the walls of the chamber.

Requiring that $d\gg\sqrt{2D/K\gamma}$ and taking relation (10) and the Einstein relation[6] into account, we obtain

$$d/r_0\gg U_T/U_c, \tag{11}$$

where $U_T=kT/e$ is the thermal potential.

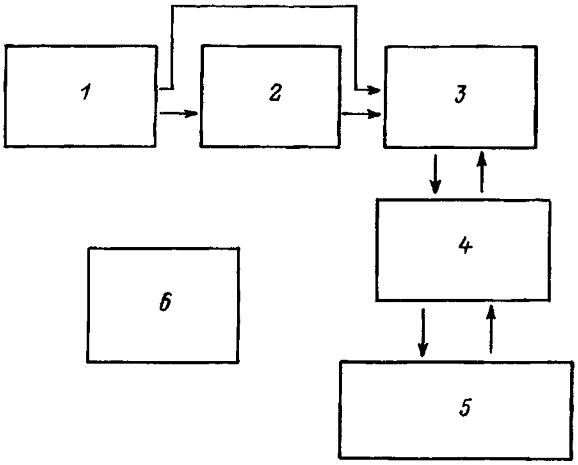

FIG. 2. Block diagram of the experimental setup: *1* — sample preparation block, *2* — additional separation chamber, *3* — drift spectrometer, *4* — RS-232 interface, *5* — IBM PC (software), *6* — electronics blocks.

A careful account of the size of the compressed beam, the use of the generalized Nernst–Einstein equation,[6] and and account of higher orders of the expansion of $\alpha(E)$ (2) and, consequently, higher orders of expansion (5a) make it possible to refine the inequality (11). However, we will leave it in the form in which it is on account of its simplicity and intuitive clarity.

The accumulated experimental data give a basis for asserting that $U_c \gg U_T$ in the majority of cases. This justifies the assumption of smallness of the parameter $\nabla r/r$, made in the derivation of Eq. (7).

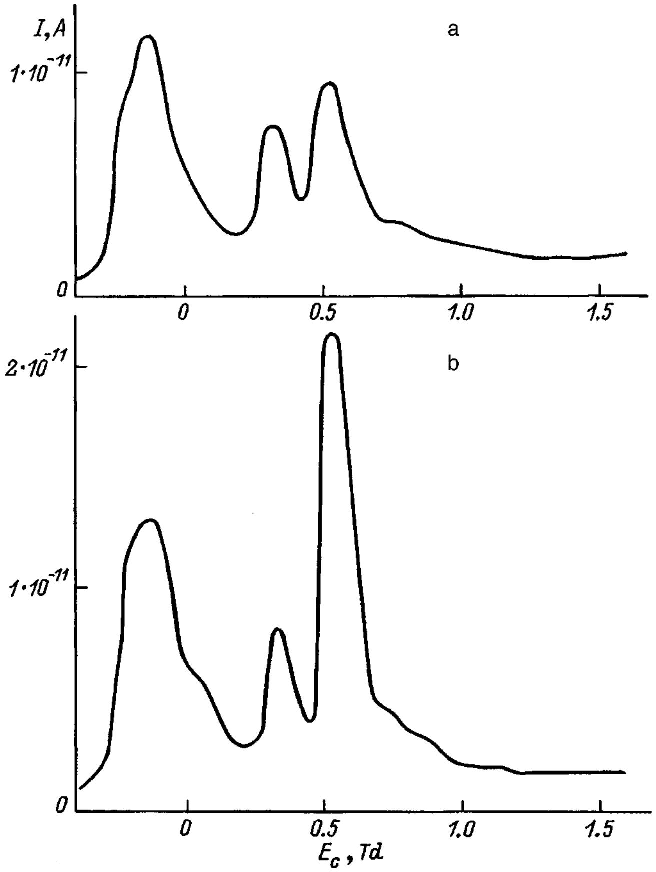

FIG. 3. Drift spectra, i.e., curves of the dependence of the output ion current I of the separation chamber on the compensation field strength E_c for planar design of the separation chamber (a) and coaxial design (b).

EXPERIMENTAL TEST

A block diagram of the experimental setup is shown in Fig. 2, and the setup itself is described in detail in Ref. 1. The gas mixture to be analyzed, which is obtained with the help of the sample preparation block, is ionized in the ionization chamber, where a β-source or surface-ionization source is located. The mixture of the ions and carrier gas is fed into the separation chamber. Both a planar and a coaxial separation chamber were used in the experiment. The planar separation chamber consists of two parallel metal plates (electrodes) of dimensions 1.5×5 cm, separated by a gap of 1 mm. The coaxial separation chamber consists of coaxially arranged cylindrical electrodes: the outer, of diameter 0.5 cm, and the inner, of diameter 0.3 cm. In the gap between the planar or coaxial electrodes the ion mixture is acted on by the electric field. To create a field of the required configuration (4), a large (range of variation of the voltage amplitude 1–3 kV) high-frequency ($T=1$ μs) voltage. The shape of the temporal variation of the field is described by the function[7]

$$f(t)=0.7\cos(2\pi t/T)+0.3\cos(4\pi t/T). \qquad (12)$$

Figure 3 presents drift spectra recorded under identical conditions in the planar (a) and coaxial (b) separation chambers. As the test mixture, we used a mixture of tripropylamine and triethylamine. The severalfold increase in the height of the peaks for $E_c>100$ V/cm is an indication of a reduction in ion losses in the coaxial separation chamber.

It is also interesting to compare the dependence of the ion loss coefficient in the separation chamber $K_L=I_{\text{inp}}/I_{\text{out}}$, equal to the ratio of the input and output ion currents, on the separating field strength E_s for a planar and a coaxial separation chamber.

To set up the experiment correctly, a modification was made in the experimental setup. A second separation chamber was placed between the ionizer and the separation chamber equipped with the necessary electronic equipment. It was tuned to an isolated, pronounced peak of the drift spectrum corresponding to material with a high electron or proton affinity, and E_c was recorded. The ion current at the output of this chamber served as the input current for the (planar or coaxial) separation chamber in question. Such an arrangement guarantees a stable current of ions of one sort at the input to the separation chamber and allows one to measure the loss coefficient in the analysis channel as a function of E_s. The magnitude of the ion current at the output of the additional separation chamber was monitored in order to ensure a quantitative value of K_L.

The dependence $\ln K_L(E_s)$ for the planar (a) and the coaxial (b) separation chamber is plotted in Fig. 4. $(M+H)^+$ ions were used, obtained by β-ionization of tripropylamine

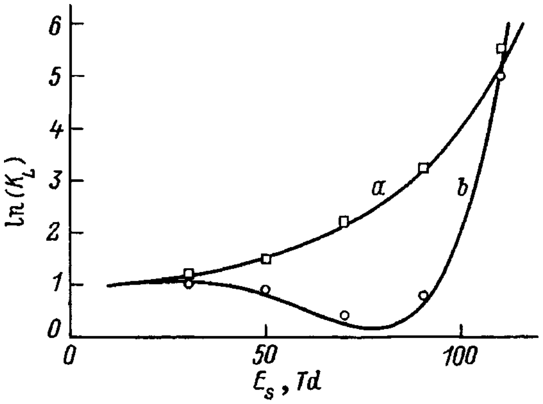

FIG. 4. Logarithm of the ion loss coefficient $\ln(K_L)$ as a function of the separating field strength E_s for planar design of the separation chamber (a) and coaxial design (b).

vapors in an atmosphere of air.[5] The calculated curves were obtained by solving the ion diffusion equation in the separation chamber in the τ-approximation with allowance for the compression effect.

CONCLUSION

A new method for reducing diffusion losses of ions in a drift spectrometer based on the use of a spatially nonuniform electric field for ion separation has been proposed and calculated. Experimental confirmation of this effect has been obtained.

The author conveys his thanks to U. Kh. Rasulev, É. G. Nazarov, and I. A. Buryakov for fruitful discussions and assistance in experimental confirmation of the effect.

[1] I. A. Buryakov, E. V. Krylov, E. G. Nazarov, and U. Kh. Rasulev, Int. J. Mass Spectrom. Ion Processes **128**, 143 (1993).

[2] M. P. Gorshkov, Inventor's Certificate (USSR) No. 966583 [in Russian], International Classification 01 No. 27/62; publ. Byull. Izobret. No. 38 (1982).

[3] I. A. Buryakov, E. V. Krylov, A. L. Makas' *et al.*, Pis'ma Zh. Tekh. Fiz. **17**(12), 60 (1991) [Tech. Phys. Lett. **17**, 412 (1991)].

[4] I. A. Buryakov, E. V. Krylov, and V. P. Soldatov, Inventor's Certificate (USSR) No. 1485808 [in Russian], G01 No. 27/62; publ. Byull. Izobret. No. 16 (1989).

[5] I. A. Buryakov, E. V. Krylov, A. L. Makas' *et al.*, Zh. Anal. Khim. **48**, No. 1, 156 (1993).

[6] E. A. Mason and E. W. McDaniel, *Transport Properties of Ions in Gases* (Wiley, New York, 1988).

[7] E. V. Krylov, Prib. Tekh. Éksp., No. 4, 114 (1991).

Translated by Paul F. Schippnick

Efficiency of excitation of space-charge waves in a thin-film semiconductor structure with a single strip Schottky barrier

A. I. Mikhaĭlov and S. A. Sergeev

N. G. Chernyshevski Saratov State University, 410601 Saratov, Russia

(Submitted December 8, 1997)
Zh. Tekh. Fiz. **69**, 128–130 (January 1999)

Results of a theoretical analysis of the influence of various factors on the efficiency of excitation of space-charge waves in thin-film semiconductor structures by a single strip Schottky barrier are presented. It is shown that to increase the efficiency of conversion of a microwave signal into space-charge waves, it is advisable to use a Schottky barrier with a small contact potential with optimized values of the width of the Schottky barrier and the electron concentration in the film. © *1999 American Institute of Physics.* [S1063-7842(99)02301-6]

One of the most promising classes of devices of functional microelectronics in the microwave range is the class of space-charge-wave (SCW) devices in semiconductors with negative differential conductivity (NDC).[1,2] They can fulfill various radio-engineering functions connected with the processing of microwave signals down to the millimeter range.[1–5] In the development and design of functional SCW devices in thin-film semiconductor structures with negative differential conductivity for the 8-millimeter range, studies on the optimization of the topological-design and electrophysical parameters of thin-film semiconductor structures and SCW excitation elements have taken on special value. This has to do with the fact that the limiting frequency of SCW amplification is found in this range.

As the coupling elements of thin-film semiconductor structures with an electrodynamical system providing excitation of space-charge waves, presently the most often used are single strip Schottky barriers, an important property of which is their wideband character. The present paper presents results of a theoretical analysis of the influence of the topological-design and electrophysical parameters of a thin-film semiconductor structure and its coupling elements on the efficiency of excitation of space-charge waves by a single strip Schottky barrier.

When a microwave signal is fed to the input reverse-biased strip Schottky barrier, modulation of the depth of the depletion region under the Schottky barrier takes place with the frequency of the input microwave voltage. Under these conditions, the z component of the electric field vector, E_z, in the n-GaAs film under the Schottky barrier is modulated with the same frequency (Fig. 1a). Neglecting diffusion, the z component of the total current under the strip Schottky barrier is given by the expression

$$I=W[2a-b(V)]\left\{qnv(E_z)+\varepsilon\varepsilon_0\frac{dE_z}{dt}\right\}, \tag{1}$$

where W is the aperture of the semiconductor structure, $2a$ is the thickness of the n-GaAs film,

$$b(V)=\sqrt{\frac{2\varepsilon\varepsilon_0(\varphi_0-V)}{qn_0}} \tag{2}$$

is the depth of the depletion region under the Schottky barrier, which depends on the voltage V, ε is the relative dielectric constant of n-GaAs, ε_0 is the electric constant, q is the absolute value of the charge of the electron, n is the electron concentration in the n-GaAs film, φ_0 is the contact potential of the strip contact with the Schottky barrier, n_0 is the equilibrium electron concentration, $v(E_z)$ is the drift velocity of the electrons under the Schottky barrier, which depends on the electric field strength E_z, and t is time.

We assume that superimposed on the constant voltage

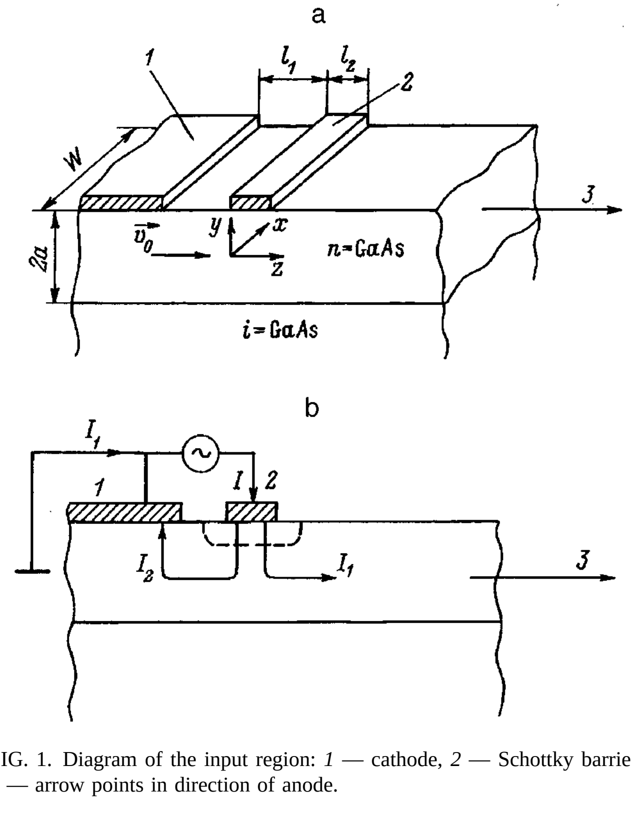

FIG. 1. Diagram of the input region: *1* — cathode, *2* — Schottky barrier, *3* — arrow points in direction of anode.

V_0, a small variable voltage V_1 with frequency ω is applied to the Schottky barrier, i.e.,

$$V = V_0 + V\exp(i\omega t); \quad V_1 \ll V_0. \tag{3}$$

In the case when a microwave generator in the input part of the device is connected between the Schottky barrier and the cathode, the plan of the input part has the form shown in Fig. 1b. The total current I flowing into the Schottky barrier is divided into two components — I_1 and I_2: the current I_2 goes to the cathode, and the current I_1 goes to the anode. In the ideal case, as a consequence of the high impedance of the segment between the Schottky barrier and the anode in comparison with the impedance of the narrow segment between the Schottky barrier and the cathode, $I_1 \ll I_2, I$. Thus, following the technique outlined in Ref. 6, it is possible to obtain an expression for the coupling coefficient of the electric field strength of the space-charge wave and the microwave signal on the Schottky barrier

$$K = \frac{dE_z}{dV} = -\frac{1}{(2a-b_0)}\frac{1}{b_0}\frac{v_0}{\omega_d}\left[\left(1+\frac{v_0}{l_2}\frac{1}{\omega_d}\right)+i\frac{\omega}{\omega_d}\right]^{-1}, \tag{4}$$

where b_0 is the value of $b(V)$ for $V = V_0$; $\omega_d = (qn_0\mu_d)/(\varepsilon\varepsilon_0)$; and μ_d is the differential mobility of the electrons in the n-GaAs wafer corresponding to the static electric field strength E_0.

As can be seen from Eq. (4), the coupling coefficient K is in general complex, which points to the existence of a phase difference between the microwave voltage at the input to the Schottky barrier and the electric field strength of the space-charge wave under it.

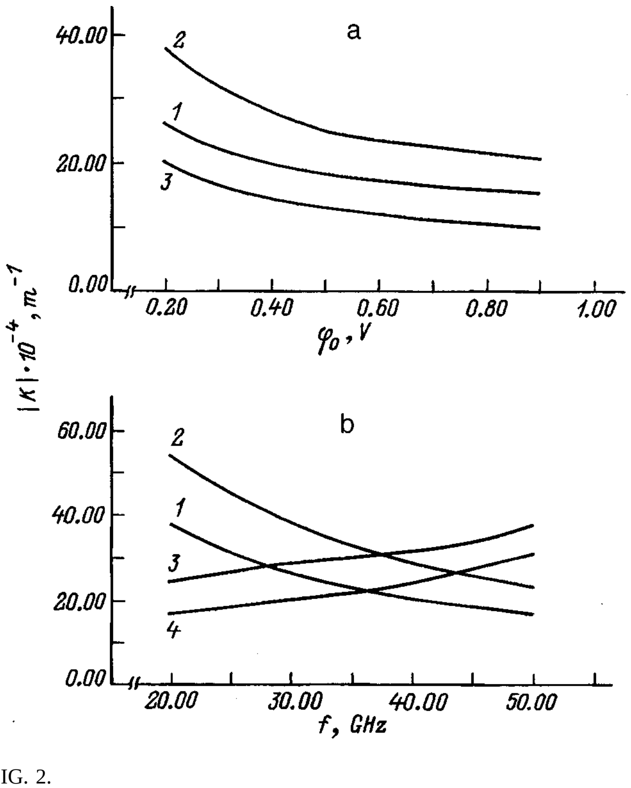

FIG. 2.

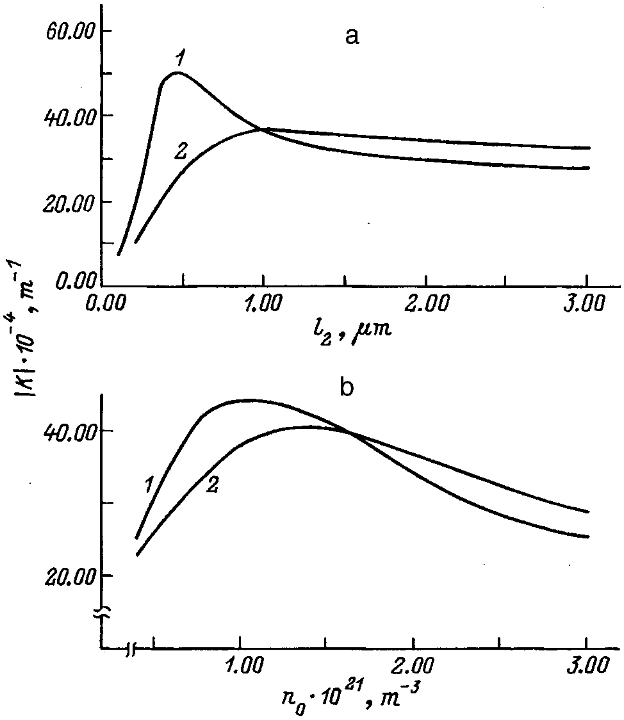

FIG. 3.

Figures 2 and 3 plot the dependence of the modulus of the coupling coefficient $|K|$, calculated with the help of formula (4), on φ_0, $f = \omega/2\pi$, n_0, and l_2. These dependences were calculated for the following parameter values corresponding to n-GaAs assuming that the static electric field under the Schottky barrier $E_0 = 5.5$ kV/cm: $v_0 = 1.7 \times 10^7$ cm/s, $\varepsilon = 12.9$ (Ref. 7), and $2a = 5$ μm. The dependence of μ_d on f for n-GaAs was taken from Ref. 8. In all of the calculations we set $V_0 = -1$ V.

Figure 2a shows the dependence of $|K|$ on the contact potential φ_0 for $f = 30$ GHz ($\mu_d = -0.128$ m^2/V$\cdot$s), $l_2 = 1$ μm, and $n_0 = 5\times 10^{20}$ (curve *1*), 10^{21} (curve *2*), and 5×10^{21} m^{-3} (curve *3*). As can be seen, $|K|$ for a Schottky barrier with a small value of φ_0 is higher than $|K|$ for a Schottky barrier with $\varphi_0 = 0.7-0.9$ V, which is more typical for a Schottky barrier on n-GaAs. This has to do with the fact that for smaller values of φ_0 the modulation coefficient of the capacitance and the depth of the depletion region below the Schottky barrier are increased,[9] i.e., for efficient excitation of space-charge waves in a thin-film semiconductor structure with negative differential conductivity it is expedient to use Schottky barriers with $\varphi_0 = 0.2-0.3$ V, which, on the one hand, ensures a high gain coefficient, and on the other, guarantees a high temperature stability of operation of the device since in this case $\varphi_0 \gg kT/q$, where k is the Boltzmann constant and T is the temperature.

Figure 2b shows the dependence of $|K|$ on the frequency of the microwave signal f for $\varphi_0 = 0.2$ V, $l_2 = 1$ μm, and the electron concentration in the working layer $n_0 = 5\times 10^{20}$ (curve *1*), 10^{21} (curve *2*), 3×10^{21} (curve *3*), and 5

$\times 10^{21}\,\mathrm{m}^{-3}$ (curve *4*). The foregoing analysis shows that for $n_0 = 2\times 10^{21}\,\mathrm{m}^{-3}$ the nature of the dependence of $|K|$ on f changes: it changes from a falling to a growing dependence. Such a change is a direct result of the fact that the calculations allowed for the frequency dispersion of the differential mobility of the electrons. This circumstance points to the necessity of taking account of the dependence of the differential electron mobility on the frequency in the design of the coupling elements of space-charge-wave devices. The obtained dependences of $|K|$ on f show that using different n_0 under the Schottky barrier can, in a goal-specific way, correct the amplitude–frequency characteristics of the coupling elements and the entire device as a whole.

Figure 3a shows the dependence of $|K|$ on the width of the Schottky barrier l_2 for $\varphi_0 = 0.2\,\mathrm{V}$ and $f = 30\,\mathrm{GHz}$ ($\mu_d = -0.128\,\mathrm{m}^2/\mathrm{V}\cdot\mathrm{s}$) for two values of the equilibrium electron concentration in the working layer $n_0 = 2\times 10^{21}$ (curve *1*) and 10^{21} (curve *2*). Figure 3b shows the dependence of $|K|$ on n_0 for $\varphi_0 = 0.2\,\mathrm{V}$ and $l_2 = 1\,\mu\mathrm{m}$ for two values of the frequency: $f = 25$ (curve *1*) and $30\,\mathrm{GHz}$ (curve *2*).

The nonmonotonicity of the dependence of $|K|$ on l_2 and on n_0 is due to the change of sign of the real part of K when

$$\omega_d \tau = -1, \tag{5}$$

where $\tau = l_2 / v_0$ is the transit time of the electrons under the Schottky barrier.

The results obtained here can be used in the development and design of various space-charge-wave devices in thin-film semiconductor structures with negative differential conductivity in the short-wavelength part of the microwave range.

[1] A. A. Barybin, Mikroélektronika **8**(1), 3 (1979).

[2] V. A. Ivanchenko and A. I. Mikhaĭlov, *Abstracts of the All-Union Conference ''Electronics: Data Converters''* [in Russian], Moscow, Nizhniĭ Novgorod, 1991, p. 12.

[3] A. I. Mikhaĭlov, Pis'ma Zh. Tekh. Fiz. **21**, No. 21, 89 (1995) [Tech. Phys. Lett. **21**, 902 (1995)].

[4] A. I. Mikhaĭlov and S. A. Sergeev, Izv. Vyssh. Uchebn. Zaved. Radioélektronika **38**, No. 9–10, pp. 43–51 (1995).

[5] A. I. Mikhaĭlov and S. A. Sergeev, Pis'ma Zh. Tekh. Fiz. **22**, No. 24, 75 (1996) [*sic*].

[6] K. Kumabe and H. Kande, Int. J. Electron. **58**, 587 (1985).

[7] M. E. Levinshteĭn, Yu. K. Pozhela, and M. S. Shur, *The Gunn Effect* [in Russian], Sov. Radio, Moscow, 1975.

[8] H. D. Rees, Solid State Commun. **7**, 267 (1969).

[9] A. I. Mikhaĭlov, Élektron. Tekh. Ser. 1, Élektronika SVCh, No. 6, 28 (1981).

Translated by Paul F. Schippnick

Single and double electron capture processes in slow Ne^{q+}–He ($q=10,6$) collisions

V. K. Nikulin and N. A. Gushchina

A. F. Ioffe Physicotechnical Institute, Russian Academy of Sciences, St. Petersburg, Russian Academy of Sciences, 194021 St. Petersburg, Russia

(Submitted August 25, 1997)
Zh. Tekh. Fiz. **69**, 15–28 (January 1999)

The cross sections for single and double electron capture to the states $Ne^{9+}(n)$ with $n=3-6$ and $Ne^{8+}(3l,n'l')$, $Ne^{8+}(4l,n'l')$ with $n'\geqslant 4$ and also the cross sections for single electron capture to the states $Ne^{5+}(3)$ in collisions of Ne^{10+} and Ne^{6+} with He atoms are calculated for collision energies in the interval from 10 to 150 keV. The calculation is carried out in the multichannel Landau–Zener, Nikintin, and Landau–Zener–Chaplik models with allowance for the radial coupling of the channels at crossing points of the energies of the quasidiabatic two-electron states of the quasimolecule. The energies of the two-electron states are calculated in the effective potential method to first order in perturbation theory in the residual electron–electron interaction. The energies of the adiabatic states in the neighborhoods of the crossings of quasidiabatic terms are determined by the configuration interaction method.
It is found that in Ne^{10+}–He collisions the electron is captured mainly to the $n=5$ state of the Ne^{9+} ion. The cross section for double electron capture to the $3lnl'$ state ($n\geqslant 4$) of the Ne^{8+} ion is an order of magnitude smaller than the cross section for single electron capture. The contribution to the total cross section for double electron charge transfer from the $4l4l'$, $4l5l'$, and $4l6l'$ states is approximately 25%. The dependence of the cross sections for double electron charge transfer on the values of l and l' is investigated. [S1063-7842(99)00301-3]

INTRODUCTION

Collisions between multiply charged ions and atomic targets have been studied intensively in the last few years.[1] Charge transfer processes in these collisions are the most efficient mechanisms of excitation transfer. Of particular interest is the study of charge transfer reactions of the ions Ne^{q+} and Ar^{q+} ($q=1-10$) with H, He, and H_2 on account of the role of Ne and Ar impurities in plasma cooling processes in thermonuclear fusion devices. To estimate the contribution to the cooling from charge transfer processes it is necessary to have estimates for their total and partial cross sections.

In collisions of a multiply charged ion with a neutral atom the most probable process is single-electron quasiresonant charge transfer to excited ionic states with binding energies close to the ionization potential of the atom. If the atomic shell has equivalent electrons, as in the helium atom, there can also be double electron capture (DEC) to unstable excited states of the ion, which decay by autoionization or radiative decay. These DEC processes are of particular interest in connection with the problem of collisional correlation effects (CCEs). These effects in slow atomic collisions should be manifested through the probability of quasidiabatic transitions between quasimolecular states (QMSs), i.e., through the value of the effective coupling at those internuclear distances where one has near-resonance conditions, which determine the dominant reaction channels. CCEs should be particularly noticeable[2] for doubly excited QMSs in the Coulomb field of the multiply charged quasimolecule. These states can include a significant mixture of interacting electronic configurations, and this should be manifested in the partial cross sections for DEC. At the present time there are directly conflicting points of view as to both the possible mechanisms of DEC and the role of CCEs.

CCEs in DEC reactions have been investigated recently (in Ref. 2, for example) with the use of an atomic basis in the coupled-channel method. This method in principle permits one to study indirectly the details of the mechanisms of charge transfer reactions through a change in the corresponding matrix elements of the dynamic coupling.

For a physically transparent study of the mechanisms of charge transfer it is necessary to optimize the quasimolecular basis and to refine the concept of the independent-particle model accordingly. For a crude description of the charge transfer reaction of stripped multiply charged ions on the hydrogen atom, it is well known that one need analyze only a few pseudocrossings between one-electron two-atom molecular orbitals (OETAMOs). Specifically, of the multiplet of states of an ion Ze which are degenerate at infinity, only those terms with parabolic quantum numbers $[Z-1,0;\ Z-2,0]$ undergo quasicrossings with the ground-state term of the hydrogen atom.[1,3] The reason for these ‘‘selection rules’’ is the special additional symmetry due to the possibility of separation of variables in in the two-center quantum-mechanical problem.

For multielectron quasimolecules it turns out to be possible to preserve this symmetry provided that the effective potential, which takes into account the optimal screening of the nuclei by electrons, satisfies the requirement of separation of variables in spheroidal coordinates. In this way[4] one can obtain diabatic screened two-atom molecular orbitals (STAMOs) having the same symmetry properties as the OETAMOs. The values of the diagonal matrix elements of the exact Hamiltonian of the quasimolecule — the QMSs calculated on the single-determinant wave functions in the STAMO basis — turn out to be rather close to the values obtained in self-consistent Hartree–Fock calculations. Therefore, these quasidiabatic QMSs are naturally considered, in the spirit of quantum chemistry, to be the corresponding independent-particle states. In this paper the quasidiabatic QMSs discussed above are basic to the investigation of CCEs.

CALCULATION OF THE STAMO BASIS FOR THE SYSTEM Ne^{10+}–He

The two-electron QMSs describing the entrance and exit channels of the reaction

$$\mathrm{Ne}^{10+}+\mathrm{He}(1s^2)\rightarrow\begin{cases}\mathrm{He}^{+}(1s)+\mathrm{Ne}^{9+}(nl),\\ \mathrm{He}^{2+}+\mathrm{Ne}^{8+}(nl,n'l'),\end{cases} \tag{1}$$

are calculated in the one-configuration approximation

$$\phi_i(r_1,r_2)=\frac{1}{\sqrt{2}}(\varphi_k(r_1)\varphi_l(r_2)+\varphi_k(r_2)\varphi_l(r_1)) \tag{1a}$$

in a basis of the STAMOs φ_j. The molecular orbitals φ_j are identified by a set of spherical quantum numbers $j=(nlm)$ of the state of the united atom (UA) to which the given orbital goes over as $R\rightarrow 0$. The STAMOs are determined by solving the two-center problem

$$H_i\varphi_i=\left[-\frac{\nabla^2}{2}-\frac{Z_1}{r_1}-\frac{Z_2}{r_2}+V_{\mathrm{eff}}^{(i)}(R,r_1,r_2)\right]\varphi_i=\varepsilon_i(R)\varphi_i \tag{2}$$

with the effective potential $V_{\mathrm{eff}}^{(i)}$ specified[4] in the parametric form

$$V_{\mathrm{eff}}^{(i)}=\frac{1}{2}\left[\frac{a_1^{(i)}-b_1^{(i)}}{r_1}+\frac{a_1^{(i)}+b_1^{(i)}}{r_2}+\frac{\tilde{a}_1^{(i)}+Ra_0^{(i)}}{r_1r_2}+\frac{b_2^{(i)}(r_1-r_2)^2}{Rr_1r_2}\right], \tag{3}$$

where R is the internuclear distance and r_1 and r_2 are the distances from the electron to the nuclei with charges Z_1 and Z_2, respectively (atomic units are used throughout).

The scheme for determining the effective potential parameters $a_0^{(i)}$, $\tilde{a}_1^{(i)}$, $a_1^{(i)}$, $b_1^{(i)}$, and $b_2^{(i)}$ for a heteronuclear system are given in Appendix A. The effective potential method has the shortcoming that the different STAMOs are not orthogonal, and that substantially complicates the calculation of the energies of the adiabatic states of the quasimolecule by the configuration interaction method. Therefore, we shall henceforth use orthogonal STAMOs satisfying Eq. (2) with the a single effective potential that optimally describes the entrance-channel orbitals.

In the present scheme of determining the parameters $V_{\mathrm{eff}}^{(i)}$ we need to know not only the value ε_{sa}^{i} to which the energy $\varepsilon_i(R)$ of the molecular orbital tends as $R\rightarrow\infty$ (for the entrance-channel orbital it is the energy of a $1s$ electron in the He($1s^2$) atom), we also need to know the energy ε_{ua}^{i} to which $\varepsilon_i(R)$ goes over in the limit of the united atom, i.e., the set of quantum numbers i characterizing the entrance-channel orbital must be known beforehand. And this in turn depends on the parameters of the effective potential. For example, according to the well-known rules[5] relating the terms of isolated atoms with the terms of the united atom in the problem of two Coulomb centers Z_1 and Z_2, for the nuclear charges under consideration ($Z_1=2$ and $Z_2=10$) one should use the $5g\sigma$ OETAMO (see Appendix B) as the entrance-channel function (the orbital of the eZ_1 type). Here the $5g$ state of the Ne^{10+} ion is the state to which the orbital $6h\sigma$ will go over as $R\rightarrow\infty$. When the screening of the charge Z_1 is taken into account in a rough way so as to get the correct value for the energy of the entrance channel in the limit of separated atoms, one should take as the entrance-channel function the $6h\sigma$ OETAMO ($Z_1^*=1.6875$, $Z_2=10$). This can be understood if it is taken into account[3] that the energies of molecular orbitals differing in only one of the spheroidal quantum numbers k,q,m cannot cross. This is the situation for the orbitals $5g\sigma$ ($k=m=0$, $q=4$) and $6h\sigma$ ($k=m=0$, $q=5$). The energies of these orbitals for $Z_1=2$ and $Z_2=10$ are degenerate at $R=\infty$. When screening of the charge Z_1 is introduced, the energy of the eZ_1 term at $R=\infty$ (the energy of a $1s$ electron in the helium atom) becomes higher than the energy of the $5g$ electron in the Ne^{10+} ion, and, because for $R=0$ the energy of the $6h\sigma$ orbital is higher than the energy of the $5g\sigma$ orbital, for $Z_1^*=1.6875$ one should use the $6h\sigma$ OETAMO as the entrance-channel function.

To determine the parameters of the effective potential we use the energy of a $1s$ electron in the He atom: $\varepsilon_{SA}^{(1)}=-1.42$, $Z_{s1}=1.6875$, $n_{s1}=1$, $\Delta_1=0$, $N_2=0$. Here Z_{s1} is the effective charge, which is related to the energy ε_{s1} as $Z_{s1}=n_{s1}\sqrt{2|\varepsilon_{sa}^{(1)}|}$; $\Delta_1=n_1^{(1)}-n_2^{(1)}$; n_{s1}, $n_1^{(1)}$, and $n_2^{(1)}$ are the principal quantum number and parabolic quantum numbers of the atomic state to which the entrance-channel orbital goes over in the limit of separated atoms; N_2 is the number of electrons around the Z_2 nucleus in this limit. We have assumed that for our V_{eff} the $6h\sigma$ orbital should be used as the entrance channel and that for determining the parameters $\tilde{a}_1$ and a_1 (see expressions (17) and (16) of Appendix A) we have used the energies of the $6f$ and $6g$ electronic levels in the Mg^{10+} ion:[6] $\varepsilon_{6f}=-1.7646(\varepsilon_j)$ and $\varepsilon_{6g}=-1.748(\varepsilon_i)$, which gave the parameter values $\tilde{a}_1=-0.864$ and $a_1=0.964$. The parameters a_0 and b_1, according to expressions (23) and (22) in Appendix A, have the values $a_0=0.142$ and $b_1=0.481$. For these values of the parameters of the effective potential (3) the energy of the $5g\sigma$ orbital (of the eZ_2 type) for $R\rightarrow\infty$ lies below the energy $\varepsilon_{6h\sigma}(\infty)=\varepsilon_{SA}^{(1)}$. It is easy to deduce that for $R=\infty$ one has

$$\varepsilon_{5g\sigma}(\infty)=-\frac{[Z_2-(a_1+b_1)/2]^2}{2n_{s2}^2}=-1.72\quad(n_{s2}=5).$$

Figure 1 shows the energies of the $3d\sigma$, $4f\sigma$, $5g\sigma$, and $6h\sigma$ STAMOs obtained for this potential. For the calculation

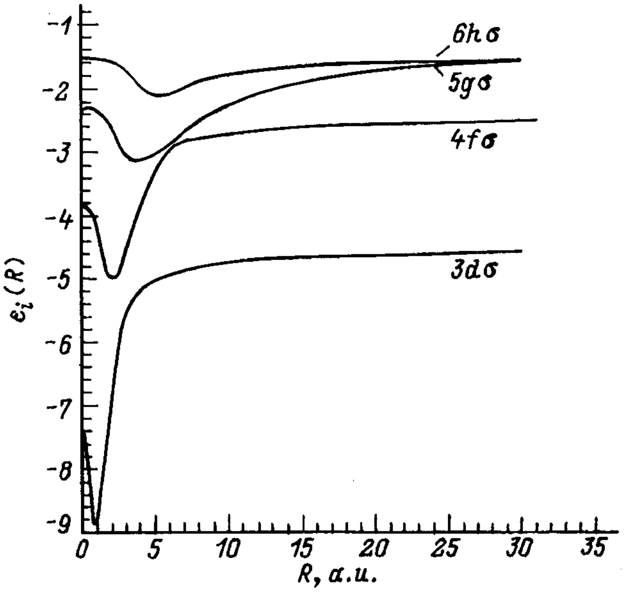

FIG. 1. Energies of STAMOs for the quasimolecule Ne^{10+}–He.

of the one-electron energies ε_i and the one-electron wave functions φ_i we used a program written previously.[4] As we see from Fig. 1, at large distances ($R\simeq 30$ a.u.), where the quasimolecular wave functions are almost completely concentrated around one of the nuclei, there is a quasicrossing of the $6h\sigma$ and $5g\sigma$ orbitals. It is known that upon passage through the region of the quasicrossing of the energies of two states there occurs a sharp change in the wave functions of these states as a result of the transition of the electron from one nucleus to the other. For this reason the $5g\sigma$ STAMO for $R<30$ a.u. becomes the orbital of the eZ_1 type and plays the role of the MO of the entrance channel. As the internuclear distance decreases (for $R\simeq 6$ a.u.) there occurs a quasicrossing of the energies of the $5g\sigma$ and $4f\sigma$ STAMOs, which, as expected, should have a substantial influence on the probability of population of the different channels of the reaction (1). For $R\leqslant 6$ a.u. the $4f\sigma$ STAMO becomes the entrance-channel orbital (orbital of the eZ_1 type).

TWO-ELECTRON STATES OF THE Ne^{10+}–He QUASIMOLECULE

The STAMO basis obtained is used for calculating[7] the total energies E_i of the two-electron diabatic states

$$E_i=\langle\phi_i|H|\phi_i\rangle, \tag{4}$$

$$H=\sum_{i=1}^{2}\left(-\frac{\nabla_i^2}{2}-\frac{Z_1}{r_{1i}}-\frac{Z_2}{r_{2i}}\right)+\frac{1}{r_{12}}, \tag{5}$$

where $\phi_i=[\psi_k(r_1)\psi_l(r_2)+\psi_k(r_2)\psi_l(r_1)]/\sqrt{2}$ is the one-configuration wave function (OWF), r_i are the coordinates of the ith electron, r_{1i} and r_{2i} are the distances for the ith electron to the nuclei Z_1 and Z_2, respectively, and r_{12} is the distance between the electrons.

The two-electron energies are calculated to first order of perturbation theory in the residual interaction $W=1/r_{12}-(V_{\text{eff}}(r_1)+V_{\text{eff}}(r_2))$:

$$E_i=\varepsilon_k+\varepsilon_l+J_{kl}^c+J_{kl}^{ex}-(V_{kk}+V_{ll}),$$

where $J_{kl}^c=\langle\psi_k(r_1)\psi_l(r_2)|1/r_{12}\psi_k(r_1)\psi_l(r_2)\rangle$ is the Coulomb integral, $J_{kl}^{ex}=\langle\psi_k(r_1)\psi_l(r_2)1/r_{12}|\psi_k(r_2)\psi_l(r_1)\rangle$ is the exchange integral, and $V_{kk}=\langle\psi_k|V_{\text{eff}}|\psi_k\rangle$ and $V_{ll}=\langle\psi_l|V_{\text{eff}}|\psi_l\rangle$ are the average values of the effective potential in the states ψ_k and ψ_l.

The adiabatic states in the neighborhood of the crossing points of the diabatic terms are constructed by the configuration interaction (CI) method. In this method the wave function of the system, which satisfies the equation

$$H\Phi_i^a=E_i^a\Phi_i^a, \tag{6}$$

is written as a linear combination of OWFs,

$$\Phi_i^a=\sum_{k=1}^{N}c_k\phi_k, \tag{7}$$

and the energies E_i^a ($i=1,\ldots,N$) of the adiabatic states for a basis of orthogonal OWFs are found as the roots of the equation

$$\det|\hat{H}-E_i^a\hat{I}|=0, \tag{8}$$

where $\hat{H}$ is the matrix of the total Hamiltonian (5), calculated in the basis of OWFs, $\hat{I}$ is the unit matrix, and N is the number of interacting configurations.

With allowance for two interacting configurations ϕ_i and ϕ_j, we find from Eq. (8) that

$$E_{i,j}^a=\frac{H_{ii}+H_{jj}}{2}\pm\sqrt{\frac{(H_{ii}-H_{jj})^2}{4}+H_{ij}^2}, \tag{9}$$

and the energy splitting $\Delta_{ij}(R_{ij}^c)=|E_i^a(R_{ij}^c)-E_j^a(R_{ij}^c)|$ at the crossing point R_{ij}^c of the diabatic states ($\mathrm{H}_{ii}(\mathrm{R}_{ij}^c)=\mathrm{H}_{jj}(\mathrm{R}_{ij}^c)$) has the value $\Delta_{ij}(R_{ij}^c)=2H_{ij}(R_{ij}^c)$.

Calculations showed that for calculating the cross sections for the processes (1) of single electron charge transfer (SECT) and double electron charge transfer (DECT) to the ionic states $Ne^{9+}(n)$ with $n=3$–6 and $Ne^{8+}(n,n')$ with $n=3$–4 and $n'=4$–6 the set of basis functions need include only the one-configuration states listed in Table I. The charge transfer channels include only the Σ states, i.e., for calculating the probabilities of their population only the radial and potential interactions between channels were taken into account, and these do not couple states of the quasimolecule having different projections of the orbital angular momentum onto the axis of the molecule. The right-hand column of Table I gives the atomic limits of the OWFs for $R\rightarrow\infty$. In writing these limits it was taken into account that for the internuclear distances under consideration ($R<30$ a.u.) the orbital of the eZ_1 type (the entrance-channel orbital) is $5g\sigma$.

The results of a calculation of the R dependence of the electronic energies E_i of the diabatic states listed in Table I are plotted in Fig. 2. The dashed curves represent the energies of the states which describe the channels of SECT. One should notice the region of strong interaction of the entrance channel $\phi_{12}(5g\sigma^2)$ with the charge transfer channels $\phi_8(4f\sigma^2)$ and $\phi_9(4f\sigma 5g\sigma)$ in the region of internuclear distances $R\simeq 5.6$–6.4 a.u.; this strong interaction is due to

TABLE I. Wave functions of the two-electron states of the quasimolecule $(\mathrm{NeHe})^{10+}$ and their atomic limits as $R\rightarrow\infty$.

ϕ_i	Limit as $R\rightarrow\infty$
$\phi_1=\frac{1}{\sqrt{2}}[3d\sigma(1)4d\sigma(2)+3d\sigma(2)4d\sigma(1)]$	$\mathrm{Ne}^{8+}(3,4)+\mathrm{He}^{2+}$
$\phi_2=\frac{1}{\sqrt{2}}[3d\sigma(1)4f\sigma(2)+3d\sigma(2)4f\sigma(1)]$	$\mathrm{Ne}^{8+}(3,4)+\mathrm{He}^{2+}$
$\phi_3=\frac{1}{\sqrt{2}}[3d\sigma(1)5d\sigma(2)+3d\sigma(2)5d\sigma(1)]$	$\mathrm{Ne}^{8+}(3,5)+\mathrm{He}^{2+}$
$\phi_4=\frac{1}{\sqrt{2}}[3d\sigma(1)5d\sigma(2)+3d\sigma(2)5g\sigma(1)]$	$\mathrm{Ne}^{9+}(3)+\mathrm{He}^{+}(1s)$
$\phi_5=\frac{1}{\sqrt{2}}[3d\sigma(1)6g\sigma(2)+3d\sigma(2)6g\sigma(1)]$	$\mathrm{Ne}^{8+}(3,6)+\mathrm{He}^{2+}$
$\phi_6=\frac{1}{\sqrt{2}}[3d\sigma(1)6h\sigma(2)+3d\sigma(2)6h\sigma(1)]$	$\mathrm{Ne}^{8+}(3,5)+\mathrm{He}^{2+}$
$\phi_7=\frac{1}{\sqrt{2}}[3d\sigma(1)7i\sigma(2)+3d\sigma(2)7i\sigma(1)]$	$\mathrm{Ne}^{8+}(3,6)+\mathrm{He}^{2+}$
$\phi_8=4f\sigma(1)4f\sigma(2)$	$\mathrm{Ne}^{8+}(4,4)+\mathrm{He}^{2+}$
$\phi_9=\frac{1}{\sqrt{2}}[4f\sigma(1)5g\sigma(2)+4f\sigma(2)5g\sigma(1)]$	$\mathrm{Ne}^{9+}(4)+\mathrm{He}^{+}(1s)$
$\phi_{10}=\frac{1}{\sqrt{2}}[4f\sigma(1)6h\sigma(2)+4f\sigma(2)6h\sigma(1)]$	$\mathrm{Ne}^{8+}(4,5)+\mathrm{He}^{2+}$
$\phi_{11}=\frac{1}{\sqrt{2}}[4f\sigma(1)7i\sigma(2)+4f\sigma(2)7i\sigma(1)]$	$\mathrm{Ne}^{8+}(4,6)+\mathrm{He}^{2+}$
$\phi_{12}=5g\sigma(1)5g\sigma(2)$	$\mathrm{He}(1s^2)$
$\phi_{13}=\frac{1}{\sqrt{2}}[5g\sigma(1)6h\sigma(2)+5g\sigma(2)6h\sigma(1)]$	$\mathrm{Ne}^{9+}(5)+\mathrm{He}^{+}(1s)$
$\phi_{14}=\frac{1}{\sqrt{2}}[5g\sigma(1)7i\sigma(2)+5g\sigma(2)7i\sigma(1)]$	$\mathrm{Ne}^{9+}(6)+\mathrm{He}^{+}(1s)$
$\phi_{15}=\frac{1}{\sqrt{2}}[3d\sigma(1)5p\sigma(2)+3d\sigma(2)5p\sigma(1)]$	$\mathrm{Ne}^{8+}(3,5)+\mathrm{He}^{2+}$

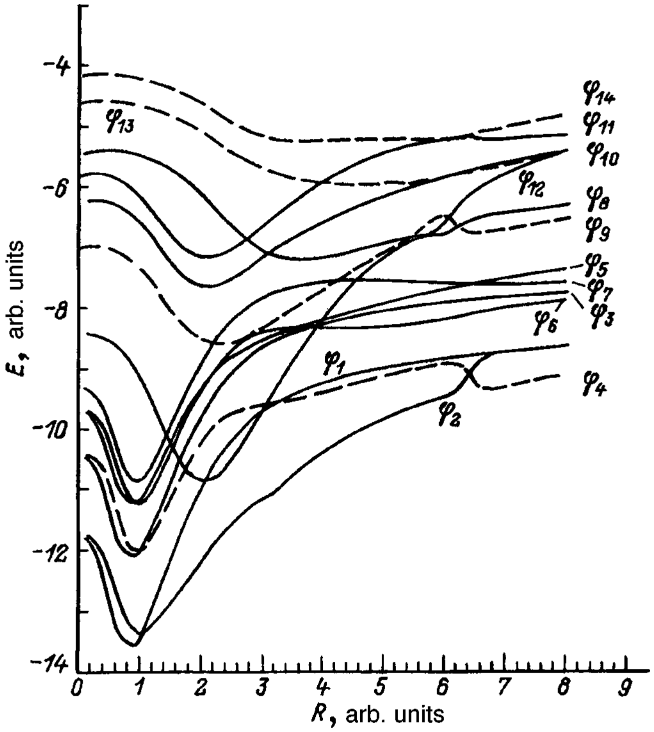

FIG. 2. Two-electron diabatic energies $E_i(R)$ of the states of the quasimolecule Ne^{10+}–He listed in Table I.

the quasicrossing of the one-electron orbitals $5g\sigma$ and $4f\sigma$. It follows from an analysis of the correlation diagram presented in Fig. 2 that it is specifically through these charge transfer channels that the atomic states $\mathrm{Ne}^{9+}(3)$ and $\mathrm{Ne}^{8+}(3l,n'l')$ with $n'=4$–6 (states ϕ_1–ϕ_6) are populated. An exception is the channel $\phi_7(3d\sigma 7i\sigma)$, which describes the charge transfer to the $3d6h$ state of the Ne^{8+} ion. It can be populated directly through the entrance channel in the region of internuclear distances $R\simeq 3.7$ a.u.

CALCULATION OF THE SECT AND DECT CROSS SECTIONS FOR THE Ne^{10+}–He REACTION

The cross sections for the charge transfer processes (1) are calculated for a rectilinear trajectory in the multichannel Landau–Zener and Nikitin models. In these models it is assumed that the transition between adiabatic states occurs at their quasicrossing points. The transition probability at a crossing of the energies of quasidiabatic states ϕ_i and ϕ_j have been calculated in the Landau–Zener–Chaplik approximation[8] with allowance for the radial coupling of these states at their crossing point R_{ij}^c:

$$p_{ij}^{LZ}(\rho,v)=\begin{cases}0, & \text{if}\quad \rho>R_{ij}^c,\\ \exp\left[-\dfrac{\pi\Delta_{ij}^2}{2F_{ij}v_R}-\dfrac{2\pi\kappa_{ij}^2v_R}{F_{ij}}\right], & \text{if}\quad \rho\leqslant R_{ij}^c,\end{cases}\tag{10}$$

where ρ is the impact parameter, F_{ij} is the difference of the slopes of the terms at their crossing point, $v_R=v[1-(\rho/R_{ij}^c)^2]^{1/2}$ is the radial velocity at the point $R=R_{ij}^c$, v is the velocity of the incoming particle, $\kappa_{ij}=\langle\phi_i|d/dR|\phi_j\rangle$ is the matrix element of the radial coupling between the quasidiabatic states at their crossing point.

For an orthogonal basis the matrix elements κ_{ij} are nonzero only for states $\phi_i(\psi_k,\psi_l)$ and $\phi_j(\psi_k,\psi_l)$ for which one of the MOs coincides. In that case K_{ij} is expressed in terms of the matrix element of the radial coupling between the MOs ψ_l and $\psi_{l'}$ as

$$\kappa_{ij}=\langle\phi_i(\psi_k,\psi_l)|\frac{d}{dR}|\phi_j(\psi_k,\psi_{l'})\rangle$$

$$=\begin{cases}\sqrt{2}\langle\psi_l|\dfrac{d}{dR}|\psi_{l'}\rangle, & \text{if}\quad \psi_k=\psi_{l'},\\ \langle\psi_l|\dfrac{d}{dR}|\psi_{l'}\rangle, & \text{if}\quad \psi_k\neq\psi_{l'}.\end{cases}$$

This last expression has been calculated in terms of the overlap integrals of the STAMOs.[9]

The probability of a nonadiabatic passage through the regions of the quasicrossings of the diabatic states ϕ_i and ϕ_j has been calculated in the Nikitin model:[10]

TABLE II. Parameters of the Landau–Zener and Landau–Ziner–Chaplik ($\kappa \neq 0$) models for calculation of the probabilities p_{ij}^{LZ} [Eq. (10)].

$i, j\ (\phi_i - \phi_j)$	R_{ij}^c	$\Delta_{i,j}$	F_{ij}	κ_{ij}
14,12 ($5g\sigma 7i\sigma - 5g\sigma^2$)	1.610E 01	0.120E−03	0.425E−01	0.200E−02
12,13 ($5g\sigma^2 - 5g\sigma 6h\sigma$)	8.200E 00	0.262E−00	0.144E 00	0.127E−00
12,10 ($5g\sigma^2 - 4f\sigma 6h\sigma$)	7.900E 00	1.670E−04	0.220E 00	0.000E 00
13,10 ($5g\sigma 6h\sigma - 4f\sigma 6h\sigma$)	7.230E 00	0.760E−02	1.067E 00	0.364E 00
13,10 ($5g\sigma 6h\sigma - 4f\sigma 6h\sigma$)	6.400E 00	0.482E−01	0.452E 00	0.364E 00
8,9 ($4f\sigma^2 - 4f\sigma 5g\sigma$)	6.20E 00	0.223E−00	1.400E−00	0.230E 00
12,9 ($5g\sigma^2 - 4f\sigma 5g\sigma$)	6.060E 00	0.312E 00	2.300E−00	0.388E−01
8,12 ($4f\sigma^2 - 5g\sigma^2$)	5.700E 00	0.486E 00	0.261E−00	0.000E 00
12,9 ($5g\sigma^2 - 4f\sigma 5g\sigma$)	5.460E 00	0.170E−00	0.480E 00	0.129E−02
8,9 ($4f\sigma^2 - 4f\sigma 5g\sigma$)	5.300E 00	0.272E−00	0.374E 00	0.388E−01
7,8 ($3d\sigma 7i\sigma - 4f\sigma^2$)	4.600E 00	0.716E−04	0.950E 00	0.000E 00
7,9 ($3d\sigma 7i\sigma - 4f\sigma 5g\sigma$)	4.200E 00	0.110E−01	0.548E 00	0.000E 00
8,5 ($4f\sigma^2 - 3d\sigma 6g\sigma$)	3.880E 00	0.484E−03	1.035E 00	0.000E 00
8,3 ($4f\sigma^2 - 3d\sigma 5d\sigma$)	3.830E 00	0.262E−02	1.035E−00	0.000E 00
8,6 ($4f\sigma^2 - 3d\sigma 6h\sigma$)	3.820E 00	0.852E−03	1.335E 01	0.000E 00
4,1 ($3d\sigma 5g\sigma - 3d\sigma 4d\sigma$)	3.280E 00	0.577E−01	0.402E−00	0.000E 00
8,1 ($4f\sigma^2 - 3d\sigma 4d\sigma$)	2.860E 00	0.376E−01	1.830E−00	0.000E 00
8,1 ($4f\sigma^2 - 3d\sigma 4d\sigma$)	2.200E 00	0.584E−01	2.250E−00	0.000E 00

$$p_{ij}^N(\rho, v) = \begin{cases} 0, & \text{if } \rho > R_{ij}^p, \\ \exp(-\pi\xi_c)\dfrac{\sinh[\pi(\xi - \xi_c)]}{\sinh(\pi\xi)}, & \text{if } \rho \leqslant R_{ij}^p, \end{cases} \tag{11}$$

where

$$\xi = \frac{\Delta\varepsilon_{ij}}{\alpha_{ij} v} \quad \text{and} \quad \xi_c = \frac{\xi}{2}(1 - \cos\theta_{ij}),$$

$\Delta\varepsilon_{ij}$ is the energy difference of the adiabatic states for $R \geqslant R_{ij}^p$, α_{ij} and θ_{ij} are model parameters that appear in the expression for the function $f_{ij}(R)$ which approximates the gap $\Delta_{ij}(R) = |E_i^a(R) - E_j^a(R)|$ between the adiabatic states in the neighborhood of their quasicrossing point,

$$f_{ij}(R) = \Delta_{ij}\{1 - 2\cos\theta_{ij}\exp[-\alpha_{ij}(R - R_{ij}^p)] + \exp[-2\alpha_{ij}(R - R_{ij}^p)]\}^{1/2},$$

$$(E_i^a \geqslant E_j^a), \tag{12}$$

and R_{ij}^p is the center of the nonadiabaticity region.

In the present paper all the quantities R_{ij}^p, $\Delta\varepsilon_{ij}$, α_{ij}, and θ_{ij} appearing in expression (12) were treated as parameters and were determined from the condition of minimization of the functional

$$F_{ij}(R_{ij}^p, \Delta\varepsilon_{ij}, \alpha_{ij}, \theta_{ij}) = \sum_{l=1}^{k} (f_{ij}(R_l) - \Delta_{ij}(R_l))^2.$$

Tables II and III give the values of the Landau–Zener, Landau–Zener–Chaplik, and Nikitin model parameters which were obtained from an analysis of the energies of two-electron states and which were used to calculate the probabilities of a single passage through the crossing and quasicrossing regions of the diabatic states listed in Table I.

In calculating the populations of the different channels of reaction (1) we also took into account the rotational interaction between the Σ and Π states of the quasimolecule at small internuclear distances (these states are degenerate at $R = 0$). The probability of these transitions was estimated from the formula[11]

TABLE III. Parameters of the Nikitin model for calculating the probabilities p_{ij}^N [Eq. (11)].

$i, j\ (\phi_i - \phi_j)$	$R_{i,j}^p$	$\Delta\varepsilon_{ij}$	θ_{ij}	α_{ij}
12,13 ($5g\sigma^2 - 5g\sigma 6h\sigma$)	7.270E 00	0.027E 00	1.570E 00	3.686E 00
4,2 ($3d\sigma 5g\sigma - 3d\sigma 4f\sigma$)	6.220E 00	0.500E 00	1.280E−00	0.403E 00
11,14 ($4f\sigma 7i\sigma - 5g\sigma 7i\sigma$)	5.890E 00	0.422E 00	0.075E 00	0.481E 00
11,13 ($4f\sigma 7i\sigma - 5g\sigma 6h\sigma$)	3.930E 00	0.600E 00	0.151E 00	1.290E 00
12,7 ($5g\sigma^2 - 3d\sigma 7i\sigma$)	3.720E 00	1.000E 00	0.436E 00	0.587E 00
5,6 ($3d\sigma 6g\sigma - 3d\sigma 6h\sigma$)	3.630E 00	0.499E 00	0.080E 00	0.623E 00
12,10 ($5g\sigma^2 - 4f\sigma 6h\sigma$)	3.060E 00	0.512E 00	0.419E 00	2.000E 00
9,3 ($4f\sigma 5g\sigma - 3d\sigma 5d\sigma$)	3.010E 00	0.953E−00	0.365E−00	0.675E 00
4,8 ($3d\sigma 5g\sigma - 4f\sigma^2$)	3.000E 00	1.000E 00	0.195E 00	1.618E 00
9,15 ($4f\sigma 5g\sigma - 3d\sigma 5p\sigma$)	2.950E 00	0.724E 00	0.397E 00	0.950E 00
9,6 ($4f\sigma 5g\sigma - 3d\sigma 6h\sigma$)	2.900E 00	0.500E 00	0.345E 00	0.360E 00
9,5 ($4f\sigma 5g\sigma - 3d\sigma 6g\sigma$)	2.890E 00	0.815E 00	0.197E 00	0.842E 00
4,8 ($3d\sigma 5g\sigma - 4f\sigma^2$)	1.760E 00	1.706E 00	0.181E 00	1.850E 00

TABLE IV. $\Sigma - \Pi$ transitions taken into account at small internuclear distances.

Σ state (atomic limit as $R \to 0$)	Π state (atomic limit as $R \to 0$)	A
$\phi_4(3d\sigma 5g\sigma)$ $(\mathrm{Ne}^{9+}(3))$	$\phi(3d\sigma 5g\pi)$ $(\mathrm{Ne}^{8+}(3,5))$	0.0358
$\phi_6(3d\sigma 6h\sigma)$ $(\mathrm{Ne}^{8+}(3,5))$	$\phi(3d\sigma 6h\pi)$ $(\mathrm{Ne}^{8+}(3,6))$	0.0009
$\phi_9(4f\sigma 5g\sigma)$ $(\mathrm{Ne}^{9+}(4))$	$\phi(4f\sigma 5g\pi)$ $(\mathrm{Ne}^{8+}(4,5))$	0.0358
$\phi_{10}(4f\sigma 6h\sigma)$ $(\mathrm{Ne}^{8+}(4,5))$	$\phi(4f\sigma 6h\pi)$ $(\mathrm{Ne}^{8+}(4,6))$	0.0009

$$p^{\mathrm{rot}}(\rho) = 2G(\rho)\exp(-c_1 D^3), \tag{13}$$

where

$$c_1 D^3 = \frac{2A\rho^3}{v\cos^2(\theta/2)}\left[\frac{2}{3} + \frac{11}{6}\sin^2(\theta/2) + \frac{1}{2}(\pi+\theta)\left(\frac{3}{2} + \sin^2(\theta/2)\right)\tan(\theta/2)\right];$$

θ is the scattering angle for the Coulomb trajectory, which is related to the impact parameter by the expression

$$\cot(\theta/2) = Mv^2\rho/(Z_1 Z_2);$$

M is the reduced mass; $G(\rho)$ is the cutoff factor, given by

$$G(\rho) = \frac{(\sin(\theta/2) + c_2 D)^2}{2 + (c_2 D)^2},$$

$$c_2 D = \frac{2\pi}{3\Gamma(4/3)}\left(\frac{A}{3v}\right)^{1/3}\rho\cos(\theta).$$

In deriving formula (13) it was assumed that the energy difference ΔE of the Σ and Π states that are degenerate at $R=0$ can be described to sufficient accuracy at small internuclear distances by a quadratic dependence: $\Delta E \simeq AR^2$. In calculating the charnge transfer cross sections we took into account only the $\Sigma - \Pi$ transitions that lead to a redistribution of the populations between different channels of the reaction (1). Table IV gives the $\Sigma - \Pi$ transitions that were considered and the values of the constant A which were obtained from an analysis of the energy differences of the corresponding MOs and which were used in calculating the corresponding transition probabilities.

The cross section $\sigma_k(v)$ of the reaction (1) involving a transition of the quasimolecule from the initial state (ϕ_{12}) to the final state ϕ_k was calculated as

$$\sigma_k(v) = 2\pi\int_0^\infty \rho P_k(\rho, v)\, d\rho, \tag{14}$$

where $P_k(\rho,v)$ is the probability of population of the state ϕ_k as the nuclei fly apart, which was calculated by adding up the probabilities of all the possible transitions between states of the quasimolecule as R changes from ∞ to ρ as the nuclei come together and from ρ to ∞ as they fly apart.

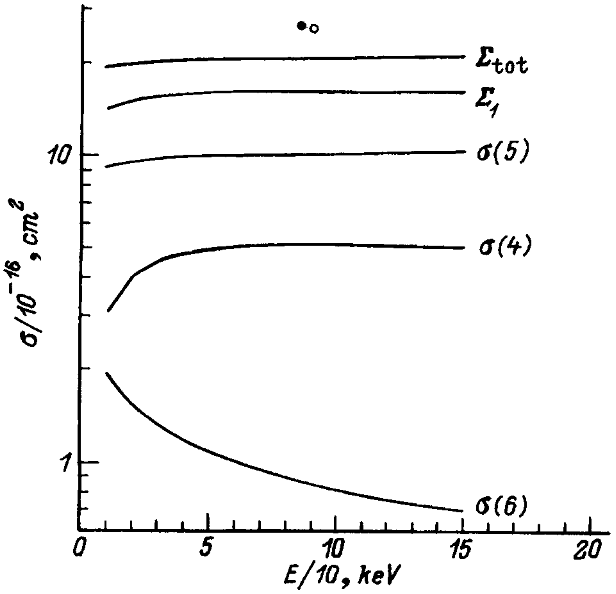

FIG. 3. Single electron capture cross sections $\sigma(n)$ for capture to the ionic states $\mathrm{Ne}^{9+}(n)$, the total SEC cross section Σ_1, the sum Σ_{tot} of the total cross section for single-electron capture and the double electron capture cross sections $\sigma(4,4)$, $\sigma(4,5)$, and $\sigma(4,6)$: ● and ○ are the experimental data[12,13] for the total cross section Σ_{tot} at collision energies $E=86$ and 90 keV.

Setting $k=4$, 9, 13, and 14 in Eq. (14), we obtain, according to the right-hand column in Table I, the cross sections $\sigma(n)$ for single electron capture (SEC) to ionic states $\mathrm{Ne}^{9+}(n)$ with $n=3$, 4, 5, and 6. The dependence of the cross section $\sigma(n)$ on the collision energy is shown in Fig. 3. We see that the largest values are for the cross sections of SEC to the ionic states $\mathrm{Ne}^{9+}(n)$ with $n=5$ and 4, which are populated directly through the entrance channel $\phi_{12}(5g\sigma^2)$ at large internuclear distances ($R>6$ a.u.) as a result of single electron transitions $\phi_{12}(5g\sigma^2) \to \phi_{13}(5g\sigma 6h\sigma)$ and $\phi_{12}(5g\sigma^2) \to \phi_9(4f\sigma 5g\sigma)$. The main contribution to the cross section $\sigma(5)$ comes from the region of quasicrossing ($R_{12,13} \simeq 7.27$ a.u.) of the state $\phi_{13}(5g\sigma 6h\sigma)$ with the entrance channel ϕ_{12}, while the contribution from the crossing point ($R^c_{12,13} = 8.2$ a.u.) of these states is unimportant. As the nuclei come together there is a decrease in the populations of the $\phi_{13}(5g\sigma 6h\sigma)$ channel on account of a redistribution of the probability to the states $\phi_{10}(4f\sigma 6h\sigma)$ ($R^c_{10,13} \simeq 6.4$ a.u.) and $\phi_{11}(4f\sigma 7i\sigma)$ ($R^c_{11,13} \simeq 3.93$ a.u.) and the channel $\phi_9(4f\sigma 5g\sigma)$, through which the population of the state $\phi_8(4f\sigma^2)$ occurs at $R^c_{9,8} = 5.3$ a.u. and the population of a series of states $\phi(3l\sigma 5l'\sigma)$ occurs in the region of internuclear distances $R^c_{9,8} \simeq 2.8$–3.0 a.u. This is probably the cause of the weak dependence of the cross sections $\sigma(5)$ and $\sigma(4)$ on the collision energy E. For E in the range from 20 to 150 keV they are practically independent of the collision energy. The mechanisms of population of the one-electron states with $n=6$ and 3 in the Ne^{9+} ion are different from the mechanism described above for the population of one-electron states with $n=4$ and 5.

The $\phi_{14}(5g\sigma 7i\sigma)$ channel, which as $R \to \infty$ describes the capture of an electron to the $n=6$ state of the Ne^{9+} ion, is populated through the SECT channel $\phi_{13}(5g\sigma 6h\sigma)$ as a result of single and double electron transitions: as the nuclei come together (at $R^c_{11,13} \simeq 3.93$ a.u.) the state $\phi_{11}(4f\sigma 7i\sigma)$ is populated through the channel $\phi_{13}(5g\sigma 6h\sigma)$, and then, as they fly apart (at $R^c_{11,14} \simeq 7.23$ a.u.), it is populated through the channel $\phi_{14}(5g\sigma 7i\sigma)$:

$$\phi_{13}(5g\sigma 6h\sigma) \rightarrow \phi_{11}(4f\sigma 7i\sigma) \rightarrow \phi_{14}(5g\sigma 7i\sigma)$$

(the channel $\phi_{14}(5g\sigma 6h\sigma)$ is populated through the entrance channel $\phi_{12}(5g\sigma^2)$ at $R_{12,13} \simeq 7.27$ a.u.). The population of the $\phi_{14}(5g\sigma 7i\sigma)$ channel does not take place through the entrance channel, since the region of internuclear distances $R_{12,14} \sim 16$ a.u., where the crossing of these channels occurs, is passed through diabatically and does not influence the SEC cross section $\sigma(6)$.

Population of the channel $\phi_4(3d\sigma 5g\sigma)$, which describes SECT to the $n=3$ state of the Ne^{9+} ion as $R \rightarrow \infty$, occurs at $R<6$ a.u. through the channel $\phi_8(4f\sigma^2)$ ($R^c_{4,8} \simeq 3$ and 1.76 a.u.). In the region of internuclear distances $R \simeq 5.3$–6.2 a.u., as a result of a quasicrossing of the one-electron orbitals $4f\sigma$ and $5g\sigma$, there occurs a substantial redistribution of the population of the entrance channel among three states: $\phi_{12}(5g\sigma^2)$, $\phi_8(4f\sigma^2)$, and $\phi_9(4f\sigma 5g\sigma)$. Analysis of the probabilities of passage through the crossing points of these states in the indicated region of internuclear distances showed that the channel $\phi_8(4f\sigma^2)$ is populated mainly through the SECT channel $\phi_9(4f\sigma 5g\sigma)$ at $R^c_{9,8} \simeq 5.3$ a.u. Consequently, the population of the $\phi_4(3d\sigma 5g\sigma)$ channel occurs as a result of the following chain of single and double electron transitions: $\phi_{12}(5g\sigma^2) \rightarrow \phi_9(4f\sigma 5g\sigma) \rightarrow \phi_8(4f\sigma^2) \rightarrow q_4(3d\sigma 5g\sigma)$.

In view of what we have said, one expects that the probabilities of population of the channels $\phi_{14}(5g\sigma 7i\sigma)$ and $\phi_4(3d\sigma 5g\sigma)$ will be significantly smaller than the probabilities of population of the channels $\phi_{13}(5g\sigma 6h\sigma)$ and $\phi_9(4f\sigma 5g\sigma)$, which are populated directly through the entrance channel $\phi_{12}(5g\sigma^2)$ at $R>6$ a.u. In addition, as the nuclei fly apart there occurs a strong decrease in the population of the $\phi_4(3d\sigma 5g\sigma)$ states on account of a transition at $R \simeq 6.4$ a.u. (the quasicrossing region of the $4f\sigma$ and $5g\sigma$ orbitals) to the states $\phi_2(3d\sigma 4f\sigma)$. As a result, the SEC cross section $\sigma(3)$ is less than 10^{-19} cm^2 throughout the interval of collision energies considered, and because it is so small we have not shown it in Fig. 3. The values obtained for the total SEC cross section $\Sigma_1 = \sigma(3) + \sigma(4) + \sigma(5) + \sigma(6)$ are shown in Fig. 3. The results of a calculation of the double electron capture cross sections $\sigma(n,n')$ to the $nln'l'$ states of the Ne^{8+} ion with $n=3,4$ and $n'=4$–6 are given in Fig. 4.

Because of the presence of a quasicrossing of the $4f\sigma$ and $5g\sigma$ one-electron orbitals, the main contribution to the double electron capture cross sections $\sigma(4,4)$ and $\sigma(4,5)$ comes from the channels $\phi_8(4f\sigma^2)$ and $\phi_{10}(4f\sigma 6h\sigma)$, respectively, so that $\sigma(4,4) \simeq \sigma_8$ and $\sigma(4,5) \simeq \sigma_{10}$. It is seen from the correlation diagram (Fig. 2) that the population of the $\phi_8(4f\sigma^2)$ channel, which describes DECT to the ionic state $\mathrm{Ne}^{8+}(4,4)$, can occur either directly through the entrance channel $\phi_{12}(5g\sigma^2)$ at $R^c_{8,12} \simeq 5.7$ a.u. (correlated double electron transition) or through the SECT channel $\phi_9(4f\sigma 5g\sigma)$ (at $R_{9,8} \simeq 5.3$ a.u.) as a result of two successive single electron transitions: $\phi_{12}(5g\sigma^2) \rightarrow \phi_9(5g\sigma 4f\sigma) \rightarrow \phi_8(4f\sigma^2)$ (uncorrelated double electron transition). As we have said, a calculation showed that the population of the state $\phi_8(4f\sigma^2)$ occurs mainly through the $\phi_9(4f\sigma 5g\sigma)$ channel. As the collision velocity v increases, the probability of direct population of the $\phi_8(4f\sigma^2)$ channel through the entrance channel $\phi_{12}(5g\sigma^2)$ increases, and for $v=1$ a.u. it amounts to $\simeq 20\%$ of the total probability of population of the $\phi_8(4f\sigma^2)$ channel. It turns out not to be important to take into account the radial coupling of the channels $\phi_{12}(5g\sigma^2)$, $\phi_8(4f\sigma^2)$, and $\phi_9(4f\sigma 5g\sigma)$ in the region of the strong potential interaction between them (for $R \simeq 6$ a.u.). The population of the channel $\phi_{10}(4f\sigma 6h\sigma)$, which describes DECT to the ionic state $\mathrm{Ne}^{8+}(4,5)$ occurs through the SECT channel $\phi_{13}(5g\sigma 6h\sigma)$ at $R_{10,13} \simeq 6.4$ a.u. as a result of two single electron transitions: $\phi_{12}(5g\sigma^2) \rightarrow \phi_{13}(5g\sigma 6h\sigma) \rightarrow \phi_{10}(4f\sigma 6h\sigma)$ (uncorrelated double electron transition). Here a substantial contribution to the DECT cross section $\sigma(4,5)$ is given by the radial interaction of the channels $\phi_{10}(4f\sigma 6h\sigma)$ and $\phi_{13}(5g\sigma 6h\sigma)$ at their crossing point $R^c_{10,13} \simeq 6.4$ a.u. Including the radial coupling increased the cross section $\sigma(4,5)$ at $E=150$ keV by almost an order of magnitude. The double electron capture cross section $\sigma(4,5)$, calculated without including the radial interaction between channels, is shown by the dashed curves in Fig. 4. The contribution to the total cross section $\sigma(4,5)$ from the $\phi(4f\sigma 5g\pi)$ state, which is populated at small internuclear distances through the $\phi_9(4f\sigma 5g\sigma)$ channel as a result of the rotational interaction, is unimportant.

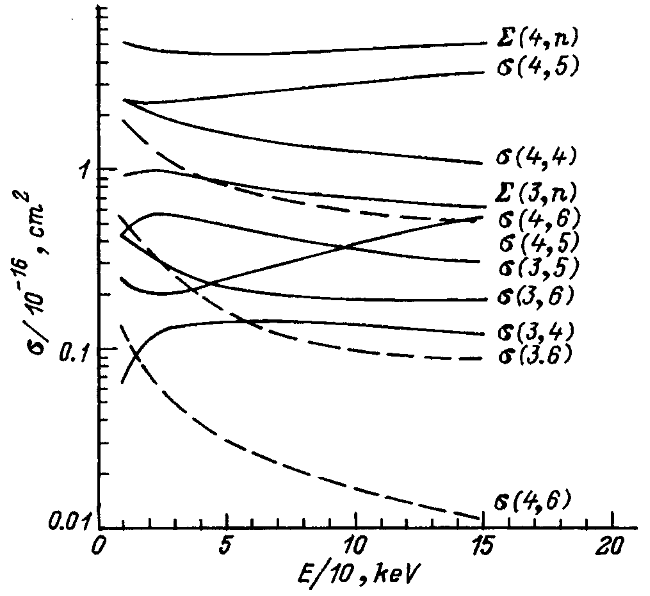

FIG. 4. Cross sections $\sigma(n,n')$ for double electron capture to the ionic states $\mathrm{Ne}^{8+}(n,n')$. The dashed curves show the cross section $\sigma(4,5)$ calculated without including the radial coupling between the $\phi_{10}(4f\sigma 5g\sigma)$ and $\phi_{13}(5g\sigma 6h\sigma)$ channels, and the cross sections $\sigma(4,6)$ and $\sigma(3,6)$, calculated without including the rotational interaction at small internuclear distances between the channels $\phi_{13}(5g\sigma 6h\sigma)$, $\phi(5g\sigma 6h\pi)$ and the channels $\phi_6(3d\sigma 6h\sigma)$, $\phi(3d\sigma 6h\pi)$; $\Sigma(3,n)$ and $\Sigma(4,n)$ are the sums of the corresponding partial cross sections.

In the calculation of the cross section $\sigma(4,6)$ we took into account the probabilities of population of two channels: $\phi_{11}(4f\sigma 7i\sigma)$ and $\phi(4f\sigma 6h\sigma)$. The first channel is populated at $R^c_{11,13} \simeq 3.93$ a.u. through the state $\phi_{13}(5g\sigma 6h\sigma)$ as a result of the double electron transition $\phi_{13}(5g\sigma6h\sigma)\rightarrow\phi_{11}(4f\sigma7i\sigma)$ (the channel $\phi_{13}(5g\sigma6h\sigma)$ is populated through the ground channel $\phi_{12}(5g\sigma^2)$ at $R\sim8.2$ a.u.). However, as the nuclei fly apart (at $R\simeq7.2$ a.u.) the SECT channel $\phi_{14}(5g\sigma7i\sigma)$ is populated through it, and this leads to a decrease in the population of the $\phi_{11}(4f\sigma7i\sigma)$ channel. The second channel $\phi(4f\sigma6h\pi)$ is populated through the channel $\phi_{10}(4f\sigma6h\sigma)$ at small internuclear distances as a result of the rotational coupling between channels. Calculations showed that at the collision energies under consideration the population of the $4l6l$ states in the Ne^{8+} ion occurs mainly at small internuclear distances. For comparison of the contributions to the total cross section $\sigma(4,6)$ from the two indicated channels, the dashed curves in Fig. 4 show the cross section $\sigma(4,6)$ obtained with only the channel $\phi_{11}(4f\sigma7i\sigma)$ taken into account.

Figure 3 shows the sum Σ_{tot} of the double electron capture cross sections $\sigma(4,4)$, $\sigma(4,5)$, and $\sigma(4,6)$ and the total SEC cross section Σ_1 for comparison with the available experimental data for $E=86$ keV ($\Sigma_{\mathrm{tot}}=2.63\times10^{-15}$ cm^2; Ref. 12) and for $E=90$ keV ($\Sigma_{\mathrm{tot}}=2.60\times10^{-15}$ cm^2; Ref. 13). Our calculation gives a somewhat too low value for the cross section at $E=90$ keV, viz., $\Sigma_{\mathrm{tot}}\simeq2.1\times10^{-15}$ cm^2. The distribution of two-electron states to the total cross section Σ_{tot} is of the order of 25%.

In calculating the double electron capture cross sections $\sigma(3l,n'l')$ we investigated in detail the dependence of these cross sections on the values of the azimuthal quantum numbers l and l'. For this we included in the set of basis functions all of the one-configuration states that in the limit of separated atoms describe the states of the ion $Ne^{8+}(3l,n'l')$ with $n'=4$–6, $l'=1,\dots,n'-1$ for $l=1,2$, viz., $\phi(3l\sigma4l'\sigma)$, $\phi(3l\sigma5l'\sigma)$, $\phi(3l\sigma6l'\sigma)$. Figure 5a–5c gives the energies of these states as functions of the internuclear distance; Tables V and VI give the necessary parameters of the Landau–Zener and Nikitin models for calculating the probabilities of single passage through the regions of the crossings and quasicrossings of the additionally introduced states with the states listed in Table I.

We see from Fig. 5a, which shows the energies of the channels of charge transfer to the $3l4l'$ states of the Ne^{8+} ion, that the population of these channels can occur both directly, through the channel $\phi_8(4f\sigma^2)$, and also through the channel $\phi_4(3d\sigma5g\sigma)$. Here the state $\phi(3p\sigma4p\sigma)$ is populated only through the channel $\phi_8(4f\sigma^2)$, while the states $\phi_2(3d\sigma4f\sigma)$ and $\phi(3p\sigma4f\sigma)$ are populated only through the channel $\phi_4(3d\sigma5g\sigma)$. Calculations of the partial cross sections $\sigma(3l4l')$, presented in Fig. 6a, showed that they depend strongly on l'. This was to be expected, considering the scatter in the Landau–Zener model parameters given in Table V for $n'=4$. The main contribution ($\sim$90%) to the double electron capture cross section $\sigma(3,4)$ is from the channel $\phi_2(3d\sigma4f\sigma)$. Population of this channel occurs as a result of the following single and double electron transitions: $\phi_{12}(5g\sigma^2)\rightarrow\phi_9(4f\sigma5g\sigma)\rightarrow\phi_8(4f\sigma^2)\rightarrow\phi_4(3d\sigma5g\sigma)$ $\phi_{12}(5g\sigma^2)\rightarrow\phi_9(4f\sigma5g\sigma)\rightarrow\phi_8(4f\sigma^2)\rightarrow\phi_4(3d\sigma5g\sigma)\rightarrow\phi_2(3d\sigma4f\sigma)$. To an accuracy of 1% one can write $\sigma(3,4)\simeq\sigma_2+\sigma_1$, where σ_1 is the next-largest contribution to the cross section $\sigma(3,4)$, from the channel $\phi_1(3d\sigma4d\sigma)$.

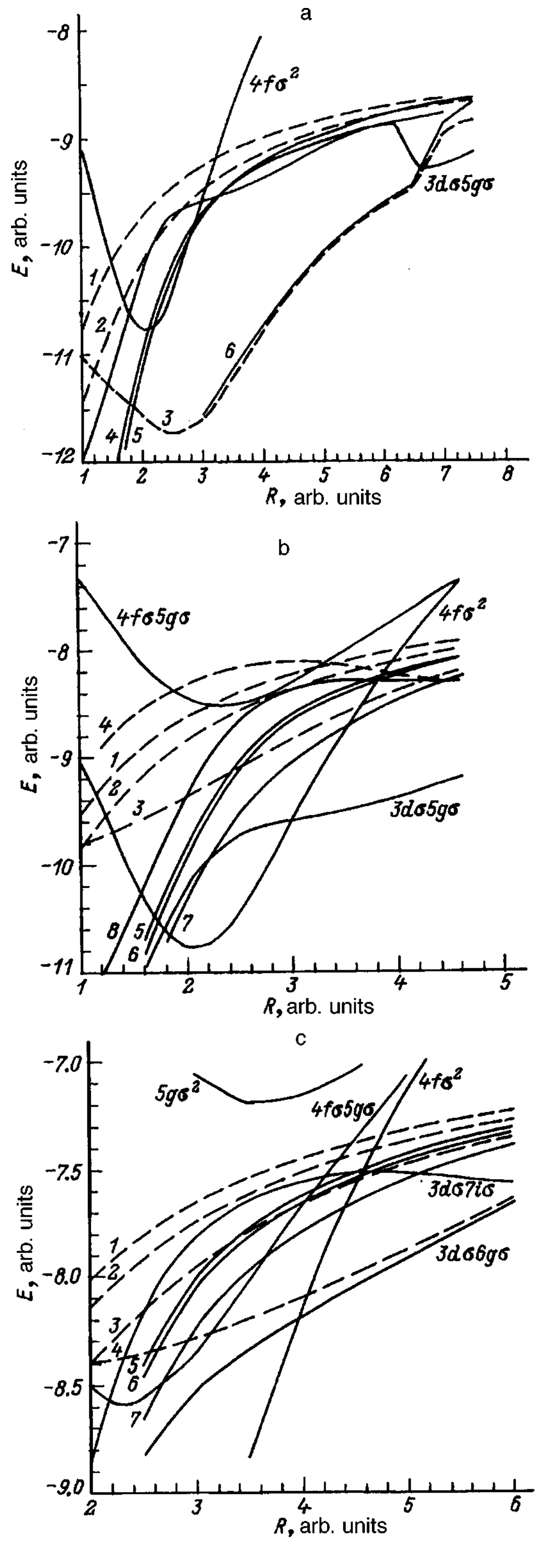

FIG. 5. Energies of the channels of charge transfer to the $3l4l'$ states of the Ne^{8+} ion (a): *1* — $\phi(3p\sigma4p\sigma)$, *2* — $\phi(3p\sigma4d\sigma)$, *3* — $\phi(3p\sigma4f\sigma)$, *4* — $\phi(3d\sigma4p\sigma)$, *5* — $\phi(3d\sigma4p\sigma)$, *6* — $\phi(3d\sigma4f\sigma)$; to the $3l5l'$ states of the Ne^{8+} ion (b): *1* — $\phi(3p\sigma5p\sigma)$, *2* — $\phi(3p\sigma5d\sigma)$, *3* — $\phi(3p\sigma5f\sigma)$, *4* — $\phi(3p\sigma6h\sigma)$, *5* — $\phi(3d\sigma5p\sigma)$, *6* — $\phi(3d\sigma5d\sigma)$, *7* — $\phi(3d\sigma5f\sigma)$, *8* — $\phi(3d\sigma6h\sigma)$; to the $3l6l'$ states of the Ne^{8+} ion (c): *1* — $\phi(3p\sigma6p\sigma)$, *2* — $\phi(3p\sigma6d\sigma)$, *3* — $\phi(3p\sigma6f\sigma)$, *4* — $\phi(3p\sigma6g\sigma)$, *5* — $\phi(3d\sigma6p\sigma)$, *6* — $\phi(3d\sigma6d\sigma)$, *7* — $\phi(3d\sigma6f\sigma)$.

The situation with the population of the $3l5l'$ states in the Ne^{8+} ion is somewhat more complicated. As we see

TABLE V. Additional crossing points of the diabatic states ϕ_i,ϕ_j taken into account in the calculation of the cross sections for DECT to the ionic states $Ne^{8+}(3l,n'l')$ and the Landau–Zener model parameters corresponding to them.

n'	$\phi_i-\phi_j$	R^c_{ij}	Δ_{ij}	F_{ij}	κ_{ij}
6	$4f\sigma^2-3p\sigma6d\sigma$	4.540E 00	0.100E−03	0.905E−00	0.000E 00
	$4f\sigma5g\sigma-3p\sigma6d\sigma$	4.420E 00	0.436E−03	0.360E−00	0.000E 00
	$4f\sigma^2-3d\sigma6d\sigma$	4.420E 00	0.828E−03	0.885E−00	0.000E 00
	$4f\sigma^2-3p\sigma6f\sigma$	4.410E 00	0.714E−03	0.900E−00	0.000E 00
	$4f\sigma^2-3d\sigma6f\sigma$	4.300E 00	0.494E−03	0.870E−00	0.000E 00
	$4f\sigma5g\sigma-3p\sigma6f\sigma$	4.160E 00	0.266E−02	0.305E−00	0.000E 00
	$4f\sigma5g\sigma-3d\sigma6d\sigma$	4.180E 00	0.204E−02	0.290E−00	0.000E 00
	$4f\sigma^2-3p\sigma6g\sigma$	3.970E 00	1.080E−03	1.070E−00	0.000E 00
	$4f\sigma5g\sigma-3d\sigma6f\sigma$	3.700E 00	0.260E−02	0.235E−00	0.000E 00
	$4f\sigma5g\sigma-3p\sigma6g\sigma$	3.080E 00	0.302E−02	0.410E−00	0.000E 00
	$4f\sigma5g\sigma-3d\sigma6f\sigma$	2.700E 00	0.130E−01	0.535E−00	0.000E 00
5	$4f\sigma^2-3p\sigma5f\sigma$	3.660E 00	0.306E−02	1.005E−00	0.000E 00
	$4f\sigma^2-3d\sigma5f\sigma$	3.520E 00	0.731E−03	0.950E−01	0.000E 00
	$4f\sigma5g\sigma-3p\sigma5p\sigma$	3.240E 00	0.293E−02	0.360E−00	0.000E 00
	$4f\sigma5g\sigma-3p\sigma5p\sigma$	2.230E 00	0.492E−02	0.895E−00	0.000E 00
4	$3d\sigma5g\sigma-3p\sigma4f\sigma$	6.420E 00	0.179E−01	3.450E−00	0.000E 00
	$3d\sigma5g\sigma-5d\sigma4p\sigma$	3.280E 00	0.657E−02	0.350E−00	0.000E 00
	$4f\sigma^2-3p\sigma4p\sigma$	3.220E 00	0.362E−02	1.385E−00	0.000E 00
	$4f\sigma^2-3p\sigma4d\sigma$	3.060E 00	0.558E−03	1.310E−00	0.000E 00
	$4f\sigma^2-3d\sigma4p\sigma$	2.910E 00	0.250E−03	1.055E−00	0.000E 00
	$3d\sigma5g\sigma-3p\sigma4d\sigma$	2.680E 00	0.106E−01	0.275E−00	0.000E 00
	$4f\sigma^2-3d\sigma4p\sigma$	2.120E 00	0.232E−02	1.750E−00	0.000E 00
	$3d\sigma5g\sigma-3p\sigma4d\sigma$	2.100E 00	0.157E−01	0.350E−00	0.000E 00
	$4f\sigma^2-3p\sigma4d\sigma$	1.690E 00	0.575E−02	2.600E−00	0.000E 00
	$4f\sigma^2-3p\sigma4p\sigma$	1.500E 00	0.308E−01	3.200E−00	0.000E 00

from Fig. 5b, in this case the charge transfer channels $\phi(3p\sigma5d\sigma)$, $\phi(3p\sigma5f\sigma)$, $\phi_{15}(3d\sigma5p\sigma)$, $\phi(3d\sigma5d\sigma)$, $\phi(3d\sigma5f\sigma)$, and $\phi_6(3d\sigma6h\sigma)$ not only have crossings with the channels $\phi_8(4f\sigma^2)$ and $\phi_9(4f\sigma5g\sigma)$ but also have quasicrossings with the the latter in the region of internuclear distances $R\simeq2.5$–3.0 a.u. In this case, since the potential interactions of the $\phi(3l\sigma5l'\sigma)$ states with the channels $\phi_8(4f\sigma^2)$ and $\phi_9(4f\sigma5g\sigma)$ at the crossing points with them are small (see Table V, $n'=5$), one expects that the main contribution to the charge transfer cross section $\sigma(3,5)$ will be from the indicated quasicrossing regions. Calculations of the partial cross sections $\sigma(3l5l')$ have shown (Fig. 6b) that the largest values are those for the partial cross sections for charge transfer to the states $3d5d$, $3d5p$, and $3d5g$ of the Ne^{8+} ion, since $\sigma(3,5)\simeq\sigma_3+\sigma_6+\sigma_{15}$. But it is the channels $\phi_3(3d\sigma5d\sigma)$, $\phi_{15}(3d\sigma5p\sigma)$, and $\phi_6(3d\sigma6h\sigma)$, which describe charge transfer to these states, that have the ''optimum'' minimum values of the gap ($\Delta E^a_{\min}$) in the region of the quasicrossings of the $\phi(3l\sigma5l'\sigma)$ states with the channel $\phi_9(4f\sigma5g\sigma)$: the respective values of $\Delta E^a_{\min}$ are 0.348 ($R\simeq3.01$ a.u.), 0.292 ($R\simeq2.89$ a.u.), and 0.170 ($R\simeq2.90$ a.u.). To see that the population of the channels $\phi_3(3d\sigma5d\sigma)$, $\phi_{15}(3d\sigma5p\sigma)$, and $\phi_6(3d\sigma6h\sigma)$ occurs mainly through the channel $\phi_9(4f\sigma5g\sigma)$ and not through $\phi_8(4f\sigma^2)$, we performed a calculation in which transitions between the indicated states and the $\phi_9(4f\sigma5g\sigma)$ state were not taken into account. The partial cross sections $\sigma(3d5g)$ and $\sigma(3d5d)$ obtained in that calculation are shown by the dashed curves in Fig. 6b (the cross section $\sigma(3d5p)<10^{-21}$ cm^2 and is not shown in the figure). The calculations confirmed that the population of the channels $\phi_3(3d\sigma5d\sigma)$, $\phi_{15}(3d\sigma5p\sigma)$, and $\phi_6(3d\sigma6h\sigma)$, which are responsible for charge transfer to the $3l5l'$ states of the Ne^{8+} ion, occurs through the SECT channel $\phi(4f\sigma5g\sigma)$ as a result of the following electronic transitions:

$$\phi_{12}(5g\sigma^2)\to\phi_9(4g\sigma5g\sigma)\to\begin{cases}\phi_3(3d\sigma5d\sigma),\\ \phi_{15}(3d\sigma5p\sigma),\\ \phi_6(3d\sigma6h\sigma).\end{cases}$$

TABLE VI. Additional regions of quasicrossings of the two-electron states ϕ_i and ϕ_j taken into account in the calculation of the cross sections for DECT to the ionic states $Ne^{8+}(3l,n'l')$ and the Nikintin model parameters corresponding to them.

n'	$\phi_i-\phi_j$	R^p_{ij}	$\Delta\varepsilon_{ij}$	θ_{ij}	α_{ij}
5	$4f\sigma5g\sigma-3d\sigma5f\sigma$	2.810E 00	0.993E−00	0.805E−00	0.802E 00
	$4f\sigma5g\sigma-3p\sigma5d\sigma$	2.740E 00	1.500E−00	0.012E−00	0.201E 00
	$4f\sigma5g\sigma-3p\sigma5f\sigma$	2.660E 00	0.967E−00	0.572E−00	0.697E 00

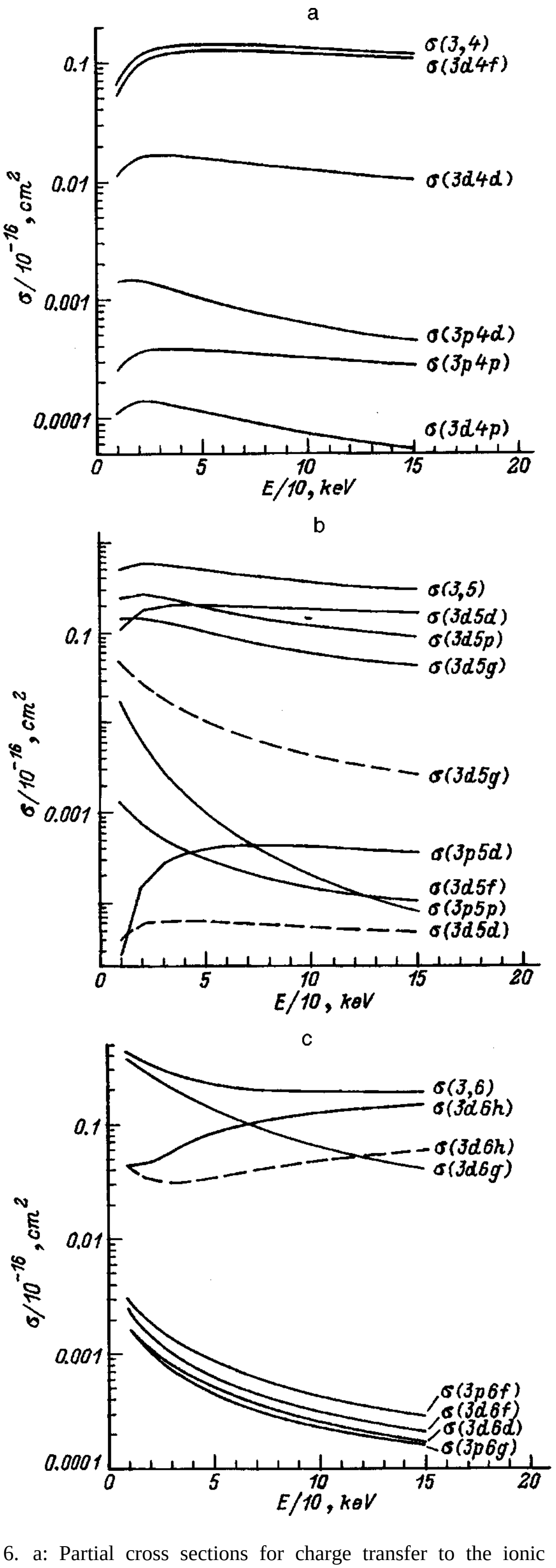

FIG. 6. a: Partial cross sections for charge transfer to the ionic states $Ne^{8+}(3l4l')$ and the total cross section $\sigma(3,4)$ for DECT; b: $Ne^{8+}(3l5l')$ and $\sigma(3,5)$; the dashed curves show the results of a calculation of the cross sections $\sigma(3d5d)$ and $\sigma(3d5g)$ obtained without taking into account the potential interaction of the channels $\phi_3(3d\sigma5d\sigma)$ and $\phi_6(3d\sigma6h\sigma)$ with the SECT channel $\phi_9(4f\sigma5g\sigma)$; c: $Ne^{8+}(3l6l')$ and $\sigma(3,6)$, the dashed curve is the cross section $\sigma(3d6h)$ obtained without including the contribution from the channel $\phi(3d\sigma6h\pi)$.

TABLE VII. Cross sections for double electron capture at collision energy of 150 keV for the system Ne^{10+}–He.

n, *n′* (10^{-16} cm^2)	$\sigma(n, n')$ (10^{-16} cm^2)	$\sigma(n, n')^{\text{exp}}$ (10^{-16} cm^2)
3, 4	0.118	0.52±0.16
3, 5	0.304	0.39±0.12
3, 6	0.187	0.23±0.07
4, 4	1.065	0.79±0.24
4, 5	3.401	1.10±0.33
4, 6	0.540	0.30±0.09

Note: The cross sections $\sigma(n,n')$ were obtained in the present paper, while $\sigma(n,n')^{\text{exp}}$ are the experimental data of Ref. 14.

Inclusion of the rotational interaction between the $\phi_4(3d\sigma5g\sigma)$ and $\phi(3d\sigma5g\pi)$ states at small internuclear distances does not give a substantial contribution to the DECT cross section $\sigma(3,5)$. The population of the $3l6l'$ states in the Ne^{8+} ion occurs in an analogous way. Figure 5c shows the energies of the corresponding charge transfer channels as functions of the internuclear distance R. The main contribution to the cross section $\sigma(3,6)$ is from the regions of the quasicrossing of the $\phi_5(3d\sigma6g\sigma)$ channel with the SECT channel $\phi_9(4f\sigma5g\sigma)$ at $R\simeq3$ a.u. ($\Delta E^a_{\text{min}}=0.206$) and the quasicrossing of the $\phi_7(3d\sigma7i\sigma)$ channel with the entrance channel $\phi_{12}(5g\sigma^2)$ at $R\simeq3.8$ a.u. ($\Delta E^a_{\text{min}}=0.420$). Here the state $\phi_5(3d\sigma6g\sigma)$ is populated through the SECT channel $\phi_9(4f\sigma5g\sigma)$: $\phi_{12}(5g\sigma^2)\rightarrow\phi_9(4g\sigma5g\sigma)\rightarrow\phi_5(3d\sigma6g\sigma)$, while the channel $\phi_7(3d\sigma7i\sigma)$ is populated directly through the entrance channel $\phi_{12}(5g\sigma^2)$ (at $R<6$ a.u.): $\phi_{12}(5g\sigma^2)\rightarrow\phi_9(3d\sigma7i\sigma)$. However, as a calculation shows, in this case there is a appreciable contribution to the total DECT cross section $\sigma_($3,6 from the channel $\phi(3d\sigma6h\pi)$, which is populated at small internuclear distances through the state $\phi_6(3d\sigma6h\sigma)$ as a result of the rotational interaction. For comparison the dashed curves in Fig. 4 and Fig. 6c show the cross sections $\sigma(3,6)$ and $\sigma(3d6h)$ obtained without including the contribution from the $\phi(3d\sigma6h\pi)$ channel.

Table VII shows a comparison of the results of our calculation of the DECT cross section $\sigma(n,n')$ with the available experimental data[14] for a collision energy of 150 keV. For $n=3$, $n'=5$,6 and $n=4$, $n'=4$ the values obtained for the cross sections are in good agreement with experiment. The results of the calculations for $\sigma(3,4)$ and $\sigma(4,6)$ differ by approximately a factor of 2 from the experimental data, and the result for $\sigma(4,5)$ is off by a factor of approximately 3.

CALCULATION OF THE SINGLE ELECTRON CAPTURE PROCESS IN THE COLLISION Ne^{6+}–He

For the collision of the incompletely stripped ion Ne^{6+} with helium atoms there are both experimental and theoretical data available on the total cross sections for SEC. We know of only one calculation[15] of the cross section, which was done in the coupled-channel method in a basis of atomic orbitals, and only for a collision energy of 2 keV. There are experimental data on the total capture cross sections in the intervals of collision energy $E<2$ keV[16] and $E\sim20$–120 keV.[17] It is therefore of interest to calculate the cross sections over a wide energy interval, both to complete the data

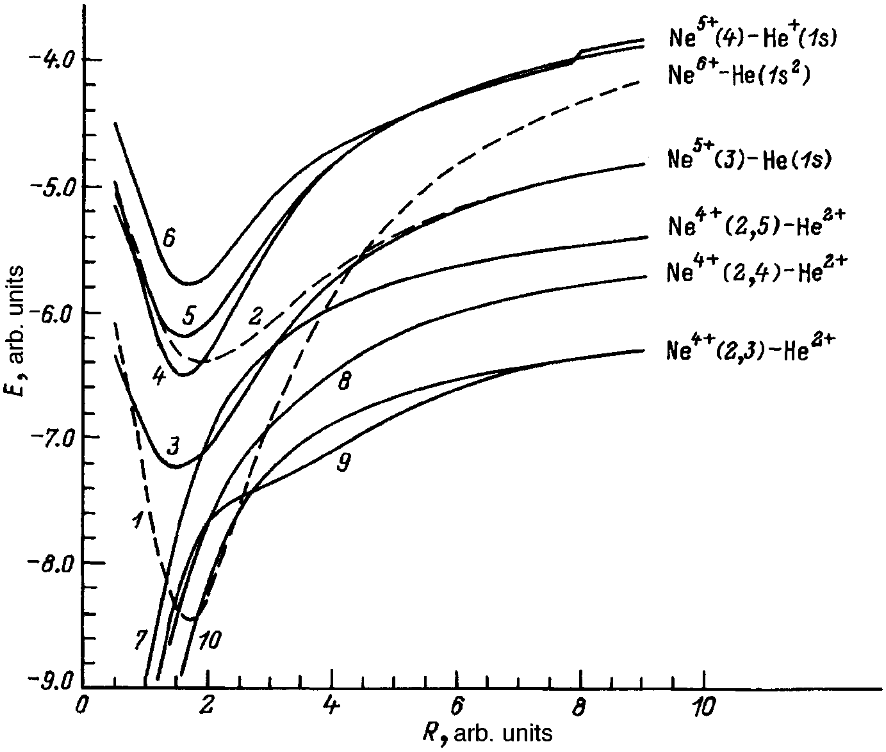

FIG. 7. Energies of the diabatic two-electron states ϕ_i of the quasimolecule Ne^{6+}–He: *1* — $i=\phi(3d\sigma^2)$, *2* — $\phi(3d\sigma 4f\sigma)$, *3* — $\phi(3p\sigma 3d\sigma)$, *4* — $\phi(3d\sigma 4p\sigma)$, *5* — $\phi(3d\sigma 4d\sigma)$, *6* — $\phi(3d\sigma 5g\sigma)$, *7* — $\phi(2p\sigma 5d\sigma)$, *8* — $\phi(2p\sigma 4d\sigma)$, *9* — $\phi(2p\sigma 4f\sigma)$, *10* — $\phi(2p\sigma 3p\sigma)$.

and for comparison of the calculation with experimental data, since previous estimates[16] for $E<2$ keV in the framework of the multichannel Landau–Zener model with the model parameters gave values of the cross sections that are an order of magnitude smaller than the experimental values. We will not concern ourselves with the DECT cross sections for the system Ne^{6+}–He, as this process presumably gives an insignificant contribution to the total cross section.

The one-electron diabatic molecular orbitals ψ_i from which the two-electron quasimolecular state (1a) is constructed and which describe the entrance and exit channels of the reaction

$$Ne^{6+}(1s^2 2s^2)+He(1s^2)\rightarrow Ne^{5+}(1s^2 2s^2 nl) + He^{+}(1s), \qquad (15)$$

were determined from the Schrödinger equation (2), and the parameters of the effective potential (3) that were found to optimally describe the entrance-channel orbital $4f\sigma$ are as follows (for nuclear charges $Z_1=2$ and $Z_2=6$): $\tilde{a}_1=-2.005$, $a_1=1.361$, $a_0=0.275$, $b_1=0.01$, $b_2=-1.011$.

Analysis of the energies and wave functions of the calculated one-electron molecular states showed that at an internuclear distance $R\simeq 14$ a.u., when the quasimolecular wave functions are still almost completely concentrated around one of the nuclei, there is a quasicrossing of the energy of the entrance-channel orbital $4f\sigma$ (the orbital of the eZ_1 type for $R>14$ a.u.) with the energy of the $3d\sigma$ orbital, and, accordingly, there is a sharp change in the wave functions of these states, due to the transition of an electron from one nucleus to the other, as a result of which for $R<14$ a.u. the role of the entrance-channel function passes over to the $3d\sigma$ orbital.

Figure 7 shows the energies of the two-electron diabatic states for the quasimolecule $(NeHe)^{6+}$ and indicates the atomic limits of these states for $R\rightarrow\infty$. Analysis of the correlation diagram obtained shows that the SEC processes are governed mainly by single electron transitions between the $\Sigma(3d\sigma^2)$ state of the entrance channel of reaction (15) and the charge transfer states $\Sigma(3d\sigma 4f\sigma)$ and $\Sigma(3d\sigma 3p\sigma)$ in the interval of internuclear distances $R\simeq 4.3$–4.7 a.u., and also by the transition at small internuclear distances between the state of the entrance channel and the $\Pi(3d\sigma 3d\pi)$ state, which is degenerate with it at $R=0$. All of the channels indicated above describe charge transfer to the ionic state $Ne^{5+}(n=3)$. Crossings between the entrance-channel term $\Sigma(4f\sigma^2)$ and the terms corresponding to charge transfer to the ionic states $Ne^{5+}(n=4)$, which lie at $R>17$ a.u., occur almost diabatically at the investigated collision velocities v from 0.06 to 0.6 a.u. and do not give an appreciable contribution to the total SECT cross section. Population of the $\Sigma(3d\sigma 4d\sigma)$ channel through the SECT channel $\Sigma(3d\sigma 4f\sigma)$ at $R\simeq 2$ a.u. likewise does not contribute appreciably to the total SECT cross section.

To determine the probability of nonadiabatic transition in the neighborhood of the crossing point R_{12} of the terms $\Sigma(3d\sigma^2)$ and $\Sigma(3d\sigma 4f\sigma)$ we used the exponential model of Nikitin (11). To determine the parameters of the potential interaction in the neighborhood of the crossing point we calculated the adiabatic states of the interaction of two configurations (9), from an analysis of which we obtained the following model parameters:

$$R_{12}: \quad R_p=4.64, \quad \Delta\varepsilon=0.632,$$

$$\alpha=0.542, \quad \theta=0.229.$$

The probability of a nonadiabatic transition between the states $\Sigma(3d\sigma^2)$ and $\Sigma(3d\sigma 3p\sigma)$ and $\Sigma(3d\sigma 4d\sigma)$ and

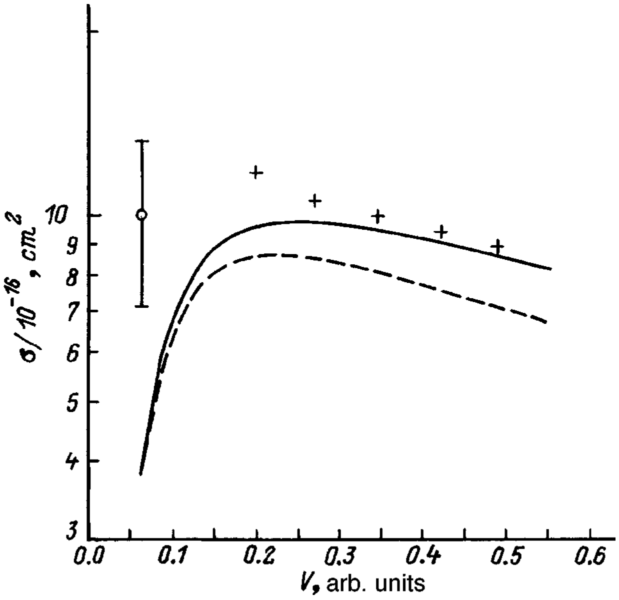

FIG. 8. Total cross section for SEC to the state $Ne^{5+}(3)$ in a Ne^{6+}–He collision: ○ and + show the experimental data of Refs. 16 and 17, respectively (the absolute error is ~30%).

$\Sigma(3d\sigma 4f\sigma)$ at their crossing points (R_{13} and R_{24}) were calculated in the Landau–Zener–Chaplik approximation (10). The following values of the model parameters were obtained:

R_{13}: $R_c=4.34$, $\Delta=0.0056$,

$F=0.315$, $\kappa=0.023$;

R_{24}: $R_c=1.90$, $\Delta=0.0276$,

$F=0.580$, $\kappa=0.0202$.

The probability of a transition between the diabatic states $\Sigma(3d\sigma^2)$ and $\Pi(3d\sigma 3d\pi)$ at small internuclear distances on account of the rotational interaction was estimated according to formula (13), under the assumption that the energy difference between these states is described well enough by the energy difference between the $3d\sigma$ and $3d\pi$ molecular orbitals. The constant A was taken equal to 0.149.

The results of the calculation of the total cross section for SECT to the ionic state $Ne^{5+}(n=3)$ are shown in Fig. 8. The results are in good agreement with the experimental data of Ref. 17, which are also plotted in the figure.

The authors are grateful for support from the Russian Fund for Fundamental Research (Project No. 96-02-16915) and MAGATÉ (Contract No. 8553/RB).

APPENDIX A. DETERMINATION OF THE PARAMETERS $A_0^{(i)}$, $\tilde{a}_1^{(i)}$, $A_1^{(i)}$, $B_1^{(i)}$, AND $B_2^{(i)}$ OF THE EFFECTIVE POTENTIAL $V_{\mathrm{eff}}^{(i)}$ FOR HETERONUCLEAR QUASIMOLECULES

The effective potential (3) used here permits separation of variables in Eq. (2) in the spheroidal coordinate system $\lambda=(r_1+r_2)/R$, $\mu=(r_1-r_2)/R$, $\phi=\arctan y/x$ (the y axis is perpendicular to the plane of collision). The general form of the potential that satisfies this requirement is

$$V_{\mathrm{eff}}^{(i)}(\lambda,\mu,\phi)=\frac{1}{R(\lambda^2-\mu^2)}[f(\lambda)+g(\mu)].$$

Expanding the functions $f(\lambda)$ and $g(\mu)$ in a series in powers of λ and μ and keeping the first nonvanishing terms of the expansion, we find for a heteronuclear system ($Z_1\neq Z_2$) that

$$f(\lambda)=a_0^{(i)}+\tilde{a}_1^{(i)}/R+a_1^{(i)}\lambda \quad \text{and} \quad g(\mu)=b_1^{(i)}\mu,$$

$$b_2^{(i)}=0.$$

The parameters $a_1^{(1)}$ and $\tilde{a}_1^{(i)}$ depend only on the state of the electron in the united atom to which the orbital under consideration goes over in the limit $R\to 0$ (Ref. 5) and are given in terms of the energy ε_{ua}^i and splitting of the sublevels in the shell with the given n:

$$\tilde{a}_1^{(i)}=\min\left(-\frac{c_1(1-x)-2c^2x}{(1-x)^2}\pm\sqrt{\frac{c_1(1-x)-2c^2x}{(1-x)^4}-\frac{c_1^2-c^2(2l+1)^2}{(1-x)^2}}\right), \tag{16}$$

$$a_1^{(i)}=Z_1+Z_2-\sqrt{2|\varepsilon_{ua}^i|}\left(n-\frac{2l+1}{2}+\sqrt{\frac{(2l+1)^2}{4}+\tilde{a}_1^{(i)}}\right), \tag{17}$$

where

$$x=\varepsilon_{ua}^i/\varepsilon_{ua}^j, \quad i=(n,l,m), \quad j=(n,l-1,m),$$

$$c=(\sqrt{x}-1)+\frac{2l-1}{2}+\frac{2l+1}{2}\sqrt{x},$$

$$c_1=\frac{(2l-1)^2}{4}+\frac{(2l+1)^2}{4}x-c^2. \tag{18}$$

The parameters $a_0^{(i)}$ and $b_1^{(i)}$ are given in terms of the energy of the molecular orbital in the limit $R\to\infty$ (the limit of separated atoms). Here the scheme for determining the parameters is the same for orbitals of the eZ_1 and eZ_2 types (in which the electron is found near the Z_1 or Z_2 nucleus, respectively, in the limit of separated atoms). The expressions obtained for the coefficients in this case differ only in the overall sign in the expression for the coefficient b_1.

Let us consider the determination of the parameters for an orbital of the eZ_1 type, for which we set $i=1$. The energy of a molecular orbital of this type for $R\to\infty$ is expressed as follows in terms of the parameters of the effective potential:

$$\varepsilon_1(R)=-\frac{\tilde{Z}_1^2}{2n_{s1}^2}-\frac{1}{R}\left(\tilde{Z}_2-\frac{\tilde{a}_1^{(1)}}{2n_{s1}^2}+\frac{\Delta_1}{2n_{s1}}a_0^{(1)}\right)+O\left(\frac{1}{R^2}\right), \tag{19}$$

where $\tilde{Z}_1=Z_1-(a_0^{(1)}+a_1^{(1)}-b_1^{(1)})/2$; $\tilde{Z}_2=Z_2-(a_1^{(1)}+b_1^{(1)})/2$; $\Delta_1=n_1^{(1)}-n_2^{(1)}$, $n_{s1}=n_1^{(1)}+n_2^{(1)}+m+1$; n_{s1},

$n_1^{(1)}$, and $n_2^{(1)}$ are the principal and parabolic quantum numbers of the electron state to which the MO in question goes over in the limit of separated atoms.

From the requirement that expression (19) tend asymptotically to the energy of the atomic state to which the given STAMO goes over as $R\to\infty$, i.e., that

$$\varepsilon_1(R)\to\varepsilon_{sa}^{(1)}-\frac{Z_2-N_2}{R}\equiv-\frac{Z_{s1}^2}{2n_{s1}^2}-\frac{Z_2-N_2}{R},\quad R\to\infty,$$

where N_2 is the number of electrons around nucleus Z_2 in the limit of separated atoms and Z_{s1} is the effective charge, which is related to the electron energy $\varepsilon_{sa}^{(1)}$ by the relation $Z_{s1}=n_{s1}\sqrt{2|\varepsilon_{sa}^{(1)}|}$, we obtain the following two equations for determining the parameters of the effective potential:

$$Z_1-\frac{a_0^{(1)}+a_1^{(1)}-b_1^{(1)}}{2}=Z_{s1}, \tag{20}$$

$$Z_2-N_2=Z_2-\frac{a_1^{(1)}+b_1^{(1)}}{2}-\frac{\tilde{a}_1^{(1)}}{2n_{s1}^2}Z_{s1}+\frac{\Delta_1}{2n_{s1}}a_0^{(1)}. \tag{21}$$

From Eqs. (20) and (21) we find that

$$b_1^{(1)}=a_0^{(1)}+a_1^{(1)}-2(Z_1-Z_{s1}), \tag{22}$$

$$a_0^{(1)}=\frac{2((Z_1-Z_{s1})-a_1^{(1)}-\tilde{a}_1^{(1)}Z_{s1}/2n_{s1}^2+N_2)}{1-\Delta_1/n_{s1}}. \tag{23}$$

APPENDIX B. CHOICE OF THE ENTRANCE-CHANNEL FUNCTION THAT AS $R\to\infty$ DESCRIBES THE STATE OF A 1*s* ELECTRON IN THE He ATOM IN THE SYSTEM Ne^{10+}–He

In the spheroidal coordinate system $\lambda=(r_1+r_2)/R$, $\mu=(r_1-r_2)/R$, ϕ, the wave function ψ_i satisfying Eq. (2) has the form

$$\psi_i(r_1,r_2;R)=N_{kqm}(R)\Pi_{mk}(\lambda,R)\Sigma_{mq}(\mu,R)\frac{\exp\pm im\phi}{\sqrt{2\pi}}, \tag{24}$$

where the spheroidal quantum numbers k, q, and m are equal to the number of zeros of the radial (Π_{mk}), angular (Σ_{mq}), and azimuthal parts of the wave function ψ_i.

For the problem of two Coulomb centers, from the condition that the number of zeros of the functions Π_{mk} and Σ_{mq} does not change as the internuclear distance varies we obtain relations^5 linking the terms of the separated atoms ($R=\infty$) and the terms of the united atom ($R=0$).

As $R\to0$ the equation for Π_{km} goes over to the equation for the radial part of the wave function of a hydrogenlike atom with the charge Z_1+Z_2, and the equation for Σ_{qm} goes over to the equation for associated Legendre polynomials, from which one immediately gets a relation between the spherical and spheroidal quantum numbers:

$$k=n-l-1\quad\text{and}\quad q=l-|m|. \tag{25}$$

For $R\to\infty$ the spheroidal coordinates go over to parabolic coordinates, and the functions Π_{mk} and Σ_{mq} go over to the solutions of the one-center problem in a parabolic coordinate system. In particular, for the eZ_1 term of interest to us ($Z_1\leqslant Z_2$)

$$\psi_i(r;R)\to\frac{\sqrt{2Z_1^3}}{n_{s1}^2}f_{n_1^{(1)}m}(\xi)\times f_{n_2^{(1)}m}(\tau)\frac{\exp\pm im\phi}{\sqrt{2\pi}},\quad R\to\infty, \tag{26}$$

where for $R\to\infty$ one has $\xi=R(\lambda-1)$ and $\tau=R(\mu+1)$; $n_1^{(1)}$ and $n_2^{(1)}$ are the parabolic quantum numbers, which are related to the principal quantum number n_{s1} of the state of the electron in an isolated atom by the relation $n_{s1}^{(1)}=n_1^{(1)}+n_2^{(1)}+m+1$ and are equal to the number of zeros of the radial $f_{n_1^{(1)}m}(\xi)$ and angular $f_{n_2^{(1)}}(\tau)$ parts of the atomic function.

From the condition that the number of zeros of the radial and angular parts of the wave function of the two-center problem does not change, one obtains^5 a relation between the spheroidal quantum numbers and the parabolic quantum numbers of the state of an isolated atom:

$$k=n_1^{(1)},$$

$$q=\begin{cases}2n_2^{(1)}+1+\mathrm{Int}(n_{s1}(Z_2-Z_1)/Z_1),\\ \quad\text{if }\ n_{s1}Z_2/Z_1\text{is not an integer},\\ 2n_2^{(1)}+(n_{s1}(Z_2-Z_1)/Z_1),\\ \quad\text{if }\ n_{s1}Z_2/Z_1\text{is an integer}.\end{cases} \tag{27}$$

For $Z_1=2$ and $Z_2=10$, Eqs. (25) and (27) give $l=4$ and $n=5$ for the entrance-channel function (the $2s$ function of the He$^+$ ion), i.e., we find that the $5g\sigma$ OETAMO in the limit of large R describes a state of the electron around the He$^+$ ion. If screening of the nuclear charge Z_1 is introduced by setting $Z_1=1.6875$, as is done in a number of studies in order to get the correction asymptotic value of the energy of the entrance channel at large R, then, as follows from relations (25) and (27), one must use the $6h\sigma$ OETAMO as the entrance-channel function.

[1] R. K. Janev and H. Winter, Phys. Rep. **117**, 265 (1985).

[2] J. P. Hansen and K. Taulbjerg, Phys. Rev. A **45**, R4214 (1992).

[3] I. V. Komarov, L. I. Ponomarev, and Yu. S. Slavyanov, *Spheroidal and Coulomb Spheroidal Functions* [in Russian], Nauka, Moscow (1976), 319 pp.

[4] V. K. Nikulin and N. A. Guschina, J. Phys. B **11**, 3553 (1978).

[5] S. S. Gernshteĭn and V. D. Krivchenkov, Zh. Éksp. Teor. Fiz. **40**, 1491 (1961) [JETP **13**, 1044 (1961)].

[6] I. M. Band and M. B. Trzhaskovskaya, LIYaF AN SSSR Preprint No. 90 [in Russian], Leningrad Institute of Nuclear Physics, Academy of Sciences of the USSR, Gatchina (1974), 54 pp.

[7] V. K. Nikulin and A. V. Samoylov, Phys. Lett. A **89**, 225 (1982).

[8] A. V. Chaplik, Zh. Éksp. Teor. Fiz. **43**, 462 (1962) [Sov. Phys. JETP **16**, 331 (1962)].

[9] O. Halkjaer and J. Linderberg, Int. J. Quantum Chem. **13**, 475 (1979).
[10] E. E. Nikitin and S. Ya. Umanskiĭ, *Nonadiabatic Transitions in Slow Atomic Collisions* [in Russian], Atomizdat, Moscow (1978), 272 pp.
[11] Yu. N. Demkov, C. V. Kunasz, and V. N. Ostrovskii, Phys. Rev. A **18**, 2097 (1978).
[12] V. V. Afrosimov, A. A. Basalaev, E. D. Donets *et al.*, *XII ICPEAC. Abstracts of Contributed Papers* (1981), Vol. 2, p. 690.
[13] S. Bliman, M. Bonnefoy, J. J. Bonnet *et al.*, Phys. Scr. **T3**, 63 (1983).
[14] F. Fremont, H. Merabet, J. Y. Chesnel *et al.*, Phys. Rev. A **50**, 3117 (1994).
[15] J. P. Hansen and L. R. Andersson, J. Phys. B **22**, L285 (1989).
[16] L. R. Andersson, J. O. P. Pedersen, A. Barany *et al.*, J. Phys. B **22**, 1603 (1989).
[17] Yu. S. Gordeev, D. Dijkkamp, A. G. Drentje *et al.*, Phys. Rev. Lett. **50**, 1842 (1983).

Translated by Steve Torstveit

Collinear interaction of bichromatic radiation with one acoustic wave in biaxial crystals

V. M. Kotov

Institute of Radio Engineering and Electronics, Russian Academy of Sciences, 141120 Fryazino, Moscow Region, Russia

(Submitted December 8, 1997)
Zh. Tekh. Fiz. **69**, 131–132 (January 1999)

The regime of collinear interaction of bichromatic optical radiation in biaxial crystals is considered. It is shown that the possibility of the realization of such an interaction is due to dispersion of the optical axes in a biaxial crystal. *© 1999 American Institute of Physics.* [S1063-7842(99)02401-0]

The collinear interaction of light and sound is widely used in tunable filters and very promising acoustooptical (AO) devices by reason of the high selectivity of this form of diffraction.[1] The present paper considers collinear interaction in biaxial crystals, where two optical beams with different wavelengths interact simultaneously with one acoustic wave. Such diffraction can be realized thanks to dispersion of the optical axes of a biaxial crystal.

Figure 1a depicts a cross section of the wave-vector surface of a biaxial crystal by the xz plane, which contains the optical axes. Bichromatic radiation with wave vectors $\mathbf{k}_1$ and $\mathbf{k}_2$ propagates at the angle β to the z axis. Here $\mathbf{N}_1$ and $\mathbf{N}_2$ are the directions of the optical axes for radiation with wavelengths λ_1 and λ_2, respectively. The beam directions $\mathbf{k}_1$ and $\mathbf{k}_2$ lie between $\mathbf{N}_1$ and $\mathbf{N}_2$. For some value of the angle β the relation

$$\mathbf{k}_1' - \mathbf{k}_1 = \mathbf{k}_2 - \mathbf{k}_2' = \mathbf{q}, \tag{1}$$

is satisfied, where $\mathbf{k}_1'$ and $\mathbf{k}_2'$ are the diffracted beams and $\mathbf{q}$ is the wave vector of the acoustic wave.

This is also the condition of collinear diffraction of bichromatic radiation on one acoustic wave. As will become clear from what follows, if dispersion of the optical axes is absent, such diffraction is impossible.

In the plane containing the optical axes, the cross sections of the wave-vector surfaces of monochromatic radiation are described by the relations[1]

$$k_x^2 + k_z^2 = k_m^2, \qquad \frac{k_x^2}{k_g^2} + \frac{k_z^2}{k_p^2} = 1, \tag{2}$$

where k_x and k_z are the projections of the light wave vector on the x and z axes, respectively; $k_m = 2\pi N_m/\lambda$; $k_g = 2\pi N_g/\lambda$; $k_p = 2\pi N_p/\lambda$ (N_g, N_m, and N_p are the largest, intermediate, and smallest indices of refraction of the crystal).

Let the indices of refraction for radiation with wavelength λ_1 be equal to N_g, N_m, and N_p, and for radiation with wavelength λ_2—n_g, n_m, and n_p. Then, taking relations (2) into account, it is not hard to transform Eq. (1) into the form

$$\frac{2\pi}{\lambda_1}\left(N_m - \frac{N_g N_p}{\sqrt{N_p^2 \sin^2\beta + N_g^2 \cos^2\beta}}\right) = \frac{2\pi}{\lambda_2}\left(n_m - \frac{n_g n_p}{\sqrt{n_p^2 \sin^2\beta + n_g^2 \cos^2\beta}}\right). \tag{3}$$

Expression (3) can be reduced to a fourth-order equation in $\sin^2\beta$

$$P_4 \sin^8\beta + P_3 \sin^6\beta + P_2 \sin^4\beta + P_1 \sin^2\beta + P_0 = 0, \tag{4}$$

where $P_4 = c_1^2 c_2^2 A_1^4$,

$$P_3 = 2c_1 c_2 A_1^2 [B_1^2 c_2 + B_2^2 c_1 - A_1^2 (c_1 + c_2)],$$

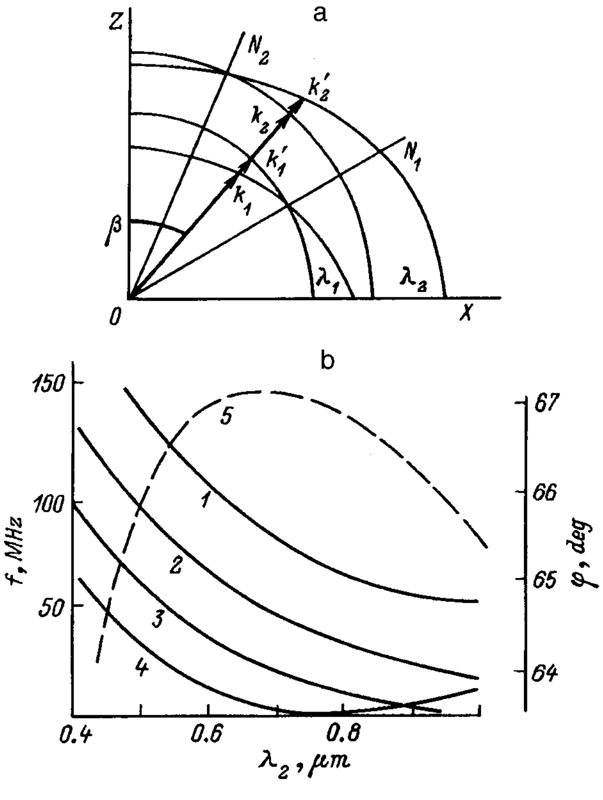

FIG. 1. Collinear diffraction of bichromatic optical radiation in biaxial crystals.

$$P_2=[B_1^2c_2+B_2^2c_1-A_1^2(c_1+c_2)]^2$$
$$+2c_1c_2A_1^2(A_1^2-B_1^2-B_2^2)-4B_1^2B_2^2c_1c_2,$$
$$P_1=2[B_1^2c_2+B_2^2c_1-A_1^2(c_1+c_2)](A_1^2-B_1^2-B_2^2)$$
$$+4B_1^2B_2^2(c_1+c_2),$$
$$P_0=(A_1^2-B_1^2-B_2^2)^2-4B_1^2B_2^2. \tag{5}$$

Here

$$A_1=\lambda_2\lambda_1^{-1}N_m+n_m,\quad B_1=n_p,\quad B_2=\lambda_2\lambda_1^{-1}N_p,$$
$$c_1=1-(n_p/n_g)^2,\quad c_2=1-(N_p/N_g)^2. \tag{6}$$

Assigning the values of λ_1 and λ_2, we determine the angle β from Eqs. (5), and the wave vector q from Eq. (1).

Figure 1b plots the dependence of the sound frequency of collinear acoustooptical diffraction of bichromatic radiation on the light wavelength λ. The calculations are for the biaxial crystal α-HIO$_3$, whose indices of refraction were taken from Ref. 2. For simplicity we assume that the light wave diffracts on a transverse acoustic wave whose velocity $v=1.85\times10^5$ cm/s does not change with variation of the angle β. The dependences were constructed in the following way: the wavelength of the ''reference'' radiation λ_1 was assigned, and the wavelength of the radiation with wavelength λ_2 varied within the range 0.4–1.0 μm; λ_2 is plotted along the abscissa. Curves *1–4* correspond to λ_1 equal to 0.4, 0.5, 0.63, and 0.8 μm. Curve *5* reflects the dispersion of the optical axes of a single crystal of α-HIO$_3$—the dependence of the angle φ (the right vertical axis) between the large principal axis and the optical axis of the crystal on the wavelength λ. The angle φ was calculated as indicated in Ref. 1 on the basis of the data in Ref. 2. It can be seen that in the wavelength interval $0.4\leqslant\lambda\leqslant0.63$ μm the angle φ varies quite dramatically, which provides good conditions for the realization of collinear diffraction of bichromatic radiation (curves *1–3* correspond to high values of the sound frequency f).

In the wavelength interval $0.63\leqslant\lambda\leqslant0.8$ μm the angle φ varies only weakly, which degrades the characteristics of the AO interaction (curve *4* describes low values of the frequency in the indicated range). In other words, the conditions of collinear AO interaction of bichromatic radiation with one acoustic wave will be best in biaxial crystals with strong dispersion of the optical axes.

Regarding the curves in Fig. 1b, it is necessary to add the following: Eq. (3) for $\lambda_1=\lambda_2$ is satisfied for any angle β, which leads to an indeterminacy in the sound frequency at which diffraction takes place. However, in Fig. 1b, such an indeterminacy at the corresponding points is absent (e.g., curve *2*, describing collinear diffraction of radiation with the ''reference'' wavelength $\lambda_1=0.5$ μm, for λ_2 also equal to 0.5 μm, assigns the sound frequency the single value $f=90$ MHz). Elimination of the multivaluedness of the frequency is due to the fact that every such point is an approximation of neighboring points at which there is no indeterminacy.

On the basis of the foregoing we may draw the following conclusions: in biaxial crystals it is possible to realize collinear AO interaction of bichromatic radiation with one acoustic wave over a wide range of wavelengths of the optical radiation. This possibility is due, first of all, to dispersion of the optical axes, which is present in the overwhelming majority of biaxial crystals.

This work was completed with the support of the Russian Fund for Fundamental Research (Grant No. 96-02-16136-a).

[1] V. I. Balakshiĭ, V. N. Parygin, and L. E. Chirkov, *Physical Foundations of Acoustooptics* [in Russian], Radio i Svyaz', Moscow, 1985, 280 pp.

[2] *Acoustic Crystals* [in Russian], edited by M. P. Shaskol'skaya (Nauka, Moscow, 1982), 632 pp.

Translated by Paul F. Schippnick

Influence of physical and chemical surface treatment on the photoluminescence of porous silicon

I. E. Maronchuk, M. N. Naĭdenkov, M. V. Naĭdenkova, A. V. Sarikov, and T. L. Voloshina

Kherson State Technical University, 325008 Kherson, Ukraine

(Submitted February 9, 1998)
Zh. Tekh. Fiz. **69**, 133–134 (January 1999)

It is shown that surface treatment of porous silicon in inorganic acids and solutions of metal chlorides leads to an increase in the intensity of photoluminescence of this material. In the case of chlorides, a short-wavelength shift of the photoluminescence maximum is also observed. The effect of a brief high-temperature anneal in vacuum on the photoluminescence of porous silicon is investigated. Such treatment is observed to cause partial degradation. © *1999 American Institute of Physics.* [S1063-7842(99)02501-5]

Luminescent porous silicon (PS) has attracted the interest of many researchers in connection with its potential use as cheap material in various devices of present-day opto- and microelectronics. The appearance of visible luminescence in porous silicon is explained on the basis of various models. The model that has found the widest application is based on size quantization, which attributes the luminescence to transitions in zero- and one-dimensional nanocrystallites, and its degradation, to processes taking place on the surface of these nanocrystallites.[1]

The aim of the present paper is to investigate the influence of chemical surface treatment in solutions of metal salts and in acids and high-temperature annealing on the total intensity and spectrum of its photoluminescence (PL).

Porous-silicon layers were prepared by electrochemical etching of boron-doped *p*-type silicon wafers with resistivity 5.5 $\Omega \cdot$cm and orientation (100) in an electrolyte with the composition $H_2O:HF:C_2H_5OH = 1:1:2$ with an average current density of 5 mA/cm^2 for 30 min. The prepared structures were rinsed in deionized water and cleaved into samples so that the chemical treatments in all the solutions used could be performed on one structure. This made it possible to exclude differences in the photoluminescence due to the technique of preparation of the porous silicon, and permitted studying the effect on it of the treatment alone.

Chemical treatment of as-prepared (unannealed) layers of porous silicon was performed in solutions of the metal chlorides CsCl, NaCl, $ZnCl_2$, $BaCl_2$ and the concentrated acids HCl, H_2SO_4, HNO_3, and H_3PO_4 at room temperature and their boiling temperatures.

High-temperature anneals of the as-prepared samples were carried out in a vacuum of 6×10^{-6} Torr at a temperature of 1000 °C for $15-40$ s. Before carrying out the anneals, the samples were stored in a working vacuum at 200 °C for $5-10$ min to remove from the surface nanocrystals of elements and compounds adsorbed during growth of the porous layer.

Photoluminescence spectra of as-prepared samples and samples that had been subjected to chemical treatment were recorded at room temperature with the help of an MDR-2 monochromator. Photoluminescence was excited by a gas-discharge argon laser ($\lambda = 514.5$ nm) with excitation power $0.1-1$ W/cm^2. The photoluminescence intensities of the treated porous-silicon layers were normalized to the intensities of the control samples, which were not subjected to treatment. For the annealed samples we performed only a qualitative estimate of changes in the photoluminescence spectrum and total intensity.

Treatment of porous-silicon surfaces in aqueous solutions of $BaCl_2$, CsCl, $ZnCl_2$, and NaCl led to growth of the photoluminescence intensity and a shift of the peak toward the blue end of the spectrum (curves *1–4* in Fig. 1 in comparison with curve *5* for the untreated samples). The photoluminescence intensity increased with increase of the concentration of the solution and the peak shift grew with growth of the percent ionic character of the chemical bond in the metal chloride.

For nanocrystallites of porous silicon the relation $B/S \ll l_D$ is characteristic, where B is the volume, S is the surface area of the crystallite, and l_D is the screening length. Under this condition, the adsorptivity of ionized molecules of acceptor and donor type decreases dramatically and adsorption of the polar molecules forming the coordination cage of the bond is more important. Adsorption of polar molecules leads to an abrupt decrease of the surface recombination rate.[2] This also explains the increase in the photoluminescence intensity after treatments in solutions of metal chlorides. The short-wavelength shifts of the photoluminescence peaks are obviously also associated with the dipole moments of the adsorbed molecules since the short-wavelength shift increased with increase of the latter (Fig. 1).

The photoluminescence spectra of the samples treated in acids at 300 K for 15 min are shown in Fig. 2. The photoluminescence peaks of the samples treated in HCl (curve *1*) were shifted toward large energies in comparison with the peaks for the untreated samples (curve *5*) and for the samples treated in H_2SO_4 (curve *2*), HNO_3 (curve *3*), and H_3PO_4 (curve *4*). Studies of the dependence of the photoluminescence intensity on the storage time in the various acids indicate that treatment in HNO_3 for $1-5$ min gives a fivefold

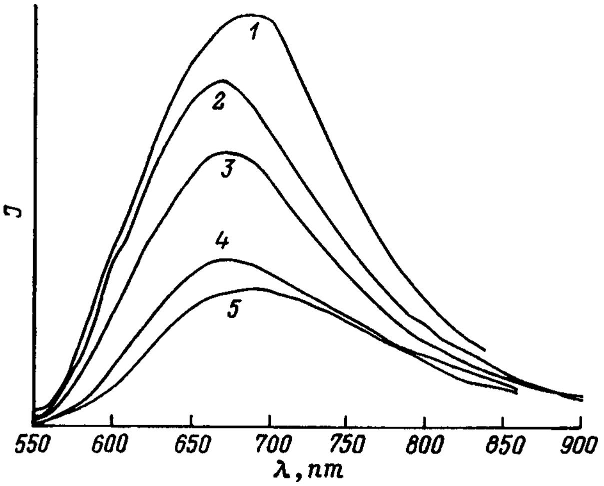

FIG. 1.

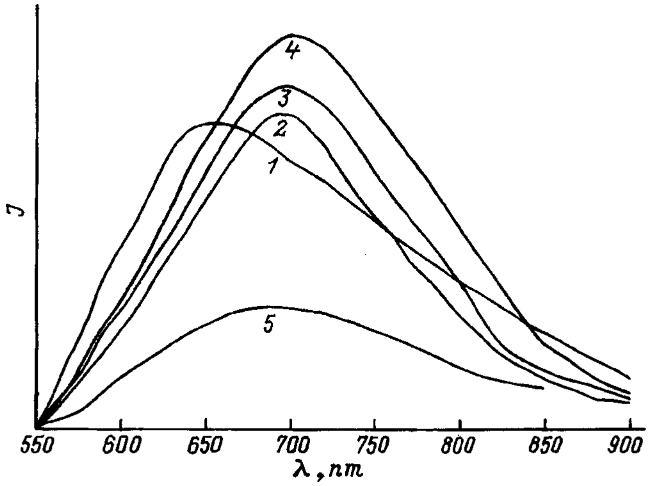

FIG. 2.

increase. Further treatment in HNO_3 decreases the photoluminescence intensity of porous silicon. For the other acids this dependence is less pronounced.

Treatment of the porous-silicon samples in acids at their boiling points for 1–3 min led to a growth of the photoluminescence intensity and a decrease in its degradation. The increase in the photoluminescence intensity after surface treatment of porous silicon in acids is obviously due to a decrease in nonradiative surface recombination. It is well known that a silicon surface, prepared by chemical etching, is coated with a hydrated oxide film. Coordination-bonded water molecules on a completely hydrated oxide film surface block the coordination-unsaturated centers and lower the recombination rate on the surface through fast states.[3] A substantial drawback of such a surface is its degradation, associated with nonuniformity of the hydrated oxide coating and mechanical strains due to the different lattice constants of silicon and the oxide film. Treatment of a porous-silicon surface in H_2SO_4, HNO_3, or H_3PO_4 reduces the nonuniformities and strains in the oxide film by replacing the coordination-bonded water molecules by complexes containing sulfur, nitrogen, and phosphorus. This leads to a decrease in the density of surface states and an enhancement of the resistance to degradation of the photoluminescence of porous silicon. The difference in the photoluminescence intensities of samples treated in different acids is probably due to the different adsorptivities of these complexes. The photoluminescence intensity of the annealed samples was lowered by a factor of two. The position of the emission maximum in this case did not change.

[1] Y. Kanemitsu, Phys. Rep. **263**, 1 (1995).
[2] A. V. Rzhanov, *Electronic Processes on Semiconductor Surfaces* [in Russian], Nauka, Moscow, 1971.
[3] V. F. Kiselev, *Surface Phenomena in Semiconductors and Insulators* [in Russian], Nauka, Moscow, 1970.

Translated by Paul F. Schippnick

Luminescence properties of calcium-iodide crystals

S. S. Novosad

I. Franko L'vov State University, 290602 L'vov, Ukraine

(Submitted February 9, 1998)
Zh. Tekh. Fiz. **69**, 135–136 (January 1999)

The effect of the conditions of preparation, temperature, and the action of x rays on the luminescence properties of calcium-iodide scintillation crystals is investigated. On the basis of the results of a study of the spectral characteristics of CaI_2 and $CaI_2:H_2$ crystals for optical and x-ray excitation in the temperature range 90–400 K, also taking into account the results of a study of the luminescence properties of CaI_2 crystals activated by Cl^-, Br^-, OH^-, and Ca^{2+} impurities, it is suggested that the 236-nm band observed in the excitation spectra of crystals of calcium iodide may be caused by an uncontrollable hydrogen impurity. The luminescence of these crystals with maximum at 395 nm is ascribed to radiative recombination of excitons trapped at H^- ions. [S1063-7842(99)02601-X]

Among inorganic spectrometric scintillators, CaI_2 and CaI_2:Eu crystals are characterized by the highest light yield and the best energy resolution.[1–3] The luminescence properties of calcium-iodide based scintillators have been studied only sparsely due to the high degree of deliquescence of the compound and the difficulty of preparing pure and perfect crystals.[1,2] The present Communication reports results of a study of the influence of the conditions of preparation, temperature, and the action of x rays on the luminescence properties of calcium-iodide scintillation crystals.

In the photoluminescence excitation spectra of calcium-iodide crystals grown by the Stockbarger method in evacuated quartz ampoules from the salt, purified by the ion-exchange method,[3] a band at 236 nm has been detected in the long-wavelength falloff of the exciton absorption at 295 K. The 236-nm excitation band is sensitive to the conditions of preparation of the crystals. Its intensity is weakened by activation of the crystals with the oxygen-containing impurity $Ca(OH)_2$ (Ref. 3) and the halide from the gas phase, and by high-dose x-irradiation, annealing, and aging.[4] The intensity of this band grows if the ampoule is continuously pumped down during growth, and is also increased by quenching and by increasing the purity of the crystallites.

Excitation and photoluminescence spectra of $CaI_2:H_2$ crystals, grown from a charge that had been heat-treated to the melting temperature of the compound in a hydrogen atmosphere before growth, are shown in Fig. 1. It follows from Fig. 1a that the excitation spectrum of this crystal at 295 K also exhibits a band at 236 nm (curve *1*). As the temperature is lowered to 90 K, the intensity of this band weakens (curve *2*). Quenching of the 236-nm excitation band when the crystal is heated to 400 K is accompanied by the appearance of a new band with a maximum at 244 nm (curve *3*).

The photoluminescence spectrum of $CaI_2:H_2$ at 295 K coincides with the photoluminescence spectrum of CaI_2 and contains a wide, non-elementary band with its maximum at 410 nm (Fig. 1b, curve *1*). At 90 K the photoluminescence spectrum of CaI_2 with a hydrogen impurity is characterized by a 390-nm band (Fig. 1b, curve *2*). The maximum of this band is located at a 10–15 nm shorter wavelength than the maximum of the photoluminescence band of intentionally unactivated CaI_2. A band at 430 nm is observed in the photoluminescence spectrum of $CaI_2:H_2$ at 400 K (Fig. 1b, curve *3*).

The largest x-ray luminescence yield of an unactivated CaI_2 crystal grown by the Stockbarger method was observed in the temperature interval 180–280 K. In this temperature region the x-ray luminescence spectra of CaI_2 are similar to the photoluminescence spectra and are distinguished by a 410–415 nm band. Weakening of the x-ray luminescence intensity when the crystal is heated to 400 K or cooled down to 90 K compared with the indicated temperature interval (Fig. 2a, curve *1*) is accompanied by a shift of the maximum of the luminescence band to 430 and 445 nm, respectively

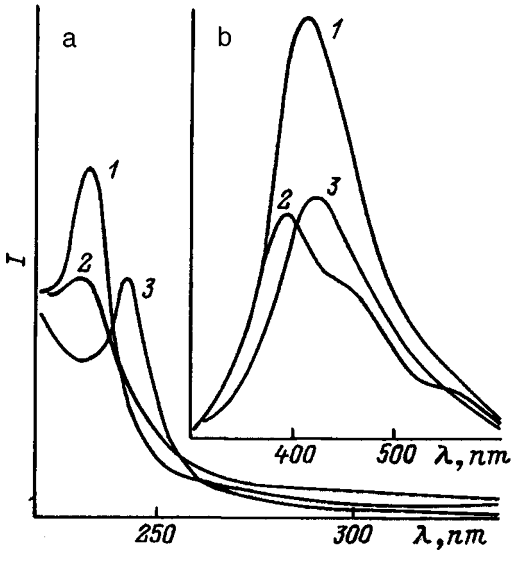

FIG. 1. Excitation spectra (a) and photoluminescence spectra (b) of a $CaI_2:H_2$ crystal at temperatures 295 (*1*), 90 (*2*) and 400 K (*3*).

(Fig. 2a, curve *2*). The temperature dependence of the intensity and spectral composition of x-ray luminescence of $CaI_2:H_2$ is closely analogous to the characteristics of unactivated CaI_2.

We have established that the x-ray luminescence spectra of CaI_2 crystals grown by the Kiropoulos method and zone melting are similar to the x-ray luminescence spectra of CaI_2 crystals grown by the Stockbarger method.

Weakening of the intensity of the 236-nm excitation band during irradiation of potassium iodide by x rays at 295 nm does not lead to the appearance of radiation-induced absorption in the spectral range 250−650 nm. Here a weak storage by the crystal of its light sum is observed, which is realized in thermally stimulated luminescence peak (TSL) at 365 K upon heating of the crystal (Fig. 2b, curve *1*). Thermal or optical ($\lambda > 650$ nm) liberation of the light sum stored in CaI_2 leads to restoration of the excitation band at 236 nm.

At 90 K during x-ray calcium-iodide crystals store a light sum that is roughly two orders of magnitude greater than the light sum at 295 K. On the TSL curve of Stockbarger-grown CaI_2 crystal, in addition to the intense non-elementary peak with maximum at 138 K two additional weak peaks are detected at 100 and 120 K (Fig. 2b, curve *2*). Activation of a calcium-iodide crystal from solution by the oxygen-containing impurity $Ca(OH)_2$ leads to a redistribution of the intensity in favor of the peak at 100 K. It follows from these data that the capture levels of CaI_2 crystals corresponding to the TSL peaks in the temperature interval 90−150 K can be caused by defects associated with an uncontrollable oxygen and hydrogen impurity as well as thermal defects.

Note that CaI_2 crystals at 90 K store a light sum that is roughly an order of magnitude less than that stored by NaI : Tl, and at 295 K they are not outdone by this scintillator in radiation hardness. When recording gamma radiation from a ^{137}Cs source, the prepared unactivated CaI_2 crystals were characterized by an energy resolution of 4.5−6.0% and a 1.5−1.9 times greater light yield than NaI : Tl.

Analysis of the obtained data taking into account data on the spectral composition of thermally stimulated luminescence, phosphorescence, and photostimulated luminescence of CaI_2 and $CaI_2:H_2$ crystals and also data on the spectral characteristics of CaI_2:Ca, CaI_2:Cl, CaI_2:Br, and $CaI_2:Ca(OH)_2$ crystals showed that the non-elementary luminescence bands of calcium-iodide crystals in the spectral range 300−650 nm can be represented by components with maxima around 345, 395, 425, and 520 nm, where the main component of the luminescence with maximum at 395 nm is very sensitive to the action of ionizing radiation and heat.

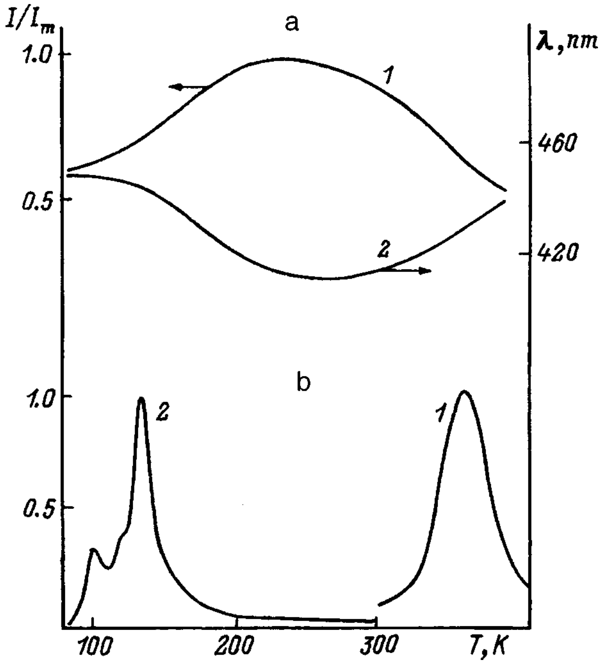

FIG. 2. a — temperature dependence of the intensity (*1*) and position of the maximum of the x-ray luminescence band (*2*) of a CaI_2 crystal; b — TSL curves of this crystal irradiated with x radiation at 295 (*1*) and 90 K (*2*).

The 236-nm excitation band of calcium-iodide crystals is similar in its characteristics to the *u* band observed in the absorption spectra of alkali-halide crystals.[5] This points to the possibility of a connection with H^- ions, which are present in calcium-iodide crystals as an uncontrollable impurity. The luminescence peak of CaI_2 at 395 nm can be assigned to radiative recombination of excitons trapped at H^- ions.[4,5] An intrinsic luminescence of calcium iodide at 325 nm due to self-trapped excitons is observed for x-ray excitation of the crystals in the temperature interval 4.2 −60 K. At 90 K this emission in the x-ray luminescence spectra of these crystals is manifested in the form of barely noticeable steps in the spectral interval 310−340 nm.

[1] R. Hofstadter, E. W. O'Dell, and S. T. Schmidt, IEEE Trans. Nucl. Sci. **NS-11**(3), 12 (1964).

[2] L. V. Viktorov, V. M. Skorikov, V. M. Zhukov, and B. V. Shul'gin, Izv. Akad. Nauk SSSR, Neorg. Mater. **27**, 2005 (1991).

[3] S. S. Novosad, Vestn. L'vov. Univ. Ser. Fiz., No. 11, Éksp. Teor. Fiz., Vishcha Shkola, L'vov (1976), pp. 44–47.

[4] S. S. Novosad and N. K. Gloskovskaya, *Abstracts of the Fourth All-Union Conference on Radiation Physics and Chemistry of Ionic Crystals* [in Russian] (Salaspils, 1978), Pt. 1, p. 143.

[5] A. V. Egranov and E. A. Radzhabov, *Spectroscopy of Oxygen and Hydrogen Impurity Centers in Alkali-Halide Crystals* [in Russian], Nauka, Novosibirsk, 1992.

Translated by Paul F. Schippnick

TECHNICAL PHYSICS VOLUME 44, NUMBER 1 JANUARY 1999

On the breakup of gas bubbles in a liquid under the action of a finite-amplitude pressure wave

V. G. Kovalev

Institute of Pulsed Processes and Technologies, 327018 Nikolaev, Ukraine

(Submitted March 18, 1998)
Zh. Tekh. Fiz. **69**, 137–139 (January 1999)

A mechanism for breaking up gas bubbles in a liquid in a high-intensity pressure wave field is considered. Breakup criteria are obtained. An anomalous dependence of the breakup pressure on the initial bubble radius is found and explained. © *1999 American Institute of Physics.* [S1063-7842(99)02701-4]

In Ref. 1 in the quasi-acoustic approximation I obtained the equations of the dynamics of nonspherical oscillations of a gas bubble in a liquid. In the derivation of the indicated equation the boundary conditions were reduced to a mobile surface by taking a limit. Since the oscillations of the bubble are assumed to be axially symmetric, the velocity potential of the external hydrodynamic field, the radius vector and velocity of the surface of the bubble, the Laplace pressure, and other spatial characteristics of the process were represented in the form of expansions in Legendre polynomials. Next, restricting the development to the zeroth and second terms of the expansion,[2] I obtained the equations of the dynamics of nonspherical oscillations in the two-mode approximation, which allowed me to consider the process of breakup of a bubble when acted upon by a high-intensity pressure wave.[3] As a reference case, I chose a wave with a step-function profile, for which the breakup pressure is minimal.

The aim of the present paper is to study the process of bubble breakup, which, taking account of the substantial nonlinearity of the equations obtained in Ref. 1, is best pursued by numerical experiment.

The initial state of the bubble is characterized by the initial radius vector of its surface, which in the two-mode approximation can be represented as

$$R(\theta,t)=R_s(t)+R_e(t)(3\xi^2-1),$$

where R_s and R_e are the amplitudes of the spherical and nonspherical components, respectively, and $3\xi^2-1$ is the Legendre polynomial of first order.

Thus, as the characteristics we can choose the initial value of the spherical component R_{s0}, which we will call the initial radius, and the ratio of the components $e_0=R_{e0}/R_{s0}$, which we will call the initial asphericity. We will call the current values of the indicated quantities the radius and asphericity of the bubble, respectively.

First we should determine the pressure of the reference wave at which breakup occurs. The results of calculations of the breakup pressure for representative values of the initial radius and initial asphericity are shown in Table I.

As a whole, there is nothing surprising about the nature of the dependence of the breakup pressure on the indicated characteristics: the smaller the initial asphericity of the bubble, the higher the breakup pressure. However, there are two nontrivial features: the abrupt growth of the breakup pressure and the change of sign in its dependence on the initial radius for $R_{e0}/R_{s0}<0.11$ necessitates a more detail study of the process.

Since the mechanical system under consideration possesses two degrees of freedom, its phase space is four-dimensional; however, of its six projections the most informative is the projection onto the V_s, V_e plane shown in Fig. 1. Here, if we take the initial radius of the bubble to be equal to 1 mm, the initial relative asphericity to be equal to 0.1, and the pressure in the incident wave to be equal to 535, 538, 540 MPa (curves *1–3*, respectively), then the last pressure value corresponds to breakup.

It is convenient to divide the phase trajectory into three segments corresponding to the three stages of the process. In the first segment, all three phase trajectories go almost straight down (coalescing as they go). Thus, this stage is characterized by a significant decrease of the zeroth mode of R_s, while V_e remains essentially equal to zero, i.e., the absolute value of the asphericity does not vary, but its relative value $e=R_e/R_s$ increases, but only because of the decrease of R_s.

In the second stage, in which some differences in the phase trajectories already begin to show up, they nevertheless go almost horizontally, which implies a dramatic decrease in R_e. The fact that the trajectories in this segment go horizontally indicates that this process occurs at the time of dynamic braking of collapse, when the acceleration of the zeroth mode vanishes, and the speed of collapse reaches its maximum value. Note that the velocities of the modes, V_s

TABLE I. Dependence of breakup pressure P_B (MPa) on the initial radius R_{s0} and relative initial asphericity R_{e0}/R_{s0}.

R_{s0}, mm	R_{e0}/R_{s0}									
	0.3	0.2	0.15	0.12	0.11	0.105	0.102	0.1	0.08	0.06
1	0.8	1.7	3.8	10.7	27	98.0	300	540	4900	37×10^3
0.1	0.85	1.9	3.9	10.9	27	96.0	295	530	4860	36×10^3
0.01	1.4	2.4	4.0	11.2	27	95.5	289	527	4710	34×10^3
0.001	2.5	4.5	5.1	12.0	27	85.0	268	490	4500	23×10^3

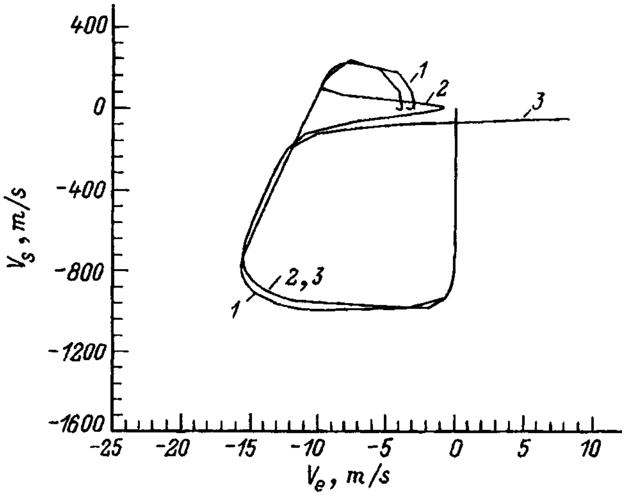

FIG. 1.

and V_e, differ by almost two orders of magnitude; therefore, despite some decrease in the absolute asphericity, the relative asphericity continues to grow.

In the third stage of the process, when the size of the bubble reaches its minimum, a large positive acceleration of the zeroth mode develops, accompanied by emission into the liquid of a short, positive, high-intensity pressure pulse. Simultaneously, a positive phase of pulsations of the second mode develops; however, since the outer pressure in this stage is summed together with the emission of a positive pulse, the acceleration of the second mode turns out to be much greater in absolute value than in the first stage. Therefore, the phase trajectory in this segment is sloped. Note that up to breakup $|V_s|>|V_e|$; thus, at this stage the relative asphericity continues to grow despite a decrease in the absolute nonsphericity R_e.

As can be seen from Fig. 2, for $e\sim 1$ an attraction zone arises, whose boundary for a given outer pressure is defined by the magnitude of the relative asphericity, in other words, by the magnitude of the second mode of the Laplace pressure $P_{\sigma e}$. Since the gas pressure in the bubble is assumed to be uniform over the volume and equal to the outer pressure while the surface-tension pressure in the neck zone of the bubble has negative sign, we can take equality of the indicated pressures as our criterion of the boundary of the attraction zone of the trajectories. We may express the second mode of the pressure in the form[1]

$$P_{\sigma e}=\frac{2\sigma e(17e-10)}{R_s(1-e)}.$$

The determination of the exact value of R_s when the phase trajectory approaches the instability zone is a complicated problem. However, it is possible to estimate it from the form of the phase trajectories in the R_s, V_s plane by assuming that at large pressures the minimum radius of the bubble is approximately one-third of its final steady-state adiabatic radius.[4,5] Then

$$R_s\approx\frac{R_{s0}}{3}\left(1+\frac{P_w}{P_0}\right)^{-\frac{1}{3\gamma}},$$

where P_w is the pressure in the incident wave.

Now, setting $P_{\sigma e}=P_w$, we obtain an estimate of the boundary of the attraction zone

$$e_R=1-\frac{42}{R_{s0}}\left(\frac{P_w}{P_0}\right)^{-\left(1+\frac{1}{3\gamma}\right)}.$$

For $P_w=540$ MPa and $R_{s0}=1$ mm calculation gives the value $e_R=0.997$, which is in good agreement with Fig. 2.

To estimate further, it is necessary to assume that at the instant of breakup $e\approx 1$. Thus, breakup starts up at $R_e\approx R_s$. Next, we take into account that, with the exception of cases of very large initial asphericity, i.e., small breakup pressures, $|V_s|\gg|V_e|$. Thus, at the instant of breakup $R_e\approx R_{e0}$ and $R_s\approx R_e=e_0R_{s0}$. Thus, at the instant of breakup

$$R_s=\frac{R_{s0}}{3}\left(1+\frac{P_w}{P_0}\right)^{-\frac{1}{3\gamma}}.$$

Hence we obtain an estimate for the breakup pressure

$$P_w\approx P_0+\frac{P_0}{(3e_0)^{3\gamma}}.$$

The above estimate explains both the comparatively weak dependence of the pressure on the initial radius and its dramatic growth with decrease of the initial asphericity. If we take into account the fact that R_e in reality decreases somewhat in the time leading up to the instant of breakup, then the dependence $P_w(e_0)$ becomes still more abrupt.

Let us consider, finally, the question of the influence of the initial bubble radius on the breakup pressure. The comparatively weak dependence of the breakup point on the initial radius indicates that the main factor in the given case is the ratio of the two components of the surface-tension pressure, where the indicated ratio plays the main role in the initial stage of the process, when both pressures are commensurate with the gas pressure in the bubble. The spherical

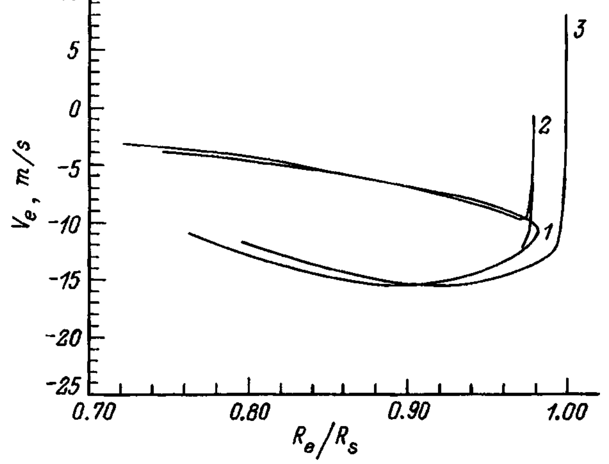

FIG. 2.

component $P_{\sigma s}$ has a stabilizing effect, i.e., it helps lower the asphericity. The role of $P_{\sigma e}$, as was shown above, is just the opposite.

Let us consider the question of the sign of the quantity $(\partial(P_{\sigma e}/P_{\sigma s}))/\partial R_s$. It is easy to see that this quantity has a minimum at $\zeta = R_e/(R_s - R_e) = 0.12$. Thus, as the initial radius is decreased, i.e., for $\delta R_s < 0$, the quantity $\partial(P_{\sigma e}/P_{\sigma s})/\partial R_s \delta R_s$ is negative for $\zeta > 0.12$ and positive for $\zeta < 0.12$. This implies that in the initial stage the destabilizing role of $P_{\sigma e}$ decreases as one goes to finer and finer bubbles if $\zeta > 0.12$, and increases if $\zeta < 0.12$. The equilibrium point $\zeta = 0.12$ describes the situation in which the breakup pressure is independent of the initial radius of the bubble. Since ζ and e are linked by the relation $e = \zeta/(1 + \zeta)$, we find that the initial asphericity $e_0 = 0.107$ corresponds to the equilibrium point, which is in good agreement with the data shown in Table I.

To summarize, the results obtained here allow one not only to estimate the breakup pressure of a bubble as a function of its initial radius and asphericity, but also to understand the mechanisms of the not completely trivial form of the indicated dependence.

[1] V. G. Kovalev, Pis'ma Zh. Tekh. Fiz. **22**, No. 24, 79 (1996) [Tech. Phys. Lett. **22**, 1034 (1996)].

[2] M. S. Plesset and T. P. Mitchell, Quart. Appl. Math. **13**, 419 (1956).

[3] R. I. Nigmatulin, *Dynamics of Multiphase Media* [in Russian], Nauka, Moscow, 1987, Pt. II.

[4] Study of the process of high-voltage electrical discharge in a two-phase medium. Account of NIR/IIPT National Academy of Sciences of the Ukraine, No. GR 01910008378 (Nikolaev, 1993).

[5] V. G. Kovalev, *Abstracts of the Seventh Scientific School ''Physics of Pulsed Discharges in Condensed Media''* [in Russian], Nikolaev, 1995, p. 122.

Translated by Paul F. Schippnick

The second law of thermodynamics and the limiting capabilities of heat engines

A. M. Tsirlin

Institute of Programming Systems, Russian Academy of Sciences, 152140 Pereslavl'-Zalesskiĭ, Russia

(Submitted April 15, 1998)
Zh. Tekh. Fiz. **69**, 140–142 (January 1999)

[S1063-7842(99)02801-9]

INTRODUCTION

The occasion for writing this Note is the appearance of a series of publications by G. V. Skornyakov,[1–3] in which he asserts that in thermodynamic systems employing the phenomenon of self-organization it is possible to achieve a negative production of entropy. Hence it immediately follows that it is possible to build a heat engine having an efficiency greater than the Carnot value. But this opens the door to the theoretical possibility of bringing the efficiency of a heat engine as close as one wants to unity. Thus, glittering possibilities are opened up in the realm of energetics. Skornyakov also proposes a design for a heat engine whose working medium, with the use of a vortical turbine, is stratified into liquid and vapor, which thereby delivers ''self-organization.'' This, he claimes, citing a theorem by Yu. L. Klimantovich,[4] implies the negative production of entropy.

It seems to me that the assertions of G. V. Skornyakov are in error, his reference to Yu. L. Klimantovich is unjustified, and the overturning of the second law of thermodynamics is as improbable as the overturning of the law of conservation of energy. The possibilities of a heat engine with fixed power are limited not only by the Carnot efficiency, but by a substantially smaller value. Below I will discuss in more detail on these statements and derive an estimate for the efficiency of a fixed-power machine.[5]

SELF-ORGANIZATION AND THE PRODUCTION OF ENTROPY IN A SYSTEM

Let us consider a thermodynamic system consisting of two reservoirs at temperatures T_+ and T_- and a working medium (Fig. 1). The working medium can have concentrated parameters (the temperature at any instant is the same over the given volume) or distributed parameters (the temperature varies across a heat flux). In the first case, the working medium is in successively in contact with the two reservoirs (a heat engine); in the second case, these contacts are continuous and spatially separated (a turbine). Following the lead of Refs. 1–3, we will consider the second case.

We write the equations of thermodynamic balance for the system of Fig. 1. These are the balance equations for energy, mass, and entropy. In the given case, mass exchange is absent; therefore only energy and entropy balance remain. The equations of energy balance and entropy balance of the system between the reservoirs take the form

$$q_+ - q_- - p = 0, \tag{1}$$

$$\sigma_+ - \sigma_- + \sigma_{\text{in}} = \frac{q_+}{T_+} - \frac{q_-}{T_-} + \sigma_{\text{in}} = 0. \tag{2}$$

Here q_+ and q_- are the heat flux from the hot reservoir and to the cold reservoir, respectively, and p is the power of the heat engine. Analogously, σ_+ and σ_- are the entropy fluxes, and σ_{in} is the production of entropy in the system.

Eliminating the heat flux q_- and taking as the efficiency the ratio of the power p to the heat delivered to the system, q_+, we write

$$\eta = \frac{p}{q_+} = \eta_K - T_- \frac{\sigma_{\text{in}}}{q_+}. \tag{3}$$

Here $\eta_K = 1 - (T_-/T_+)$ is the Carnot efficiency. For successive contact with the reservoirs with durations τ_1 and τ_2, the production of entropy consists of three terms: the production of entropy during heat transfer from each of the reservoirs

$$\sigma_1 = \int_0^{\tau_1} q_1(T_+, T_1(\tau)) \left(\frac{1}{T_1(\tau)} - \frac{1}{T_+} \right) d\tau, \tag{4}$$

$$\sigma_2 = \int_0^{\tau_2} q_2(T_2(\tau), T_-) \left(\frac{1}{T_-} - \frac{1}{T_2(\tau)} \right) d\tau \tag{5}$$

and the production of entropy σ_{pT} due to the creation of a flux of matter and energy in the working medium. For any law of heat transfer the integrands in Eqs. (4) and (5) are positive. In order for the quantity η to exceed η_k, the production of entropy in the working medium must be negative and greater in absolute value than $\sigma_1 + \sigma_2$. If the working medium has concentrated parameters, which may be assumed to be only approximately the case for the heat engine, then $\sigma_{pT} = 0$. In all the remaining cases $\sigma_{pT} > 0$, and no self-organization will make this quantity negative.

Skornyakov believes that σ_{pT} can be made negative and cites a theorem by Klimantovich,[4] but does not cite its for-

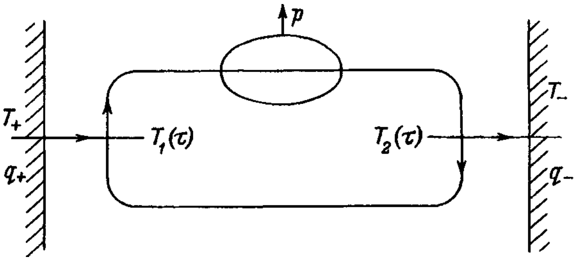

FIG. 1.

mulation. In all of this, Klimantovich only proposes a means for counting up the entropy in a nonuniform (''self-organized'') flux and asserts that it is less than it would be under the same conditions in a uniform flux. Let us dwell on this question in more detail.

The principle of a minimum production of entropy of I. Prigogine[6,7] asserts that in the stable regime of an open thermodynamic system the production of entropy σ in it is minimal. At first glance, this principle stands in contradiction with the fact that under certain conditions the stable regime of an open system is one in which nonuniformity with respect to the spatial and/or temporal coordinate is observed (self-organization).

In fact there is no contradiction if we replace σ by $\overline{\sigma}$, the production of entropy averaged over time and space, and take into account that the minimum of $\overline{\sigma}$ xmust be sought under certain constraints imposed on the system, which in the self-organization regime are also averaged. For example, consider the production of entropy during heat transfer through a layer of liquid. For some value of the average heat flux $\overline{q}$ the average production of entropy $\overline{\sigma}$ is minimal in the regime in which the liquid becomes nonuniform in every cross section. Thus, the condition for the appearance of self-organization reduces the the question, when is

$$\min_{x} \overline{\sigma(x)} \text{under conditions in which } \overline{f(x)}=f_0 \tag{6}$$

less than

$$\min_{x} \sigma(x) \text{under conditions in which } f(x)=f_0 . \tag{7}$$

Here x is the vector of variables on which both σ and these constraints depend; f is the vector-valued function of constraints (flux rate, heat load, etc.). This condition is expressed by the following statement[8]:

$$\overline{\sigma^0}=\max_{\lambda} \min_{x}[\sigma(x)+\lambda(f(x)-f_0)]<\sigma(x^0)=\sigma^0, \tag{8}$$

where x^0 is the optimal solution of the nonlinear programming problem (7).

Condition (8) is a necessary and sufficient condition. Its physical meaning is especially simple for the case in which f and x are scalars. Then it is possible to construct the dependence $\sigma(f)$. Condition (8) implies that for $f=f_0$ the convex envelope of this function passes below its graph.

An example: let us consider the process of heat transfer with a prescribed average intensity of the heat flux

$$\overline{q(T)}=\overline{[k(T-T_0)]^{0.5}}=q_0$$

and entropy production

$$\sigma(T)=q(T)\left(\frac{1}{T_0}-\frac{1}{T}\right)$$

for $T_0<T\leqslant T_m$. After eliminating T we obtain

$$\sigma(q)=\frac{q^3}{T(kT_0+q^2)} .$$

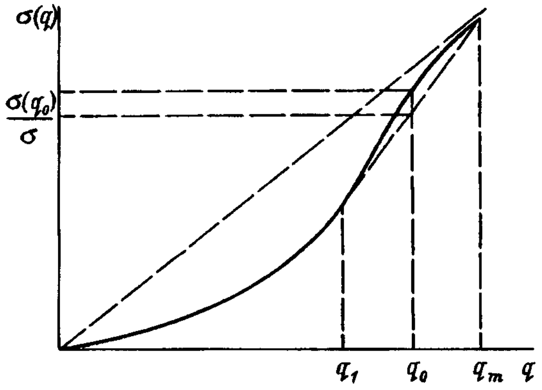

FIG. 2.

The function $\sigma(q)$ and its convex envelope over the set $0<q\leqslant q_m=q(T_m)$ are shown in Fig. 2. The minimum of the average entropy production is reached when T takes the values T_m and T_1 and the heat flux takes the values q_m and q_1. In this case, the average value of q should be equal to the prescribed value q_0. It is not hard to show that according to condition (8) the expression

$$\sigma(T)+\lambda(q(T)-q_0)$$

reaches its maximum with respect to λ and its minimum with respect to T at the points T_1 and T_m.

The production of entropy for some times or at some points, allowing for the dynamics of the system, can be negative, but on average it is always greater than zero.

LIMITING POSSIBILITIES OF FIXED-POWER HEAT ENGINES

In the last 30 years a new branch of thermodynamics has been actively developed—the thermodynamics of finite times.[9] This approach examines the limiting possibilities of thermodynamic systems (efficiency indicators, dissipation, etc.) with an additional constraint on the duration of a process or on the average intensity of the fluxes. The starting point of the development of finite-time thermodynamics can be linked with the appearance of Refs. 10 and 11 on the limiting power of a heat engine. Let the heat fluxes be given by

$$q^+=\alpha_+(T_+-T_1), \quad q^-=\alpha_-(T_2-T_-). \tag{9}$$

The coefficients α_+,α_- reflect the dimensions and material of the heat-exchange surface. The temperatures T_1 and T_2 and the times τ_1 and τ_2 are subject to choice. The limiting power $p_{\max}$ turns out to be equal to[10]

$$p_{\max}=\frac{\alpha_+\alpha_-}{(\sqrt{\alpha_+}+\sqrt{\alpha_-})^2}(\sqrt{T_+}-\sqrt{T_-})^2, \tag{10}$$

and the corresponding efficiency of the heat engine

$$\eta^0_{p_{\max}}=1-\frac{\sqrt{T_-}}{\sqrt{T_+}}<\eta_k . \tag{11}$$

If the power of the engine $p_0<p_{\max}$ is assigned, then for systems with two reservoirs it is possible to pose the problem of the limiting value of the efficiency of a heat engine for

$p=p_0$. This problem was solved in Ref. 5. It turns out that the efficiency of a heat engine does not exceed the value

$$\eta^0_{p_0}=\frac{2\,\delta k}{\delta k+1-\sqrt{(1-k)(1-k\,\delta^2)}}, \tag{12}$$

where $k=p_0/p_{\max}$ and $\delta=(\sqrt{T_+}-\sqrt{T_-})/(\sqrt{T_+}+\sqrt{T_-})$.

It is clear from Eq. (3) that the problem of the limiting efficiency is equivalent to the problem of the minimum production of entropy. In the derivation of estimate (12) it was assumed that $\sigma_{pT}=0$ and that for the processes of heat exchange the conditions of minimum dissipation are fulfilled,[12] which for an arbitrary heat-transfer law $q(T_p,T)$ and for any possible variation of the temperature of the reservoir T_p with the contact time τ have the form

$$q^2(T_p,T)=C\,\frac{\delta q}{\delta T}\,T^2, \quad \forall\tau. \tag{13}$$

The constant C depends on the prescribed averaged intensity of the heat flux.

CONCLUSION

In the above-mentioned works of G. V. Skornyakov the assumption of the possibility of negative entropy production in a nonuniform thermodynamic system is in error. Nonuniformity of the system can lower the spatiotemporal average of the entropy production if the constraints imposed on the system are also averaged. But this average entropy production will always be positive.

The proof of a theorem in mathematics, if it is logically derived from the fundamental axioms, does not allow it to be subjected to doubt without subjecting the axioms themselves to doubt. For physical laws it is the same. They should only not contradict one another and be confirmed in any correctly formulated experiment.

The works of G. V. Skornyakov do not contain any proof of a contradiction by the second law of thermodynamics of any other fundamental law of physics and are not based on any experimental material. All of the accumulated experience of mankind to date confirms the validity of this law, and the probability that it is in error is as small as the probability that the particles of a gas in a closed vessel will simultaneously collect in one of its halves.

[1] G. V. Skornyakov, Pis'ma Zh. Tekh. Fiz. **15**, No. 22, 12 (1989) [Tech. Phys. Lett. **15**, 833 (1989)].

[2] G. V. Skornyakov, Zh. Tekh. Fiz. **65**, 35 (1995) [Tech. Phys. **40**, 18 (1995)].

[3] G. V. Skornyakov, Zh. Tekh. Fiz. **66**, 3 (1996) [Tech. Phys. **41**, 1 (1996)].

[4] Yu. L. Klimantovich, Usp. Fiz. Nauk **158**, No. 1, 59 (1989) [Sov. Phys. Usp. **32**, 416 (1989)].

[5] L. I. Rozonoér and A. M. Tsirlin, A. i T., No. 1, 70 (1983); *ibid.*, No. 2, 88 (1983); *ibid.*, No. 3, 50 (1983).

[6] V. N. Orlov and L. I. Rozonoér, in Tenth All-Union Conference on Problems of Control [in Russian], Nauka, Moscow, 1986.

[7] G. Nicolis and I. Prigogine, *Self-Organization in Non-Equilibrium Systems* (Wiley, New York, 1977).

[8] A. M. Tsirlin, Dokl. Akad. Nauk SSSR **323**, 271 (1992) [*sic*].

[9] A. M. Tsirlin, *Methods of Averaged Optimization and Their Applications* (Nauka-Fizmatlit, Moscow, 1979).

[10] I. I. Novikov, Atomnaya Énergiya, No. 3, 409 (1957).

[11] F. L. Curzon and B. Ahlborn, Am. J. Phys. **43**, 22 (1975).

[12] V. Mironova, A. Tsirlin, V. Kazakov, and R. J. Berry, J. Appl. Phys. **76**, 629 (1994).

From the Editorial Board

The second law of thermodynamics is one of the fundamental axioms of physics. So far, not one experiment has been found to be in contradiction with this axiom. Therefore, some very extraordinarily serious reasons would be in order to justify a consideration of the question of the non-observance of the second law. We are not able to discover any such reasons in the published literature. In light of this, the editorial board of the Journal of Technical Physics deems it inexpedient to continue the discussion of the validity of the second law of thermodynamics on the pages of this journal.

Translated by Paul F. Schippnick

Dissociative excitation of the cesium atom in *e*–CsCl collisions

Yu. M. Smirnov

Moscow Power Institute, 111250 Moscow, Russia

(Submitted November 25, 1996; resubmitted October 6, 1997)
Zh. Tekh. Fiz. **69**, 29–34 (January 1999)

The dissociative excitation of the cesium atom in collisions of slow electrons with cesium chloride molecules is studied by the method of extended crossed beams with detection of the optical signal from the crossing region. Forty-seven cross sections for the excitation of spectral lines of CsI in the spectral region 347–852 nm are measured at an electron energy of 100 eV, and 10 optical excitation functions (OEFs) are recorded. It is found that the dependence of the excitation cross sections on the principal quantum number of the upper level in the spectral series of Cs I corresponds to a power law. The characteristic values of the constants in the power law are determined for each of the investigated series. © *1999 American Institute of Physics.* [S1063-7842(99)00401-8]

Although research on inelastic electron–atom and electron–molecule collisions was originally motivated by interest in the fundamental, purely physical aspects of these phenomena, the subsequent development of plasma physics and chemistry has given rise to many technical fields for which such research is extremely topical. Among these important and promising technical fields that have been growing intensively in the past decades is nonequilibrium plasma chemistry.

It has been stated that in order to study the physics of chemically active plasmas, it is necessary to investigate molecular processes involving the participation of electrons, such as the dissociation of excited and unexcited molecules by electron impact.[1] In a relatively dense plasma with a comparatively low electron temperature the atomic products of dissociation are predominantly in the ground state. However, in the presence of faster electrons, e.g., in a plasma initiated by an electron beam, a significant role can be played by dissociative excitation, a process in which the products of dissociation will immediately be found in excited states. Since the rates of chemical reactions for unexcited and excited particles can differ greatly — by as much as tens of orders of magnitude[2] — information about the concentrations of atoms and other heavy particles in different excited states is extremely important for the development of theoretical and applied plasma chemistry.

There are classes of molecules for which there are no electronically excited bound states. When taken out of the electronic ground state (by electron impact, for example), such molecules inevitably dissociate, sometimes with the formation of excited particles. Among the simplest molecules of this type are alkali halides, which are closely similar to one another both in their physico-chemical properties and in the structure of the molecules and the character of their interaction with slow electrons.

A systematic study of inelastic collisions of electrons with alkali halides can not only yield information about the individual behavior of specific molecules (LiF, NaBr, etc.) but can also provide a factual basis for investigating the behavioral trends of the cross sections for dissociative excitation. In view of the absence of any theoretical predictions for these rules, they can initially be based only on experimental results and will be of an empirical nature. However, as the experimental results are accumulated and generalized, eventually a theoretical interpretation should emerge by which the physical nature of the observed regularities and irregularities can be understood.

To minimize the experimental uncertainties the molecules should all be studied on the same experimental apparatus and by a unified and stable technique. With the advent of the method of extended crossed beams,[3,4] such a series of experiments can now be carried out for the alkali halides The unification of the technique and experimental conditions for molecules of the alkali halide class is made substantially easier by the aforementioned similarity of their physico-chemical properties. Although such studies have already been carried out for 13 alkali halides, for the cesium halides so far results have been obtained only for the fluoride.[5] The present paper reports a continuation of this cycle of research with a study of the dissociative excitation of the cesium atom in collisions of electrons with cesium chloride molecules.

As has been noted previously,[6] a feature of the method of extended crossed beams is the large interaction region, which is 2–3 orders of magnitude larger in volume than in the conventional crossed beams method. The corresponding increase in the optical signal substantially increases the information that can be obtained in the extended crossed beams method and makes it possible to study a wider range of objects and processes.

An extended molecular beam was formed by vaporizing a powder of cesium chloride placed in a tantalum crucible. The powder was subjected to a prolonged preliminary heating in the crucible under medium vacuum conditions (around 2×10^{-3} Pa) to drive off the water vapor from the comparatively hydroscopic cesium chloride. The outer surface of the crucible was heated by a 7 keV electron beam focused to a diameter of about 40 mm to provide a more uniform heating of the whole surface of the crucible. At a temperature of 1000 K the density of molecules in the crossing region of the molecule and electron beams reached 1.2×10^{11} cm^{-3}.

The thermic excitation of the molecules in the crucible gives rise to a wide distribution of the molecules over vibrational–rotational levels of the electronic ground state. Since both radiative and collisional relaxation during passage from the crucible to the collector are negligible under the conditions of the present experiment, the distribution that is originally formed is preserved up until the interaction of the molecules with the electrons in the beam crossing region. Measurement of this distribution is at the limit of the present-day capabilities and cannot be done in the existing apparatus; for this reason the Boltzmann distribution was used to estimate the populations of the vibrational levels with vibrational quantum number v. The vibrational quantum was taken to have the value $\omega_e = 212$ cm^{-1}, which is the average of the values $\omega_e = 214.165$ cm^{-1} (for the ^{133}Cs^{35}Cl molecule) and $\omega_e = 209.55$ cm^{-1} (for the ^{133}Cs^{37}Cl molecule).[7] We then obtain the following values of the populations (in percent of the total concentration of molecules in the beam): $v=0$ (25.7%), 1 (18.9%), 2 (13.9%), 3 (10.2%), 5 (5.54%), 10 (1.18%). In all, 81.7% of the total number of molecules are found on the levels with $v=0-5$. Both the values of the excitation cross sections and the OEFs can depend substantially on the vibrational level of the molecule prior to the collision. In Ref. 8 this was observed for excitation of the spectral bands of N_2 and N_2^+ from vibrationally excited states of the nitrogen molecule. However, in Ref. 8 the final state of the molecule, like the initial state, was discrete, whereas in the present experiment the final state belongs to the continuous energy spectrum.

Quite recently two papers[9,10] appeared in which the dependence of the excitation and dissociation cross sections on the vibrational quantum number v_i of the initial state were investigated by a computational method. The calculations were done by the impact-parameter method for molecules of hydrogen and deuterium. It was shown that in the case of excitation of the singlet states $B^1\Sigma_u^+$ and $C^1\Pi_u$ of the H_2 molecule, the cross sections increase by a factor of 2–4 as v_i increases from 0 to 10 and 12, respectively, after which they begin to decrease with further increase in v_i. Analogous results were obtained for the deuterium molecule, but the maximum cross sections are reached at $v_i=14-15$ and 18–19.

In the case of direct dissociation there is also an increase in the cross sections as v_i increases for $v_i=0-3$ and a decrease in the cross sections for $v_i \geqslant 10$, while for intermediate values $v_i=3-10$ there is oscillatory behavior. At the same time, in the case of dissociation through a radiation cascade the cross sections change comparatively little over the range $v_i=0-12$ and begin to increase sharply at $v_i=13$ or 14. The results of these studies show that the behavior of the cross sections as functions of v_i can be rather complicated. Carrying the dependences found in those studies over to alkali halide molecules without the appropriate analysis can hardly be correct, since the structure and spectra of these molecules are extremely different from those of the homoatomic molecules H_2 and D_2. However, it should be noted that as the temperature changes, the distribution of the molecules over vibrational levels as calculated in the present paper varies much more slowly that the total density of molecules (in the presence of a condensed phase). For this reason the measured values of the cross sections can be used in practical calculations of plasma characteristics over a rather wide temperature interval.

The emission spectrum arising in collisions of monokinetic electrons of energy 100 eV with cesium chloride molecules was investigated over the wavelength interval 190–860 nm. Besides the spectral lines of atomic chlorine and singly charged positive ions of cesium and chlorine there are also lines of the cesium atom in the spectral region 347–852 nm. The results of the measurements for Cs I are presented in Table I, which gives the wavelength λ, the corresponding transition, the internal quantum number J, the energies of the lower E_l and upper E_n levels (reckoned from the ground state of the cesium atom), the values of the excitation cross sections Q_{100} for 100 eV electrons and $Q_{\max}$ at the maximum of the OEF, the position of the maximum $E_{\max}$, and the number of the OEF according to the numbering of the curves in Fig. 1. The OEFs were measured in the range of appearance energy up to 100 eV. The error in the measurements of the relative values of the cross sections were 3–10%, depending on the intensity of the spectral line and its position in the spectrum. The error in the determination of the absolute values of the cross sections ranged from ± 22 to $\pm 30\%$. The possible linear polarization of the spectral lines, especially in the near-threshold region of electron energies, was not measured at this stage of the experiment and has not been taken into account, but its possible contribution to the error in our apparatus does not exceed 10% in the spectral interval 250–850 nm, even for 100% polarization of the line.

As we did for the other molecules investigated previously, we analyze the behavior of the cross sections of dissociative excitation in the spectral series of the cesium atom in e–CsCl collisions. It has been shown previously that both for the cesium atom[5] and for other alkali metals[6,11] the dissociative excitation cross sections Q in the spectral series have a power-law dependence on the principal quantum number n of the upper level:

$$Q = A_i \cdot n^{-\alpha_i}. \tag{1}$$

Here A_i and α_i are constants whose values can be determined for each of the spectral series. Since a function of the form (1) is a straight line on a logarithmic scale, the results of the present experiment for electron energy 100 eV are plotted in logarithmic coordinates in Fig. 2. We see that there is an appreciable and systematic deviation from the power law only on the initial (small n) parts of the P^0 series. For the S, D, and F^0 series the cross sections conform to a power law over a wide range of variation of the principal quantum number. The values of the constants A_i and α_i for the investigated series of the cesium atom are given in Table II. The most rapid variation of the cross sections as functions of n occurs in the P^0 series, followed in order by the S, D, and F^0 series. The same picture is found for the other molecules

TABLE I. Effective cross sections for dissociative excitation of the cesium atom.

λ, nm	Transition	J	E_l, eV	E_n, eV	Q_{100}, 10^{-18} cm^2	$Q_{\max}$, 10^{-18} cm^2	E max, eV	OEF
347.681	$6s^2S-10p^2P^0$	1/2–3/2	0	3.56	0.33	–	–	–
348.006	$6s^2S-10p^2P^0$	1/2–1/2	0	3.56	0.17	–	–	–
361.146	$6s^2S-9p^2P^0$	1/2–3/2	0	3.43	0.69	–	–	–
361.730	$6s^2S-9p^2P^0$	1/2–1/2	0	3.43	0.35	–	–	–
387.615	$6s^2S-8p^2P^0$	1/2–3/2	0	3.20	1.84	1.92	55	*5*
388.861	$6s^2S-8p^2P^0$	1/2–1/2	0	3.19	0.89	0.94	55	*2*
455.528	$6s^2S-7p^2P^0$	1/2–3/2	0	2.72	7.70	8.47	40	*4*
459.317	$6s^2S-7p^2P^0$	1/2–1/2	0	2.70	4.13	4.30	50	*1*
515.268	$6p^2P^0-14d^2D$	1/2–3/2	1.38	3.79	0.20	–	–	–
519.673	$6p^2P^0-13d^2D$	1/2–3/2	1.38	3.77	0.26	0.27	80	*10*
525.656	$6p^2P^0-12d^2D$	1/2–3/2	1.38	3.74	0.32	–	–	–
530.140	$6p^2P^0-13s^2S$	1/2–1/2	1.38	3.72	0.145	–	–	–
530.378	$6p^2P^0-14d^2D$	3/2–5/2	1.45	3.79	0.42	–	–	–
534.094	$6p^2P^0-11d^2D$	1/2–3/2	1.38	3.71	0.53	–	–	–
535.035	$6p^2P^0-13d^2D$	3/2–5/2	1.45	3.77	0.51	0.52	80	*10*
535.08	$6p^2P^0-13d^2D$	3/2–3/2	1.45	3.77				
540.666	$6p^2P^0-12s^2S$	1/2–1/2	1.38	3.68	0.25	–	–	–
541.361	$6p^2P^0-12d^2D$	3/2–5/2	1.45	3.47	0.77	–	–	–
541.428	$6p^2P^0-12d^2D$	3/2–3/2	1.45	3.74				
546.192	$6p^2P^0-13s^2S$	3/2–1/2	1.45	3.72	0.21	–	–	–
546.594	$6p^2P^0-10d^2D$	1/2–3/2	1.38	3.65	0.66	–	–	–
550.288	$6p^2P^0-11d^2D$	3/2–5/2	1.45	3.71	0.90	–	–	–
550.385	$6P^2P^0$ $11d^2D$	3/2–3/2	1.45	3.71				
556.841	$6p^2P^0-11s^2S$	1/2–1/2	1.38	3.61	0.37	–	–	–
557.367	$6p^2P^0-12s^2S$	3/2–1/2	1.45	3.68	0.34	–	–	–
563.521	$6p^2P^0-10d^2D$	3/2–5/2	1.45	3.65	1.22	–	–	–
563.667	$6p^2P^0-10d^2D$	3/2–3/2	1.45	3.65				
566.402	$6p^2P^0-9d^2D$	1/2–3/2	1.38	3.57	0.95	1.02	50	*7*
574.572	$6p^2P^0-11s^2S$	3/2–1/2	1.45	3.61	0.53	–	–	–
583.883	$6p^2P^0-10s^2S$	1/2–1/2	1.38	3.51	0.58	–	–	–
584.514	$6p^2P^0-9d^2D$	3/2–5/2	1.45	3.57	1.90	2.10	50	*9*
601.049	$6p^2P^0-8d^2D$	1/2–3/2	1.38	3.45	1.36	–	–	–
603.409	$6p^2P^0-10s^2S$	3/2–1/2	1.45	3.51	0.85	–	–	–
621.310	$6p^2P^0-8d^2D$	3/2–5/2	1.45	3.45	2.58	–	–	–
625.022	$5d^2D-11f^2F^0$	3/2–5/2	1.80	3.78	0.81	–	–	–
628.860	$5d^2D-11f^2F^0$	5/2–7/2	1.81	3.78	1.00	–	–	–
632.621	$5d^2D-10f^2F^0$	3/2–5/2	1.80	3.76	0.97	–	–	–
635.455	$6p^2P^0-9s^2S$	1/2–1/2	1.38	3.34	0.87	–	–	–
643.197	$5d^2D-9f^2F^0$	3/2–5/2	1.80	3.72	1.10	–	–	–
647.262	$5d^2D-9f^2F^0$	5/2–7/2	1.81	3.72	1.36	–	–	–
658.602	$5d^2D-8f^2F^0$	3/2–5/2	1.80	3.68	2.87	–	–	–
658.651	$6p^2P^0-9s^2S$	3/2–1/2	1.45	3.34				
662.866	$5d^2D-8f^2F^0$	5/2–7/2	1.81	3.68	1.81	–	–	–
672.329	$6p^2P^0-7d^2D$	1/2–3/2	1.38	3.23	2.60	2.89	35	*6*
682.465	$5d^2D-7f^2F^0$	3/2–5/2	1.80	3.61	1.83	–	–	–
687.046	$5d^2D-7f^2F^0$	5/2–7/2	1.81	3.61	2.21	–	–	–
697.330	$6p^2P^0-6d^2D$	3/2–5/2	1.45	3.23	3.76	4.32	35	*8*
721.930	$5d^2D-6g^2G$	3/2–7/2, 9/2	1.80	3.51	1.23	–	–	–
722.854	$5d^2D-7f^2F^0$	3/2–5/2	1.80	3.51	2.78	–	–	–
727.070	$5d^2D-6g^2G$	5/2–7/2, 9/2	1.81	3.51	1.75	–	–	–
727.990	$5d^2D-6f^2F^0$	5/2–5/2	1.81	3.51	3.27	–	–	–
727.996	$5d^2D-6f^2F^0$	5/2–7/2	1.81	3.51				
852.115	$6s^2S-6p^2P^0$	1/2–3/2	0	1.45	82.7	94.0	35	*3*

investigated previously. The monotonic character of the curves indicates that perturbations of the respective upper levels are small or absent. In view of the lack of data from other authors for the CsCl molecule it is not possible at present to compare the results, but the values obtained for A_i and α_i can be compared and contrasted with the corresponding values of the constants for e–Cs electron–atom collisions;[12] the results are presented in Table II. Such a comparison shows that in the case of direct excitation of the cesium atom the rate of change of the cross sections is substantially higher in all the spectral series, although the ordering of the series S, D, F^0 is preserved.

Passing now to an analysis of the possible mechanisms of dissociative excitation of the cesium atom in e–CsCl collisions, we can write the following reactions corresponding to the lowest appearance energies:

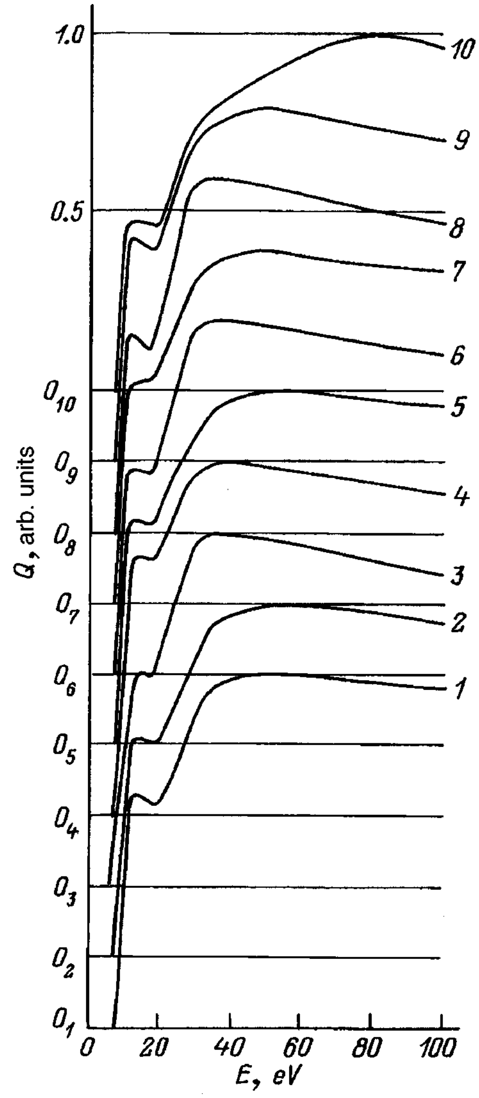

FIG. 1. Optical excitation functions of the cesium atom.

$$\mathrm{CsCl}+e\rightarrow \mathrm{Cs}^*+\mathrm{Cl}^- \quad (3.68), \tag{2}$$

$$\rightarrow \mathrm{Cs}^*+\mathrm{Cl}+e' \quad (7.30), \tag{3}$$

$$\rightarrow \mathrm{Cs}^*+\mathrm{Cl}^*+e' \quad (\sim 17.3), \tag{4}$$

$$\rightarrow \mathrm{Cs}^*+\mathrm{Cl}^+ +e'+e'' \quad (20.27). \tag{5}$$

Here e, e', and e'' are the incoming electron, the scattered electron, and an electron ejected as a result of ionization, respectively; the asterisks denote particles found in excited states. The numbers in parentheses next to the reactions give the calculated values of the appearance energy without allowance for the initial distribution of the molecules over vibrational–rotational levels of the electronic ground state of the molecule or the possible conversion of a portion of the energy of the incoming electron to kinetic energy of the heavy particles. The calculated values of the appearance energy are the sums of the following contributions: 1) the energy of dissociation of the CsCl molecule, $E_d=4.58$ eV (p. 15 of Ref. 7); 2) the energy of excitation of the 455.528 nm spectral line of Cs I from the ground state of the cesium atom, $E_{\mathrm{ex}}=2.72$ eV (Ref. 13); 3) in the case of reaction (4) the additional energy of excitation of the chlorine atom from the ground state to low-lying excited states, around 10.0 eV (pp. 400–404 of Ref. 13); 4) in the case of reaction (5) the additional energy of ionization of the chlorine atom from its ground state, $E_i=12.97$ eV (Ref. 14). In addition, in reaction (2) it is necessary to subtract from the sum E_d+E_{ex} the electron affinity of the chlorine atom $\chi=3.62$ eV (p. 76 of Ref. 14).

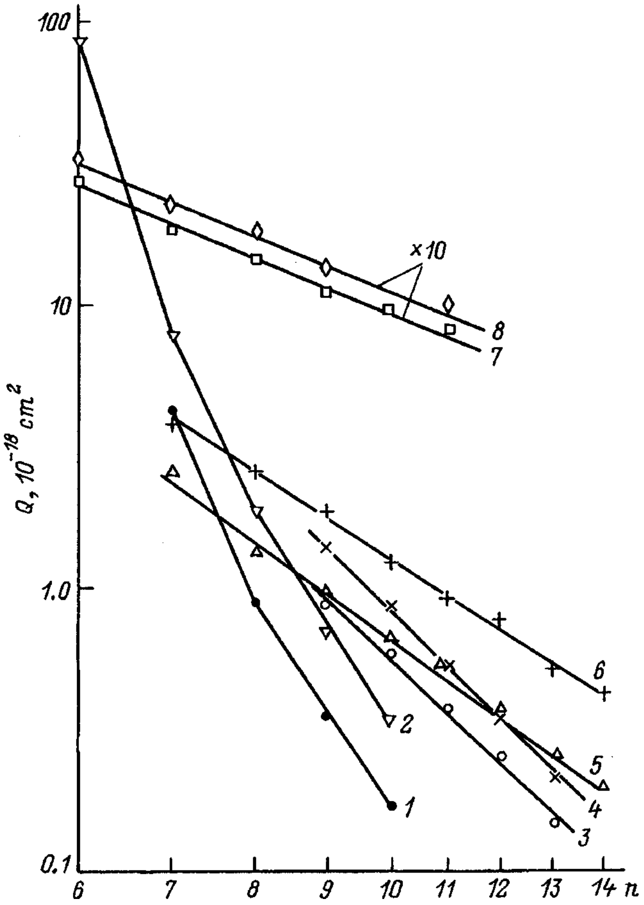

FIG. 2. Plots of $Q=f(n)$ for the spectral series of the cesium atom: *1* — $6s^2S_{1/2}$–$np^2P^0_{1/2}$, *2* — $6s^2S_{1/2}$–$np^2P^0_{3/2}$, *3* — $6p^2P^0_{1/2}$–$ns^2S_{1/2}$, *4* — $6p^2P^0_{3/2}$–$ns^2S^0_{3/2}$, *5* — $6p^2P^0_{1/2}$–$nd^2D_{3/2}$, *6* — $6p^2P^0_{3/2}$–$nd^2D_{3/2,5/2}$, *7* — $5d^2D_{3/2}$–$nf^2F^0_{5/2}$, *8* — $5d^2D_{5/2}$–$nf^2F^0_{5/2,7/2}$.

The measured value of the appearance energy for the 455.528 nm line is 7.1±0.3 eV, which agrees within the experimental error with the appearance energy for reaction (3). The fact that there is no optical signal above the noise level of the detection system at lower energies indicates that the role of reaction (2) is negligible. At the same time, this fact indicates the absence of impurity cesium atoms in the molecular beam. It is very likely that even an extremely small atomic impurity in this energy region would be detectable, since the OEFs for direct excitation of the Cs I lines have maxima precisely in the region below 7 eV.[15]

After attaining a relatively low maximum in the near-threshold region, the OEF stops rising, and for certain spectral lines there is even a drop. The resumption of significant growth of the OEFs up to the main maximum commences at different lines in the energy interval 16–20 eV and apparently corresponds to the actuation of reaction channels (4)

TABLE II. Values of the constants A_i and α_i for the spectral series of Cs I in collisions of electrons with CsCl molecules. $1.69(-4) = 1.69 \times 10^{-4}$

	n		α_i		A_i, cm^2	
Series	Present study	Ref. 12	Present study	Ref. 12	Present study	Ref. 12
$6s^2S_{1/2}-np^2P^0_{1/2}$	6–7		–		–	
$6s^2S_{1/2}-np^2P^0_{3/2}$	6–7		15.8		1.69(−4)	
$6s^2S_{1/2}-np^2P^0_{1/2}$	8–10		7.50		5.43(−12)	
$6s^2S_{1/2}-np^2P^0_{3/2}$	8–10		7.71		1.75(−11)	
$6p^2P^0_{1/2}-ns^2S_{1/2}$	9–13	8–12	4.79	8	3.35(−14)	9.55(−10)
$6p^2P^0_{3/2}-ns^2S_{1/2}$	9–13		4.88		6.25(−14)	
$6p^2P^0_{1/2}-nd^2D_{3/2}$	7–14	7–14	3.66	5.2	3.04(−15)	1.29(−12)
$6p^2P^0_{3/2}-nd^2D_{5/2}$	7–14		3.29		2.44(−15)	
$5d^2D_{3/2}-nf^2F^0_{5/2}$	6–11	5–10	2.05	4.7	1.04(−16)	6.84(−14)
$5d^2D_{5/2}-nf^2F^0_{7/2}$	6–11		2.01		1.16(−16)	

and (5). It is not possible to make a clear choice between (4) and (5) on the basis of the present experiment, since the place where the growth of the OEF resumes is determined only to an accuracy of ±1.0 eV and also since the appearance energy in reaction (4) has a large uncertainty, inasmuch as it is not known precisely which of the levels or which group of levels of the chlorine atom play the main role in reaction (4).

For observation of reaction (5) it is necessary to detect the unexcited singly charged chlorine ions, but our working apparatus is not equipped with mass-spectrometric detection. Reaction (4) can be observed from the emission spectrum of the chlorine atom (leaving aside the possibility of metastable levels). As was mentioned previously, the spectrograms contain not only cesium lines but also the spectral lines of atomic and singly charged chlorine. Although several tens of lines were recorded for each of Cl I and Cl II, all of them have comparatively small excitation cross sections of around 10^{-19} cm^2. At the same time the resonance lines, which give the decisive contribution to the total cross sections of inelastic collisions for the majority of atoms and ions, lie in the vacuum ultraviolet part of the spectrum for both the atom and singly charged ion of chlorine and are inaccessible to study on our existing apparatus. The plan of such a study should include simultaneous recording of the optical and mass spectra and extension of the spectral range into the VUV and IR regions. The latter is hardly possibility at present because of the comparatively low sensitivity of IR detectors.

[1] A. A. Ivanov and T. K. Soboleva, *Nonequilibrium Plasma Chemistry* [in Russian], Atomizdat, Moscow (1978), 264 pp.
[2] D. I. Slovetskiĭ, *Mechanisms of Chemical Reactions in Nonequlibrium Plasmas* [in Russian], Nauka, Moscow (1980), 310 pp.
[3] Yu. M. Smirnov, *Physics of Electronic and Atomic Collisions* [in Russian], Izd. FTI AN SSSR, Leningrad (1985), pp. 183–193.
[4] Yu. M. Smirnov, J. Phys. II **4**, 23 (1994).
[5] Yu. M. Smirnov, Zh. Prikl. Spektrosk. **64**, 20 (1997).
[6] Yu. M. Smirnov, Zh. Fiz. Khim. **70**, 692 (1996).
[7] K. S. Krasnov (ed.), *Molecular Constants of Inorganic Compounds. A Handbook* [in Russian], Khimiya, Leningrad (1979), 446 pp.
[8] Yu. M. Smirnov, Khim. Vys. Energ. **21**, 267 (1987).
[9] R. Celiberto and T. N. Rescigno, Phys. Rev. A **47**, 1939 (1993).
[10] R. Celiberto, U. T. Lamanna, and M. Capitelli, Phys. Rev. A **50**, 4778 (1994).
[11] Yu. M. Smirnov, Chem. Phys. **1992**, 379 (1995).
[12] I. P. Zapesochnyĭ and L. L. Shimon, Opt. Spektrosk. **20**, 753 (1966).
[13] A. N. Zaĭdel', V. K. Prokof'ev, S. M. Raĭskiĭ *et al.*, *Tables of Spectral Lines* [in Russian], Nauka, Moscow (1969), 782 pp.
[14] A. A. Radtsig and B. M. Smirnov, *Handbook of Atomic and Molecular Physics*, Atomizdat, Moscow (1980), 240 pp.
[15] I. P. Zapesochnyĭ and L. L. Shimon, Izv. Akad. Nauk SSSR, Ser. Fiz. **27**, 1037 (1963).

Translated by Steve Torstveit

TECHNICAL PHYSICS VOLUME 44, NUMBER 1 JANUARY 1999

Selective infrared multiphoton dissociation of molecules in a pulsed gasdynamic flow of small extent

G. N. Makarov, D. E. Malinovskiĭ, and D. D. Ogurok

Institute of Spectroscopy, Russian Academy of Sciences, 142092 Troitsk, Moscow District, Russia

(Submitted October 28, 1997)
Zh. Tekh. Fiz. **69**, 35–41 (January 1999)

The isotopically selective IR multiphoton dissociation of molecules (here CF_3I) in a pulsed gasdynamic flow of small extent (the length of the flow in space is $\Delta x_{\mathrm{fl}} \leqslant 1$ cm) is investigated under conditions such that the entire flow is irradiated by high-intensity IR laser radiation. The use of a flow of small extent permits achieving high dissociation yields of resonantly excited molecules in the entire volume of the flow and thus to obtain a highly enriched residual gas in one radiation cycle. The method described gives a 400-fold enrichment of the residual gas in the isotope ^{13}C when a pulsed molecular flow of CF_3I of natural isotopic composition is irradiated by just a single laser pulse. The dissociation yield in this case is practically unity, and the selectivity $\alpha \geqslant 10$. *© 1999 American Institute of Physics.* [S1063-7842(99)00501-2]

INTRODUCTION

A topical problem in isotope separation by IR multiphoton dissociation of molecules is to increase the isotopic selectivity of the dissociation process, especially in the separation of isotopes in molecules with a small isotope shift (e.g., OsO_4, UF_6, ...).

An effective way of increasing the selectivity of dissociation is to cool the gas in gasdynamic jets or flows.[1–3] Then, however, one is faced with problems in connection with the collection of the products formed. Because of the high chemical activity of the radicals formed in the dissociation of molecules and their low concentration when gasdynamic jets are used, it is difficult to investigate the efficient collection of the products of dissociation and the subsequent chemical reactions. Reactions on the walls can be predominant and can substantially alter the kinetics and the channels of product formation. In addition, in the dissociation of molecules with a small isotope shift the selectivities achieved are ordinarily not very high ($\alpha \leqslant 2$–5). As a result, it is impossible to obtain a highly enriched product in a single cycle of irradiation of the initial gas. It is therefore better in many cases to ''burn up'' the unwanted component in the initial mixture and enrich the residual gas in the desired isotope.

However, when gasdynamic jets or flows are used, it is impossible to achieve a high coefficient of enrichment of the residual gas unless the gas is circulated and repeatedly irradiated. Because of the comparatively low duty factor of laser pulses, only a tiny fraction η of the molecules in the flow can be irradiated in one cycle:

$$\eta = \frac{\Delta x_L f}{v_x}, \tag{1}$$

where Δx_L is the dimension of the laser beam in the direction of the x axis, f is the repetition frequency of the laser pulses, and v_x is the average flow velocity.

Here we assume that the laser beam is directed perpendicular to the x axis and that the flow in the direction of the y and z axes is bounded and completely irradiated by the laser beam.

When high-power periodically pulsed CO_2 lasers[4] are used for isotope separation, one can achieve parameters $\Delta x_L \approx 1$ cm and $f \approx 500$ Hz. For a typical mean velocity of the molecular flow $v_x \approx 5 \times 10^4$ cm/s the fraction of the molecules irradiated comes to $\eta \approx 10^{-2}$ (here we have assumed that the pulse duration of a TEA CO_2 laser satisfies $\tau_p \leqslant 1\ \mu s \ll \Delta x_L / v_x$, and therefore during the laser pulse the position of the flow in space is practically unchanged). With a dissociation yield $\beta \approx 0.2$, the fraction of molecules in the flow that will be dissociated during the irradiation is $\eta_\beta \approx \eta\beta \approx 2 \times 10^{-3}$. Consequently, in one irradiation cycle the enrichment coefficient in the residual gas will be negligibly small.

The situation is improved if one uses pulsed molecular flows. For a characteristic duration of the nozzle ''open'' pulse $\tau_{\mathrm{noz}} \approx 200 \mu s$ the molecular flow will have a spatial extent $\Delta x_{\mathrm{fl}} \approx v_x \tau_{\mathrm{noz}} \approx 10$ cm. In this case one laser pulse can irradiate a fraction $\eta = \Delta x_L / \Delta x_{\mathrm{fl}} \approx 0.1$ of the molecules in the flow. For $\beta \approx 0.2$ we obtain $\eta_\beta \approx 2 \times 10^{-2}$. This is still a comparatively small fraction, though, and so the enrichment coefficient in the residual gas will still be small.

The situation is fundamentally different when one uses a molecular flow of short extent ($\Delta x_{\mathrm{fl}} \leqslant 1$ cm), which can be obtained with a nozzle having a short ''open'' time ($\tau_{\mathrm{noz}} \leqslant 20\ \mu s$). In this case the entire flow can be irradiated by a high-intensity IR laser beam. Then the enrichment coefficient in the residual gas will be determined mainly by the dissociation yield of resonantly excited molecules. For a dissociation yield $\beta \approx 1$, even in the case of a moderate selectivity $\alpha \geqslant 3$ one can obtain a highly enriched residual gas as a result of the irradiation of a mixture of isotopomers by just a single laser pulse. Since the absorption spectra of molecules narrow considerably upon cooling in a gasdynamic flow,[3] one can obtain a comparatively high selectivity $\alpha \geqslant 5$–10 even at high energy densities of the laser radiation and thereby limit the consumption of the desired isotopic component. It is this approach that is developed in the present study.

CHOICE OF OBJECT OF STUDY

The CF_3I molecule was chosen as the object of study for the following reasons. It has a rather low dissociation energy (≈ 2.3 eV)[5] and dissociates efficiently at moderate laser energy flux densities $\Phi \leqslant 4$ J/cm^2 (Ref. 6–9). Therefore, for this compound it is easy to achieve conditions under which the dissociation yield is practically unity. Its dissociation products (C_2F_6 and I_2) are stable. The IR multiphoton excitation and dissociation of CF_3I have been quite well studied,[6–10] including in molecular beams.[11] The CF_3I molecule had originally been considered for use as the initial substance for large-scale laser separation of carbon isotopes.[12] The IR absorption spectra of the isotopomers $^{12}CF_3I$ and $^{13}CF_3I$ are also well known, and the isotope shifts in these spectra have been measured;[13] this makes it easier to choose the frequencies for dissociation of the molecules.

CONNECTION BETWEEN THE PARAMETERS OF THE ELEMENTARY SEPARATION EVENT UNDER THE GIVEN EXPERIMENTAL CONDITIONS

Under conditions such that the entire molecular flow is irradiated by the laser beam, the concentration of molecules in a two-component mixture after the laser pulse has acted are given by

$$N_1 = N_{10}(1-\beta_1), \tag{2}$$

$$N_2 = N_{20}(1-\beta_2), \tag{3}$$

where N_{10} and N_{20} are the concentrations of isotopic molecules in the initial mixture, and β_1 and β_2 are the dissociation yields of these molecules, respectively.

Suppose that the laser radiation is tuned to resonance with the molecular vibrations in such a way that the molecules of the type denoted by the subscript 1 are predominantly dissociated, i.e., $\beta_1 > \beta_2$. We define the selectivity of the dissociation in the usual way:

$$\alpha = \beta_1/\beta_2. \tag{4}$$

The enrichment coefficient in the residual gas will be given by the expression

$$K_2^{\text{res}} = \frac{N_2/N_1}{N_{20}/N_{10}} = \frac{N_2 N_{10}}{N_{20} N_1} \tag{5}$$

or, with allowance for Eqs. (2), (3), and (4),

$$K_2^{\text{res}} = \frac{1-\beta_2}{1-\beta_1} = \frac{1-\beta_1/\alpha}{1-\beta_1}. \tag{6}$$

The enrichment coefficient in the dissociation products will be given by

$$K_1^{\text{prod}} = \frac{N_{1\text{prod}}}{N_{2\text{prod}}} \Bigg/ \frac{N_{10}}{N_{20}} = \frac{\beta_1 N_{10}}{\beta_2 N_{20}} \Bigg/ \frac{N_{10}}{N_{20}} = \beta_1/\beta_2 = \alpha. \tag{7}$$

Thus in order to obtain a product highly enriched in some isotope it is necessary to have rather high selectivity of dissociation, which is not always achievable, particularly in the case of molecules with a small isotope shift. At the same time one can obtain (even at a comparatively low selectivity $\alpha \geqslant 3$) a highly enriched residual gas if the dissociation of the molecules is carried out under conditions such that the entire molecular flow is irradiated by intense laser radiation and the dissociation yield of resonantly excited molecules reaches values close to unity.

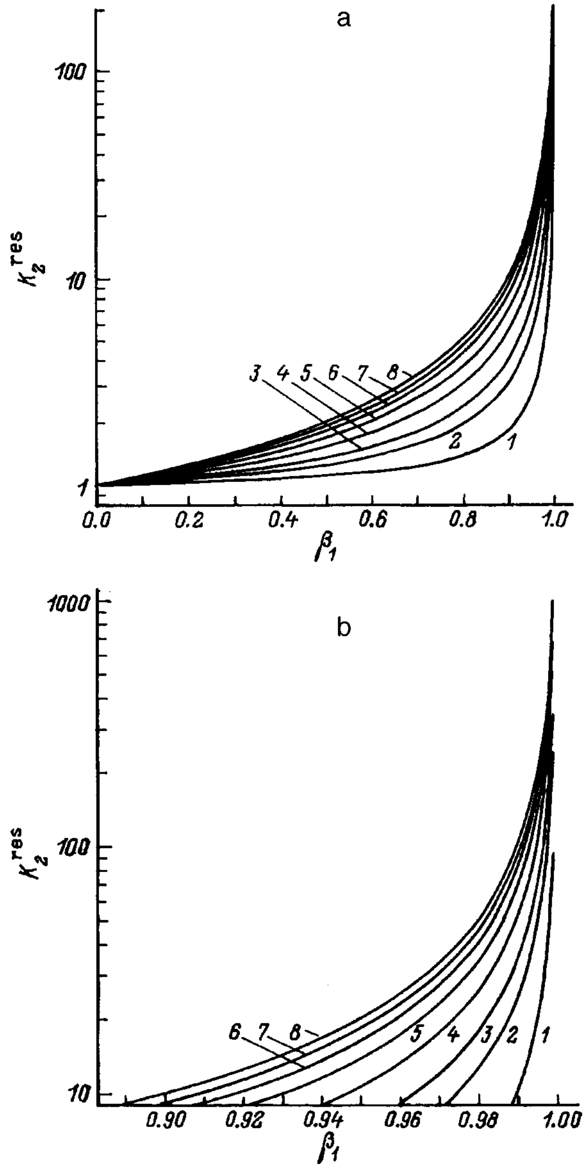

FIG. 1. Dependence of the enrichment coefficient K_2^{res} in the residual gas on the dissociation yield β_1 for different values of the selectivity in the irradiation of a two-component mixture of isotopomers under the conditions $\beta_1 > \beta_2$ and: $0 \leqslant \beta_1 < 1$ (a), or $0.9 \leqslant \beta_1 < 1$ (b); the curves are for $\alpha = 1.1$ (*1*), 1.3 (*2*), 1.5 (*3*), 2 (*4*), 3 (*5*), 5 (*6*), 10 (*7*), and 100 (*8*).

It follows from relation (6) that the enrichment coefficient in the residual gas, K_2^{res}, depends weakly on the selectivity α (provided that $\alpha \geqslant 3$) and depends very strongly on the dissociation yield in the region $\beta \approx 1$. This is plainly seen from the curves of $K_2^{\text{res}}(\beta_1)$ shown in Fig. 1. For example, if $\beta_1 \approx 0.95$, then as α varies from 2 to 10^3, the coefficient K_2^{res} varies from ≈ 10 to ≈ 20, i.e., by only a factor of 2. While it

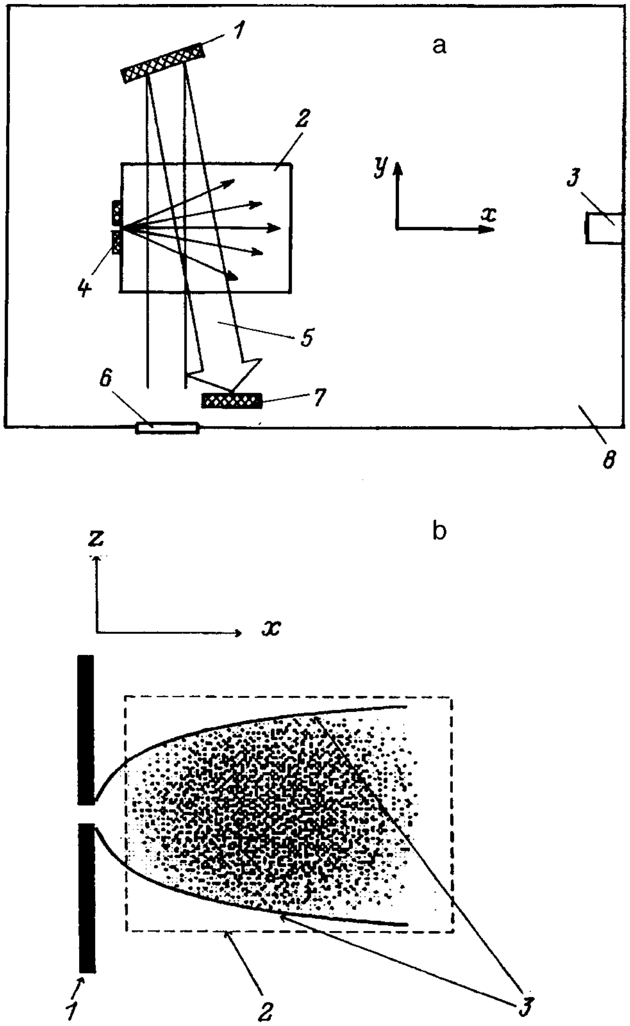

FIG. 2. a: Diagram of the experiment: *1* — mirror, *2* — strips shaping the flow, *3* — pyroelectric detector, *4* — pulsed nozzle, *5* — laser beam, *6* — window, *7* — absorber, *8* — vacuum chamber. b: Geometry of the irradiation of the molecular flow by the laser beam: *1* — pulsed nozzle, *2* — cross section of the laser beam, *3* — strips shaping the molecular flow.

is practically independent of the value of α (for $\alpha \geqslant 3$), K_2^{res} reaches rather high values as $\beta \rightarrow 1$. For example, for $\alpha = 5$ an increase of β_1 from 0.9 to 0.99 leads to an increase in K_2^{res} from $\cong 10$ to $\cong 100$ ($K_2^{\text{res}} \rightarrow \infty$ as $\beta_1 \rightarrow 1$). Consequently, under conditions such that the entire flow is subjected to laser irradiation and the dissociation yield of resonantly excited molecules reaches unity ($\beta_1 \approx 1$), one can obtain a highly enriched residual gas after only one radiation pulse. These are the conditions that were realized in the present experiments.

EXPERIMENT

A diagram of the experiment is shown in Fig. 2a. The molecular flow in the experiments was obtained using a pulsed nozzle of the current-loop type.[14,15] The duration of the ''open'' pulse of the nozzle was $\approx 18 \mu$s (at half height). The aperture diameter of the nozzle was 0.75 mm. The gas pressure above the nozzle could be varied from ≈ 1 to 5 atm. The number of molecules emitted from the nozzle per pulse, N, depended on the gas pressure above the nozzle. At a CF_3I pressure above the nozzle of ≈ 2 atm, for example, $N \approx 10^{16}$ mol./pulse. The nozzle could operate in the single-pulse mode or at a repetition frequency of up to 1 Hz.

The vacuum chamber (of volume $V_{\text{ch}} = 20$ liters) in which the molecular flow was formed was pumped down to a pressure $\leqslant 10^{-5}$ torr by a TMH-500 turbomolecular pump (pumping rate of 500 liter/s). The pressure in the chamber was monitored by a PMI-10 ionization gauge. The number of molecules emitted from the nozzle per pulse, N, was determined from the pressure change Δp in the vacuum chamber after n nozzle pulses with the vacuum pump shut off:

$$N = (p_{\text{fin}} - p_{\text{in}}) V_{\text{ch}} / nkT = \Delta p V_{\text{ch}} / nkT \quad (T \cong 300\,\text{K}). \tag{8}$$

The duration of the ''open'' pulse of the nozzle τ_{noz} and the average flow velocity v_x were determined with a pyroelectric detector by a time-of-flight technique described in Refs. 16 and 17. The mean velocity of the molecular flow of CF_3I in the excitation zone was $v_x = 400 \pm 20$ m/s.[18]

The molecular flow was shaped (Fig. 2b) by means of two thin (100 μm) metal strips mounted directly at the nozzle exit in such a way that they formed a dihedral angle with the edge parallel to the y axis. In the xz plane they had a variable radius of curvature. The maximum divergence angle of the strips (at the exit section of the nozzle) was $\approx 60°$. The strips had dimensions of 2.5×2.5 cm. The minimum distance between them (at the nozzle aperture) was ≈ 1.5 mm, and the maximum distance was ≈ 8 mm. Since the ''bunches'' of molecules emitted from the nozzle had a length $\Delta x_{\text{fl}} = v_x \tau_{\text{noz}} \leqslant 7.5$ mm (at half height), these bunches lay completely in the space between the strips. It was in this region that the molecules were subjected to irradiation.

The molecules were excited with a frequency-tunable TEA CO_2 laser. The radiation pulse consisted of a peak of duration ≈ 100 ns (at half height) and a ''tail'' of duration $\approx 0.5 \mu$s in which $\approx 50\%$ of the total energy of the pulse was contained. The total energy per pulse was 3 J. The laser energy was measured by a TPI-1 absolute energy meter. The laser radiation was focused by a lens ($f_L = 1$ m) and was directed into the vacuum chamber to the region between the strips bounding the molecular beam. The laser beam was perpendicular to the direction of the flow. The minimum distance from the exit section of the nozzle to the edge of the excitation zone was ≈ 3 mm. In the interaction region with the flow the cross section of the laser beam was $\approx 6 \times 6$ mm. In the vertical direction (along the z axis) the laser beam completely illuminated the space between the strips bounding the flow, while its dimension along the x axis $\Delta x_L \approx 6$ mm was smaller than the length of the flow $\Delta x_{\text{fl}} \approx 7.5$ mm. In order to completely illumination the flow the laser beam was reflected by a mirror at a small angle to the backward direction. With this measure the dimension of the illuminated region in the direction of the x axis was $\Delta x_L \approx 12$ mm. Thus under the experimental conditions the molecular beam could be entirely irradiated by high-intensity laser radiation. The energy flux density of the laser in the excitation region of the molecules was as high as 8 J/cm^2. At such a value of the energy flux density the dissociation yield of CF_3I molecules is practically unity.[9,12]

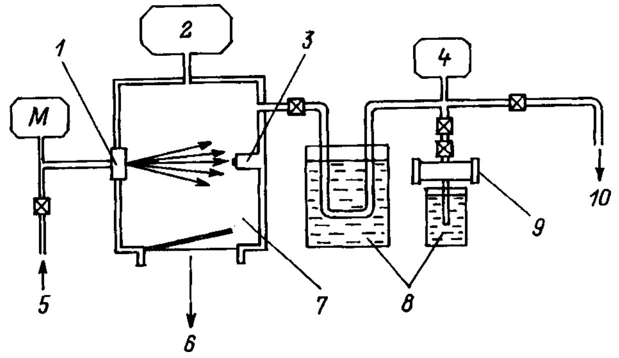

FIG. 3. Diagram of the collection of the residual gas and products: *1* — vacuum nozzle, *2* — PMI-10 ionization gauge, *3* — pyroelectric detector, *4* — PMT-6 pressure gauge, *5* — system for admission of gas, *6* — diffusion pump, *7* — vacuum chamber, *8* – liquid nitrogen, *9* — optical cell, *10* — to vacuum pump.

The nozzle, the CO_2 laser, and the system for detecting the molecular flow, which included a pyroelectric detector, an amplifier ($\times 100$), and an S9-8 digital oscilloscope, was triggered by a GI-1 delayed pulse generator. The synchronization of the laser pulse with the molecular flow was monitored by the pyroelectric detector according to the signal induced at the detector by excited CF_3I molecules.[17,18]

PROCEDURES FOR COLLECTION AND ANALYSIS OF THE RESIDUAL GAS AND DISSOCIATION PRODUCTS

The vacuum chamber in which the molecular flow was formed had an additional pumping channel (Fig. 3) with a liquid-nitrogen-cooled cryogenic trap right at the exit from the chamber, an optical cell with an ''appendix'' trap, and a PMT-6 pressure gauge.

The procedure for irradiating and collecting the gas consisted of the following. First the vacuum chamber and cryogenic trap were pumped down to a pressure of $\approx 10^{-5}$ Torr by the turbomolecular pump. Then the pump channel of the chamber was closed, the cryogenic trap was flooded with liquid nitrogen, the nozzle and CO_2 laser were actuated, and the process of irradiating the gas in the flow began. The CF_3I gas remaining after the irradiation and the products formed (mainly C_2F_6) were collected in the trap. An irradiation cycle consisted of several tens or hundreds of pulses (from 50 to 500 pulses). During the irradiation the pressure in the vacuum chamber did not rise above 10^{-2} torr. In fact, after 500 pulses, for example, a total of $N_\Sigma \approx N \cdot n \cdot 10^{16} \times 500 \approx 5 \times 10^{18}$ particles had been emitted from the nozzle. For a chamber volume $V_{\mathrm{ch}} \approx 2 \times 10^4$ cm^3 the increment of the pressure would equal $\Delta p_{\mathrm{ch}} \approx \Delta NkT/V_{\mathrm{ch}} \approx 2.5 \times 10^{14} kT \approx 7 \times 10^{-3}$ Torr. The effective pressure of the molecules in the flow in the irradiation zone was $p_{\mathrm{eff}} \approx NkT/V_{\mathrm{fl}} \approx 0.2$ Torr ($V_{\mathrm{fl}} \approx 1$ cm^3 is the volume of the flow).

After the end of an irradiation cycle, oxygen was admitted into the chamber to a pressure of ≈ 1 torr in order to completely collect the residual gas and dissociation products in the cryogenic trap. The gas was then slowly pumped out of the chamber through the trap. In this way the oxygen was pumped out but the CF_3I and C_2F_6 were condensed in the trap. The pumping time was $\leqslant 30$ min. The chamber was pumped down to a pressure of $\approx 3 \times 10^{-3}$ Torr. Then the pumping was stopped, and the gas from the trap was collected in the optical cell for IR and mass analysis. The thawing of the cryogenic trap and collection of the gas in the optical cell were monitored with a PMT-6 pressure gauge. Since the saturated vapor pressure of CF_3I and C_2F_6 at liquid-nitrogen temperature is rather low ($< 10^{-4}$ Torr), the procedure described was capable of collecting practically all of the CF_3I and C_2F_6 from the chamber into the optical cell.

Infrared analysis of the gas was carried out with a Specord 75 1R infrared spectrometer. The absorption of the gases was measured in the 680–1400 cm^{-1} range, which includes the most intense absorption bands of the CF_3I and C_2F_6 molecules.[19] Recording of the absorption in several bands is necessary to improve the accuracy of determination of the amount of gas collected. The enrichment of the residual gas in the isotope ^{13}C or ^{12}C was determined from the IR absorption spectrum of the CF_3I molecules in the ν_4 vibrational band (1187 cm^{-1}; Ref. 13), where the absorption spectra of the isotopomers $^{12}CF_3I$ and $^{13}CF_3I$ are rather well resolved ($\Delta \nu_{\mathrm{is}} = 33$ cm^{-1}). The enrichment was determined more precisely from the mass spectra. The mass analysis of the gas was done on an MKh-7303 mass spectrometer. The isotopic composition of CF_3I was determined from the ion peaks of CF_3I^+ ($m/e = 196$ and 197), and that of C_2F_6 from the ion peaks of $C_2F_5^+$ ($m/e = 119$, 120, and 121).

RESULTS AND DISCUSSION

The excitation of the CF_3I molecules was done in the ν_1 vibrational band (1075 cm^{-1} for $^{12}CF_3I$ and 1047.1 cm^{-1} for $^{13}CF_3I$).[13] The isotope shift in this band is $\Delta \nu_{\mathrm{is}} = 27.9$ cm^{-1} (Ref. 13). The $^{12}CF_3I$ molecules were excited by the $9R(10)$ line of the laser (1071.9 cm^{-1}) or by the $9R(12)$ line (1073.3 cm^{-1}), while the $^{13}CF_3I$ molecules were excited by the $9P(24)$ line (1043.2 cm^{-1}). As was established in Ref. 11, the $9R(10)$ and $9R(12)$ lines are optimal for dissociation of $^{12}CF_3I$ molecules cooled in a pulsed gasdynamic jet. The $9P(24)$ line is shifted from the $9R(10)$ line toward the red end of the spectrum by an amount approximately equal to the isotope shift.

The results are presented in Fig. 4a–e. Figure 4a shows the absorption spectrum of CF_3I molecules emerging into the chamber in a molecular beam from the nozzle in the absence of laser irradiation. As expected, the ratio of the isotopomers in the mixture corresponds to the natural abundance (concentration of $^{13}C \approx 1.1\%$, $^{12}C/^{13}C \approx 99\%$). Figure 4b shows the absorption spectrum of CF_3I molecules irradiated in the flow by the $9R(10)$ line of the laser at an energy flux density of the laser radiation $\Phi \approx 8$ J/cm^2. In this experiment the laser radiation crossed the flow in only one direction (the mirror reflecting the laser beam in the backward direction had not been mounted). Therefore, not all the molecules in the flow were subjected to irradiation ($\Delta x_L < \Delta x_{\mathrm{fl}}, \Delta x_L \approx 6$ mm, $\Delta x_{\mathrm{fl}} \approx 7.5$ mm at half height). An almost 7-fold enrichment of the residual gas in the isotope ^{13}C was obtained ($K_{13}^{\mathrm{res}} \cong 6.8$). Figure 4c shows the absorption spectrum of molecules irradiated in the flow by the $9R(12)$ line of a laser at $\Phi \approx 3.5$ J/cm^2 under conditions such that the entire flow was illuminated by

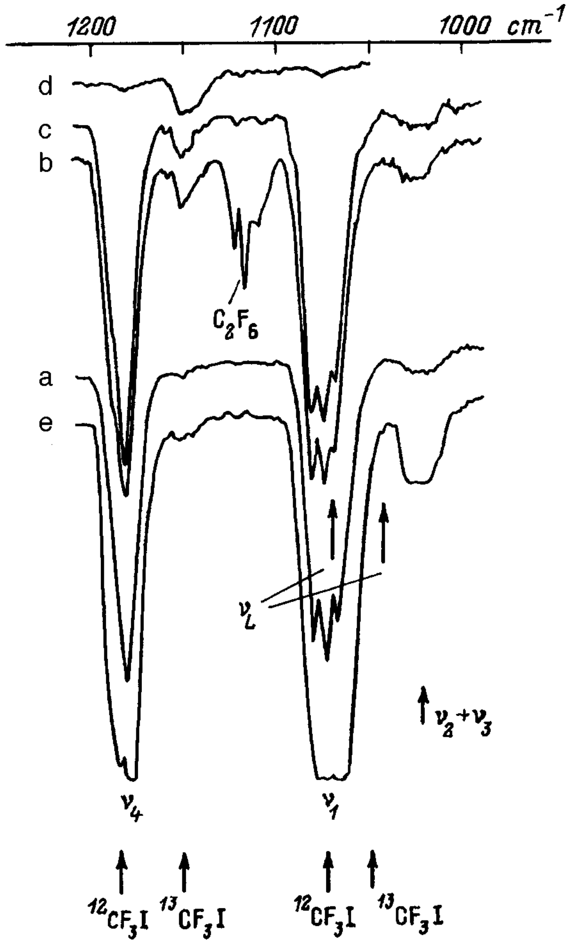

FIG. 4. Infrared absorption spectra of CF_3I molecules of natural isotopic composition before irradiation (a) and after irradiation in a molecular flow under resonance excitation of the molecules $^{12}CF_3I$ (b–d) and $^{13}CF_3I$ (e).

the laser radiation (the reflecting mirror was mounted, so that $\Delta x_L \approx 12$ mm). An approximately 5-fold enrichment of the residual CF_3I gas in the ^{13}C isotope was obtained ($K_{13}^{\mathrm{res}} \cong 5.2$). At the value of the energy flux density of the exciting radiation that was used, the dissociation yield of CF_3I is close to but not quite equal to unity.[9,12] Finally, Fig. 4d shows the absorption spectrum of molecules irradiated by the $9R(10)$ line of the laser under conditions such that the entire flow was illuminated by high-intensity laser radiation ($\Phi \approx 7.5$ J/cm^2, $\Delta x_L \approx 12$ mm). It is seen that practically all the $^{12}CF_3I$ molecules that had been present in the natural mixture ($\approx 99\%$) have been dissociated. The residual CF_3I gas consists mainly of $^{13}CF_3I$ molecules ($\geqslant 82\%$). In this experiment an almost 400-fold enrichment of the residual CF_3I gas in the ^{13}C isotope was obtained. The selectivity measured from the product C_2F_6 and also estimated from the IR absorption spectra of CF_3I (with allowance for the fraction of $^{12}CF_3I$ molecules that have been dissociated) has a value $\alpha \geqslant 10$. A more accurate value of the selectivity could not be determined, since the range of the measurable intensities of the mass peaks in our mass spectrometer was $< 10^3$. The dissociation yield of $^{12}CF_3I$ molecules in this experiment was $\beta_{12} \approx 99.8\%$.

As we mentioned above, in the present experiments the selectivity and dissociation yield and also the enrichment of the residual gas do not depend on the number of irradiation pulses but characterize the separation process in each individual pulse. A series of pulses must be used only for obtaining large amounts of enriched gas. Consequently, the reported values of the enrichment coefficients of the residual gas were achieved as a result of the irradiation of a CF_3I molecular flow by a single laser pulse.

Figure 4e shows the absorption spectrum of CF_3I molecules irradiated in the flow by the $9P(24)$ line of the laser, which is in resonance with the $^{13}CF_3I$ molecules, at an energy flux density of the laser radiation $\Phi \approx 8$ J/cm^2. As in the case of Fig. 4b, in this experiment the molecular flow was not completely covered by the laser beam (the mirror was absent). We see that the concentration of $^{13}CF_3I$ molecules in the residual gas is significantly lower than in the initial gas. An approximately 2-fold enrichment of the residual gas in the isotope ^{12}C has occurred ($K_{12}^{\mathrm{res}} \cong 2.2$). The selectivity of dissociation as measured in terms of the product C_2F_6 here had a value $\alpha_{13} \approx 11$. The comparatively low selectivity in the dissociation of $^{13}CF_3I$ molecules is due to the fact that the band which is to be excited in that molecule, i.e., the ν_1 band of $^{13}CF_3I$, is close to the $\nu_2 + \nu_3$ band of the $^{12}CF_3I$ molecule (≈ 1028 cm^{-1}; Ref. 13). It should be noted that the enrichment in the residual gas achieved through excitation of the $^{13}CF_3I$ molecules is smaller by a factor of 1.5–2 than that achieved through excitation of the $^{12}CF_3I$ molecules, under the same irradiation conditions. This is probably due to the presence of an exchange reaction between the $^{13}CF_3$ radicals and the initial $^{12}CF_3I$ molecules. It was also found that the amount of the product C_2F_6 formed falls off sharply with decreasing concentration of the CF_3I molecules in the flow. This is undoubtedly due to the mechanism of C_2F_6 formation in binary collisions of CF_3 radicals.

Let us now use the experimental value obtained for the enrichment coefficient $K_{13}^{\mathrm{res}} \approx 6.8$ (the case in Fig. 4b) to estimate the fraction η of molecules in the flow that are irradiated by the laser beam. In the case when the flow is not completely irradiated by the laser beam, the yield β_1 in Eq. (6) must be replaced by $\beta_{1\,\mathrm{eff}}$ ($\beta_{1\,\mathrm{eff}} = \beta_1 \eta$). Substituting the values $\alpha = 10$ and $K_{13}^{\mathrm{res}} = 6.8$ into Eq. (6), we get $\beta_{1\,\mathrm{eff}} = 0.86$. Since $\beta_1 = \beta_{12} \approx 1$, this means that $\eta \approx 0.86$.

Relation (6) can also be used to determine the dissociation yield of the $^{12}CF_3I$ molecules in the case of irradiation at $\Phi \approx 3.5$ J/cm^2 (the case in Fig. 4c). Substituting the values $\alpha_{12} = 10$ and $K_{13}^{\mathrm{res}} = 5.2$ into Eq. (6), we obtain the value $\beta_{12} \approx 0.82$.

CONCLUSION

We have developed an approach using isotopically selective IR multiphoton dissociation of molecules to obtain a highly enriched residual gas in a single cycle of irradiation. The approach is based on the use of a pulsed molecular flow of short extent ($\Delta x_{\mathrm{fl}} \leqslant 1$ cm).

Isotopically selective IR multiphoton dissociation in a pulsed gasdynamic flow of short extent was investigated for the case of CF_3I molecules. Conditions were realized under which the entire flow was subjected to laser irradiation, and values practically equal to unity were achieved for the dissociation yield of resonantly excited molecules. An approximately 400-fold enrichment of the residual gas in the ^{13}C isotope was obtained in a molecular flow of CF_3I of natural isotopic composition irradiated by a single laser pulse.

Since in the approach described in this paper one achieves high enrichment coefficients in the residual gas at moderate selectivities $(\alpha \geqslant 2-3)$, it might also be applicable to molecules with a small isotope shift. This approach can be used for high purification of substances in the gas phase. To increase the productivity of the apparatus and for more efficient use of the laser radiation, it would be advisable to use pulsed slot nozzles.

The authors are grateful to E. A. Ryabov for valuable advice in the formulation of the problem, to V. N. Lokhman and A. G. Umnov for a helpful discussion, to M. V. Sotnikov and D. Yu. Petrov for assistance in conducting the experiments, and to A. P. Sviridov for providing the CF_3I sample.

This study was supported in part by the Russian Fund for Fundamental Research, Grant No. 96-02-16421-a.

[1] J. B. Anderson, in *Gasdynamics*, Vol. 4, Marcel Dekker, New York (1974), pp. 1–91.

[2] G. Scoles (ed.), *Atomic and Molecular Beam Methods*, Oxford University Press, New York–Oxford (1988).

[3] D. H. Levy, L. Wharton, and R. E. Smalley, in *Chemical and Biochemical Applications of Lasers*, Vol. 11, Academic Press, New York (1977), pp. 1–41.

[4] E. P. Velikhov, V. Yu. Baranov, V. S. Letokhov *et al.*, in *Pulsed CO_2 Lasers and Their Application for Isotope Separation* [in Russian], Nauka, Moscow (1983), p. 304.

[5] L. V. Gurvich, G. V. Karachentsev, V. N. Kondrat'ev *et al.*, in *Breaking Energies of Chemical Bonds. Ionization Potential and Electron Affinity* [in Russian], edited by V. N. Kondrat'ev, Nauka, Moscow (1974), p. 351.

[6] M. Drouin, M. Gauthier, R. Pilson, and P. Hackett, Chem. Phys. Lett. **60**, 16 (1978).

[7] M. Gauthier, P. A. Hackett, and C. Willis, Chem. Phys. **45**, 39 (1980).

[8] V. N. Bagratashvili, V. S. Doljikov, V. S. Letohov, E. A. Ryabov, Appl. Phys. **20**, 231 (1979).

[9] V. N. Bagratashvili, V. S. Dolzhikov, V. S. Letokhov *et al.*, Zh. Éksp. Teor. Fiz. **77**, 2238 (1979) [Sov. Phys. JETP **50**, 1075 (1979)].

[10] S. Bittenson and P. L. Houston, J. Chem. Phys. **67**, 4819 (1977).

[11] V. M. Apatin and G. N. Makarov, Kvantovaya Élektron. (Moscow) **10**, 1435 (1983) [Sov. J. Quantum Electron **13**, 932 (1983)].

[12] G. I. Abdushelishvili, O. N. Avotkin, V. N. Bagratashvili *et al.*, Kvantovaya élektron. (Moscow) **9**, 743 (1982) [Sov. J. Quantum Electron. **12**, 459 (1982)].

[13] W. Fuss, Spectrochim. Acta **38**, 829 (1982).

[14] G. I. Dimov, Prib. Tekh. Eksp. No. 5, pp. 168–171 (1968).

[15] W. R. Gentry and C. F. Giese, Rev. Sci. Instrum. **49**, 595 (1978).

[16] V. M. Apatin and G. N. Makarov, Zh. Éksp. Teor. Fiz. **84**, 15 (1983) [Sov. Phys. JETP **57**, 8 (1983)].

[17] V. M. Apatin, L. M. Dorozhkin, G. N. Makarov, G. M. Pleshkov, Appl. Phys. **29**, 273 (1982).

[18] G. N. Makarov, Zh. Éksp. Teor. Fiz. **108**, 404 (1995) [JETP **81**, 218 (1995)].

[19] D. G. Veĭblen, *Fluorine and Its Compounds*, edited by D. Saĭmong, IL, Moscow (1956), pp. 431–483.

Translated by Steve Torstveit

TECHNICAL PHYSICS VOLUME 44, NUMBER 1 JANUARY 1999

Interaction of a shock wave with a bubble screen

V. S. Surov

Chelyabinsk State University, 454136 Chelyabinsk, Russia

(Submitted June 30, 1997; resubmitted February 3, 1998)
Zh. Tekh. Fiz. **69**, 42–48 (January 1999)

The passage of a shock wave through a layer of bubbly liquid is considered. An exact solution is constructed in the case of a normal screen with a pressure pulse in the form a semi-infinite step. The results of numerical modeling by a modified Godunov method are presented for long and short pressure pulses. © *1999 American Institute of Physics.* [S1063-7842(99)00601-7]

INTRODUCTION

The capabilities of bubble screens for shielding from explosive loads, for example, are well known.[1–3] The interaction of shock waves (SWs) with bubble screens was discussed in Refs. 4–6. In those papers an isothermal model of the gas–liquid medium was used in the analysis. However, under conditions of hindered heat exchange between the gas and liquid, e.g., in the presence of a surfactant in the mixture or under conditions of elevated initial pressure, and in a number of other cases,[7] it is necessary to use an adiabatic model. Therefore, in the present paper calculations are performed for both models of the dispersion medium. We also note that in Ref. 4 and 5 the calculations were continued only up to the first shock wave transmitted behind the screen; reverberation was not considered. In Ref. 5 the shielding effect of an inverse bubble screen was attributed to the lowering of the amplitude of the first shock wave transmitted behind the screen. However, as is shown below, it is impossible to judge the real efficacy of such screens from the data. Complete information is given by numerical modeling based on the general equations of motion of the dispersion medium.

MODEL OF A BUBBLY LIQUID

In this study we used a one-velocity, one-pressure model of a heterogeneous mixture consisting of a compressible gaseous component and a liquid component. The small-scale pulsations of the bubbles were not taken into account. The mixture found at a given point in space was characterized by (in addition to the pressure and velocity) an average density ρ and a specific internal energy ε, which are determined from the relations

$$\rho=\rho_g+\rho_l=\alpha_g\rho_g^0+\alpha_l\rho_l^0,$$

$$\rho\varepsilon=\rho_g\varepsilon_g+\rho_l\varepsilon_l,\quad \alpha_g+\alpha_l=1, \tag{1}$$

where ρ_g and ρ_l are the reduced densities, $\alpha_g=\rho_g/\rho_g^0$ and $\alpha_l=\rho_l/\rho_l^0$ are the volume fractions, and ρ_g^0 and ρ_l^0 are the true densities. The indices g and l denote the parameters pertaining to the gaseous and liquid components.

Applying the conservation laws for mass, momentum, and energy to some individual selected volume of the dispersion medium, we obtain a system of integral equations from which, after a number of familiar manipulations, we obtain the differential equations of the mixture, which have the form of gasdynamic equations.

We shall assume that the thermodynamic parameters of the liquid obey the binomial equation of state

$$p=(\gamma_*-I)\rho_l^0\varepsilon_l+c_*^2(\rho_l^0-\rho_*), \tag{2}$$

where γ_*,ρ_*, and c_* are constants which determine its properties.

In particular, for water one has $\gamma_*=5.59$, $\rho_*=1000$ kg/m^3, and $c_*=1515$ m/s. The gas was assumed to be an ideal gas with an adiabatic index γ. In this case the equation of state of the mixture becomes

$$\frac{\rho_0}{\rho}=\alpha_{l0}\left(\frac{p_0+p_*}{p+p_*}\right)^{\frac{1}{\gamma_*}}+\alpha_{g0}\left(\frac{p_0}{p}\right)^{\frac{1}{\gamma}}, \tag{3}$$

where $p_*=\rho_*c_*^2/\gamma_*$.

The speed of sound is calculated from the expression

$$c^2=\frac{\rho_0}{\rho^2}\left[\frac{\alpha_{l0}}{\gamma_*(p+p_*)}\left(\frac{p_0+p_*}{p+p_*}\right)^{\frac{1}{\gamma_*}}+\frac{\alpha_{g0}}{\gamma p}\left(\frac{p_0}{p}\right)^{\frac{1}{\gamma}}\right]^{-1}, \tag{4}$$

and the corresponding Riemann invariants have the form

$$s=u-\sigma(p);\quad r=u+\sigma(p),$$

$$\sigma(p)=\int_{p_1}^{p}\frac{1}{\rho c}=\int_{p_1}^{p}\frac{dp}{\sqrt{\rho_0}}\times\sqrt{\frac{\alpha_{l0}}{\gamma_*(p+p_*)}\left(\frac{p_0+p_*}{p+p_*}\right)^{\frac{1}{\gamma_*}}+\frac{\alpha_{g0}}{\gamma p}\left(\frac{p_0}{p}\right)^{\frac{1}{\gamma}}}dp. \tag{5}$$

In a number of cases one can without loss of accuracy neglect the compressibility of the liquid fraction. In that case the formulas given above simplify to[8]

$$c=\frac{c_0\rho_0}{\rho}\left(\frac{\alpha_{g0}\rho}{\rho_0-\alpha_{l0}\rho}\right)^{\frac{\gamma+1}{2}}, \tag{6}$$

$$s(p)=u-\frac{2c(\rho_0-\alpha_{l0}\rho)}{(\gamma-I)\rho_0},$$

$$r(p)=u+\frac{2c(\rho_0-\alpha_{l0}\rho)}{(\gamma-I)\rho_0}, \tag{7}$$

where

$$c_0=\sqrt{\frac{p_0\gamma}{\alpha_{g0}\rho_0}}$$

is the speed of sound in the undisturbed medium.

If it is assumed that during the shock compression each component of the mixture is compressed along an individual shock adiabat,[9] the equation for the shock adiabat in the mixture becomes

$$\frac{\rho_0}{\rho}=\alpha_{l0}\frac{\chi_*(p+p_*)+p_0+p_*}{\chi_*(p_0+p_*)+p+p_*}+\alpha_{g0}\frac{\chi p+p_0}{\chi p_0+p}, \tag{8}$$

where

$$\chi=\frac{\gamma-1}{\gamma+1},\quad \chi_*=\frac{\gamma_*+1}{\gamma_*+1}.$$

The expression for the shock adiabat in the case of an incompressible liquid fraction is simply

$$\frac{\rho_0}{\rho}=\alpha_{l0}+\alpha_{g0}\frac{\chi p+p_0}{\chi p_0+p}. \tag{9}$$

The isothermal version of the model are obtained from the corresponding expressions of the adiabatic theory by formally setting $\gamma=1$. In that case it is assumed that the gas temperature in the bubbles behind the shock front remains constant and equal to the temperature of the liquid.

SELF-SIMILAR SOLUTION

Let us investigate the problem of the incidence of a ''long'' shock wave, with a profile in the form of a semi-infinite step with a known pressure p_s behind its front and propagating through a homogeneous medium at rest with a volume concentration of gas in the mixture α_{g0} and a pressure p_0, onto a gas–liquid screen of thickness L_0. The fraction of gas in the screen α_{g0}^{sc} is assumed to be higher than that in the medium, $\alpha_{g0}^{\text{sc}}>\alpha_{g0}$. In this case the problem has a self-similar solution. The parameters of the mixture behind the shock front, which are also identified by the subscript s, are calculated from the Rankine–Hugoniot relations together with the equation of state (8):

$$\rho_s=\frac{\rho_0}{\alpha_{l0}\lambda_*+\alpha_{g0}\lambda},\quad u_s=\sqrt{\frac{(p_s-p_0)(\rho_s-\rho_0)}{\rho_s\rho_0}},$$

$$D=\frac{\rho_s u_s}{\rho_s-\rho_0},\quad \alpha_{ls}=\frac{\alpha_{l0}\lambda_*}{\alpha_{g0}\lambda+\alpha_{l0}\lambda_*},$$

$$\lambda_*=\frac{\chi_*(p_s+p_*)+p_0+p_*}{\chi_*(p_0+p_*)+p_s+p_*},\quad \lambda=\frac{\chi p_0+p_s}{\chi p_s+p_0}.$$

Here D is the velocity of propagation of the shock wave, and u_s is the velocity of the mixture behind the shock front. Figure 1a shows a diagram of the shock-wave pattern arising in the interaction. Time is reckoned from the instant that the front of the incident shock wave touches the surface of the screen. Arising at that instant $t=0$ are a radiation rarefaction wave reflected from the layer and a shock wave SW_1 moving through the screen with a velocity D_1. Since the Riemann r-invariant is constant in the first wave, we obtain, taking Eq. (5) into account,

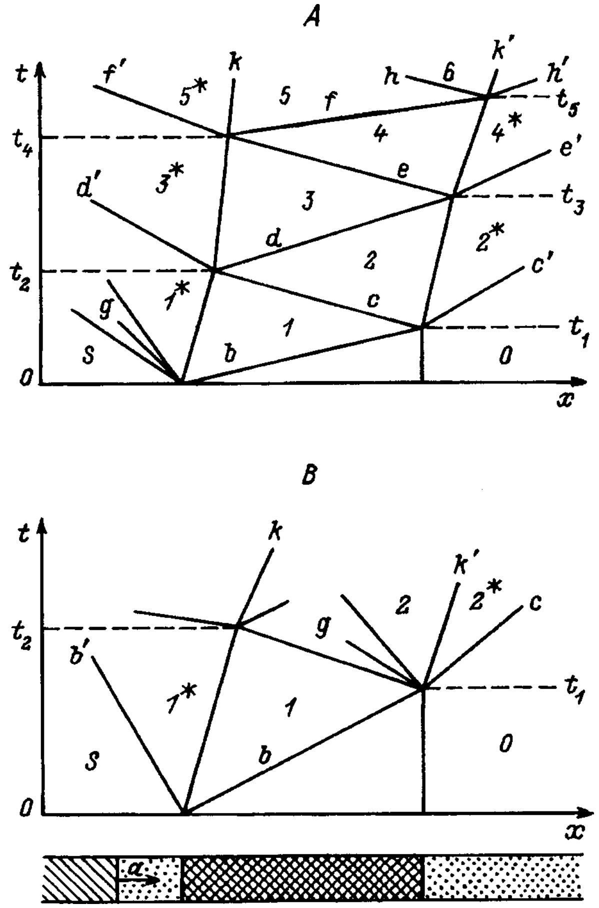

FIG. 1. Wave diagrams of the interaction of a shock wave with a layer of bubbly liquid for the normal (A) and inverse (B) screens: a – shock wave SW, b — SW_1, b' — SW_1^*, c — SW_2, c' — SW_2^*, d — SW_3, d' — SW_3^*, e — SW_4, e' — SW_4^*, f — SW_5, f' — $\text{SW}_5^* h$ — SW_6, h' — SW_6^*, g — rarefaction wave, k — contact discontinuity CD_1, k' — CD_2

$$u_s-u_1'=\int_{p_s}^{p_1'} f_1(p)\,dp, \tag{10}$$

where

$$f_1(p)=\frac{1}{\sqrt{\rho_s}}\left\{\frac{\alpha_{gs}}{\gamma p}\left(\frac{p_s}{p}\right)^{\frac{1}{\gamma}}+\frac{\alpha_{ls}}{\gamma_*(p+p_*)}\left(\frac{p_s+p_*}{p+p_*}\right)^{\frac{1}{\gamma_*}}\right\}^{1/2}.$$

The primes denote the parameters belonging to region *1** in Fig. 1a. The pressure in the incident shock wave and behind the centered rarefaction wave are related in accordance with (3) by the expression

$$\frac{\rho_s}{\rho_1'}=\alpha_{gs}\left(\frac{p_s}{p_1'}\right)^{\frac{1}{\gamma}}+\alpha_{ls}\left(\frac{p_s+p_*}{p_1'+p_*}\right)^{\frac{1}{\gamma_*}}. \tag{11}$$

The system of Rankine–Hugoniot relations for SW_1, which are expressions of the conservation laws for mass and momentum in passage through the wave front, have the form

$$(\rho_1^{\text{sc}}-\rho_0^{\text{sc}})D_1=\rho_1^{\text{sc}}u_1^{\text{sc}}, \tag{12}$$

$$\rho_1^{\text{sc}}u_1^{\text{sc}}D_1=p_1^{\text{sc}}+\rho_1^{\text{sc}}(u_1^{\text{sc}})^2-p_0,$$

$$\frac{\rho_0^{\text{sc}}}{\rho_1^{\text{sc}}}=\alpha_{g0}^{\text{sc}}\frac{p_0+\chi p_1^{\text{sc}}}{p_1^{\text{sc}}+\chi p_0}+\alpha_{l0}^{\text{sc}}\frac{p_0+p_*+\chi_*(p_1^{\text{sc}}+p_*)}{p_1^{\text{sc}}+p_*+\chi_*(p_0+p_*)}.$$

At the contact boundary between regions *1* and *1′* (Fig. 1A) the pressure and velocity do not change, so that the following matching conditions hold:

$$u_1^{\text{sc}}=u_1'=u_1,\quad p_1^{\text{sc}}=p_1'=p_1. \tag{13}$$

From relations (10)–(13) we obtain after a number of transformations an equation for calculating the pressure p_1 at the contact discontinuity:

$$u_s-\int_{p_s}^{p_1}f_1(p)dp=\left\{\frac{(p_1-p_0)}{\rho_0^{\text{sc}}}\left(1-\alpha_{g0}^{\text{sc}}\frac{\chi p_1+p_0}{\chi p_0+p_1}-\alpha_{l0}^{\text{sc}}\frac{p_0+p_*+\chi_*(p_1+p_*)}{p_1+p_*+\chi_*(p_0+p_*)}\right)\right\}^{1/2}. \tag{14}$$

The desired root of equation (14) was calculated numerically by the standard procedure for solving nonlinear equations. The integral on the left-hand side of Eq. (14) was also evaluated numerically. After the pressure p_1 is determined, the remaining parameters are expressed in explicit form using Eqs. (10)–(12).

At the time $t_1=L_0/D_1$ the shock wave SW_1 reaches the back surface of the screen, and in interacting with that surface forms a reflected wave SW_2 and a wave SW_2^* that penetrates behind the screen. For the reflected wave SW_2, which moves through the bubble screen at a velocity D_2, we have the following system of Rankine–Hugoniot equations relating the values of the parameters in regions *1* and *2* in Fig. 1A:

$$(\rho_2^{\text{sc}}-\rho_1^{\text{sc}})D_2=\rho_2^{\text{sc}}u_2^{\text{sc}}-\rho_1^{\text{sc}}u_1,$$

$$(\rho_2^{\text{sc}}u_2^{\text{sc}}-\rho_1^{\text{sc}}u_1)D_2=p_2^{\text{sc}}+\rho_2^{\text{sc}}(u_2^{\text{sc}})^2-p_1-\rho_1^{\text{sc}}(u_1)^2,$$

$$\frac{\rho_1^{\text{sc}}}{\rho_2^{\text{sc}}}=\alpha_{g1}^{\text{sc}}\frac{p_1+\chi p_2^{\text{sc}}}{p_2^{\text{sc}}+\chi p_1}+\alpha_{l1}^{\text{sc}}\frac{p_1+p_*+\chi_*(p_2^{\text{sc}}+p_*)}{p_2^{\text{sc}}+p_*+\chi_*(p_1+p_*)}. \tag{15}$$

For the penetrating wave SW_2^*, which separates regions *2** and *0*, we have the analogous system of equations

$$(\rho_1''-\rho_0)D_2^*=\rho_1''u_1'';\quad \rho_1''u_1''D_2^*=p_1''+\rho_1''(u_1'')^2-p_0,$$

$$\frac{\rho_0}{\rho_1''}=\alpha_{g0}\frac{p_0+\chi p_1''}{p_1''+\chi p_0}+\alpha_{l0}\frac{p_0+p_*+\chi_*(p_1''+p_*)}{p_1''+p_*+\chi_*(p_0+p_*)}. \tag{16}$$

The double primes denote the parameters pertaining to region *2**. In addition, it is necessary to take into account the continuity of the pressure and velocity at the contact boundary between regions *2* and *2**:

$$u_2^{\text{sc}}=u_1''=u_2,\quad p_2^{\text{sc}}=p_1''=p_2. \tag{17}$$

After some transformations of relations (15)–(17), we obtain an equation for calculating p_2:

$$u_1-\left\{\frac{(p_2-p_1)}{\rho_1^{\text{sc}}}\left(1-\alpha_{g1}^{\text{sc}}\frac{p_1+\chi p_2}{p_2+\chi p_1}-\alpha_{l1}^{\text{sc}}\frac{p_1+p_*+\chi_*(p_2+p_*)}{p_2+p_*+\chi_*(p_1+p_*)}\right)\right\}^{1/2}$$
$$=\left\{\frac{(p_2-p_0)}{\rho_0}\left(1-\alpha_{g0}\frac{p_0+\chi p_2}{p_2+\chi p_0}-\alpha_{l0}\frac{p_0+p_*+\chi_*(p_2+p_*)}{p_2+p_*+\chi_*(p_0+p_*)}\right)\right\}^{1/2}, \tag{18}$$

which is solved numerically. SW_2 reaches the contact boundary at the time

$$t_2=\frac{L_0}{D_1}\frac{(D_1+|D_2|)}{(u_1+|D_2|)}.$$

The subsequent reflections of the shock wave from the contact boundaries of the bubble screen (Fig. 1A) are calculated in an analogous way; these occur at the times

$$t_3=\frac{L_0-u_2t_1+(D_3-u_1)t_2}{D_3-u_2},$$

$$t_4=\frac{L_0-u_2T_1+(u_3-u_1)t_2+(u_2+|D_4|)t_3}{u_3+|D_4|},$$

$$t_5=\frac{L_0-u_2t_1+(u_3-u_1)t_2+(u_2-u_4)t_3+(D_5-u_3)t_4}{D_5-u_4},$$

$$t_6=\{u_5+|D_6|\}^{-1}\{L_0-u_2t_1+(u_3-u_1)t_2+(u_2-u_4)t_3+(u_5-u_3)t_4+(u_4+|D_6|)t_5\},\quad \ldots .$$

Reverberation of the waves in the screen is observed until the pressures in front of the screen and behind it have become equal.

Figure 2 shows the time dependence of the pressure near the contact boundary on the side of the incident shock wave and behind the screen for various concentrations of the gas in the liquid and in the screen, as obtained in the adiabatic ($\gamma=1.4$) and isothermal ($\gamma=1$) models. The pressure in the incident shock wave was $p_2=0.5$ MPa, and the initial pressure was $p_0=0.1$ MPa. The thickness of the screen was $L_0=1$ m. In Ref. 5 it is conjectured that 3–4 transits of the waves are sufficient for equalization of the pressure in front of and behind the screen. It follows from the present calculations that the number of transits of the waves depends importantly on the volume fraction of gas in the screen. In particular, we see from Fig. 2 that at a gas concentration of 10% it requires more than twenty transits of the waves in order for the pressures to become equal.

Figure 3 shows the time dependence of the concentrations of the gas in the screen near its boundaries on the side on which the shock wave is incident and on the opposite side, and also the time dependence of the thickness of the screen for one version of the calculation. It follows from an analysis of the data presented in Fig. 2 and 3 that the screen is compressed over time, the volume fraction of gas in it is lowered, and the pressure in the screen tends toward the value in the incident shock wave. Note that the degree of

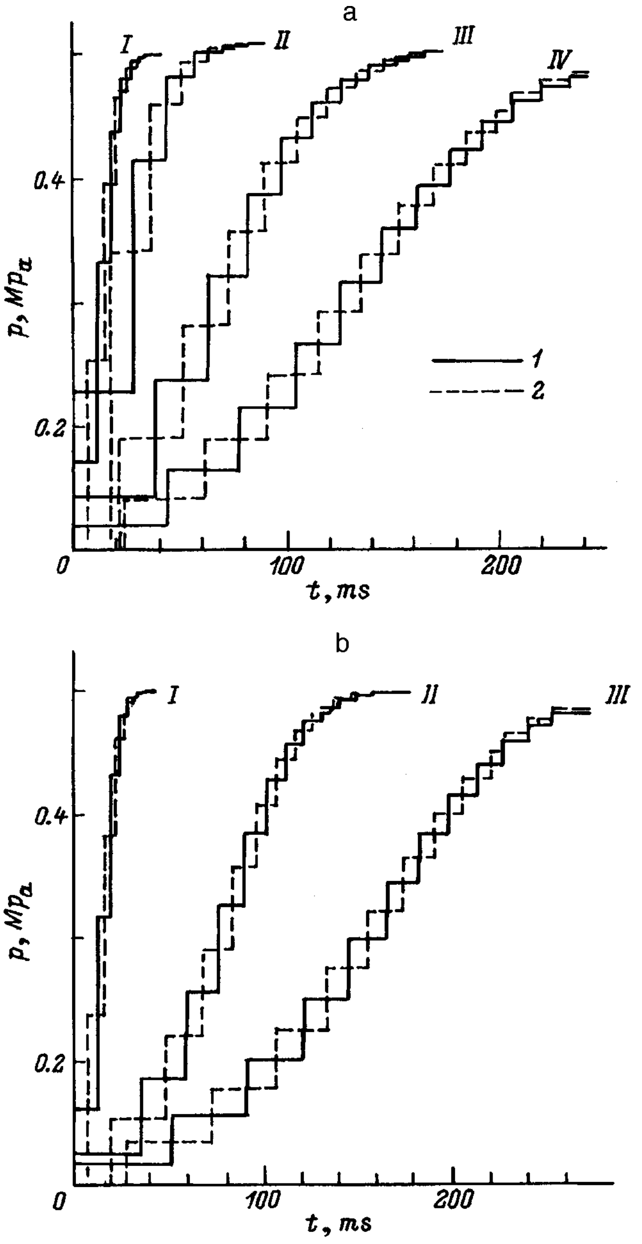

FIG. 2. Plots of $p(t)$ to the left of the layer (*1*) and behind the layer (*2*) for versions with and without a gas content in the screen, as calculated in the adiabatic model (a): $\alpha_{g0}^{\mathrm{sc}}=0.01$ (*I*), 0.1 (*II–IV*), $\alpha_{g0}=0$ (*I,IV*), 0.01 (*II*), $\alpha_{g0}=0.001$ (*III*), and in the isothermal model (b): $\alpha_{g0}^{\mathrm{sc}}=0.01$ (*I*), 0.05 (*II*), 0.1 (*III*); $\alpha_{g0}=0$.

compression of the screen according to the isothermal model is higher than in the adiabatic model. As p_s increases, the delay time provided by the bubble screen is rapidly diminished. For example, for a shock wave with a pressure behind the front $p_s=5$ MPa and propagating through a bubble-free liquid ($\alpha_{g0}=0$, $p_0=0.1$ MPa), for a bubble screen with a thickness of 1 m and a volume gas concentration $\alpha_{g0}^{\mathrm{sc}}=0.01$ (0.1) the delay time is only 2 (20) ms. The delay time is influenced substantially by the gas concentration outside the screen (Fig. 2), as was pointed out in Ref. 5. We note that the results of the calculation depend weakly on the type of gas used to form the bubble screen (bubble screens using hydrogen, helium, nitrogen, and air were considered).

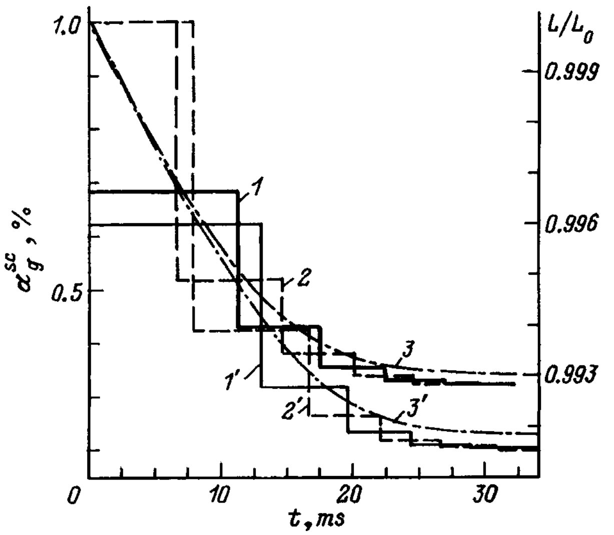

FIG. 3. Plots of $\alpha_{g0}^{\mathrm{sc}}(t)$ at the left (*1*) and right (*2*) boundaries of the screen and of the relative thickness of the layer (*3*) for the version with $\alpha_{g0}=0$, $\alpha_{g0}^{\mathrm{sc}}=0.01$, as obtained in the adiabatic model. The curves labeled with the primed numbers were obtained in the isothermal model.

It should be noted that the type of gas affects whether the isothermal or adiabatic model of the dispersion medium must be used.[7]

If the gas concentration in the screen is lower than in the surrounding two-phase medium, then the interaction regime changes (Fig. 1B). Such screens are called inverse screens in Ref. 5. For this case it is impossible to construct an analytical solution for an extended time interval in view of the non-self-similar nature of the problem of reflection of the rarefaction wave from the contact boundary of the screen. However, for a short incident shock wave the shielding effect of the screen can be estimated, following Ref. 5, from the ratio p_2/p_s, where p_2 is the pressure behind the front of the first shock wave after it has passed behind the screen. Figure 4 shows the calculated attenuation coefficients of the shock wave for different values of the volume fractions of the gas in the mixture and in the screen ($p_0=0.1$ MPa) as obtained in the adiabatic and isothermal models from relations analogous to those used in the preceding problem for a normal screen. We note that information about the real shielding effect of inverse bubble screens can be obtained only from numerical modeling or a physical experiment.

NUMERICAL CALCULATIONS

The foregoing analysis can be used to investigate the interaction of a pulse in the form of a semi-infinite step with a normal bubble screen. In the case of a finite pulse and for inverse screens it is necessary to integrate the general differential equations of the one-velocity model of a heterogeneous mixture. As was shown above, bubble screens are effective at comparatively high gas concentrations in the screen. In that case the compressibility of the carrier liquid can be neglected, and therefore in the calculations that follow we have used the equations

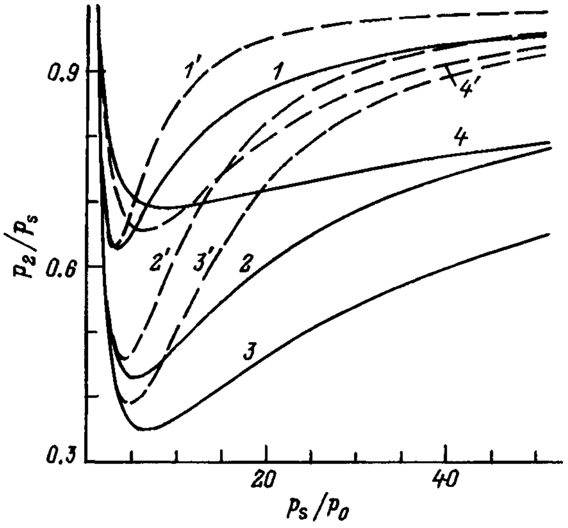

FIG. 4. Curves of the attenuation coefficient versus the intensity of the incident shock wave, calculated in the adiabatic model for the versions with $\alpha_{g0}=0.01$, 0.05, and 0.1 for $\alpha_{g0}^{\mathrm{sc}}=0$ (*1–3*); $\alpha_{g0}=0.1$ for $\alpha_{g0}^{\mathrm{sc}}=0.01$ (*4*). The curves labeled with the primed numbers were obtained in the isothermal model.

$$\frac{\partial\rho}{\partial t}+\frac{\partial\rho u}{\partial x}=0,\quad \frac{\partial\rho u}{\partial t}+\frac{\partial(p+\rho u^2)}{\partial x}=0, \tag{19}$$

$$\frac{\partial\rho e}{\partial t}+\frac{\partial(\rho e+p)u}{\partial x}=0;$$

$$\frac{\partial\alpha}{\partial t}-\frac{\partial(1-\alpha)u}{\partial x}=0. \tag{20}$$

Here $e=\varepsilon+0.5u^2$ is the total specific energy of the mixture and $\rho\varepsilon=\rho_g\varepsilon_g+\rho_l\varepsilon_l$ is its internal energy per unit volume. System (19) is an expression of the conservation laws for mass, momentum, and energy for the mixture as a whole, and Eq. (20) is the continuity equation for the incompressible fraction. The equation of state for the gas is

$$\varepsilon_g=\frac{p}{(\gamma-I)\rho_g^0}.$$

The specific internal energy of the liquid component was assumed constant ($\varepsilon_l=\mathrm{const}$). Thus the equation of state of the mixture takes the form

$$\varepsilon=\frac{\alpha p}{(\gamma-I)\rho}+\frac{\rho_l\varepsilon_l}{\rho}. \tag{21}$$

The system of equations (19)–(21) was integrated by a modified Godunov method.[10] As we know, the Godunov method uses as a mass operation the problem of the decay of an arbitrary discontinuity for a dispersion medium, the complete solution of which is given in Ref. 7 for the isothermal version of the model and in Ref. 8 for the adiabatic version.

Calculations were carried out for the problem of a shock wave of amplitude $p_s=2$ MPa propagating through a gas–liquid mixture with a volume concentration of the gas $\alpha_{g0}=0.01$ and a pressure $p_0=0.1$ MPa and incident on a bubble screen of thickness $L_0=0.4$ m and gas volume fraction $\alpha_{g0}^{\mathrm{sc}}=0.1$. The time was reckoned from the instant that the front of the incident shock wave touches the screen. Figure 5a–5c shows the calculated distributions of the pressure and concentration of the gas at characteristic points in time according to the adiabatic model. Figure 6a shows the $p(t)$ curves obtained in the calculation at points in front of the screen ($x=0.32$ m) and behind it ($x=1$ m) according to the adiabatic model ($\gamma=1.4$). The calculations according to the isothermal model gave similar results.

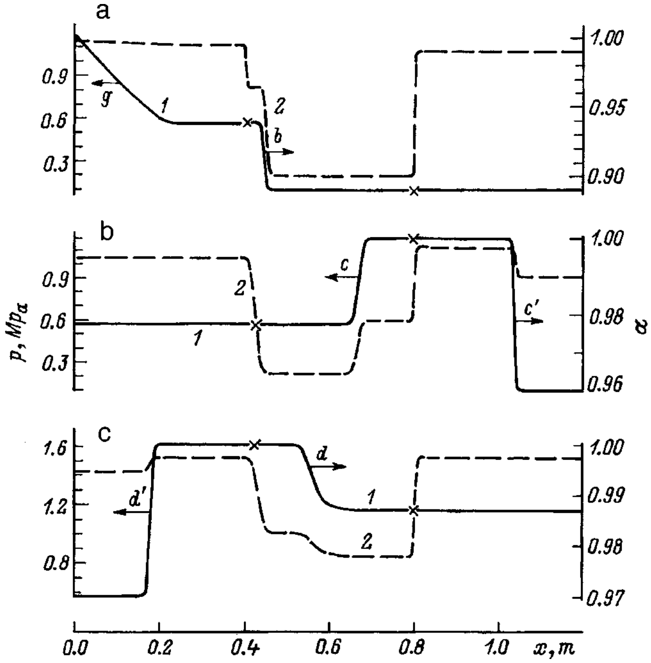

FIG. 5. Plots of $p(x)$ and $\alpha(x)$ (*1,2*) calculated at the times $t=0.55$, 5.2, and 6.7 ms (a–c) in the adiabatic model: the positions of the boundaries of the screen are indicated by crosses; g – rarefaction wave, b — SW_1, c — SW_2, c' — SW_2^*, d — SW_3, d' — SW_3^*.

After the shock wave interacts with the screen, the pressure in front of the screen falls on account of the rarefaction wave propagating to the left from the screen. The shock wave moves through the screen, reflecting off its walls, and at each reflection shock waves are emitted on different sides of the screen. After a certain time has passed, the pressure to the left and right of the screen equalizes, approaching the value of p_s in the incident shock wave, in agreement with the self-similar solution. We note that with each passage of the shock wave through the screen the gas concentration in the screen is lower, and therefore the subsequent crossing requires less time, so that the frequency with which the screen emits waves increases (Fig. 6), tending toward a limiting frequency $\omega_*\approx D/2L_0$, where D is the velocity of the shock wave incident on the screen.

For the inverse screen the geometric dimensions were chosen the same as for the normal screen, the intensity of the incident shock wave was $p_s=2$ MPa, and the fractional concentrations of gas inside and outside the screen were $\alpha_{g0}^{\mathrm{sc}}=0.01$ and $\alpha_{g0}=0.05$, respectively. The initial pressure was $p_0=0.1$ MPa. The corresponding curves of $p(t)$ in front of and behind the screen at the same points as for the normal screen are shown in Fig. 6b. Unlike the case for the normal screen, in front of the inverse screen a high-pressure zone is

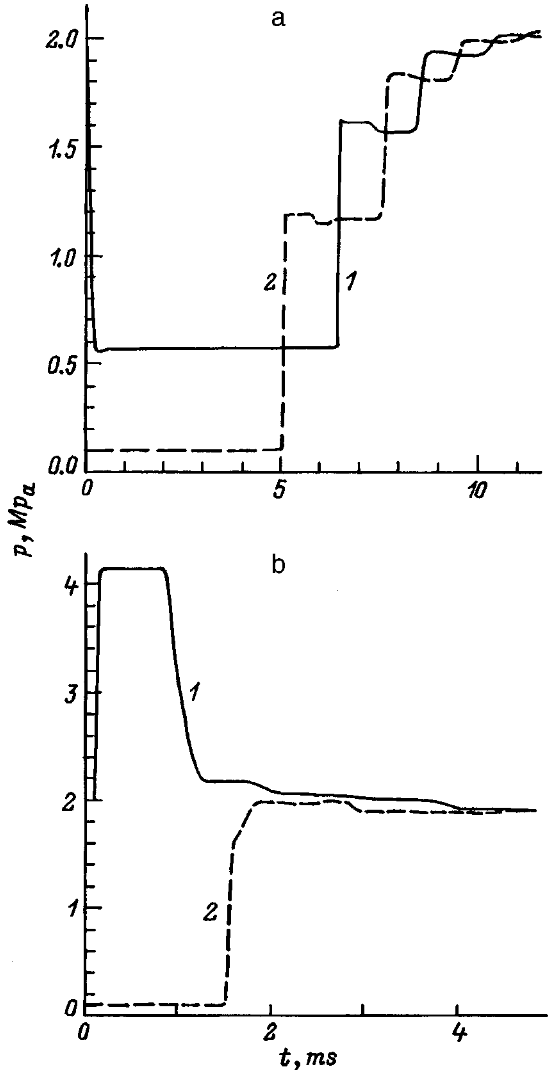

FIG. 6. Plots of $p(t)$ in front of (*1*) and behind (*2*) the screen for a normal screen (a) and an inverse screen (b) in the case of an extended pressure pulse.

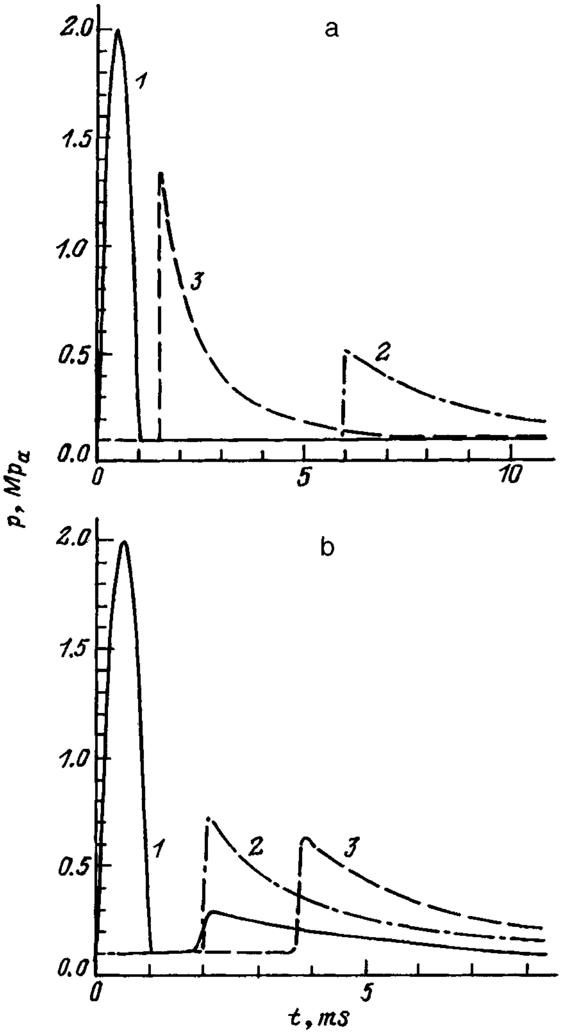

FIG. 7. Plots of $p(t)$ at the point of initiation (*1*) and behind the screen (*2*) for the normal (a) and inverse (b) screens in the case of a short pressure pulse, and also in the absence of the screen (*3*) at the same points as for curve *2*.

formed which becomes washed out over time on account of the periodic emission of rarefaction waves to the left from the screen. To the right the screen emits shock waves. As a result of multiple interactions the pressure in front of the screen and behind it approaches the level p_s of the pressure in the incident shock wave, as it does in the case of the normal screen. However, the time delay provided by the screen is shortened on account of the higher propagation velocity of the shock wave in the screen.

Let us discuss the interaction of short pressure pulses (solitons) with bubble screens. The pressure pulse is generated near the left-hand boundary of the calculation region $(x=0)$ and is specified in the form a positive phase of the sinusoid:

$$p(t)=p_0+p_m\sin(\pi t/t_0),\quad 0\leqslant t\leqslant t_0,$$

$$p(t)=p_0,\quad t>t_0. \tag{22}$$

Figure 7a and 7b shows the calculated data for a pressure pulse with parameters $p_0=0.1$ MPa, $p_m=1.9$ MPa, and $t_0=1$ ms, interacting with a normal screen $(\alpha_{go}^{\mathrm{sc}}=0.1$, $\alpha_{g0}=0.01)$ and with an inverted screen $(\alpha_{g0}^{\mathrm{sc}}=0.01$, $\alpha_{g0}=0.05)$. The calculations were carried out in the adiabatic model. It follows from the calculations that an originally sinusoidal pulse will rather rapidly take on a ''triangular'' profile (Fig. 7) on account of the ''gradient catastrophe.'' Here the compression wave (the right half of the sinusoid) is transformed into a shock wave in which the medium is driven in the direction of motion of the soliton. Behind it propagates a rarefaction wave which brakes the medium and behind which the pressure is restored to its undisturbed value. It follows from the data presented above that, together with the instantaneous lowering of the pulse amplitude one simultaneously observates a growth in the extent of the wave, so that the pulse ''spreads out'' over time. This is not due to the dissipative properties of the medium (the medium is ideal) but is due to the general properties of solitary waves.[11] We note that for the conditions under consideration, when one is investigating comparatively short time intervals, the presence of an artificial viscosity, which is inherent to the numerical scheme used, does not fundamentally influence the character of the dependences obtained. We also note that the reverberation effect is also observed in the investigated case of short waves, but is is expressed in a much weaker form than for the long waves.

Let us compare the calculations with experiment. The experiments of Ref. 3 investigated the effect of a bubble screen on the parameters of the refracted waves. A pressure pulse was generated by detonating an explosive charge above a free surface of water. The bubble screen was 0.2 m thick and had a gas volume fraction of 5.2%. The air bubbles were encased in a resin envelope and were restrained from floating up by a thin metal framework. The pressure in front of the screen was 6.7 MPa. In the screen and behind it the pressure was measured to be 1.7 and 2.6 MPa, respectively. In the calculations the pressure pulse was specified to have a sinusoidal dependence (22) with parameters $p_0 = 0.1$ MPa, $p_m = 7.7$ Mpa, and $t_0 = 0.33$ ms. The amplitude of the incident shock wave near the screen was 6.4 MPa. The values of the pressure in the screen and behind it were calculated in the adiabatic model as 2.0 and 2.58 MPa, which are close to the values obtained in the experiment. We note that in the given case it is necessary to use the adiabatic model of the bubbly liquid, since under the experimental conditions the heat transfer between the gas and liquid could be neglected.

Figure 8 shows the calculated curves and experimental[3] data for the coefficient of attenuation of the shock wave as a function of α_{g0}. It is seen from the figure that the isothermal model gives substantially lower values of the attenuation coefficient.

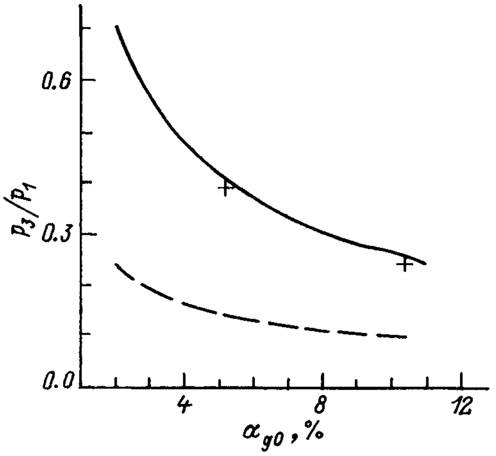

FIG. 8. Coefficient of attenuation of the shock wave by the screen as a function of α_{g0} for the adiabatic (solid curve) and isothermal (dashed curve) models and the experiment of Ref. 3 (crosses).

CONCLUSION

The calculations done in this study imply that the most efficacious bubble screens from the standpoint of shielding against shock waves are the normal kind, with a higher concentration of gas than in the surrounding two-phase medium. For long shock waves incident on the screen the shielding effect derives from a time delay which is due to the reverberation of the shock wave in the screen. For a short shock wave, in addition to the delay, there is also a lessening of the amplitude of the wave transmitted through the screen.

For the inverse screen, on the contrary, the pressure pulse enters the region behind the screen sooner (Fig. 7b). In addition, for short pressure pulses the amplitude of the refracted wave may not be lower than in the absence of the screen, even though the total energy of the refracted pulse is lowered as a result of the presence of a wave reflected from the screen.

The results of this study refine the data of Ref. 5, where conclusions as to the efficacy of protective screens were reached on the basis of an approximate analysis and were more qualitative in character.

[1] Ya. I. Tseĭtlin, R. A. Gil'manov, and V. G. Nilov, Vzryvnoe Delo, No. 82/39, pp. 264–272 (1980).
[2] A. A. Gubaĭdullin, A. I. Ivandaev, R. I. Nigmatulin *et al.*, Itogi Nauki Tekh. Ser. Mekh. Zhidk. Gazov (VINITI, Moscow) **17**, 160 (1982).
[3] E. I. Timofeev, B. E. Gel'fand, A. G. Gumerov *et al.*, Fiz. Goreniya Vzryva **21**, 98 (1985).
[4] B. R. Parkin, F. R. Gilmor, and G. A. Broud, in *Underwater and Underground Explosions* [in Russian], Mir, Moscow (1974), pp. 152–258.
[5] B. E. Gel'fand, S. A. Gubin, and E. I. Timofeev, Zh. Prikl. Mekh. Tekh. Fiz., No. 1, pp. 118–123 (1982).
[6] R. I. Nigmatulin, *Dynamics of Multiphase Media*, Part II [in Russian], Nauka, Moscow (1987), 360 pp.
[7] V. S. Surov, Zh. Tekh. Fiz. **68**(11), 12 (1998) [Tech. Phys. **43**, 1280 (1998)].
[8] V. S. Surov, Fiz. Goreniya Vzryva **33**, 143 (1997).
[9] Kh. A. Rakhmatulin, Prikl. Mat. Mekh. **33**, 598 (1969).
[10] V. S. Surov, Vestn. Chelyabinskogo Univ., No. 1, pp. 116–123 (1997).
[11] P. Bhatnagar, *Nonlinear Waves in One-Dimensional Dispersive Systems* [Clarendon Press, Oxford (1979); Mir, Moscow (1983), 136 pp.].

Translated by Steve Torstveit

TECHNICAL PHYSICS VOLUME 44, NUMBER 1 JANUARY 1999

Effect of electronegative impurities on the generation of ozone in air

Yu. N. Novoselov

Institute of Electrophysics, Urals Branch of the Russian Academy of Sciences, 620219 Ekaterinburg, Russia

V. V. Ryzhov and A. I. Suslov

Institute of high-Current Electronics, Siberian Branch of the Russian Academy of Sciences,
634055 Tomsk, Russia

(Submitted October 23, 1997)
Zh. Tekh. Fiz. **69**, 49–52 (January 1999)

A self-consistent numerical model is used to investigate the effect of electronegative impurities on the ozone yield in a dielectric barrier discharge with a pulsed voltage supply, and the range of impurity concentrations giving a substantial (two- or threefold) increase in the ozone yield is established. Sulfur hexafluoride is considered as a representative component having strong electronegative properties. It is shown that a tiny admixture $[SF_6]<0.1\%$ can have an appreciable effect on the characteristics of an ozonator. The calculations are compared with published experimental data and given an interpretation. © *1999 American Institute of Physics.* [S1063-7842(99)00701-1]

INTRODUCTION

Because of wide-ranging practical applications for ozonators, the physico-chemical principles of ozone synthesis have now been well studied both experimentally and theoretically.[1] However, the role of gaseous impurities, which can substantially affect the characteristics of an ozonator, has not been adequately investigated. Such impurities include gaseous pollutants, many of which have strong electronegative properties. At the present time there is much interest in the creation of devices in which the synthesis of ozone is combined with the removal of various toxic components from the air. At the same time, an ozone generator based on a dielectric barrier discharge is very sensitive to the composition of the mixture of gases in the discharge gap. In particular, this was noted in Ref. 2, where it was found that an admixture of $SF_6<0.1\%$ can sharply (by a factor of 2–3) increase the ozone yield per unit charge passed through the gap. The case considered in Ref. 2 can often arise in practice in the purification of air to remove halogen-containing impurities, which are harmful components of the effluents from various industrial processes. Thus the investigation of ozone synthesis processes remains a topical problem.

MODEL

The efficiency of ozone formation in air in the presence of an electronegative impurity was studied using a self-consistent numerical model for an ozonator operating in the single-pulse mode in dry air. The modeling was done for a gap with one dielectric electrode. The parameters of the gap were as follows: thickness of the dielectric 1 mm ($\varepsilon=4$), length of the air gap 2 mm, air temperature 293 K. Sulfur hexafluoride SF_6 was chosen as a representative component having pronounced electronegative properties. In the model it was assumed that the discharge channel is cylindrical, with a uniform distribution of particles over the volume. Such an approach is often encountered in the analysis of plasma-chemical processes in reactors based on barrier discharges.[1] In the calculation we used a set of 200 different reactions that occur in a plasma during and after the burning stage of the discharge and involve the participation of charged particles, excited molecules, atoms, and radicals. The rate constants of the elementary processes involving electrons were calculated on the basis of a numerical solution of the Boltzmann equation. A single-pulse mode was considered, when the ozone concentration is low and its synthesis is not influenced by processes involving the production of other components. In the calculations we used values for the rate constants of gas-phase reactions from Ref. 3 and 4 and the data of Ref. 5 and 6 on the cross sections for the interaction of electrons with molecular nitrogen and oxygen. The results of the modeling were compared with the experimental data.[1–3]

In the first stage of the modeling the results of the calculations were compared with the results of the known experimental papers on the synthesis of ozone in oxygen and in air. Such parameters as the amplitude of the current pulse, the energy characteristics, and the ozone yield were compared. The best agreement ($\pm 30\%$) was obtained for ozonators based on a barrier discharge with a pulsed voltage supply.[1] The discrepancy is apparently due to the fact that in all the calculations the shape of the supply voltage pulse was specified as square. The agreement of the calculation with the experimental results of Ref. 2, in which an ozone generator with a pulsed voltage supply was also used, turned out to be not as good.

Figure 1 shows an example of the calculation of the ozone yield in a self-sustaining discharge for pure air as a function of the energy deposition in the single-pulse mode. At large energy depositions there is a simultaneous increase in the expenditure on the synthesis of the O_3 molecule and an increase in the fraction of oxides of nitrogen. At low energy depositions and short durations of the discharge pulse the

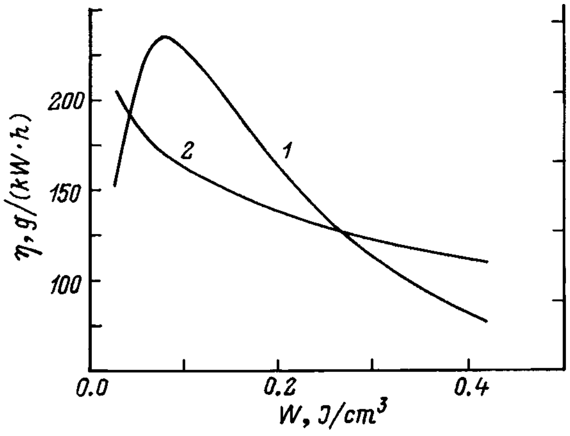

FIG. 1. Energy yield of ozone η (*1*) and the ratio $n=[O_3]/[NO_x]$ (*2*) as functions of the energy deposition W.

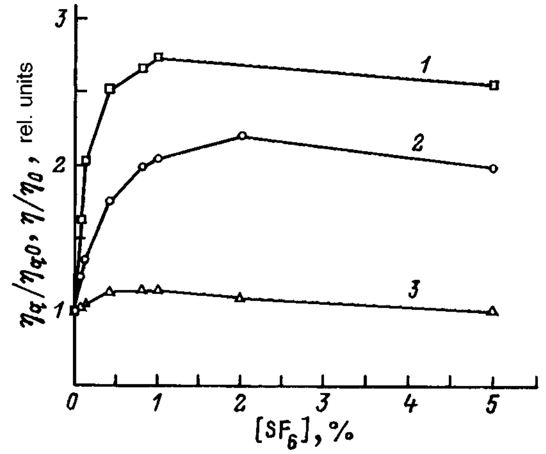

FIG. 2. Ozone yield as a function of SF_6 concentration in air: *1* — η_q/η_{q0} (the experimental data of Ref. 2); *2* — η_q/η_{q0}, *3* — η/η_0 (calculation).

efficiency of the reactor approaches the theoretical limit,[7] but here there is a noticeable increase in the production of NO_x.

At the same time, for pure oxygen the field in a self-sustaining discharge is close to optimal in terms of the parameter E/N (E is the electric field and N is the density of particles), and therefore the expenditure on the formation of O_3 is less dependent on the operating regime of the apparatus.

ELECTRONEGATIVE IMPURITIES IN AIR

The influence of an SF_6 impurity on the operation of an ozonator was investigated experimentally in Ref. 2, where a single-pulse mode of excitation of the of a barrier-discharge cell was used. Since only the current was recorded in the experiment, the O_3 yield per unit charge passed through the gap was determined from it. The change in the ozone concentration with time was measured from the absorption of ultraviolet radiation from a mercury lamp with wavelength $\lambda = 254$ nm. For single-pulse excitation a small concentration of atomic oxygen O was formed in the reactor; this atomic oxygen is then almost totally used up in the formation of O_3. Other components that might appear following repeated applications of voltage pulses to a medium and which are capable of influences the ozone formation process in the reactor are practically absent. This allows one to study experimentally the influence of various impurities on the kinetics of ozone synthesis. For example, in the given experiment it was found that a tiny concentration of SF_6 (less than 0.5%) can materially increase the O_3 yield per unit charge passed through the barrier-discharge cell in a single pulse.

Figure 2 shows, in relative units, one of the dependences (η_q/η_{q0}) that can be affected by an SF_{6ad} mixture. Here η_q is the ozone yield per unit charge, η is the energy efficiency of its formation, and η/η_0 is the energy efficiency in relative units (η_{q0} and η_0 are the O_3 yields in pure air). The data points in Fig. 2 correspond to the SF_6 concentrations chosen in the experiment. In the calculation one additional value was taken, for 2% SF_6. It should be noted that the ratio η_q/η_{q0} changes more sharply in the experiment than in the calculation. A probable reason for this is the difference in the shape of the supply voltage pulse. The ozone yield η_{q0} in the experiment is larger than that corresponding to the case of a sinusoidal supply voltage of the discharge cell.

In addition, as we see from Fig. 2, the calculated energy efficiency varies less substantially than in the experiment. These two features can be explained by Fig. 3, which shows the charge Q that has passed through the cell, the energy deposition W, the ozone concentration $[O_3]$, and the parameter E/N as functions of the SF_6 content. We see that at first there is a sharp decrease in Q on account of a decrease in current (Fig. 4); the ratio of its decrease in relative units is considerably higher than the rate of decrease of the energy deposition. The ozone concentration at the output initially varies little (this is due to an increase in the field in the discharge channel and an increase in the efficiency of O_3 generation). As E/N approaches the optimum value for air,[8] the further growth of η_q slows down, and the ozone concentration begins to fall off. When the SF_6 concentration is increased above 1% the value of η_q even decreases somewhat. The authors of Ref. 2 attribute this to quenching by the SF_6 molecule of the excited levels of nitrogen, which actively participate in the oxygen dissociation reactions. A calculation shows (Fig. 5) that SF_6 does indeed lower the efficiency

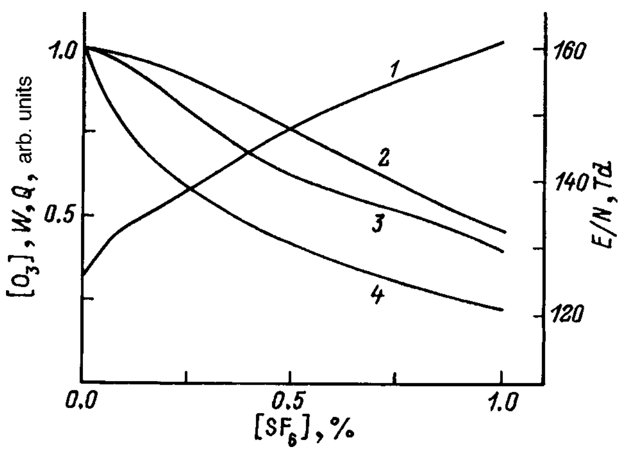

FIG. 3. The parameter E/N (*1*), ozone concentration (*2*), energy deposition W (*3*), and charge Q passed through the discharge gap (*4*) as functions of the SF_6 concentration in air.

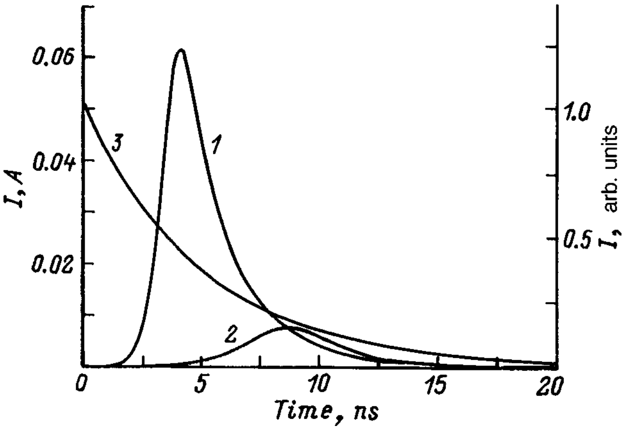

FIG. 4. Lsteady-state of the current I of a microdischarge in air (*1*) and in a mixture of air with 1% SF_6 (*2*) and the relative decay of the current at a large SF_6 concentration (*3*).

of O_3 generation to a large extent through the quenching of electronically excited states, but this process begins to be manifested in the kinetics much earlier, when the SF_6 concentration has reached only a fraction of one percent. This process is what curbs the growth of the energy yield of ozone with increasing SF_6 concentration (Fig. 3), although the yield continues to grow in the gap.

In the calculation, as in the experiment, a decline in η_q is observed, but its cause does not lie in the kinetics. When the SF_6 concentration has increased significantly the breakdown field for the gas mixture begins to approach the field existing in the gap. The character of the current flow begins to change in a qualitative way — it begins to fall off soon after the microdischarge is formed. In this situation the oxygen radicals are formed mainly against the background of a falling current, the decline of which is governed by the rate of attachment of electrons to the SF_6 molecule. In other words, the reaction operates mainly under conditions of a decaying plasma. In such a model it becomes difficult to interpret what is really going on in the plasma. For a complete foundation it is necessary to take into account the spatial distribution of particles in the gap.

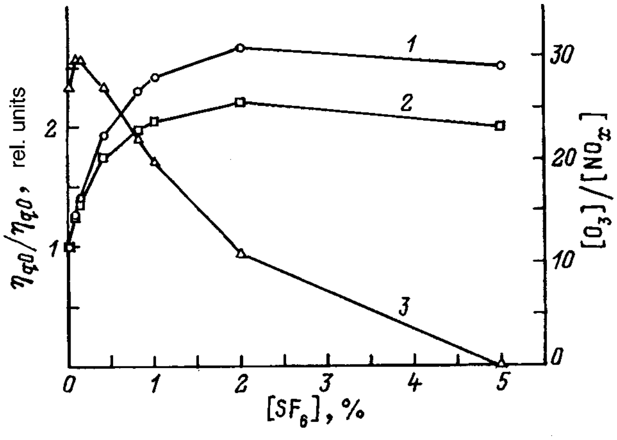

FIG. 5. Yields of ozone and of oxides of nitrogen as functions of the SF_6 concentration in air: *1* — values of η_q/η_{q0} calculated without taking the quenching of nitrogen levels into account, *2* — the same, with the quenching of nitrogen levels taken into account, *3* — the ratio of the ozone concentration to the concentration of oxides of nitrogen in the plasma.

Figure 3 shows the dependence of E/N on the SF_6 concentration in air, corresponding to the field in the channel when the discharge current has reached its maximum. From this one can judge whether the ozone yield is affected by the quenching of triplet states of nitrogen by this molecule. Although the field nearly reaches the optimum value for the formation of oxygen radicals in air, a falloff of the efficiency is actually observed. As is seen in Fig. 5, the O_3 yield increases somewhat if quenching processes are neglected.

Besides the influence on the efficiency, electronegative impurities can lead to a relative increase in the concentration of oxides of nitrogen. Figure 5 shows how the total concentration of NO_x varies in relation to the ozone concentration. Here the increase in the NO_x concentration is due to the growth of E/N and to the increase in the rate of formation of nitrogen radicals. The fraction of excited states of nitrogen falls off as the SF_6 concentration increases, and, as a result, the yield of oxygen radicals decreases while the rate of dissociation of N_2 remains almost unchanged. Therefore, owing to quenching processes the relative content of oxides of nitrogen will be higher than in pure air under the same conditions.

Thus one can distinguish roughly three characteristic intervals of impurity concentrations, which differ in the effect on the discharge characteristics. As the SF_6 concentration varies in the interval 0.05–0.5% there is a simultaneous increase in the energy efficiency of O_3 production and in the current through the gap. The efficiency in terms of current increases much more rapidly because of the strong decrease in the current, but in both cases the effect is achieved through optimization of the excitation of triplet states of nitrogen and of the direct dissociation of oxygen. The increase in the energy efficiency, however, is less than 20%. As the impurity concentration increases further to 1–2% the quenching of excited states of nitrogen becomes important. The energy efficiency of the reactor begins to decline, while the efficiency in terms of current continues to grow for the reasons stated above. When the SF_6 concentration is increased above 2% the breakdown field for the impurity becomes comparable to the field applied to the gap. It becomes difficult to form a discharge, and the efficiency in terms of current also begins to fall.

As to the range of values of the electric field applied to the gap for which the ozonator operates with good efficiency under the conditions considered, a calculation shows that it can remain at approximately the same values used in ordinary ozonators that use pure air as the initial gas (i.e., ~ 250 Td).

It should be noted that in this paper we have not considered questions of ozone production and impurity destruction in a mode using many discharge pulses. It is clear that in that case the components of the mixture and the discharge parameter will be different.

CONCLUSIONS

We have investigated the characteristics of the plasma of a dielectric barrier discharge in air containing electronegative impurities. For the single-pulse mode of excitation of the discharge we were able to establish the following.

1. As the concentration of the electronegative admixture (SF_6) varies in the interval 0.05–1.00% there is some increase in the energy efficiency of ozone formation (of the order of 15% for an SF_6 admixture of ~0.5%). This is accompanied by a severalfold decrease in the energy deposition, mainly because of a sharp decrease in the current density. This must be taken into account in the design of ozonators utilizing a self-sustaining discharge in the presence of electronegative impurities.

2. The ozone yield in terms of current increases by a factor of two or three in this interval of SF_6 concentrations, while the current itself falls off by more than an order of magnitude. At SF_6 concentrations above 1% the breakdown of the gap becomes hindered, and it is necessary to completely revise the operating mode of the ozonator.

3. Quenching of triplet states of nitrogen by the SF_6 molecule begins to have a noticeable effect on the energy yield of ozone when the concentration of this admixture reaches $\sim 10^{17}\,\mathrm{cm}^{-3}$.

4. Increasing the SF_6 concentration leads to a relative increase in the yield of NO_x in comparison with the yield of ozone, and the yield of NO_x is higher than when pure air is used.

[1] B. Eliasson and U. Kogelschatz, IEEE Trans. Plasma Sci. **PS-19**, 309 (1991).

[2] S. Okazaki, H. Niva, H. Sugimitsu *et al.*, *Proceedings of the International Symposium on High Pressure Low Temperature Plasma Chemistry*, Czechoslovakia (1996), pp. 26–30.

[3] V. G. Samoĭlovich, V. I. Gibalov, and K. V. Kozlov, *Physical Chemistry of the Barrier Discharge* [in Russian], Izd. Mosk. Gos. Univ., Moscow (1989), 176 pp.

[4] I. A. Kossyĭ *et al.*, Tr. IOF RAN **47**, 37 (1994).

[5] N. L. Aleksandrov *et al.*, Teplofiz. Vys. Temp. **19**, 22 (1981).

[6] Yu. S. Sedunov (ed.), *Atmosphere. A Handbook* [in Russian], Gidrometeoizdat, Leningrad (1991), 512 pp.

[7] B. Eliasson and U. Kogelschatz, in *Proceedings of the Eighth International Symposium on Plasma Chemistry*, Tokyo (1987), pp. 736–741.

[8] D. Braun, U. Köchler, and G. Pietsch, J. Phys. D **24**, 564 (1991).

Translated by Steve Torstveit

Electron clouds around charged particulates

A. N. Tkachev and S. I. Yakovlenko

Institute of General Physics, Russian Academy of Sciences, 117942 Moscow, Russia

(Submitted October 13, 1997)
Zh. Tekh. Fiz. **69**, 53–57 (January 1999)

Poisson's equation is used to derive an expression for the characteristics of the Debye electron cloud around a multiply charged particle. It is shown that the limiting dimension of the Debye cloud (for an infinitely large charge of the particles) varies from 0.7 to 2.2 Debye radii, depending on the geometry of the problem. A first-principles modeling of the dynamics of many electrons moving around an immobile charged center is carried out. It is shown that a metastable state which relaxes at least one thousand times more slowly than would follow from the kinetic theory is established. Calculations show that in this metastable state (which is far from thermodynamic equilibrium) there is a detailed balance of electron transitions from a state with one energy to another. The distribution of electrons over kinetic energy has a Maxwellian form, while the distribution over total energy is radically different from the Boltzmann distribution and is close to that which was established previously by the authors for a plasma of singly charged ions. The potential distribution around the immobile charge in the metastable plasma is obtained. © *1999 American Institute of Physics.* [S1063-7842(99)00801-6]

INTRODUCTION

Research on plasmas in which an important role is played by charged particles of micron size (so-called dusty plasmas) is of interest from both the fundamental and applied standpoints.[1,2] In view of the large charge that a particulate can take on, such a plasma becomes substantially nonideal even at a comparatively low density of particles. A nonideal plasma of particulates, unlike an ordinary nonideal plasma, relaxes rather slowly; it can be obtained and maintained in a nonequilibrium state by comparatively simple means (e.g., with a gas burner or rf discharge). It is then possible to form dusty-plasma crystals, drops, and clouds. The study of such a plasma is of fundamental interest, since there is still no adequate theory of the nonideal state.

A dusty plasma is often obtained in technological processes in the production of microelectronic circuits. Its properties must be known in connection with applications, in particular, to reduce the number of defective products.

In this paper we discuss certain questions relating to the formation of electron clouds around a particle of large charge. We will use both analytical methods and first-principles many-particle-dynamics (MPD) simulations.[3–5] The following treatment is limited to the simple case in which there are no other positively charged ions besides the particulates. In making concrete estimates we will often be guided by the plasma parameters obtained in the experiments of Refs. 6.

DEBYE ATOM

1) One-dimensional models. A charge surrounded by a cloud of electrons having a Boltzmann distribution will be referred to below as a Debye atom, in distinction to a Thomas–Fermi atom, in which the electrons are degenerate. The potential φ and the electric field $\mathbf{E}$ in a Debye atom are described by a Boltzmann distribution and Poisson's equation:

$$N_e = N_{e0}\exp(\varphi), \quad \mathrm{div}(\mathbf{E}) = -\exp(\varphi),$$
$$\mathbf{E} = -\mathrm{grad}(\varphi). \tag{1}$$

In this section we will use dimensionless equations: lengths are measured in units of the Debye radius $r_D = (T_e/4\pi e^2 N_{e0})^{1/2}$, where N_{e0} is the free electron density, e is the charge of the electron, and T_e is the electron temperature; the potential is measured in units of T_e/e, and the electric field in units of T_e/er_D.

In the one-dimensional (i.e., planar, cylindrically symmetric, or spherically symmetric) case Eq. (1) takes the form

$$\frac{1}{r^k}\frac{d}{dr}\left(r^k\frac{d}{dr}\varphi\right) = \exp(\varphi), \quad E = \frac{d}{dr}\varphi,$$
$$\varphi(a_0) = 0, \quad E(a_0) = 0, \tag{2}$$

where $k = 0, 1, 2$ for the planar, cylindrically symmetric, and spherically symmetric cases, respectively.

The boundary conditions are chosen so that the electric field and potential go to zero at the boundary of the atom $r = a_0$. Actually, the electric field E_0 or potential φ_0 is specified at the surface of the particulate. The value of a_0 is determined in terms of that specified value on the basis of a solution of equations (2). For the experimental conditions of Ref. 6, for example, we set $N_{e0} = 2.5\times 10^{10}$ cm^{-3} and $T_e = 0.146\,\mathrm{eV} = 1700$ K. Accordingly, $r_D = 0.002$ cm, $T_e/e = 0.146$ V, and $T_e/er_D = 82$ V/cm. At an average particle radius $r_0 = 0.4\,\mu$m ($r_0/r_D = 0.02$) and charge $Z = 500$, we have for the electric field at the surface of the particle $E_0 \equiv Ze/r_0^2 = 4.5\times 10^4$ V/cm ($E_0 e r_D/T_e = 550$). We note that the value $E_0 r_0 = 1.8$ V ($E_0 r_0 e/T_e = 12.3$) is generally not equal to the potential φ_0 at the surface of the particle; the relation between E_0 and ρ_0 is determined from the solution of equations (2).

2) Planar model. A planar geometry is realized in cases where the radius of the particle is much greater than the Debye radius. This model is of special interest in that the results are obtained in explicit analytical form.

Let the coordinate $x=r$ be directed rightward, perpendicular to the charged plane, and measured from it. Since for $k=0$ Eq. (2) does not contain explicit dependence on the coordinate, one can make a change of variables to reduce the second-order equation for the potential as a function of the coordinate to a first-order equation for the field as a function of the potential (compare with the problem of the screening of a planar charge by a plasma).[7] Integrating this equation and then the equation for the potential, we obtain explicit expressions for the potential and field as functions of the coordinate:

$$\varphi(x)=\ln\left\{1+\left[\tan\left(\frac{a_0-x}{\sqrt{2}}\right)\right]^2\right\},$$

$$E(\varphi)=\sqrt{2(\exp(\varphi)-1)}. \tag{3}$$

Here $\varphi_0=\ln(E_0^2/2+1)$ and $a_0=\sqrt{2}\arctan\sqrt{\exp(\varphi_0)-1}$ are, respectively, the potential on the plane and the coordinate of the boundary of the atom. For example, under the experimental conditions of Ref. 6, with $E_0=552.2$, one would have $\varphi_0=11.94$ and $a_0=2.21$. We note, however, that in Ref. 6 the radius of the particle was less than the Debye radius, and the planar geometry gives a somewhat overstated value of a_0 (see below).

3) Spherically and cylindrical symmetric models. As a rule the spherical case is realized in experiments. The cylindrical problem is of interest in connection with the possibility of studying the interaction of heated fine wires.

The dependence of the electric field and potential on the coordinate r is determined by numerical solution of equations (2). As we have said, the boundary condition is specified by the radius r_0 and charge Z of the particle. For example, under the experimental conditions of Ref. 6, with $E_0=552.2$ and $r_0=0.022$, one would have $\varphi_0=10.18$ and $a_0=0.8556$ in the spherically symmetric case.

Figure 1 illustrates how the boundary value of the potential φ_0 and the size a_0 of the Debye cloud depend on the electric field E_0 at the surface of the particulate, according to the numerical solutions. We see that the cloud grows in size as the charge $Z\sim E_0$ on the particle increases, but that this growth, as in the planar case, slows sharply near the limiting size. The limiting size increases somewhat with increasing radius of the particle, but the quantity a_0-r_0 is less than the limiting size of the planar Debye cloud $\pi/2^{1/2}=2.221$.

At a sufficiently large charge of the particulate the potential φ_0 on the latter is independent of its radius and is proportional to the logarithm of its charge for any geometry of the problem. At large Z the electrons are mainly concentrated near the surface of the particulate, and therefore the relation between the potential and electric field for $E_0\gg 1$ corresponds to the planar case (3). Similarly, at small E_0 the size of the atom and the potential on the surface of the particle has a linear dependence on E_0 for any geometry.

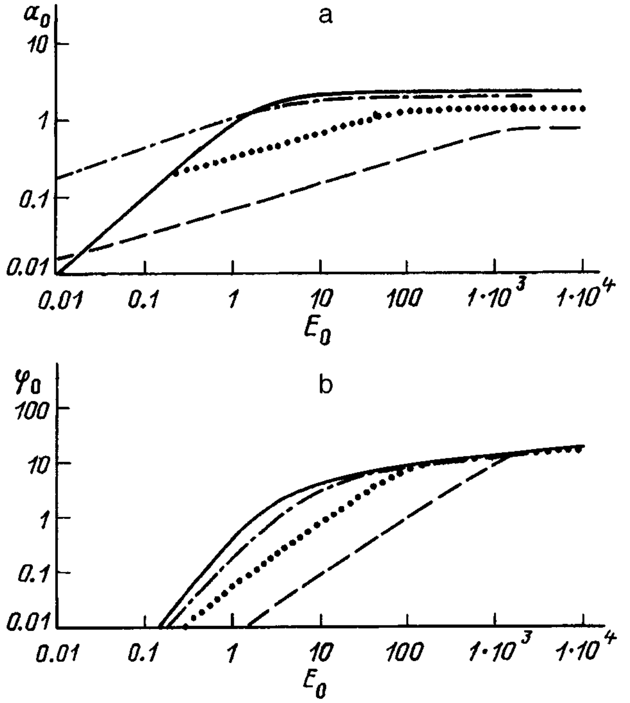

FIG. 1. The size of the Debye cloud a_0 (a) and the value of the potential φ_0 (b) on the surface of a particulate as functions of the electric field E_0 at the surface of the particulate (dimensionless quantities): the solid curves are for the planar geometry, the dot-and-dash curves for the cylindrical geometry ($r_0=0.1$, limiting value $a_0=1.95$), the dotted curves for the spherical geometry with ($r_0=0.1$, $a_0=1.34$), and the dashed curves for a spherical geometry with $r_0=0.01$, $a_0=0.746$.

We note that there is a certain inconsistency in the Debye atom model for considering a charged particle in an infinite volume. Beyond the boundary of the cloud $r>a_0$ the potential and field are equal to zero but the electron density is nonzero, so that the condition of quasineutrality is violated when this model is used to treat an infinite volume. This fact can be ignored when one is considering the field inside the atom, $r<a_0$, provided that the electron density is much larger than at the periphery. In the MPD simulation the electron gas is bounded by the dimensions of the ''box'' considered.

FIRST-PRINCIPLES SIMULATION OF A MULTIPLY CHARGED ELECTRON CLOUD

1) Metastable state. For investigating a plasma of particulates it is natural to use the methods of first-principles simulation as summarized in Refs. 3–5. A numerical solution of Newton's equations for n electrons placed into a cube of side a was considered. It was assumed that the walls of the cube reflect electrons specularly. A single infinitely heavy particle of charge $Z=n=256$ (it was assumed that it is a permeable charged sphere of radius $r_0=0.01a/n^{1/3}=2.1\times10^{-7}$ cm) was placed at the center of the cube. The initial distribution of particles was assumed Maxwellian with a temperature $T_0=0.03$ eV. Time was measured in units of the Langmuir period $T_L=2\pi/(4\pi e^2N_e/m_e)^{1/2}$.

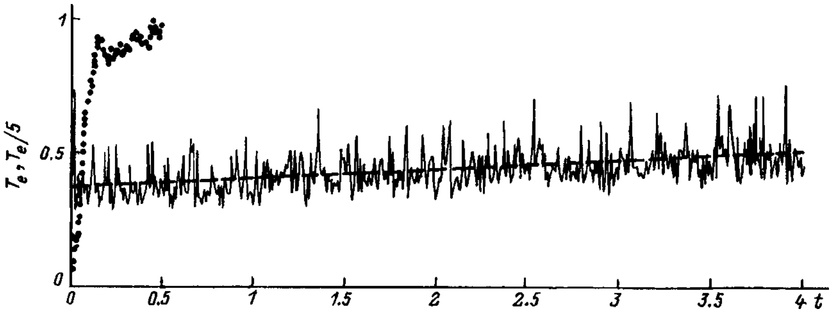

FIG. 2. Electron temperature (in eV) as a function of time (in units of the Langmuir period). The solid curve is for the ordinary calculation, the dotted curve for a calculation with permutation of the velocities of different electrons across intervals $t_f = 0.01$ (for this curve the temperature scale has been expanded $5\times$), and the dashed line is $0.3662 + 0.0344 \cdot t$.

As before,[3–5] the calculations showed that a metastable state is established over a time ~ 0.1. The electrons in this state have a Maxwellian distribution with a temperature somewhat above the initial temperature T_0. The metastable state is characterized by a nearly constant temperature $T_e = 0.42$ eV (Fig. 2), which is defined here as two-thirds of the kinetic energy. The electron distribution in the region of negative total energies is not ascending, as would be the case for a Boltzmann distribution, but descending (Fig. 3a). For a plasma of singly charged particles we had previously found an expression that gives a good description of the results of all the numerical calculations (the microfield distribution).[3–5]

For a demonstration of the metastability of the steady state that is reached we calculated the matrix $W(t,\varepsilon,\varepsilon')$, which gives the mean number of transitions from the energy point ε to the energy point ε' in time interval t. The calculations showed that it is symmetric in the steady state (Fig. 3b). In other words, in this state (which is far from thermodynamic equilibrium) there is a detailed balance of transitions. This fact, together with the fact that the relaxation processes are strongly frozen (see below) allows us to regard this steady state as metastable. The presence of a metastable state cannot be explained by the assumption that the efficiency of energy transfer in collisions of the electrons is for some reason much lower than would be expected from kinetic theory. Transitions from one energy interval to another occur rather frequently. However, ''downward'' transitions in energy are compensated not by subsequent ''downward'' transitions, as would be expected from the kinetic theory of recombination, but by inverse, ''upward'' transitions (see Ref. 5 for a more detailed discussion of this question).

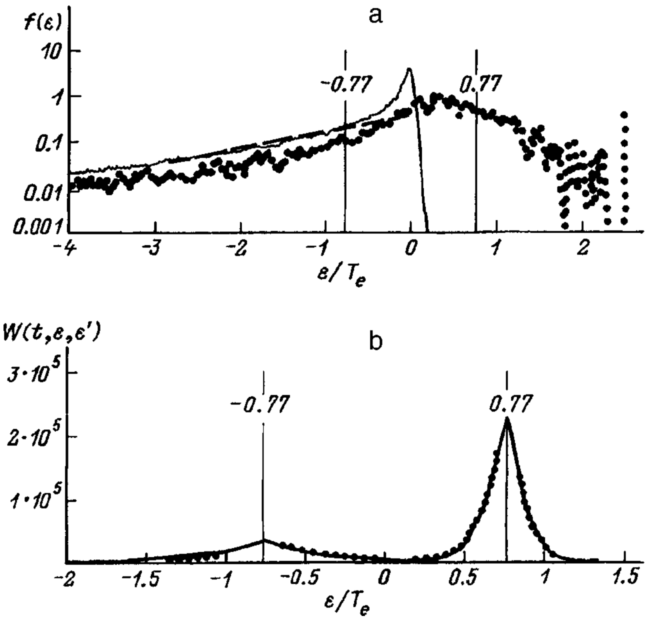

FIG. 3. Distribution functions (a) and the numbers of direct and inverse transitions (b) as functions of energy. a: The solid curve is the distribution of the electrons over potential energy, the dotted curve is their distribution over total energy, and the dashed curve is the exponential function $C\exp(0.23x)$, which approximates the decay of the distribution over potential energy. b: The number of direct transitions $\varepsilon_1 \to \varepsilon$, $\varepsilon_2 \to \varepsilon$ (solid curves) and inverse transitions $\varepsilon \to \varepsilon_1$, $\varepsilon \to \varepsilon_2$ as a function of energy; the points $\varepsilon_1 = -0.77T_e$ and $\varepsilon_2 = 0.77T_e$ are indicated by vertical lines; the transitions were considered over an interval $\Delta t = 0.5$ and were averaged over the entire time of the calculation.

When a sufficiently strong stochastic signal acts on a dynamical system, relaxation toward thermodynamic equilibrium occurs.[3–5] For example, when the velocities of different electrons are permuted (exchanged) across time intervals $t_f \ll 1$, an intense recombinational heating of the free electrons occurs (Fig. 2). This, in particular, demonstrates that the metastable state, in spite of the detailed balance of transitions, is not a state of thermodynamic equilibrium. In particular, its existence cannot account for the shift of thermodynamic equilibrium to higher ionization on account of elastic collisions of the electrons with the walls, contrary to the opinion expressed in Refs. 8 and 9 (see Refs. 5, 10, and 11 for a critique of Refs. 8 and 9).

2) On the degree of slowing of the relaxation. The calculated time for the evolution of the system is much greater than the recombination time determined by the kinetic theory. However, the recombination relaxation is almost imperceptible. Let us discuss this in more detail. According to the kinetic theory, the time required for a change in the electron density through ternary recombination is given by the expression $\tau_{\mathrm{rec}} = 0.57\gamma^{9/2}/\Lambda(\gamma)Z^3$. Here $\gamma = (2e^2N_2)^{1/3}/T_e$ is a parameter characterizing the degree of ideality of the plasma; as above, time is measured in units of T_L;

$$\Lambda(\gamma) = \begin{cases} \dfrac{1}{2}\ln\left(1 + \dfrac{9}{4\pi\gamma^3}\right), & \gamma < 0.2373 \\ 2, & \gamma \geqslant 0.2373 \end{cases}$$

is the Coulomb logarithm (the expression used for the Coulomb logarithm takes into account the results of the MPD simulation for values $\gamma > 0.24$).[12]

For ternary recombination a heating of the electrons occurs, and the rate of recombinational heating is determined by the characteristic time $\tau_{T_e}=\tau_{\mathrm{rec}}/(1+b)$, where $b=\varepsilon^*/T_e(0)$, with ε^* being the energy released per recombination event (see Refs. 11 and 13 for details).

It follows from the results of the MPD simulation that the time required for a doubling of the electron temperature has the va;ie $\tau_2=11$, while the recombination time obtained on the basis of kinetic theory is $\tau_{\mathrm{rec}}=0.026$, i.e., 400 times smaller. Actually the difference between the results of MPD calculations and the kinetic theory (freezing of the recombination) is even more substantial, since $\tau_{T_e}\ll\tau_{\mathrm{rec}}$. For example, if we take as the energy release per recombination event the energy corresponding to the particle radius, $\varepsilon^*=170$ eV (accordingly, $b=470$), we obtain $\tau_2/\tau_{T_e}=1.3\times10^5$ for the ratio of the heating time in MPD calculations to the kinetic theory result. Alternatively, if we proceed from the form of the distribution over total energy in Fig. 3a and set $\varepsilon^*\sim10\tau_e(0)$, we instead get $\tau_2/\tau_{T_e}=2\times10^3$.

3) Potential distribution. For modeling the spatial distribution of the potential in the metastable state we will use instead of the Boltzmann distribution the exponentially decaying function $N_e=N_{e0}\exp(-e\varphi/\varepsilon_0)$ (compare with the microfield distribution of Ref. 3–5). The rate of decay is characterized by ε_0. Measuring the potential in units of ε_0/e, distances in units of $r_m=(\varepsilon_0/4\pi e^2N_{e0})^{1/2}$, and the electric field in units of ε_0/er_m, we arrive at a system of equations that differs from (2) only by a change of sign in the exponent.

The solution of this system of equations in the planar case gives

$$x(\varphi)=a(\varphi_0)-a(\varphi),\quad E(\varphi)=\sqrt{2(1-\exp(-\varphi))},$$

where

$$a(\varphi)=\frac{1}{\sqrt{2}}\ln\left[\frac{\exp(-\varphi)}{2-\exp(-\varphi)-2\sqrt{1-\exp(-\varphi)}}\right].$$

We note that in this case, unlike that of the Debye cloud, the coordinate of the boundary of the electron cloud $a_0=a(\rho_0)$ can be arbitrarily large; the size of the cloud increases linearly with the potential at the particle: $a_0=a(\rho_0)=(1/2)\ln(2)\varphi_0=0.347\varphi_0$ for $\varphi_0\gg1$.

In the spherically symmetric and cylindrically symmetric cases, as for the case of the Debye cloud, the corresponding relations are found by a numerical integration of equations analogous to (2).

A comparison of the results of the MPD simulation with the Debye and non-Debye model of the electron cloud shows that the calculations correspond better to the non-Debye model (Fig. 4). This is natural, since the distribution of the density in the interior of the Debye cloud differs radically from the results of the MPD calculations (exponential decay instead of exponential growth). If one takes $a_0=a/2$, the Debye model will give a sharp increase in the potential at a distance $r_0=0.1$, which does not agree with the MPD calculations. If, on the other hand, one takes r_0 to correspond to the smallest distance of the MPD calculation, then the radius of the Debye cloud will be significantly smaller than $a/2$.

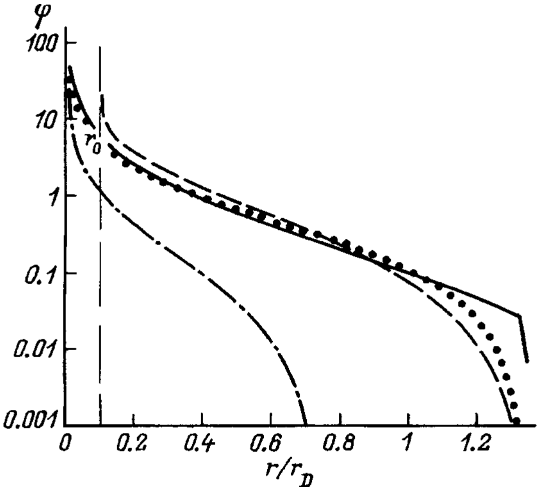

FIG. 4. Distribution of the potential over the radius: the solid curve is the MPD calculation ($r_0=0.01$, $a/2=1.35$); the dotted curve is the non-Debye model with an exponentially decaying electron density as a function of potential energy ($r_0=0.01$, $a_0=1.35$), the dashed curve is the Debye model with $r_0=0.1$, $a_0=1.35$, and the dot-and-dash curve is the Debye model with $r_0=0.01$, $a_0=0.75$.

The model based on an exponentially decaying function, on the other hand, gives a good description of the region of near and medium distances while differing somewhat from the results of the MPD calculations at the periphery. This discrepancy is apparently due to the fact that exponential decay does not precisely characterize the region of small values of the potential (Fig. 3a).

CONCLUSION

In summary, the MPD simulations of a multiply charged particle surrounded by a cloud of electrons show that such a system forms a metastable state that is far from thermodynamic equilibrium. An analogous state was obtained previously by the authors for a plasma of singly charged ions.[3–5] However, for multiply charged particles the freezing of the recombination is much more strongly expressed. Of particular interest is the fact that in a metastable state far from thermodynamic equilibrium there is a detailed balance of the transitions of electrons between states with different energy values. It is possible that the formation of dusty-plasma crystals, drops, and clouds occurs for a metastable state. This question needs additional study, including an analysis of the interaction of Debye atoms.

[1] V. E. Fortov and I. T. Yakubov, *Nonideal Plasma* [in Russian], Énergoatomizdat, Moscow (1994), 368 pp.

[2] N. N. Tsytovich, Usp. Fiz. Nauk **167**, 57 (1997).

[3] S. A. Maĭorov, A. N. Tkachev, and S. I. Yakovlenko, Usp. Fiz. Nauk **164**, 297 (1994).

[4] S. A. Mayorov, A. N. Tkachev, and S. I. Yakovlenko, Phys. Scr. **51**, 498 (1995).

[5] A. N. Tkachev and S. I. Yakovlenko, Izv. Vyssh. Uchebn. Zaved. Fiz. **40**, No. 12 (1997).

[6] V. E. Fortov, A. P. Nefedov, O. F. Petrov *et al.*, Zh. Éksp. Teor. Fiz. **111**, 467 (1997) [JETP **84**, 256 (1997)].

[7] D. V. Sivukhin, *Reviews of Plasma Physics*, Vol. 4, edited by M. A. Leontovich [Consultants Bureau, New York (1968); Atomizdat, Moscow (1964)].

[8] A. M. Ignatov, A. I. Korotchenko, V. P. Makarov *et al.*, Usp. Fiz. Nauk **165**, 113 (1995).
[9] A. A. Rukhadze, Kratk. Soobshch. Fiz., No. 9–10, p. 40 (1995).
[10] S. A. Maĭorov, A. N. Tkachev, and S. I. Yakovlenko, Usp. Fiz. Nauk **165**, 117 (1995).
[11] A. N. Tkachev and S. I. Yakovlenko, Kratk. Soobshch. Fiz. No. 9–10, p. 3 (1996).
[12] S. A. Maĭorov, A. N. Tkachev, and S. I. Yakovlenko, Izv. Vyssh. Uchebn. Zaved. Fiz. **35**(2), 10 (1992).
[13] A. N. Tkachev and S. I. Yakovlenko, Kvant. Élektron. (Moscow) **20**, 111 (1993).

Translated by Steve Torstveit

Choice of conditions of an electrical discharge for generating chemically active particles for the decomposition of impurities in water

I. M. Piskarev

D. V. Skobel'tsyn Institute of Nuclear Physics, 119899 Moscow, Russia

(Submitted November 24, 1997)
Zh. Tekh. Fiz. **69**, 58–63 (January 1999)

An electrical discharge between a liquid surface and an electrode positioned above it is considered. A second electrode, which delivers the output from a high-voltage source, is located at the bottom of the vessel containing the liquid. The conditions that must be met by the electrical discharge in order to efficiently initiate reactions in the liquid phase are analyzed. Under these conditions the number of active particles generated by the discharge turns out to depend on the concentration in the liquid of the substance with which the active particles interact. It is shown that for a corona or spark discharge the reactions can occur in a liquid layer 10–20 mm thick and that for specific reactions there exists an optimum value of the electric field at which the energy expenditures on the initiation of the reaction will be minimum.

[S1063-7842(99)00901-0]

INTRODUCTION

The plasma of an electrical discharge can be used as a source of excited particles for initiating chemical reactions on industrial scales.[1] Different possibilities for generating active particles have been discussed in the literature. For initiating reactions in the gas phase these include the following: an rf discharge in air at low pressure,[2] electron-beam initiated,[3] corona,[4] and glow[5] discharges at atmospheric pressure, and a pulsed streamer discharge.[6] For initiating reactions in a liquid the choices include a glow discharge at low gas pressure above the liquid surface,[7,8] which is known as electrolysis in a glow discharge, a pulsed discharge in the liquid,[9] ozonation,[10,11] and ozonation with blowing of a gas containing singlet oxygen through the liquid.[12]

In Refs. 13 and 14 a new approach to the problem of initiating reactions in a liquid using active particles formed in the gas phase was proposed, based on the use of a dc discharge at high electric field and low current density. Under these conditions there is an electric field in the liquid itself. The term ''electrodeless'' was proposed for the new type of reactions initiated under these conditions.

In the present paper we consider the conditions under which active particles generated in the gas phase can efficiently initiate reactions in the liquid. We present experimental results which illustrate the possibilities of this new approach to the problem.

EXPERIMENTAL CONDITIONS

A block diagram of the experimental apparatus is shown in Fig. 1. The discharge took place in a cylindrical glass vessel *13* having a base area of 10 cm^2 and a height of 36 mm up to the level of the stopper. In several experiments we used a vessel of similar shape but with a volume of 300 ml. A platinum wire electrode of diameter 0.2 mm was inserted through an opening in the bottom of the vessel, making contact with the liquid (contact electrode *9*). The vessel was closed by a Teflon stopper *12*, which had an opening for the insertion of the discharge electrode *8*, which was positioned above the surface of the liquid, and two glass tubes to permit blowing air through the vessel. Air was blown through for the purpose of maintaining a constant composition of the gas over prolonged operation. The blowing rate was $\sim$0.5 cm^3/min. The discharge electrode, made of 0.2 mm platinum wire, was mounted on a glass insulator. The thickness of the liquid layer in the vessel was varied from 5 to 30 mm (for the given area of the base of the vessel, the height of the liquid layer in millimeters is numerically equal to the volume of the liquid in milliliters). A voltage of up to 14 kV was delivered to the electrodes through a ballast resistance of 11 mΩ in the discharge electrode circuit. The average current was measured with a milliammeter in the contact electrode circuit (not shown in the figure). The shape of the current pulse was observed on an oscilloscope connected across a leg of a resistive divider in the contact electrode circuit. In the experiments on initiation of reactions the divider was removed, and the contact electrode was connected to ground through the milliammeter. The capacitance of the discharge electrode relative to ground ranged from a minimum value of a few pF, due to the capacitance of the mountings, up to 0.025 μF.

CONDITIONS OF THE ELECTRICAL DISCHARGE

1) Concentration of active particles. Let us review the requirements on a discharge intended for initiation of reactions in a liquid for the specific example of a two-particle reaction. Suppose that active radicals R^* are generated in the gas volume and that the liquid contains a substance B, the interaction of which with the radicals R^* is the topic of interest. Then, as was shown in Ref. 15, the reaction rate will be given by the relation $w_1 = Ak_1[B][R^*]$, where k_1 is the reaction rate constant, A is the relative thickness of the active layer of the liquid, i.e., the layer in which the interaction of

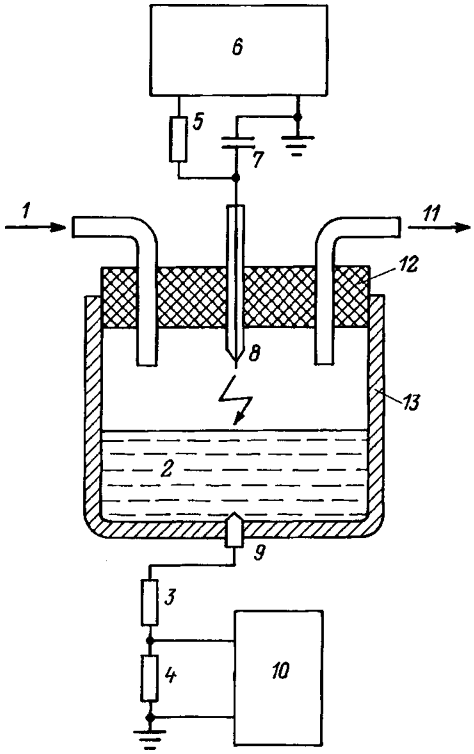

FIG. 1. Block diagram of the experimental apparatus: *1,11* — tubes for blowing air; *2* — the liquid to be treated, *3*,*4* — resistances of 160 kΩ (*3*) and 470 kΩ (*4*); *5* ballast resistance of 11 MΩ; *6* power supply (1–14 kV); *7* — capacitance of the discharge electrode relative to ground; *8* discharge electrode; *9* — contact electrode; *10* — oscilloscope; *12* — Teflon stopper; *13* — glass vessel.

the radicals from the gas phase with the substance dissolved in the liquid occurs. Calculations show[15] that in the case of water the absolute thickness of the active layer is $\sim 50\,\mu$m. The calculations in Ref. 15 were done for conditions such that the reaction occurs in a layer of thickness A and that as the substance is consumed in that layer it is replenished so as always to maintain a constant concentration over the entire volume of the liquid.

The active radicals R^* formed in the gas phase can be consumed in interactions with one another, forming inactive products, with a rate $w_2 = k_2[R^*]^2$. In order to avoid appreciable losses of active particles it is necessary to maintain the condition $w_2 \ll w_1$, or 20

$$[R^*] \ll A[B]\frac{k_1}{k_2}, \tag{1}$$

i.e., in order that the active radicals be expended mainly on the interaction with the impurity contained in the liquid, their concentration should depend on the impurity concentration and be rather low. Assuming that the thickness of the liquid layer to be treated is 20 mm (relative thickness $A = 2.5 \times 10^{-3}$), setting $k_1 = k_2$, and taking the impurity concentration as $[B] \sim 10^{-3}$ mole/l, we obtain the condition $[R^*] \ll 2.5 \times 10^{-9}$ mole/cm^3, or, in other words, the density of radicals must be much less than 10^{15} particles per cubic centimeter. Such a particle density is typical for the weakly ionized plasma of a corona or low-current spark discharge (current ~ 1 mA).

2) Dimensions of the gas cavity. Let us consider the requirements on the volume of the gas phase and shape of the gas-containing cavity. Suppose that some number R_0^* of radicals are formed in the volume per unit time during the electrical discharge. Their density will be $[R_0^*]/V_g$, where V_g is the gas volume. The loss of radicals will occur at a rate $k_2([R_0^*]/V_g)^2$, and their consumption in reactions in the liquid will occur at a rate $Ak_1[B]([R_0^*]/V_g)$. Condition (1) becomes

$$[R_0^*] \ll A[B]\frac{k_1}{k_2}V_g. \tag{2}$$

It follows that at a given rate of formation of active radicals one can always choose a volume of the gas phase small enough that condition (2) cannot hold, and the radicals formed will be lost predominantly in interactions with one another, i.e., the volume of the gas cavity must not be too small, and in particular cases it may be necessary to increase it.

If particles are lost at the walls (this pertains primarily to particles in excited states), the fraction of the particles lost in the case of a gas volume in the form of a cylinder of radius r and height h will be

$$\frac{1}{2\left(1+\dfrac{h}{r}\right)}.$$

Hence we see that the volume of the gas cavity must be increased by enlarging the radius while keeping its height to a minimum.

3) Mechanism of mixing of the liquid. Since the reaction takes place in a thin surface layer,[15] it is necessary to provide an effective mixing of the solution during the reaction as the substance is consumed in the surface layer. By diffusion alone the mixing of the liquid would occur slowly. To speed up the mixing an electric field was used. For this purpose a second electrode was placed on the bottom of the vessel. The electric field created by the flow of a dc discharge current of no more than 1 mA can reach values no higher than 1 V/cm. At such a field strength the drift velocity of the ions is ~ 0.3 mm/min (Ref. 16), i.e., the mixing of a layer of solution ~ 10 mm thick will occur over a time of the order of 30 min.

If the discharge is pulsed, then at the given applied voltages the voltage drop across the layer of liquid at the instant of breakdown will be from hundreds of volts to a few kilovolts. Then the electric field in the liquid will be hundreds of times greater than in the dc current, and the characteristic mixing time of a ~ 10 mm layer will be of the order of 10 s, since the drift velocity of the ions is proportional to the electric field,[16] which in this case has a pulsed character.

An additional factor that improves the mixing of the liquid is the ‘‘electric wind,’’[4] which is of an unsteady character and causes a funnel-shaped depression 2–3 mm deep to form on the liquid surface opposite to the discharge electrode during a corona discharge.

4) Thickness of the liquid layer. Let us estimate the thickness of the liquid layer that can be mixed during the reaction. The mixing mechanism will be assumed to be due to the passage of electrical current pulses through the liquid. The current is created by charged particles falling on the liquid during the discharge and moving through the liquid in the direction toward the electrode placed on the bottom of the vessel. During a spark discharge the part of the surface on which the spark falls has an area of $\sim 1\ \mathrm{mm}^2$. The charge that has landed on this area during the pulse creates a potential of up to 5 kV relative to ground (as was shown by direct measurements of the voltage amplitude using the divider *3,4* in Fig. 1). The motion of this charge creates a voltage distribution inside the liquid. The voltage that falls across the liquid layer during the passage of the current pulse will be determined by the resistance of that part of the liquid through which the charges move. As the region containing the groups of ions transporting the charge sinks deeper into the liquid, it will expand on account of the scattering of the ions on molecules of the liquid, the resistance of the liquid layer will become smaller, and the voltage drop will decrease. If the region occupied by the ions is cone-shaped, with its apex at the point where the spark fell, the voltage drop will be proportional to $1/d^2$, where d is the depth of the liquid layer. At a voltage on the discharge electrode of 5–10 kV, the thickness of the liquid layer that can be efficiently mixed during the reaction can be 10–20 mm (at such a thickness the voltage on the liquid layer relative to ground decreases practically to zero).

5) Mode of the electrical discharge. It follows from what we have said that an important factor in producing a reaction in a liquid by means of an electrical discharge is that the discharge have a pulsed character. For observation of the shape of the current during the discharge we used the resistive divider *3,4* and oscilloscope *10* (Fig. 1).

A corona discharge was observed under the conditions of the present experiment at discharge voltages between 7 and 14 kV at the same distance from the surface as in the spark or glow discharge. The actual distance to the liquid was somewhat larger, since a funnel-shaped depression 2–3 mm deep formed opposite the electrode on the liquid surface on account of the ‘‘electric wind.’’[4] The electric field intensity reached $\sim 5\times 10^{-16}\ \mathrm{V/cm}^2$ (50 Td). A pulsed character of the corona current was observed at voltages not strongly exceeding the threshold for ignition of the corona discharge,[17] and with further increase in voltage at a small capacitance of the discharge electrode relative to ground (of the order of a few picofarads) the discharge went over to a dc glow discharge with a quasineutral plasma column, as was observed in Ref. 18.

To preserve the pulsed character of the corona discharge current, which affords the highest electric field, it is necessary to increase the capacitance of the discharge electrode relative to ground to tens of picofarads. Then the pulsed discharge of the capacitance will lead to an increase in the current, producing a voltage drop across the discharge gap. The voltage drop violates the conditions for a self-sustaining discharge, and the discharge current falls. The pulsed voltage drop prevents the further development of the discharge, and the corona therefore becomes ‘‘flashy,’’[17] with a repetition frequency ~ 100 kHz. The capacitance and the charge stored in it are not yet sufficient for the formation of a distinct spark channel that would short the discharge gap, and the amplitude of the pulse at the surface of the liquid is of the order of 100–200 V. Thus in order that the pre-breakdown streamer of the flashy corona not lead to the formation of a glow discharge, it is necessary to have a large enough capacitance, the discharging of which will provide a current pulse that precludes the establishment of a dc regime. If the capacitance is increased further or the charging voltage increased appreciably, the charge stored in the capacitance will be sufficient for the formation of a spark channel, and the corona will become unstable and will easily pass over to a spark, the repetition frequency f of which will depend on the time constant for the charging and discharging of the capacitance *7* ($f\sim 100$–1000 Hz). The maximum electric field attainable in a spark discharge under the given experimental conditions (the limitation on the average discharge current) turns out to be approximately one-half as large as for the corona discharge.

EXPERIMENTAL RESULTS

1) Bleaching of a solution of potassium permanganate. The influence of the discharge characteristics on the production of a reaction in a liquid was investigated for the bleaching of an aqueous solution of potassium permanganate. A possible mechanism of the reaction is the interaction of potassium permanganate with hydrogen peroxide and nitric acid formed in the gas phase. Without dwelling on the details of the reaction mechanism (which was always the same), let us discuss the dependence of the bleaching time on the thickness of the liquid layer (the thickness relates to the diffusion of particles and the mixing of the solution) and the discharge parameters that govern the yield of the active particles involved in the given process. In a control experiment it was found that complete bleaching corresponds to the decomposition of over 99% of the initial $KMnO_4$. We measured the time required for complete bleaching of a $KMnO_4$ solution to the vanishing of all traces of color and the vanishing of the sediment. The error in the determination of the bleaching time was not more than 10%. Figure 2 shows the dependence of the bleaching time on the thickness of the liquid layer for the case of a definite concentration (3.8×10^{-4} mole/l of $KMnO_4$, curve *1*) and for a definite and equal amount of $KMnO_4$ in solution (3.8×10^{-6} moles, curve *2*); in the second case the thickness of the layer was regulated by adding water. It is seen that at a layer thickness of 20–25 mm the bleaching time of a liquid containing 3.8×10^{-6} moles $KMnO_4$ begins to increase, and the bleaching time of a solution with a concentration $[KMnO_4]=3.8\times 10^{-4}$ mole/l begins to grow more sharply. It follows that over the time of the reaction there is effective mixing of a layer ~ 20 mm thick. If the same discharge is carried out with both electrodes above the surface of the liquid or both completely immersed in the solution, then over a time of 20 min there were no noticeable changes in the coloring of the solution. When the discharge went over from the pulsed regime to a dc glow discharge regime there was likewise no change in the color of the solution over 20 min.

Figure 3 shows how the bleaching time of solutions with

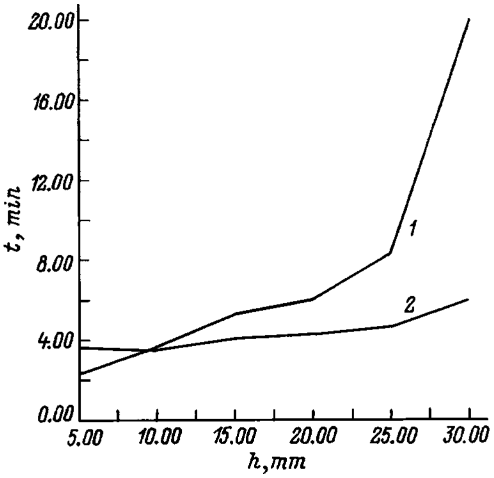

FIG. 2. Bleaching time (t) of a solution with a concentration of 3.8×10^{-4} mole/l $KMnO_4$ (*1*) and a content of 3.8×10^{-6} mole $KMnO_4$ (*2*) as a function of the volume of liquid (h is the height of the liquid layer).

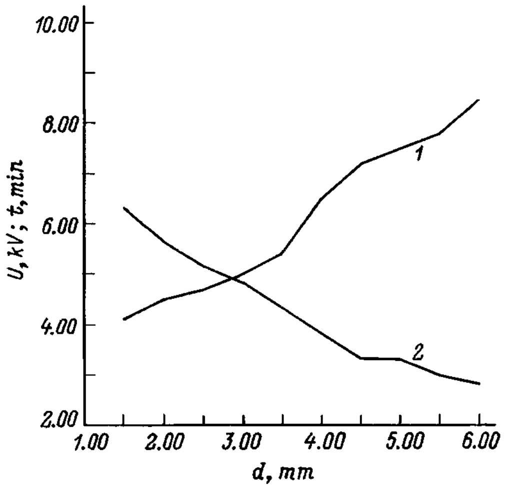

FIG. 4. Bleaching time (t) of 10 ml of a 3.8×10^{-4} mole/l solution of $KMnO_4$ (*2*) and the voltage (U) across the gap (*1*) as functions of the electrode–liquid distance d. The discharge current was 0.5 mA, and the polarity of the discharge electrode was positive.

layer thicknesses of 10 and 20 mm at $V+12.2$ kV, $I=0.5$ mA depends on the amount of $KMnO_4$ contained in it. We see that the bleaching time remains constant as an equal amount of water is added to 10 ml of a solution containing from 1.9×10^{-6} to $\sim2.3\times10^{-5}$ mole $KMnO_4$. This indicates that the layers of solution 10 and 20 mm thick are mixed with equal effectiveness.

Figure 4 shows how the voltage across the gap and the bleaching time of a 3.8×10^{-4} mole/l solution of $KMnO_4$ with a volume of 10 ml (a liquid layer thickness of 10 mm) depends on the electrode–liquid distance in the case of positive polarity of the voltage on the discharge electrode and at a current of 0.5 mA. It is seen that as the electrode–liquid distance increases, the voltage across the gap increases by approximately a factor of 2 and the bleaching time decreases by approximately the same factor. Comparing this result with the data of Table I, which gives the results of an observation of the bleaching of a solution in different discharge regimes, we can state that the reaction is determined by the yield of particles in the electric field of the gas gap and depends on the voltage applied to the gap and not on the power in the discharge (in the arc discharge, as can be seen from Table I, the power is twice as high as in the spark discharge, but the bleaching time is substantially longer). Thus in the case of $KMnO_4$ there exists an optimum value of the electric field, and the efficiency of the reaction falls off if the field is raised or lowered from that value.

The thickness of the liquid layer in which effective mixing of the solution occurs under the influence of the electric field was determined experimentally. For observation of the mixing of the solution we did an experiment on the bleaching of a 250 ml volume of liquid with a layer thickness of 80 mm in the case of a positive polarity of the voltage on the electrode, a current of 0.5 mA, and a voltage across the gap of 4.3 kV. After 12 min of reaction a layer 10 mm thick was bleached, and after 50 min a layer 20 mm thick. The entire solution was bleached in 4 h 10 min. As the voltage was raised the bleaching time of the upper 10-mm-thick layer was shortened, while the bleaching time of the entire volume remained practically unchanged. From this we see that under these conditions (i.e., for a large liquid surface) there is effective mixing of an upper layer 10 mm thick.

As we have said, when a spark falls on the surface of the liquid, a current pulse arises in the liquid, and the potential distribution inside the liquid depends on its conductivity. If the conductivity is increased the potential inside the liquid will fall faster and the mixing of the liquid will be slower. For an illustration of this assertion we did an experiment in which a 20 ml volume with a layer thickness of 20 mm was bleached in a spark discharge, with a voltage across the gap of 9.5 kV, a current of 0.5 mA, and a concentration of 3.8×10^{-6} mole/l $KMnO_4$ in distilled and in tap water. The resistance of the solution was ~100 kΩ for the solution in distilled water and ~9 kΩ for the tap water solution. The total bleaching time of the solution in distilled water was 4 min, while in the tap water it was 17 min, i.e., the bleaching time increases as the resistance of the solution decreases.

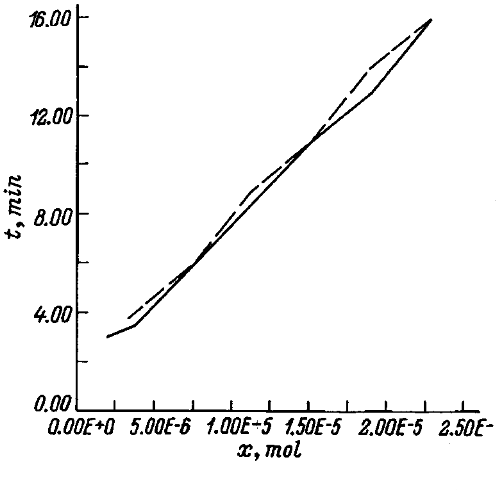

FIG. 3. Bleaching time (t) of a solution in volumes of 10 ml (dashed curve) and 20 ml (solid curve) as a function of the $KMnO_4$ concentration x in the solution.

TABLE I. Bleaching time of a 1.9×10^{-4} mole/l solution of $KMnO_4$ for different regimes of the electrical discharge in the case of positive polarity of the voltage on the discharge electrode.

Discharge characteristics					
Form	I, m	V, kV	P, W	Findings	Energy deposition, J
Corona	0.05	9.5	~0.5	Slight bleaching of solution after 30 h	15 J
Spark	0.5	8.5	~4.25	Complete bleaching of solution after 4 min	0.28 J
Arc	5	2	~10	After 20 min color diminished, although sediment remained in corners of vessel	3.33 J

2) Decomposition of potassium cyanide. We investigated the decomposition of a solution of KCN with a cyanide concentration [CN]=40 mg/l, pH=9.5 (Ref. 19). The reaction was produced in the same vessel as for the $KMnO_4$ solution. To trap the vapors of hydrocyanic acid an absorber containing a 0.1 M solution of NaOH was placed in the gas outlet. When the reaction had ended, the cyanide content in the absorber and in the reaction vessel through which the electrical discharge had passed was measured by an argentometric method. The flow rate of cyanide when the reaction was going was taken as the difference of the initial cyanide content in the first and second vessels after the reaction.

The cyanide decomposition reaction was carried out for 1 h. The temperature of the reaction vessel during the reaction was maintained constant at a level of 20–21 °C. The volume of the initial solution was taken the same each time (20 ml). The reaction was carried out at negative polarity on the discharge electrode for the different regimes of the electrical discharge (corona, spark, arc). The results of the experiment are presented in Table II. The reproducibility of the results at the same value of the current was 3% or better. These results indicate that the highest degree of decomposition of cyanides is observed for a corona discharge, when the current and number of electrons flowing in the circuit are minimal. For the spark and arc discharges the degree of decomposition is substantially lower than for the corona discharge, and changing the current for a given form of discharge did not change the degree of decomposition of the cyanides. For example, in the case of potassium cyanide the highest efficiency of decomposition is observed at the maximum attainable electric field.

As the discharge current density increases, the electric field falls off on account of screening of the external field by the space charge. The influence of the space charge on the efficiency of cyanide decomposition (dependence on the current density) was demonstrated in the following experiment. We took 20 ml of a KCN solution having a concentration of 30±1 mg/l. The decomposition of the the cyanides was carried out in a spark discharge regime at negative polarity of the voltage on the discharge electrode and at a mean current of 0.5 mA. After a 2-hour treatment the residual cyanide content was 17±1 mg/l. Then the capacitance *7* (Fig. 1) was increased to 0.025 μF. Here the mean value of the current did not change, but the character of the discharge did. Its repetition frequency became ~10 Hz. At a constant value of the average current, this means that the in-pulse value of the current increased. After a 2-hour treatment in such a regime the cyanide content became 22±1 mg/l. We see from this that as the discharge current density increases, the efficiency of cyanide decomposition decreases, even though the energy released per unit time in the spark gap remains the same.

TABLE II. The fraction of undecomposed cyanides after a 1-hour treatment of a solution by means of an electrical discharge at negative polarity on the discharge electrode for different regions of the discharge in the electrode–liquid gap.

Form of discharge	I, mA	Fraction of cyanides remaining, %
Corona	0.15	7.5
Spark	0.5	60
	1	56
Arc	3	77
	5	75

CONCLUSIONS

We have shown that when using active particles formed in an electrical discharge in a gas to initiate chemical reactions in a liquid, it is important to satisfy certain conditions: 1) the concentration of the active particles generated should be related to the concentration of the dissolved impurity with which it will interact; 2) the gas density above the liquid surface should have minimal height; 3) the electrical discharge should be pulsed; 4) the thickness of the liquid layer in which a reaction can be initiated is not over 20 mm.

The experiments done indicate that there exist optimum discharge conditions for producing specific reactions.

[1] D. N. Andreev, *Organic Synthesis in Electrical Discharges* [in Russian], edited by. A. D. Petrov, Izd. AN SSSR, Moscow–Leningrad (1953), 334 pp.

[2] K. S. Klopovskiĭ, A. S. Kovalev, D. V. Lopaev *et al.*, Fiz. Plazmy **18**, 1606 (1992) [Sov. J. Plasma Phys. **18**, 834 (1992)].

[3] N. G. Basov, V. A. Danilychev, V. I. Panteleev *et al.*, Dokl. Akad. Nauk SSSR **233**, 839 (1977) [Sov. Phys. Dokl. **22**, 213 (1977)].

[4] I. P. Vereshchagin, *Corona Discharge in Electron–Ion Technology* [in Russian], Énergoatomizdat, Moscow (1985), 160 pp.

[5] Yu. S. Akishev, A. A. Deryugin, I. V. Kochetov *et al.*, Fiz. Plazmy **20**, 585 (1994).

[6] A. P. Shvedchikov, É. V. Belousova, A. V. Polyakova *et al.*, Khim. Vysokikh Énergiĭ **26**, 317 (1992).

[7] A. Hickling, in *Modern Aspects of Electrochemistry*, No. 6, Butterworths, London (1971), 329 pp.

[8] V. I. Pavlov, Dokl. Akad. Nauk **55**, 37 (1947).

[9] A. P. Shvedchikov, É. V. Belousova, A. V. Polyakova *et al.*, Khim. Vysokikh Énergiĭ **27**, 63 (1993).

[10] V. F. Kozhinov and I. V. Kozhinov, in *Ozonation of Water* [in Russian], Stroĭizdat, Moscow (1974), p. 21.

[11] J. Hoigne, in *Process Technology for Water Treatment*, edited by S. Stucki, Plenum, New York (1988), p. 121.

[12] Yu. A. Kulagin, L. A. Shelepin, and V. N. Yaryga, Tr. Fiz. Inst. Akad. Nauk **218**, 166 (1994).

[13] I. M. Piskarev and A. I. Sevast'yanov, *Abstracts of the Sixth International Frumkinsk Symposium ''Fundamental Aspects of Electrochemistry''* [in Russian], MGU, Moscow (1995), p. 138.

[14] I. M. Piskarev, A. E. Rylova, and A. I. Sevast'yanov, Elektrokhimiya **32**, 895 (1996).

[15] I. M. Piskarev and A. I. Sevast'yanov, *Second International Congress EKVATEK-96*, Moscow (1996), p. 364.

[16] V. V. Skorcheletti, *Theoretical Electrochemistry*, Gos. Nauchno-Tekh. Izd. Khim. Lit., Leningrad (1959), 87 pp.

[17] Yu. P. Raĭzer, *Gas Discharge Physics* [Springer, New York (1997) Nauka, Moscow (1992), 438 pp.].

[18] Yu. S. Akishev, A. A. Deryugin, I. V. Karal'nik *et al.*, Fiz. Plazmy **20**, 571 (1994).

[19] I. M. Piskarev, A. E. Rylova, and A. I. Sevast'yanov, NIIYaF MGU Preprint No. 94-13/335 [in Russian], Scientific-Research Institute of Nuclear Physics, Moscow State University, Moscow (1994).

Translated by Steve Torstveit

Numerical calculation of the rate of strain of interstitial solid solutions under irradiation. I. Model of radiation creep

Yu. S. Pyatiletov and A. D. Lopuga

National Nuclear Center of the Republic of Kazakhstan, 480082 Alma-Ata, Kazakhstan

(Submitted July 8, 1996; resubmitted October 23, 1997)
Zh. Tekh. Fiz. **69**, 64–71 (January 1999)

A model of radiation creep of interstitial solid solutions is developed on the basis of the combined motion of dislocations, including their glide and climb past obstacles. The obstacles considered are forest dislocations and pileups of radiation-induced point defects. A computational formula for the rate of strain is derived which describes creep at high stresses, when the gliding dislocations overcome some of the barriers by force, and a method is described for determining the average distance traversed by a dislocation in the glide plane under the influence of the stress until it is stopped by barriers. The results are compared with those of other authors. It is shown that the formula obtained for the rate of strain goes over in particular cases to those given by the previously known SIPA, Gittus–Mansur, and glide–climb models of radiation creep.
[S1063-7842(99)01001-6]

INTRODUCTION

In developing radiation-resistant metallic materials one is faced with the problem of choosing the optimal elemental composition of the alloys, for it is well known that the admixture of even a small amount of impurities can lead to substantial changes in the physicomechanical properties, in particular, the rate of radiation-induced strain.[1–5] Therefore, the efforts of many investigators have been directed to elucidating the mechanisms by which impurity atoms influence the course of physical processes in irradiated materials. Although there are still many questions that have not been reliably answered, a number of fundamental aspects of the problem are now understood. In particular, the different channels through which impurities affect radiation creep and swelling have been identified and discussed.[6–9] Let us note those which, in our view, are of greatest interest.

First, impurity atoms can act as traps for interstitial atoms and vacancies to form stable and relatively immobile complexes which serve as additional centers of recombination of intrinsic point defects (IPDs) and reduce the rate of radiation-induced strain. Second, segregation of impurities at sinks (dislocations, voids, etc.) can alter the efficiency of capture of IPDs by these sinks, and this directly affects the rate of strain. Third, impurities can join with vacancies and interstitial atoms to form complexes having a high mobility. Thus interstitial atoms and vacancies acquire an additional channel of migration to sinks as part of these complexes, and this alters the diffusion fluxes on the whole and, hence, the rate of strain.

As we see, the influence of impurities on the rate of radiation-induced strain of irradiated metals is multifaceted. By varying the type and concentration of introduced impurities, one can in principle achieve a retardation of the creep and swelling. However, in order to take practical steps in this direction it is necessary to have a quantitative theory of the processes described above.

It should be stressed that by now there has been most impressive progress made in our understanding of processes involving the behavior of impurities in substitutional alloys.[10] There has been much less study and progress in understanding the effect of impurities on the rate of radiation-induced strain of interstitial alloys, since the shortage of reliable quantitative data in the world literature as to the qualities that govern the mobility of impurity–IPD complexes in such alloys and on the binding energies of interstitial impurities with IPDs in mobile and immobile complexes makes it difficult to develop a theory. Theoretical investigations have been started for only one aspect of the effect of impurities on the radiation-induced strain of interstitial solid solutions — the influence of impurity atmospheres around dislocations and voids on the rate of radiation creep and swelling.[11]

In previously developed models of radiation creep[12–20] only mobile IPDs are taken into account in the calculation. Nevertheless, in order to do a comprehensive investigation and to find out how impurities affect the rate of strain of interstitial alloys under irradiation with all the aforementioned channels taken into account, it is necessary first of all to have a generalized theoretical model of radiation creep, which would explicitly take into account the possibility that interstitial atoms and vacancies can migrate to sinks as constituents of mobile impurity–IPD complexes. This is the subject of the present paper. In addition, we discuss methods of numerical calculation of the physical quantities governing the rate of creep.

MODEL OF RADIATION CREEP

As an object of study we consider a model metallic sample with a cubic lattice containing edge dislocations d, voids h, and interstitial impurities i, which are characterized by sample-averaged densities ρ_d, N_h, and C_i, respectively. We assume that the sample is under irradition at an intensity G in displacements per atom per second (dpa/s) and under tension along the x_1' axis of the Cartesian coordinate system in the laboratory frame. In this coordinate system the stress tensor has a single nonzero component σ_{11}'. The components of the stress tensor in the C system of coordinates x_1, x_2, x_3 tied to the crystallographic directions [100], [010], and [001] of the sample are expressed in terms of σ_{11}' as follows:

$$\sigma_{kl} = T_{k1} T_{l1} \sigma_{11}', \tag{1}$$

where the matrix elements T_{j1} are the direction cosines between x_j $(j=1,2,3)$ and the axis of tension x_1'.

Let us assume that the dislocations contained in the sample are rectilinear, oriented along the axes x_j, and have Burgers vectors lying along these axes. The dislocations can be divided into three families with densities $\rho_d^{(j)}$, equal to 1/3 of the total dislocation density ρ_d.

The shear components of the stress tensor σ_{kl} $(k \neq 1)$ (which we will denote τ_{kl}) will cause the dislocations lying in planes normal to the x_l axis and having Burgers vectors oriented along x_k to glide in the direction x_k until they are stopped at obstacles. The diagonal components σ_{kk} affect the climb velocity $v_c^{(k)}$ of these dislocations through the stress-induced dislocation preference.[14,15]

At sufficiently high shear stresses τ_{kl} a dislocation will overcome by force some of the barrier defects, including pileups of radiation-induced point defects, which in the case considered here are voids, and will advance in the glide plane a distance L which depends on the locations of the barriers, their strength, and the external stress. Since the stress τ_{kl} is lower than the critical shear stress $\tau^{(\mathrm{cr})}$, a dislocation is not able to overcome all the barriers, and therefore, after traveling a distance L, is pinned at barriers in some stable configuration and is halted. Under irradiation it overcomes these barriers by climbing to another glide plane and again glides a distance L. This process repeats over and over. As a result, the sample is deformed, and in general both the glide and climb of dislocations contribute to the deformation. Let us first discuss the distribution of the gliding of dislocations to the rate of creep.

The process that controls the rate of strain as a result of the gliding of dislocations is their overcoming of obstacles by climb after being halted in a stable configuration. Therefore the average velocity of a dislocation in the direction of the x_k axis under the influence of a stress τ_{kl} is determined from the obvious expression

$$v = \frac{L(\tau_{kl})}{t}. \tag{2}$$

Here t is time required for the dislocation to surmount the obstacle:

$$t = \frac{\Lambda}{v_c^{(k)}}. \tag{3}$$

Here Λ denotes the average distance that the dislocation must climb in order to surmount an obstacle, which is ordinarily taken either as the average dimension λ of an obstacle[16,17] or half of that, $\lambda/2$,[18–20] and $\nu_c^{(k)}$ is the climb velocity of dislocations with Burgers vectors oriented along the x_k axis. According to Refs. 14, 16, and 20, for pure metals in which the intrinsic point defects β $(\rho = I$ denotes an interstitial atom, $\beta = V$ a vacancy) are found only in the free state and there are no complexes $i\beta$ (impurity–interstitial-atom iI and impurity–vacancy iV), the climb velocity $v_c^{(k)}$ is determined by the difference of the numbers of interstitial atoms and vacancies reaching a unit length of a type k dislocation per unit time, $I_I^{(k)} - I_V^{(k)}$. In our case this expression must be supplemented with the difference $I_{iI}^{(k)} - I_{iV}^{(k)}$ in the fluxes of impurity–interstitial-atom and impurity–vacancy complexes within which the constituent IPDs migrate to the dislocation. Thus the expression for $v_c^{(k)}$ becomes

$$v_c^{(k)} = \frac{\Omega}{b}\left(I_I^{(k)} + I_{iI}^{(k)} - I_V^{(k)} - I_{iV}^{(k)}\right) \tag{4}$$

$$= \frac{1}{b}\left[Z_I^{(k)} D_I C_I^0 + Z_{iI}^{(k)} D_{iI} C_{iI}^0 - Z_V^{(k)} D_V C_V^0 - Z_{iV}^{(k)} D_{iV} C_{iV}^0\right], \tag{5}$$

where Ω is the atomic volume and b is the modulus of the Burgers vector.

In going from Eq. (4) to (5) we have used for $I_\beta^{(k)}$ and $I_{i\beta}^{(k)}$ the expression which was first obtained by Ham[21] in describing the segregation of impurity atoms at dislocations in supersaturated solid solutions and which has subsequently been used widely in the theory of swelling and radiation creep for determining the fluxes of IPDs[14,16,19,22] and mobile impurity–IPD complexes[23,24] to dislocations. The quantities $Z_\beta^{(k)}$ and $Z_{i\beta}^{(k)}$ are parameters characterizing the efficiency of absorption by a dislocation of type k of point defects β and their complexes with impurity atoms, $Z_\beta^{(k)} = \Omega I_\beta^{(k)} / (D_b C_\beta^0)$, $Z_{i\beta}^{(k)} = \Omega I_{i\beta}^{(k)} / (D_b C_{i\beta}^0)$; D_β and $D_{i\beta}$ are the diffusion coefficients of point defects β and complexes $i\beta$; C_β^0 and $C_{i\beta}^0$ are their densities at half the distance between sinks. Since $v_c^{(k)}$ depends on the tensile component of the stresses σ_{kk}, the velocity v, according to Eqs. (2) and (3), turns out to depend on τ_{kl} and σ_{kk}. Because the density of dislocations moving in the x_k direction under the influence of the shear stress τ_{kl} is $1/6\rho_d$, the contribution of these dislocations to the creep rate component $\dot{\varepsilon}_{kl}$ is written as[25]

$$\dot{\varepsilon}_{kl} = \frac{1}{6} b \rho_d v(\tau_{kl}, \sigma_{kk}). \tag{6}$$

The creep rate component in the x_k direction due to climbing of the dislocations is given by the well-known formula[14]

$$\dot{\varepsilon}_{kk} = \frac{1}{3} b \rho_d v_c^{(k)} - \frac{1}{9} b \rho_d \sum_k v_c^{(k)}. \tag{7}$$

The second term on the right-hand side of Eq. (7) is the contribution due to swelling.

The components of the strain tensor transform on going from one coordinate system to the other in the same way as do the components of the stress tensor (see Eq. (1)); consequently, the creep rate $\dot{\varepsilon}'_{11}$ along the axis of the external load is calculated by summing the contributions from all the components $\dot{\varepsilon}_{kl}$. With allowance for what we have said, upon choosing the direction of the load axis x'_1 in the first quadrant of the C coordinate system (which does not restrict the generality of the conclusions) and specifying that direction by the angles Θ and ϕ of a spherical coordinate system tied to the C system (Θ is the angle between the x_3 and x'_1 axes, and ϕ is the angle between the x_1 axis and the projection of x'_1 on the x_1x_2 plane), we obtain an expression for the creep rate $\dot{\varepsilon}'_{11}$ of an arbitrarily oriented single-crystal sample with a cubic lattice under tension along the x'_1 axis:

$$\begin{aligned}\dot{\varepsilon}'_{11} \equiv \dot{\varepsilon} &= \sum_{k,l} T_{k1}T_{l1}\dot{\varepsilon}_{kl}\\ &= \frac{1}{6}b\rho_d\Bigg[\frac{L(\tau_{12})}{\Lambda}(v_c^{(1)}+v_c^{(2)})\sin^2\Theta\,\sin\phi\cos\phi\\ &\quad+\frac{L(\tau_{13})}{\Lambda}(v_c^{(1)}+v_c^{(3)})\sin\Theta\,\cos\Theta\,\cos\phi\\ &\quad+\frac{L(\tau_{23})}{\Lambda}(v_c^{(2)}+v_c^{(3)})\sin\Theta\,\cos\Theta\,\cos\phi\Bigg]\\ &\quad+\frac{1}{3}b\rho_d\Bigg(v_c^{(1)}\sin^2\Theta\,\cos^2\phi+v_c^{(2)}\sin^2\Theta\,\sin^2\phi\\ &\quad+v_c^{(3)}\cos^2\Theta-\frac{1}{3}\sum_j v_c^{(j)}\Bigg).\end{aligned}\tag{8}$$

The first group of terms on the right-hand side of Eq. (8) is the contribution to $\dot{\varepsilon}$ from dislocation glide ($\dot{\varepsilon}^{\mathrm{gl}}$), and the last group is the contribution from dislocation climb ($\dot{\varepsilon}^{\mathrm{cl}}$), so that $\dot{\varepsilon}=\dot{\varepsilon}^{\mathrm{gl}}+\dot{\varepsilon}^{\mathrm{cl}}$. The general expression (8) gives in particular cases the formulas for the rate of strain of pure (impurity-free) metals as given by the well-known models of radiation creep: SIPA,[14,15] Gittus–Mansur,[18,19] and glide–climb[26,27] (see Appendix); this agreement supports the validity of the model of creep described here.

At high values of the shear stress ($\tau_{kl}\geqslant 0.3\tau^{(\mathrm{cr})}$) the gliding dislocations overcome some of the barriers by force. In this case the ratio L/Λ is considerably greater than unity, and the main contribution to the rate of radiation creep is from the gliding of the dislocations. Therefore, on the right-hand side of Eq. (8) only those terms remain which contain a factor of L/Λ, i.e., we can set $\dot{\varepsilon}\cong\dot{\varepsilon}^{\mathrm{gl}}$.

Dislocations of different orientations become equivalent (give the same contribution to $\dot{\varepsilon}$) if the the most symmetric direction is chosen as the load axis — along $\langle 111\rangle$. Then, according to Eq. (1), all the shear (τ_{kl}) and tensile (σ_{kk}) components of the stress take the value $\sigma'_{11}/3\equiv\sigma$. In addition, the following relations hold: $v_c^{(1)}=v_c^{(2)}=v_c^{(3)}\equiv v_c$, $Z_\beta^{(1)}=Z_\beta^{(2)}=Z_\beta^{(3)}\equiv Z_\beta$, and $Z_{i\beta}^{(1)}=Z_{i\beta}^{(2)}=Z_{i\beta}^{(3)}\equiv Z_{i\beta}$. As a result, the formula for the creep rate (8) is substantially simplified. The expression in the square brackets, which we will denote by $\tilde{v}(\sigma'_{11},\Theta,\phi)$, is replaced by $2v(\sigma,\sigma)$, and the contribution from the climbing of dislocations goes to zero. Taking all this into account and introducing the notation

$$\xi=\frac{\tilde{v}(\sigma'_{11},\Theta,\phi)}{2v(\sigma,\sigma)},\tag{9}$$

we obtain from (8) in the general case of an arbitrary orientation of the load

$$\begin{aligned}\dot{\varepsilon}=\frac{L(\sigma)}{6\Lambda}\rho_d\xi[Z_ID_IC_I^0+Z_{iI}D_{iI}C_{iI}^0-Z_VD_VC_V^0\\ -Z_{iV}D_{iV}C_{iV}^0].\end{aligned}\tag{10}$$

The parameter ξ can take on values from zero (when the x'_1 axis coincides with one of the axes x_j) up to some value that depends on the form of the function $L(\sigma)$. Using the results of the calculation of $L(\sigma)$ in the next Section and assuming that the external tensile load is oriented randomly with respect to the axes x_1, x_2, and x_3, one can easily show that the average value of ξ is in order of magnitude equal to unity. Therefore, for estimates of the rate of radiation creep one can use formula (10) with $\xi=1$.

We see that in order to carry out quantitative calculations using formula (10) we must have an algorithm for calculating $L(\sigma)$ and the velocity of dislocation climb v_c. These questions will be addressed in the next two Sections.

DETERMINING $L(\sigma)$ BY COMPUTER SIMULATION AND APPROXIMATING THE RESULTS BY ANALYTICAL FUNCTIONS

An exact analytical calculation of $L(\sigma)$ in the case of a chaotic spatial distribution of different kinds of defects is practically impossible. Therefore, for calculating $L(\sigma)$ we use the computational scheme developed in Ref. 26, wherein $L(\omega)$ is determined by computer simulation of the motion of dislocations through a mesh of random obstacles of different strength by the technique proposed by Foreman and Makin.[28] For the model sample investigated here, which contains dislocations and voids, this computational scheme is implemented as follows. A dislocation is represented as a flexible filament of constant tension, which is originally located at the base of a rectangular simulation area and is pinned by its ends at opposite sides of this area. The dimensions of the area are chosen from considerations that the results of the simulation be independent of its length and height. It turned out that for this it is sufficient that the length of the area be at least $100l$ (where l is the average distance between barriers in the glide plane) and its height at least $8l$. In the calculations we chose the dimensions of the simulation area as $150l\times 10l$, which includes 1500 barriers. The barriers (forest dislocations and voids) were assumed to be pointlike and rigidly pinned, and their interaction with a dislocation was assumed to be short-ranged.

The force exerted by a dislocation on the jth obstacle is determined by the angle ψ_j between adjacent segments of the dislocation at the jth obstacle, and therefore the strength of the obstacle is characterized by the value of the critical angle $\psi_j^{(\mathrm{cr})}$ at which the dislocation overcomes the given obstacle. In the model considered here the material has two types of obstacles: strong — voids, characterized by values $\psi_1^{(\mathrm{cr})}<2$ rad, and weak — forest dislocations with $\psi_2^{(\mathrm{cr})}>2$ rad.[29] The

TABLE I. Values of the coefficients A and B for different combinations of $\psi_1^{(\mathrm{cr})}$ and $\psi_2^{(\mathrm{cr})}$ for the case of equal numbers of ''strong'' and ''weak'' barriers.

	$\psi_1^{(\mathrm{cr})}$							
	1.4		1.6		1.8		2.0	
$\psi_2^{(\mathrm{cr})}$	A	B	A	B	A	B	A	B
2.2	0.3564	3.3188	0.3191	3.1125	0.2437	3.8750	0.1928	4.0875
2.4	0.3639	3.4192	0.2559	3.8063	0.1979	4.1063	0.1583	4.2625
2.6	0.4265	3.3206	0.5519	3.1813	0.2670	3.8313	0.1770	4.1188
2.8	0.5840	3.0375	0.3465	3.6500	0.3310	3.6063	0.2254	4.1938

spatial distribution of barriers of the two types in the simulation area is specified by a random number generator.

When acted on by a shear stress $\tau_{kl}=\sigma$, a dislocation moves in its glide plane, overcoming by force those barriers for which the angle ψ_j is less than $\psi_j^{(\mathrm{cr})}$. If the stress σ is less than the critical shear stress, then the dislocation, after traveling a distance $L(\sigma)$, will assume a stable configuration and be halted when ψ_j at all the barriers is greater than $\psi_j^{(\mathrm{cr})}$. As a result of the simulations by this scheme we obtained the functions $L(\sigma)$ for various combinations of values $\psi_1^{(\mathrm{cr})}$ and $\psi_2^{(\mathrm{cr})}$ and for equal numbers of ''strong'' and ''weak'' barriers.

It is clear, however, that carrying out practical calculations of $L(\sigma)$ by computer simulation for each material with allowance for the specific defect structure existing in it is an inconvenient complication for researchers.[30–32] It would be much simpler and better to use analytical representations of $L(\sigma)$ if good approximations of $L(\sigma)$ by analytical functions would be found. Analysis of a large number of $L(\sigma)$ curves obtained by computer simulation satisfies shown that $L(\sigma)$ can be described for the most widely different cases by an exponential function of the form

$$L(\sigma)=A\exp\left(B\,\frac{\sigma}{\tau^{(\mathrm{cr})}}\right) \tag{11}$$

with two parameters A and B, the values of which can easily be determined for different specific situations, so that researchers can use an analytical expression for $L(\sigma)$ without resorting to computer simulations. In particular, the functions $L(\sigma)$ obtained here by computer simulation approximate to good accuracy the exponential function (11) with the coefficients A and B given in Table I.

NUMERICAL METHOD OF CALCULATING THE DISLOCATION CLIMB VELOCITY

As we see from formula (5), the climb velocity of the dislocations is determined by the fluxes to them of IPDs and mobile impurity–IPD complexes. These fluxes can be found by a numerical method if the steady-state distribution of mobile point defects in the neighborhood of the sinks are known. The latter can be obtained by solving a system of diffusion equations for vacancies, interstitial atoms, and impurity–vacancy and impurity–interstitial-atom complexes with allowance for the interactions of point defects with one another and their interaction with the elastic fields of sinks. Various approximations and models[33] are used for solving this problem: 1) the absorbing medium model, according to which it is assumed that all the sinks for point defects are uniformly smeared over the crystal; 2) the model of a periodic distribution of sinks, according to which the crystal is divided up into identical cells having the symmetry of a sink (cylinders for dislocations and spheres for voids), with a sink located at the center of each; 3) a hybrid model combining features of both of the preceding.

The absorbing medium model is usually regarded as the best of these. However, its use requires specifying boundary conditions at an infinitely large distance from the chosen sink. For this reason such a model cannot be used for numerical calculations, where one must specify a computational mesh with cells of finite dimensions. In view of what we have said here we use a hybrid model according to which the dislocation is located at the center of a cylindrical cell; in the space inside the cell the voids are assumed to be uniformly smeared, while outside the cell the crystal is represented as a uniform absorbing medium with uniformly smeared dislocations and voids.

In the general case, when it is assumed that not only the IPDs but also impurity–interstitial-atom and impurity–vacancy complexes are mobile, the following differential equations can be used to calculate the steady-state densities of these point defects in the cell in the neighborhood of a dislocation:

$$\begin{aligned}&D_V\nabla^2C_V+\frac{D_V}{k_bT}(\nabla C_V\nabla E_V^{(d)}+C_V\nabla^2E_V^{(d)})\\&\quad+G-D_Vk_V^{(h)2}C_V-\alpha C_VC_I+\gamma_{iV}C_{iV}-\mu_IC_VC_{iI}\\&\quad-\chi_VC_V(C_i^{(d)}-C_{iI}-C_{iV})=0,\end{aligned} \tag{12}$$

$$\begin{aligned}&D_I\nabla^2C_I+\frac{D_I}{k_bT}(\nabla C_I\nabla E_I^{(d)}+C_I\nabla^2E_I^{(d)})\\&\quad+G-D_Ik_I^{(h)2}C_I-\alpha C_VC_I+\gamma_{iI}C_{iI}-\mu_VC_IC_{iV}\\&\quad-\chi_IC_I(C_i^{(d)}-C_{iI}-C_{iV})=0,\end{aligned} \tag{13}$$

$$\begin{aligned}&D_{iV}\nabla^2C_{iV}+\frac{D_{iV}}{k_bT}(\nabla C_{iV}\nabla E_{iV}^{(d)}+C_{iV}\nabla^2E_{iV}^{(d)})-D_{iV}k_{iV}^{(h)2}C_{iV}\\&\quad-\alpha'C_{iV}C_{iI}+\chi_VC_V(C_i^{(d)}-C_{iI}-C_{iV})\\&\quad-\mu_IC_VC_{iI}-\gamma_{iV}C_{iV}=0,\end{aligned} \tag{14}$$

$$\begin{aligned}&D_{iI}\nabla^2C_{iI}+\frac{D_{iI}}{k_bT}(\nabla C_{iI}\nabla E_{iI}^{(d)}+C_{iI}\nabla^2E_{iI}^{(d)})-D_{iI}k_{iI}^{(h)2}C_{iI}\\&\quad-\alpha'C_{iV}C_{iI}+\chi_IC_I(C_i^{(d)}-C_{iI}-C_{iV})\\&\quad-\mu_IC_VC_{iI}-\gamma_{iI}C_{iI}=0.\end{aligned} \tag{15}$$

Here k_b is Boltzmann's constant, T is the temperature, $C_i^{(d)}$ is the density of impurity atoms in the impurity atmosphere around the dislocation;[11] $E_\beta^{(d)}(\mathbf{r})$ and $E_{i\beta}^{(d)}(\mathbf{r})$ are the interaction energies of a point defect β and a complex $i\beta$ with a dislocation surrounded by an impurity atmosphere;[11] $k_\beta^{(h)2}$ and $k_{i\beta}^{(h)2}$ are parameters characterizing the efficiency of absorption of point defects β and complexes $i\beta$, respectively, by a void; α is the mutual recombination coefficient of interstitial atoms and vacancies; α' is the recombination coefficient of complexes iI with complexes iV; μ_β is the recombination coefficient of free point defects β with impurity-trapped IPDs of the opposite type; χ_β is the capture coefficient of point defects β by impurity atoms, $\gamma_{i\beta}$ is the reciprocal of the mean time that a defect β is bound in a complex $i\beta$. These coefficients are given by the following formulas:[6,34]

$$\alpha=\frac{\omega\nu_D}{\Omega}\exp(-E_I^m/k_bT), \tag{16}$$

$$\alpha'=\frac{\omega\nu_D}{\Omega}\exp(-E_{iI}^m/k_bT), \tag{17}$$

$$\mu_I=4\pi r_I D_V/\Omega, \tag{18}$$

$$\mu_V=4\pi r_V D_I/\Omega, \tag{19}$$

$$\chi_\beta=4\pi r_{i\beta} D_\beta/\Omega, \tag{20}$$

$$\gamma_{i\beta}=\frac{D_\beta}{b_0^2}\exp(-E_{i\beta}^b/k_bT), \tag{21}$$

$$k_\beta^{(h)2}=Y_\beta 4\pi r_h N_h, \quad k_{i\beta}^{(h)2}=Y_{i\beta}4\pi r_h N_h, \tag{22}$$

where ω is the volume of the zone of mutual recombination of point defects, ν_D is a frequency of the order of the Debye frequency, r_β is the radius of the volume in which a defect β recombines with a trapped IPD of the opposite type; $r_{i\beta}$ is the radius of capture of a point defect β by an impurity atom; b_0 is a quantity of the order of the interatomic distance; $E_{i\beta}^b$ is the binding energy of a complex $i\beta$; E_I^m is the energy of migration of an interstitial atom, Y_β and $Y_{i\beta}$ are parameters characterizing the efficiency of absorption of point defects β and complexes $i\beta$ by a void; r_h is the mean radius of a void.

To solve the system of differential equations (12)–(15), it is necessary to know the boundary conditions. In view of the fact that the results of a computer simulation[35] show that the radii r_{dV}^0 and r_{dI}^0 of the zones of spontaneous capture of vacancies and interstitial atoms, respectively, by a dislocation are different ($r_{dI}^0>r_{dV}^0$), and the IPDs entering their capture zones have a positive binding energy with dislocations $E_{d\beta}^b$. Therefore, we shall assume that for $r=r_{d\beta}^0$ the concentration of IPDs of type β is equal to zero:

$$C_\beta(r_{d\beta}^0)=0. \tag{23}$$

Since $E_{d\beta}^b$ is larger than the binding energy of an impurity with an IPD of type β, at the boundary of the capture zone (at $r=r_{d\beta}^0$) the complexes $i\beta$ break apart, the IPDs going away to the dislocation and the impurity atoms returning to solution. Therefore, the boundary conditions for complexes at $r=r_{d\beta}^0$ will be

$$C_{i\beta}(r_{d\beta}^0)=0. \tag{24}$$

At the outer boundary of the cell (at $r=R_d$, where R_d is one-half the average distance between dislocations) the concentrations C_β^0 and $C_{i\beta}^0$ are determined from the system of balance equations for the densities of point defects β and $i\beta$ in an absorbing medium with uniformly smeared dislocations and voids and characterized by sink strengths

$$k_\beta^2=k_\beta^{(d)2}+k_\beta^{(h)2}, \quad k_{i\beta}^2=k_{i\beta}^{(d)2}+k_{i\beta}^{(h)2}, \tag{25}$$

where $k_\beta^{(d)2}$ and $k_{i\beta}^{(d)2}$ are the sink strengths of dislocations for defects β and $i\beta$, respectively:

$$k_\beta^{(d)2}=Z_\beta\rho_d, \quad k_{i\beta}^{(d)2}=Z_{i\beta}\rho_d. \tag{26}$$

The balance equations are obtained from (12)–(15) with the spatial derivatives equal to zero, with $k_\beta^{(h)2}$ and $k_{i\beta}^{(h)2}$ replaced by k_β^2 and $k_{i\beta}^2$, respectively, and $C_i^{(d)}(\mathbf{r})$ replaced by C_i:

$$G-D_Vk_V^2C_V^0-\alpha C_V^0C_I^0+\gamma_{iV}C_{iV}^0 \\ -\mu_IC_V^0C_{iI}^0-\chi_VC_V^0(C_i-C_{iI}^0-C_{iV}^0)=0, \tag{27}$$

$$G-D_Ik_I^2C_I^0-\alpha C_V^0C_I^0+\gamma_{iI}C_{iI}^0 \\ -\mu_VC_I^0C_{iV}^0-\chi_IC_I^0(C_i-C_{iI}^0-C_{iV}^0)=0, \tag{28}$$

$$\chi_VC_V^0(C_i-C_{iI}^0-C_{iV}^0)-D_{iV}k_{iV}^2C_{iV}^0 \\ -\mu_VC_I^0C_{iV}^0-\gamma_{iV}C_{iV}^0-\alpha'C_{iV}^0C_{iI}^0=0, \tag{29}$$

$$\chi_IC_I^0(C_i-C_{iI}^0-C_{iV}^0)-D_{iI}k_{iI}^2C_{iI}^0 \\ -\mu_IC_V^0C_{iI}^0-\gamma_{iI}C_{iI}^0-\alpha'C_{iV}^0C_{iI}^0=0. \tag{30}$$

The system of nonlinear algebraic equations (27)–(30) is solved by an iterative method on a computer. As a result we determine the boundary conditions at the outer boundary:

$$C_\beta(R_d)=C_\beta^0, \quad C_{i\beta}(R_d)=C_{i\beta}^0 \tag{31}$$

and, consequently, we can now turn to a solution of the system of equations (12)–(15).

The numerical integration of equations such as these is ordinarily done using difference schemes. We have used one such scheme, according to which equations (12)–(15) are written in a cylindrical coordinate system tied to the dislocation and then a mesh for the variables r and Θ, containing N_1 and N_2 mesh points with steps h_1 and h_2, is specified. Approximating the differential operators in (12)–(15) by difference relations at the mesh points, we arrive at finite-difference equations, which must be solved at $(N_1-2)\cdot N_2$ mesh points (the values of C at the $2N_2$ mesh points on the outer and inner boundaries of the computational cell are boundary conditions). We note that the equations obtained form a system of nonlinear equations. It is solved numerically by Newton's iteration method (see, e.g., Ref. 36). The algorithm described yields a solution of the initial system of equations (12)–(15) with a specified accuracy in an acceptable amount of time.

However, this is not yet a complete solution of the problem. The initial system of equations (12)–(15) and the equations (27)–(30) used to determine the densities C_β^0 and $C_{i\beta}^0$ at the outer boundaries of the computational cell contain the quantities $k_\beta^{(h)2}$, $k_{i\beta}^{(h)2}$, $k_\beta^{(d)2}$, and $k_{i\beta}^{(d)2}$, which in turn contain the initially unknown efficiencies of absorption of point defects by dislocations, Z_β and $Z_{i\beta}$, and by voids, Y_β and $Y_{i\beta}$. Therefore, it is necessary to seek a self-consistent solution.[8,9] The self-consistent procedure for numerical integration of equations (12)–(15) includes the following steps.

1. Equations (27)–(30) are solved using ''seed'' values Y_β, $Y_{i\beta}$ and Z_β, $Z_{i\beta}$, determined using the analytical formulas of Ref. 14. In the process, values are calculated for C^0_β and $C^0_{i\beta}$, which are boundary conditions for the system of equations (12)–(15).

2. The system of equations (12)–(15), from which the steady-state distribution of point defects β and complexes $i\beta$ in the neighborhood of a dislocation is initially determined, is integrated, and then the fluxes I_β and $I_{i\beta}$ of these defects to the dislocation are calculated by numerical differentiation; these fluxes are used to calculate Z_β and $Z_{i\beta}$ in the first iteration step.

3. By analogy with (12)–(15) a system of equations is written for calculating the densities C_β and $C_{i\beta}$ in a spherical cell around a void. Here $E^{(d)}_\beta$ and $E^{(d)}_{i\beta}$ are replaced by $E^{(h)}_\beta$ and $E^{(h)}_{i\beta}$ — the interaction energies of defects β and $i\beta$ with a void surrounded by an impurity atmosphere.[11] Within a computational cell the dislocations are uniformly smeared, and so $k^{(h)2}_\beta$ and $k^{(h)2}_{i\beta}$ are replaced by $k^{(d)2}_\beta$ and $k^{(d)2}_{i\beta}$, respectively. Outside the cell the crystal is modeled by an absorbing medium with uniformly smeared dislocations and voids. The boundary conditions at the surface of a void are specified by analogy with the dislocation case considered above, since it has been shown[37] that near a void there are also regions of spontaneous capture of IPDs, which are different for vacancies and interstitial atoms and are characterized by radii $r^0_{h\beta} > r_h$. Therefore, the densities $C_\beta(r^0_{h\beta})$ and $C_{i\beta}(r^0_{h\beta})$ are equal to zero. At the outer boundary of a cell (for $r = R_h$, where R_h is one-half the mean distance between voids) the densities C^0_β and $C^0_{i\beta}$ are determined from the system of equations (27)–(30). The numerical solution of the system of equations for C_β and $C_{i\beta}$ in a spherical cell around a void is done using a spherical coordinate system tied to the void, following the same computational scheme as was used for the dislocation case. As a result, a steady-state distribution of defects β and $i\beta$ in the neighborhood of a void is obtained, the fluxes $I^{(I)}_\beta$ and $I^{(h)}_{i\beta}$ of these defects to a void are calculated, and then the formulas

$$Y_\beta = \frac{I^{(h)}_\beta \Omega}{4\pi r_h D_\beta C^0_\beta}, \quad Y_{i\beta} = \frac{I^{(h)}_{i\beta} \Omega}{4\pi r_h D_{i\beta} C^0_{i\beta}} \tag{32}$$

are used to calculate the values $Y^{(1)}_\beta$ and $Y^{(1)}_{\mathrm{i}\beta}$ in the first iteration step. Then one returns to item 1 and proceeds with the second iteration.

This iterative process is repeated until a specified accuracy is achieved. Ultimately we obtain self-consistent equations for the sink strengths of voids and dislocations, the parameters Z_β, $Z_{i\beta}$, Y_β, $Y_{i\beta}$, and the steady-state densities of point defects in the neighborhood of the sinks (C_β, $C_{i\beta}$) and at the boundaries of the cells ($C^0_\beta, C^0_{i\beta}$). Using these data in formula (5), we obtain the desired climb velocity of dislocations.

CONCLUSION

In summary, we have described a physical model for the radiation creep of interstitial solid solutions and have obtained a computational formula for determining the creep rate $\dot{\varepsilon}$. We have shown that in the general case $\dot{\varepsilon}$ cannot be calculated analytically. We have therefore discussed numerical methods of calculating $L(\sigma)$ and v_c, which determine the creep rate.

To calculate the rate of strain for specific materials with the use of the model of creep described here, it is necessary to specify the parameter values characterizing the given material, its defect structure, the irradiation and testing conditions, and then to implement the procedure for computing $L(\sigma)$ and v_c as described in the preceding Sections. We have done such a study, and the results of calculations carried out to elucidate the influence of various factors on the rate of strain of interstitial solid solutions under irradiation will be reported later.

APPENDIX

Here we show how expression (8) in particular cases goes over to the formulas for the rate of radiation creep given by the SIPA,[14,15] Gittus–Mansur,[18,19] and glide–climb[26,27] models. We will assume that there are no complexes $i\beta$. We consider the following situations: 1) the tensile stress σ'_{11} is directed along the x_1 axis, which coincides with the crystallographic axis $\langle 100\rangle$; 2) the axis of the stress σ'_{11} lies along $\langle 110\rangle$.

Case 1: $(\sigma'_{11} \| \langle 100\rangle;\ \Theta = \pi/2;\ \phi = 0)$. It follows from Eq. (1) that the shear components τ_{kl} of the stress are equal to zero, an therefore creep occurs only on account of dislocation climb, as is assumed in the SIPA model. Then from expression (8) taken together with (5) we obtain directly the formula given by the SIPA model[14] for the rate of radiation creep:

$$\dot{\varepsilon} = \dot{\varepsilon}_{\mathrm{SIPA}} = \frac{2}{9}\rho_d [\Delta Z_I D_I C^0_I - \Delta Z_V D_V C^0_V], \tag{33}$$

where $\Delta Z_\beta = Z^{(1)}_\beta - Z^{(3)}_\beta$.

Case 2: $(\sigma'_{11} \| \langle 110\rangle;\ \Theta = \pi/2;\ \phi = \pi/4)$. According to Eq. (1), the stress components τ_{12}, τ_{21}, σ_{11}, and σ_{22} are nonzero, and therefore both the climb and glide of dislocations contribute to the creep. From expression (8) we obtain the following:

$$\begin{aligned} \dot{\varepsilon} &= \frac{\rho_d}{9}(\Delta Z_I D_I C^0_I - \Delta Z_V D_V C^0_V) \\ &\quad + \frac{L}{6\Lambda}\rho_d (Z^{(1)}_I D_I C^0_I - Z^{(1)}_V D_V C^0_V) \\ &= \frac{1}{2}\dot{\varepsilon}_{\mathrm{SIPA}} + \frac{L}{2\Lambda}\left(\frac{1}{2}\dot{\varepsilon}_{\mathrm{SIPA}} + \frac{1}{3}\dot{S}\right), \end{aligned} \tag{34}$$

where $\dot{S}$ is the rate of swelling.

The terms on the right-hand side of Eq. (34) which contain the factor L/Λ are the contribution to $\dot{\varepsilon}$ from dislocation glide. If the stress σ'_{11} is so weak that the gliding dislocations cannot overcome even one barrier by force, and the only obstacles are forest dislocations (as in the models of Gittus[18] and Mansur[19]), then we obtain from (34) the contribution to the rate of radiation creep given by the Gittus–Mansur model. Indeed, in such a situation Λ is one-half the average length of the dislocation segments ($\Lambda \simeq 1/(\sqrt{\pi\rho_d})$, and the value of L is obtained from the condition that the strain $(1/6)b\rho_d L$ correspond to the elastic bending strain ε_e of the dislocation segments. As a result, the contribution to $\dot{\varepsilon}$ due to dislocation glide can be written in the form

$$\dot{\varepsilon}^{\mathrm{gl}} = \frac{\sqrt{\pi}\varepsilon_e}{d\sqrt{\rho_d}}\left(\dot{S} + \frac{3}{2}\dot{\varepsilon}_{\mathrm{SIPA}}\right), \tag{35}$$

which agrees up to numerical coefficients with the formulas for the creep rate given by the models of Gittus [the first term on the right-hand side of (35)] and Mansur (the second term).

At high values of the stress the gliding dislocations overcome some of the barriers by force. In this case the coefficient L/Λ is considerably greater than unity, and consequently the main contribution to $\dot{\varepsilon}$ is from dislocation glide. From Eq. (34) we obtain directly

$$\dot{\varepsilon} = \frac{L}{6\Lambda}\rho_d(Z_I^{(1)}D_I C_I^0 - Z_V^{(1)}D_V C_V^0), \tag{36}$$

which agrees with the formula for the rate of radiation creep given by the glide–climb model.[27]

[1] T. M. Williams, J. Nucl. Mater. **88**, 217 (1980).

[2] Yu. M. Platov, S. V. Simakov, and A. B. Tsepelev, Fiz. Khim. Obrab. Mater. , No. 1, pp. 11–13 (1989).

[3] V. N. Voevodin, V. F. Zelenskiĭ, M. P. Zaĭdlits *et al.*, Vopr. At. Nauki Tekh. Ser. Fiz. Radiats. Povrezh. Radiats. Materialoved. (Kharkov), No. 1(12), pp. 68–71 (1980).

[4] O. A. Medvedev, A. I. Ryazanov, A. N. Lyubimov *et al.*, J. Nucl. Mater. **233–237**, 460 (1996).

[5] E. S. Aithozhin and E. V. Chumakov, J. Nucl. Mater. **233–237**, 537 (1996).

[6] L. K. Mansur and M. H. Yoo, J. Nucl. Mater. **74**, 228 (1978).

[7] L. N. Davydov and N. M. Kiryukhin, Vopr. At. Nauki Tekh. Ser. Fiz. Radiats. Povrezh. Radiats. Materialoved. (Kharkov), No. 2(13), 10–12 (1980).

[8] Yu. V. Trushin, Zh. Tekh. Fiz. **62**, 1 (1992) [Sov. Phys. Tech. Phys. **37**, 353 (1992)].

[9] Yu. V. Trushin, Zh. Tekh. Fiz. **62**, 13 (1992) [Sov. Phys. Tech. Phys. **37**, 360 (1992)].

[10] F. V. Nolfi Jr., *Phase Transformations during Irradiation* [Applied Science Publishers, London; Elsevier, New York (1983); Metallurgiya, Chelyabinsk (1989), 312 pp.].

[11] Yu. S. Pyatiletov and N. I. Edemskiĭ, Zh. Tekh. Fiz. **62**, 89 (1992) [Sov. Phys. Tech. Phys. **37**, 1089 (1992)].

[12] Z. K. Saralidze, Fiz. Met. Metalloved. **81**, 159 (1996).

[13] V. L. Indenbom and Z. K. Saralidze, *Elastic Strain Fields and Dislocation Mobility*, Vol. 31 of *Modern Problems in Condensed Matter Sciences*, edited by V. L. Indenbom and J. Lothe, North Holland, New York (1992), Ch. 12, pp. 699–744.

[14] P. T. Heald and M. V. Speight, Acta Metall. **23**, 1389 (1975).

[15] C. H. Woo, F. A. Garner, and R. A. Holt, in *Effects of Radiation on Materials*, 16th Intern. Symp. ASTM STP 1175, American Society for Testing and Materials, Philadelphia (1993), pp. 27–37.

[16] W. G. Wolfer, J. P. Foster, and F. A. Garner, Nucl. Technol. **16**, 55 (1972).

[17] S. D. Harkness, J. A. Tesk, and C.-Yu. Li, Nucl. Appl. Technol. **9**, 24 (1970).

[18] J. H. Gittus, Philos. Mag. **25**, 345 (1972).

[19] L. K. Mansur, Philos. Mag. A **39**, 497 (1979).

[20] P. T. Heald and J. E. Harbottle, J. Nucl. Mater. **67**, 229 (1977).

[21] F. S. Ham, J. Appl. Phys. **30**, 915 (1959).

[22] I. G. Margvelashvili and Z. K. Saralidze, Fiz. Tverd. Tela (Leningrad) **15**, 2665 (1973) [Sov. Phys. Solid State **15**, 1774 (1973)].

[23] G. Z. Gorbatov, Fiz. Met. Metalloved. **48**, 100 (1979).

[24] Yu. V. Trushin and A. N. Orlov, Zh. Tekh. Fiz. **56**, 1302 (1986) [Sov. Phys. Tech. Phys. **31**, 763 (1986)].

[25] J. P. Hirth and J. Lothe, *Theory of Dislocations* [McGraw-Hill, New York (1967); Atomizdat, Moscow (1972), 600 pp.].

[26] V. V. Kirsanov, Yu. S. Pyatiletov, and O. G. Tyupkina, Pis'ma Zh. Tekh. Fiz. **6**, 1183 (1980) [Sov. Tech. Phys. Lett. **6**, 506 (1980)].

[27] Yu. S. Pyatiletov, Fiz. Met. Metalloved. **54**, 1080 (1982).

[28] A. J. E. Foreman and M. J. Makin, Philos. Mag. **14**, 911 (1966).

[29] A. L. Bement Jr., Rev. Roum. Phys. **17**, 360 (1972).

[30] Yu. S. Pyatiletov and O. G. Tyupkina, Fiz. Met. Metalloved. **55**, 792 (1983).

[31] Yu. S. Pyatiletov and D. Sh. Ibragimova, Fiz. Met. Metalloved. , No. 1, pp. 17–23 (1992).

[32] D. Sh. Ibragimova, A. N. Karpikov, D. A. Nazyrova *et al.*, Preprint IFÉ NYaTs RK, No. 1-94 [in Russian], National Nuclear Center of the Republic of Kazakhstan, Alma-Ata (1994), 32 pp.

[33] A. D. Brailsford and R. Bullough, Sov. Phys. Tech. Phys. **302**, 87 (1981).

[34] A. N. Orlov and Yu. V. Trushin, in *Radiation Defects in Metallic Crystals* [in Russian], edited by Sh. Sh. Ibragimov, Nauka KazSSR, Alma-Ata (1978), pp. 30–40.

[35] V. V. Kirsanov, Yu. S. Pyatiletov, and T.É. Turkebaev, Zh. Tekh. Fiz. **55**, 698 (1985) [Sov. Phys. Tech. Phys. **30**, 411 (1985)].

[36] M. S. Bakhvalov, *Numerical Methods (Analysis, Algebra, and Ordinary Differential Equations* [in Russian], Nauka, Moscow (1973), 632 pp.

[37] S. I. Golubov and E. N. Kaipetskaya, in *Computers and the Modeling of Defects in Crystals* [in Russian], Leningrad 91982), pp. 76–77.

Translated by Steve Torstveit

TECHNICAL PHYSICS VOLUME 44, NUMBER 1 JANUARY 1999

Nonlinear theory of channeling of radiation by a ribbon-shaped stream of cyclotron oscillators

N. S. Ginzburg, I. V. Zotova, and A. S. Sergeev

Institute of Applied Physics, Russian Academy of Sciences, 603600 Nizhniĭ Novgorod, Russia

(Submitted October 13, 1997)
Zh. Tekh. Fiz. **69**, 9–14 (January 1999)

The features of the nonlinear stage of radiation from transversely bounded, magnetically steered helical and rectilinear electron streams in a homogeneous medium and in vacuum are investigated theoretically under conditions of the normal and anomalous Doppler effects. The evolution of the transverse distribution of the radiated field is investigated, and the channeling effect of the electron stream is demonstrated. It is shown that in the radiation from a helical stream in a plasmalike medium a practically complete conversion of the energy of gyrational motion of the electrons into energy of electromagnetic oscillations can occur on account of the automatic fine tuning of the radiation angle. © *1999 American Institute of Physics.* [S1063-7842(99)00201-9]

INTRODUCTION

There has been considerable interest of late in research on stimulated emission from transversely bounded streams of relativistic electrons in free space or in homogeneous media. It has been shown in a number of studies[1–12] that such a stream can not only amplify electromagnetic radiation but can also play the role of an active waveguide, shaping the spatial structure of the field (in particular, it can channel the radiated wave). It has also been demonstrated that the efficiency of radiation into free space for such electron streams can exceed that under conventional conditions, where the transverse structure of the radiation is shaped by external electrodynamic systems. This is because the self-consistent structure of the field is more favorable for efficient braking of electrons on account of the automatic fine tuning of the synchronism conditions through a change in the angle at which the wave is radiated.

Channeling effects can exist for various types of stimulated emission (undulator, Čerenkov, cyclotron). Along with some universal properties of each mechanism of radiation there are also distinctive features even for identical beam geometries, in connection with the polarization of the radiated waves, the electron bunching mechanisms, etc.

This paper is devoted to a study of the cyclotron radiation of ribbon-shaped electron stream in a uniform magnetic field under conditions of the normal and anomalous Doppler effects. The linear stage of these processes was considered in Ref. 13. In the present paper we investigate the nonlinear stage of the interaction. We show that in the case of cyclotron radiation from a transversely bounded electron stream in a homogeneous (plasmalike) medium under conditions of the normal Doppler effect one can realize essentially total conversion of the energy of gyrational motion of the electrons into energy of electromagnetic oscillations. Under conditions of the anomalous Doppler effect the radiation in the initial stage is accompanied by an increase in the transverse momentum of the electrons. However, whereas in systems with a fixed transverse structure of the field the process has a reversible character, with the energy of translational motion being periodically converted into energy of transverse motion and energy of radiation and back again,[14] in an open system the process loses periodicity on account of the loss of radiation from the interaction region.

MODEL AND BASIC EQUATIONS

Suppose we have an electron stream of thickness d in the direction of the x axis and of unbounded extent in the y direction, the electrons of which move along helical trajectories in a uniform magnetic field $\mathbf{H}=H_0\mathbf{z}$ such that the thickness of the beam is much greater than the Larmor radius of the electrons. The field radiated by such a stream can be represented as a quasi-optical wave beam specified by a vector potential

$$\mathbf{A}=\mathrm{Re}\{(\mathbf{x}_0+i\mathbf{y}_0)A(x,z)\exp(i\omega t-ihz)\}, \qquad (1)$$

where $h=n\omega/c$, with n being the refractive index of the medium and c the speed of light, and $A(x,z)$ is a slowly varying complex amplitude of the field.

Let us also suppose that the condition of cyclotron resonance holds,

$$\omega-hV_\parallel=\omega_H, \qquad (2)$$

where $\omega_H=eH_0/mc\gamma$ is the gyrofrequency, $V_\parallel$ is the translational velocity of the particles, and γ is the relativistic mass factor.

In the quasi-optical approximation the self-consistent system of equations describing the interaction of the electron stream with the radiation field consists of the equation of motion of the electrons and the parabolic equation for the amplitude of the wave beam:

$$\frac{dw}{dZ}=-\frac{\hat{p}_\perp}{\hat{p}_\parallel}\mathrm{Re}\,(ia\exp(i\theta)),$$

$$\frac{d\theta}{dZ}=\frac{\Delta+\mu w-nq}{\beta_\|}-\frac{1-\beta_\| n}{\hat{p}_\perp\hat{p}_\|}\mathrm{Re}\,(a\exp(i\theta)),$$

$$\frac{dq}{dZ}=-\frac{\hat{p}_\perp}{\hat{p}_\|}\mathrm{Re}\left(i\frac{da}{dZ}\exp(i\theta)\right),$$

$$\frac{i}{2}\frac{\partial^2 a}{\partial X^2}+\frac{\partial a}{\partial Z}=i\frac{\omega_b^2}{2\omega^2 n}F(X)\frac{1}{2\pi}\int_0^{2\pi}\frac{\hat{p}_\perp}{\hat{p}_\|}\exp(-i\theta)d\theta_0 \tag{3}$$

with the boundary conditions $w_{|Z=0}=0$, $\theta_{|Z=0}=\theta_0+r\cos\theta_0$, $\theta_0\in[0,2\pi]$, $(r\ll 1)$, $q_{|Z=0}=0$, $a_{|Z=0}=a(X)$. Here we have used the following dimensionless variables: $\omega_b=(4\pi e^2N_0/m\gamma_0)^{1/2}$ is the ‘‘transverse’’ plasma frequency, N_0 is the unperturbed density of the electron stream, $Z=(\omega/c)z$, $X=(\omega/c)x$, $w=1-(\varepsilon/\varepsilon_0)$, $\varepsilon=mc^2\gamma$ is the electron energy, $\theta=\omega t-hz-\int_0^t\omega_H dt-\arg(p_x+p_y)$, $a=(eA)/(mc^2\gamma_0)$, $\mu=n^2-1$ is the inertial bunching parameter, $\Delta=1-n\beta_{\|0}-(\omega_{H_0}/\omega)$ is the initial detuning from cyclotron resonance,

$$\hat{p}_\|=\frac{p_\|}{mc}=\beta_{\|0}-nw,$$

$$\hat{p}_\perp=\frac{p_\perp}{mc}=(\beta_{\perp 0}-2(1-n\beta_\|)w+\mu w^2)^{1/2}$$

are the longitudinal and transverse momenta of the electrons, and $q=[c(p_\|-p_{\|0})-n(\varepsilon-\varepsilon_0)]/mc^2$ is a quantity characterizing the breakdown of the integral of the motion $n\varepsilon-cp_\|=\mathrm{const}$ on account of the influence of the electron stream on the relation between the electric and magnetic components of the field (see Refs. 14 and 15 for details).

In the linear theory[13] three cases were distinguished, viz., radiation from a stream of cyclotron oscillators in a plasmalike medium with a refractive index $n<1$ under conditions of the normal Doppler effect, radiation from such a stream in vacuum $(n=1)$, in which case an autoresonance effect takes place,[16–18] and radiation from an initially rectilinear electron beam in a homogeneous medium under conditions of the anomalous Doppler effect $(n>1)$. It was shown that in all these cases the electromagnetic field that is excited in the initial stage has the form of an amplified localized wave which grows exponentially along the z axis while simultaneously decaying exponentially in the transverse direction with distance from the axis of the system. For such a wave there is a transverse flow of electromagnetic energy directed from the beam toward the periphery.

In the present paper we use numerical methods to investigate the nonlinear stage of the interaction of electrons with the electromagnetic field for the cases mentioned above. Here, as in Ref. 13, we shall assume that the electron layer is thin on the scale of the Fresnel parameter, $d^2/\lambda L\ll 1$ (here L is the characteristic length of the interaction region). This will allow us to write the function $F(X)$ describing the transverse distribution of the beam density in the form $F(X)=D\delta(X)$, where $D=(\omega/c)d$.

HELICAL ELECTRON BEAM IN A MEDIUM (PLASMA) WITH A REFRACTIVE INDEX *n*<1

For the numerical calculation we introduce the new variable $P=\sqrt{1-u}\exp(i\theta)$, where

$$u=w\frac{2}{\beta_{\perp 0}^2}(1-n\beta_{\|0}).$$

Then the system of Eqs. (3) reduces to the form

$$\frac{dP}{d\hat{Z}}+\frac{iP}{1-b(1-P^2)}(\hat{\Delta}-1+|P|^2-b\hat{q})=\frac{i\hat{a}}{1-b(1-|P|^2)}, \tag{4a}$$

$$\frac{d\hat{q}}{d\hat{Z}}=-2\frac{\mathrm{Re}\left(P^*\dfrac{d\hat{a}}{d\hat{Z}}\right)}{1-b(1-|P|^2)}, \tag{4b}$$

$$i\frac{\partial^2\hat{a}}{\partial\hat{X}^2}+\frac{\partial\hat{a}}{\partial\hat{Z}}=2iI\frac{1}{\pi}\int_0^{2\pi}\frac{Pd\theta_0}{1-b(1-|P|^2)}\delta(\hat{X}) \tag{4c}$$

with the boundary conditions

$$P|_{Z=0}=\exp(i\theta_0),\quad \theta|_{Z=0}=\theta_0+r\cos\theta_0,$$

$$\theta_0\in[0,2\pi],\quad (r\ll 1),\quad \hat{q}|_{Z=0}=0,\quad a|_{Z=0}=0. \tag{5}$$

Here

$$\hat{Z}=Z\frac{\beta_{\perp 0}^2|\mu|}{2\beta_{\|0}(1-n\beta_{\|0})},\quad \hat{X}=X\sqrt{\frac{\beta_{\perp 0}^2|\mu|}{2\beta_{\|0}(1-n\beta_{\|0})}},$$

$$\hat{a}=a\frac{2(1-n\beta_{\|0})^2}{\beta_{\perp 0}^3|\mu|},\quad \hat{q}=q\frac{4\beta_{\|0}(1-n\beta_{\|0})^2}{\beta_{\perp 0}^4|\mu|},$$

$$\hat{\Delta}=\Delta\frac{2(1-n\beta_{\|0})}{\beta_{\perp 0}^2\mu},\quad b=\frac{\beta_{\perp 0}^2}{2\beta_{\|0}n(1-n\beta_{\|0})},$$

$$I=\frac{1}{2}\frac{\omega_b^2 d}{\omega^2 c}\frac{\beta_{\|0}^{1/2}(1-n\beta_{\|0})^{5/2}}{\beta_{\perp 0}^3 n^{1/2}|\mu|^{3/2}}.$$

The results of the numerical modeling of the system of equations (4) are presented in Figs. 1 and 2. Analysis of the spatial distribution of the radiated field shows that in the linear stage of the interaction, independently of the initial conditions, at sufficient distances from the entrance cross section (Fig. 2, $Z\sim 60$) the structure of the radiated field is close to that of a localized mode.[13] Thus, in the linear stage of the interaction a regime of amplification and channeling of the radiation emitted by the electron beam occurs. In the nonlinear stage a broadening of the wave beam occurs, accompanied by the gradual radiating away of energy into the outside space. In this stage a mechanism of stochastic braking of the electrons occurs, in which the energy of the particles is converted to energy of radiation, which consists of an ensemble of waves having the same frequency but differ-

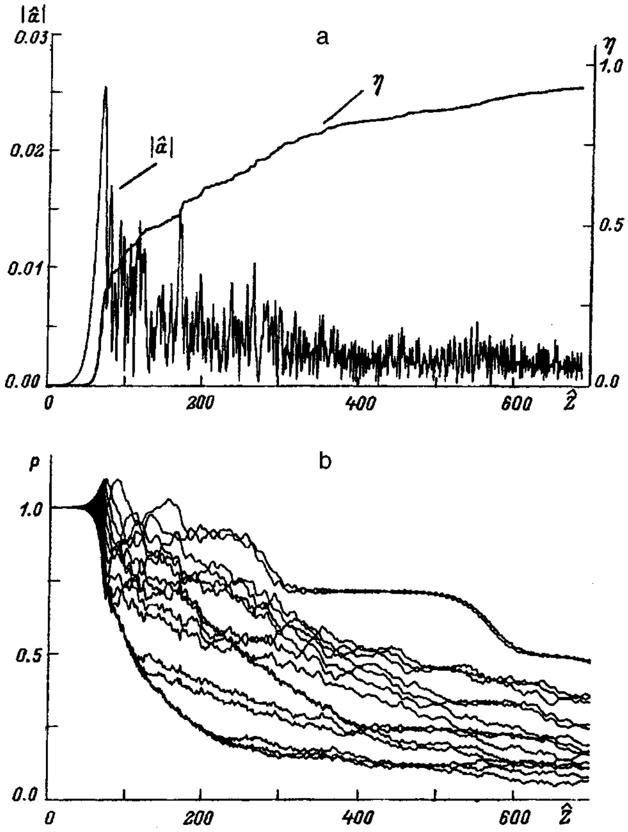

FIG. 1. The amplitude $|\hat{a}|_{|\hat{X}=0}$ of the radiated wave and the electronic efficiency η (a) and the transverse momentum of the electrons (b) as functions of the longitudinal coordinate in the case of radiation by an electron beam in a medium with a refractive index $n<1$ ($I=0.001$, $b=0.5$, $\Delta=0$).

ent wave numbers, i.e., angles of propagation with respect to the axis of the system (see the transverse spectrum of the field,

$$S_{\chi}=\frac{1}{\sqrt{\pi}}\int_{-\infty}^{+\infty} a \exp(i_{\chi}X)\,dX,$$

in Fig. 2). The mechanism of stochastic braking in this case is realized even in the case of exact initial synchronism, $\Delta=0$, unlike the case of the free-electron laser (FEL), for example.[10] The fact is that whereas in Čerenkov devices[11] and FELs the particles as they are braked interact synchronously with waves propagating at smaller and smaller angles, in our case the decelerating particles interact synchronously with waves radiated at larger and larger angles to the axis of the system (cf. Ref. 12). Indeed, it is easy to see that the increment $\Delta\psi^2$ of the angle at which a synchronous wave is radiated is related to the change $\Delta\gamma$ in electron energy as

$$\Delta\psi^2=\frac{2\mu}{n\beta_{\parallel}}\,\frac{\Delta\gamma}{\gamma_0}. \tag{6}$$

In the given case ($n<1$) we have $\mu<0$, and so $\Delta\psi>0$ for $\Delta\gamma<0$. From this we can also understand the nature of the evolution of the spectrum in Fig. 2. Whereas in a FEL in the nonlinear stage there occurs a filling of the spectrum by components with small transverse wave numbers χ, here, on the contrary, the spectrum becomes sparser as the electrons are braked. As a result, as can be seen from Fig. 2, there is practically complete transfer of the transverse energy of the electrons to energy of radiation, i.e., the electronic efficiency

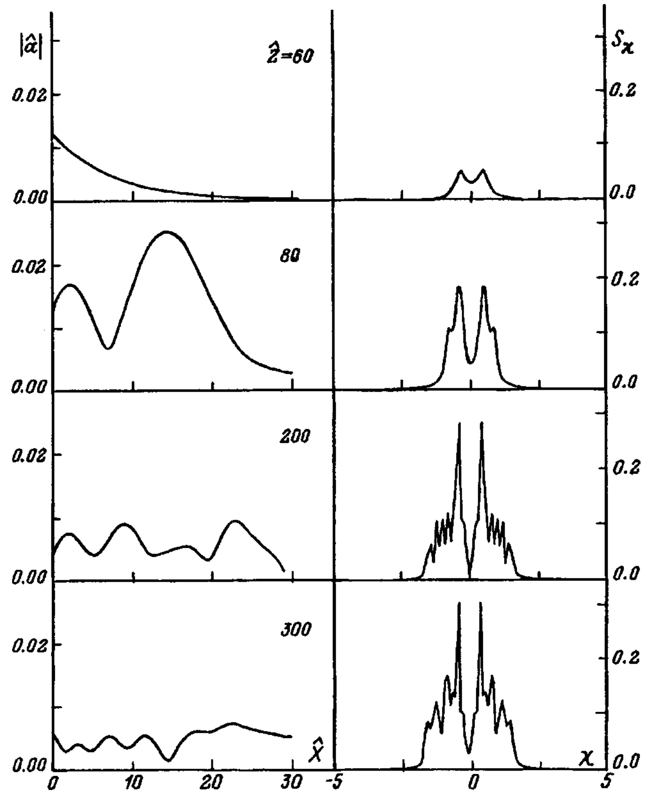

FIG. 2. Evolution of the transverse distribution of the modulus of the electromagnetic field amplitude $|\hat{a}|$ and of the angular spectrum S_{χ} for the case of radiation in a medium with refractive index $n<1$.

$$\eta=1-1/2\pi\int_0^{2\pi}|P|^2\,d\theta_0$$

approaches unity (see also Ref. 12).

HELICAL ELECTRON BEAM IN VACUUM ($n=1$)

In this case, as we know,[16–18] an autoresonance effect occurs wherein the main mechanisms of inertial bunching, the azimuthal and longitudinal, which are due to the energy dependence of the electron gyrofrequency and translational velocity, respectively, cancel each other out. As a result, the inertial bunching parameter μ goes to zero. In this case the possibility of radiation is provided by additional mechanisms, e.g., a rearrangement of the wave structure, as a result of which the autoresonance breaks down.[14,15]

Setting $\mu=0$ in the overall system of equations (3), we reduce the equation for the transverse momentum to the form

$$\frac{dP}{d\hat{Z}}+\frac{iP}{1-b(1-P^2)}(\hat{\Delta}-b\hat{q})=\frac{i\hat{a}}{1-b(1-|P|^2)}.$$

The remaining equations and boundary conditions retain the form in (4a)–(4c) and (5), with the normalized variables are taken as

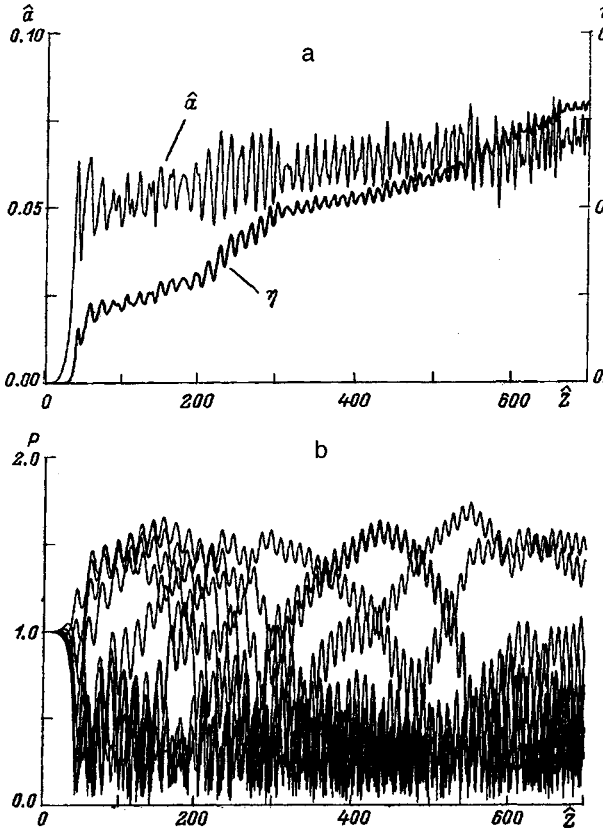

FIG. 3. The same as in Fig. 1 but for the case of radiation by an electron layer in vacuum ($n=1$): $I=0.1$, $b=0.7$, $\Delta=0$.

$$\hat{Z}=Z\frac{\beta_{\perp 0}^2}{2\beta_{\parallel 0}(1-\beta_{\parallel 0})},\quad \hat{X}=X\sqrt{\frac{\beta_{\perp 0}^2}{2\beta_{\parallel 0}(1-\beta_{\parallel 0})}},$$

$$\hat{a}=a\frac{2(1-\beta_{\parallel 0})^2}{\beta_{\perp 0}^3},\quad \hat{q}=q\frac{4\beta_{\parallel 0}(1-\beta_{\parallel 0})^2}{\beta_{\perp 0}^4},$$

$$\hat{\Delta}=\Delta\frac{2\beta_{\parallel}(1-\beta_{\parallel 0})}{\beta_{\perp 0}^2},\quad b=\frac{\beta_{\perp 0}^2}{2\beta_{\parallel 0}(1-\beta_{\parallel 0})},$$

$$I=\frac{1}{2}\,\frac{\omega_b^2 d}{\omega c}\,\frac{\beta_{\parallel 0}^{1/2}(1-\beta_{\parallel 0})^{5/2}}{\beta_{\perp 0}^3}.$$

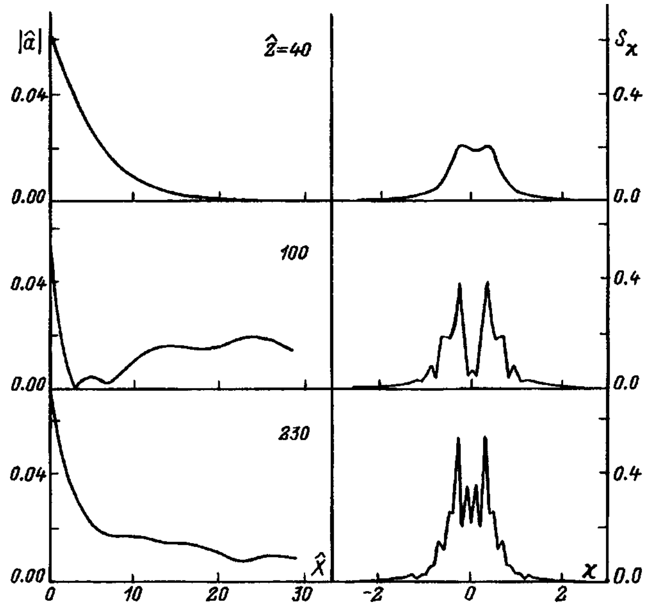

FIG. 4. The same as in Fig. 2 but for the radiation from an electron layer in vacuum under autoresonance conditions.

A numerical investigation showed that, in spite of the cancellation of the main inertial bunching mechanisms, the amplification and channeling of the radiation by a helical electron stream actually do occur at a sufficiently high initial transverse velocity of the electrons, when the condition $b>0.5$, obtained in a linear analysis,[13] is met. Accordingly, in the initial linear stage an amplified localized mode is formed (Fig. 3 and 4), the parameters of which (the growth rate and transverse decay scale of the field) are in good agreement with the results of the linear theory. However, as can be seen from a comparison of Fig. 1a and 3a, in this case the process develops considerably more slowly. Indeed, at high injection currents and initial gyrational velocities of the electrons the transverse efficiency reaches only 30% in this case, as compared to 90% in the case $n<1$ for the same normalized interaction length ~ 700. Nevertheless, as the numerical modeling showed, under conditions of autoresonance the efficiency also approaches unity asymptotically at large interaction lengths. An interesting feature of this regime is the strong oscillations of the transverse momentum and, accordingly, of the energy of certain electron fractions. The evolution of the transverse structure of the field and radiation spectrum is shown in Fig. 4. As in the previous case, upon saturation of the field in the electron channel there occurs an effective broadening of the region occupied by the electromagnetic field, on account of waves radiated in the preceding cross sections along the z axis.

RECTILINEAR ELECTRON BEAM IN A MEDIUM WITH REFRACTIVE INDEX $n>1$

As the linear theory shows, for a rectilinear electron stream the amplified localized modes exist only under conditions of the anomalous Doppler effect, $n\beta>1$. Because all of the electrons of a rectilinear beam initially have the same phase θ relative to the electromagnetic wave (unlike the case of a helical beam, where they take on any values from 0 to 2 π), the system of equations (3) simplifies substantially. Instead of an infinite number of equations describing the motion of the different fractions of the helical beam, the motion of an initially rectilinear electron stream is specified by two equations. Accordingly, there is no averaging over the entry phases in the equation of excitation, and the self-consistent system of equations (3) for $\beta_{\perp 0}=0$ can be reduced to the form

$$\frac{dP}{d\hat{Z}}+\frac{iP}{1-b|P|^2}(\hat{\Delta}+|P|^2-b\hat{q})=-\frac{i\hat{a}}{1-b|P|^2},$$

$$\frac{d\hat{q}}{d\hat{Z}}=-2\frac{\mathrm{Re}\left(P^*\dfrac{d\hat{a}}{d\hat{Z}}\right)}{1-b|P|^2},$$

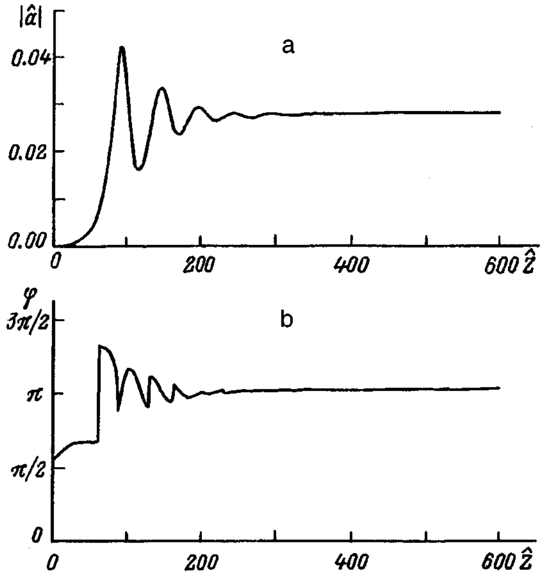

FIG. 5. Amplitude of the radiated field (a) and the phase difference φ (b) in the case of radiation by a rectilinear electron beam in a medium with refractive index $n>1$ under conditions of the anomalous Doppler effect: $I=0.05$, $b=0.2$, $\Delta=0$.

$$i\frac{\partial^2\hat{a}}{\partial\hat{X}^2}+\frac{\partial\hat{a}}{\partial\hat{Z}}=2iI\frac{P}{1-b|P|^2}\,\delta(\hat{X}) \tag{8}$$

with the boundary conditions [cf. Eq. (5)]

$$P|_{Z=0}=0,\quad \hat{q}|_{Z=0}=0,\quad a|_{Z=0}=a_0(\hat{X}). \tag{9}$$

Here

$$P=\sqrt{u}\exp(i\theta),\quad u=w\frac{2(n\beta_{\|0}-1)}{\beta_{\|0}},$$

$$\hat{Z}=Z\frac{\mu\beta_{\|0}}{2(n\beta_{\|0}-1)},\quad \hat{X}=X\sqrt{\frac{\beta_{\|0}\mu}{2(n\beta_{\|0}-1)}},$$

$$\hat{a}=a\frac{2(n\beta_{\|0}-1)^2}{\beta_{\|0}^3},\quad \hat{q}=q\frac{4(n\beta_{\|0}-1)^2}{\beta_{\|0}^3\mu},$$

$$\hat{\Delta}=\Delta\frac{2(n\beta_{\|0}-1)}{\mu\beta_{\|0}},\quad b=\frac{n\beta_{\|0}}{2(n\beta_{\|0}-1)},$$

$$I=\frac{\omega_b^2 d}{\omega c}\,\frac{(n\beta_{\|0}-1)^{3/2}}{\mu^{3/2}n^{1/2}\beta_{\|0}^{5/2}}.$$

The field structure formed in the initial stage is analogous to the two cases considered previously, i.e., there is excitation of an amplified localized mode (Figs. 5 and 6). Here it is interesting to note that in the nonlinear stage the behavior of the system is substantially different from the previously investigated[14] case of radiation under conditions of the anomalous Dopper effect in the approximation of a fixed transverse structure of the field, in particular, for waveguide propagation of radiation. Although initially in the case of a fixed transverse structure there is conversion of the energy of longitudinal motion of the particles into energy of transverse motion and electromagnetic field energy, later on, as a consequence of the conservative nature of the system, the process goes in the reverse direction: the energy of the electromagnetic field and transverse electron oscillations falls off, and the energy of longitudinal motion of the particles increases back to its original value. As a result, there is a periodic transfer of energy. For the radiation of a bounded stream of initial unexcited oscillators in a homogeneous medium, the loss of energy from the interaction region causes the amplitude of these oscillations to decay (Fig. 5). Ultimately, at a sufficiently great length of the working space the interaction of the electrons and electromagnetic field acquires a reactive character, i.e., the phase φ of the field relative to the phase of the transverse electron current approaches π (Fig. 5b). In that case the bounded electron stream acts as an effective dielectric, channeling the radiation without amplifying it. Accordingly, the field profile that is formed remains practically unchanged for $Z>400$ (Fig. 6).

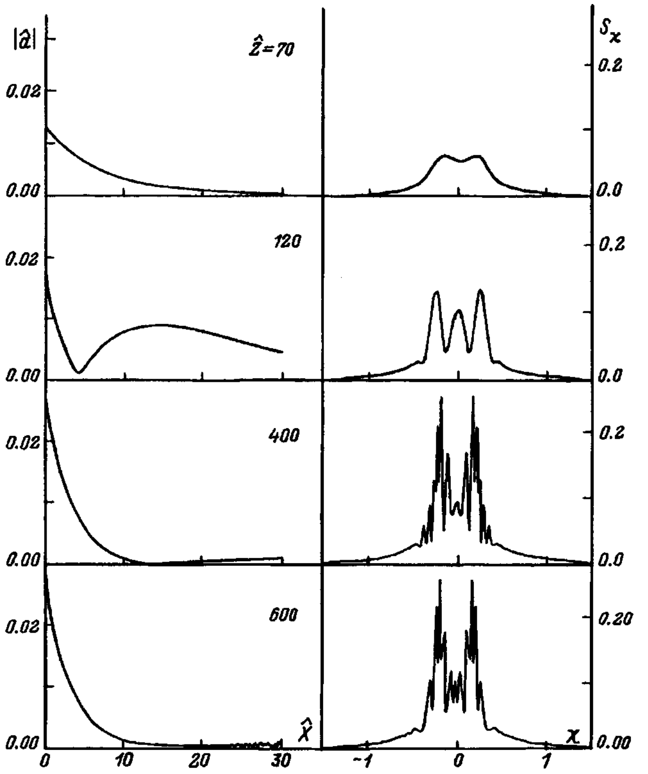

FIG. 6. Profile of the wave beam and the angular spectrum as functions of the longitudinal coordinate for radiation by an electron beam under conditions of the anomalous Doppler effect.

[1] N. F. Kovalev and M. I. Petelin, in *Relativistic Radio-Frequency Electronics* [in Russian], edited by A. V. Gaponov-Grekhov, Institute of Applied Physics, Academy of Sciences of the USSR, Gorki (1981), No. 2, pp. 63–75.

[2] C. M. Tang and P. Sprangle, Phys. Quantum Electron. **9**, 849 (1982).

[3] A. M. Kondratenko and E. L. Saldin, Zh. Tekh. Fiz. **51**, 1633 (1981) [Sov. Phys. Tech. Phys. **26**, 937 (1981)].

[4] V. I. Kanavets, A. V. Korzhenevskiĭ, and V. A. Cherepenin, Radiotekh. Élektron. **30**, 2202 (1985).

[5] N. S. Ginzburg, Opt. Commun. **43**, 203 (1982).

[6] N. S. Ginzburg, N. F. Kovalev, and N. Yu. Rusov, Opt. Commun. **46**, 300 (1983).

[7] N. S. Ginzburg and N. F. Kovalev, Pis'ma Zh. Tekh. Fiz. **13**, 274 (1987) [Sov. Phys. Tech. Phys. **13**, 112 (1987)].

[8] E. T. Scharlemann, A. M. Sessler, and I. S. Wurtele, Phys. Rev. Lett. **54**, 1925 (1985).

[9] G. T. Moor, Nucl. Instrum. Methods Phys. Res. A **250**, 381 (1986).

[10] N. S. Ginzburg and N. F. Kovalev, Pis'ma Zh. Tekh. Fiz. **13**, 274 (1987) [Sov. Phys. Tech. Phys. **13**, 112 (1987)].

[11] N. S. Ginzburg, I. V. Zotova, N. F. Kovalev, and A. S. Sergeev, Zh. Éksp. Teor. Fiz. **104**, 3940 (1993) [JETP **77**, 893 (1993)].

[12] N. S. Ginzburg, I. V. Zotova, and A. S. Sergeev, Phys. Lett. A **186**, 235 (1994).

[13] N. S. Ginzburg, Fiz. Plazmy **15**, 1274 (1989) [Sov. J. Plasma Phys. **15**, 739 (1989)].

[14] V. L. Bratman, N. S. Ginzburg, G. S. Nusinovich *et al.*, in *Relativistic Radio-Frequency Electronics* [in Russian], edited by A. V. Gaponov-Grekhov, Institute of Applied Physics, Academy of Sciences of the USSR, Gorki (1979), No. 1, pp. 157–217.

[15] N. S. Ginzburg, I. G. Zarnitsyna, and G. S. Nusinovich, Izv. Vyssh. Uchebn. Zaved. Radiofiz. **24**, 481 (1981).

[16] A. A. Kolomenskiĭ and A. N. Lebedev, Dokl. Akad. Nauk SSSR **145**, 1259 (1962) [Sov. Phys. Dokl. **7**, 745 (1963)].

[17] V. Ya. Davydovskiĭ, Zh. Éksp. Teor. Fiz. **43**, 886 (1962) [Sov. Phys. JETP **16**, 629 (1963)].

[18] A. V. Gaponov, Zh. Éksp. Teor. Fiz. **39**, 326 (1960) [Sov. Phys. JETP **12**, 232 (1960)].

Translated by Steve Torstveit

TECHNICAL PHYSICS VOLUME 44, NUMBER 1 JANUARY 1999

Autodyne detection in a semiconductor laser as the external reflector is moved

A. V. Skripal', D. A. Usanov, V. A. Vagarin, and M. Yu. Kalinkin

N. G. Chernyshevski Saratov State University, 410601 Saratov, Russia

(Submitted June 16, 1997)
Zh. Tekh. Fiz. **69**, 72–75 (January 1999)

An analysis is made of how the emission amplitude and frequency of a semiconductor laser with external optical feedback change as the external reflector is moved. It is shown that the influence of the external optical feedback on the interference signal from vibrations of the reflector can be lessened not only by lowering the feedback level but also through the choice of the distance to the vibrating object. © *1999 American Institute of Physics.* [S1063-7842(99)01101-0]

There is significant interest in the autodyne detection effect in semiconductor lasers on account of the possibility of using them in simple sensors with a high sensitivity to a reflected signal.[1,2] However, in sensors of this kind the influence of the external optical feedback distorts interference signal, and it turns out to be problematical to use the well-developed theory of homodyne interferometry.

For a semiconductor laser operating in the autodyne regime we have attempted to find conditions that would minimize the influence of the external optical feedback on the interference signal formed when the external reflector is undergoing harmonic vibrations.

The theoretical analysis is done using the composite cavity model.[3,4] In the approximation of a steady field the expressions for the amplitude of the electric field E, the carrier density N in the active region of the laser, and the frequency ω of the output mode of the laser with an external cavity can be written in the form of the following system of equations:[5]

$$E^2=(J-N/\tau_s)/G(N), \tag{1}$$

$$G_N(N-N_{\rm th})=-2\frac{k}{\tau_{\rm in}}\cos\omega\tau, \tag{2}$$

$$\omega_0\tau=\omega\tau+\frac{\tau}{\tau_{\rm in}}=k(1+\alpha^2)^{1/2}\sin(\omega\tau+\psi), \tag{3}$$

where the angle $\psi=\arctan(\alpha)$, ω_0 is the resonance frequency of the internal cavity of the laser diode, $G(N)$ is the gain, J is the number of carriers injected into a unit volume per unit time, τ_s is the carrier lifetime with respect to spontaneous recombination, $\tau_{\rm in}$ is the round-trip time of the radiation in the diode cavity, τ is the round-trip time of the external cavity, k is the feedback coefficient, G_N is the differential gain, α is the coefficient of broadening of the laser line, $N_{\rm th}$ is the carrier density at the lasing threshold of the laser diode in the absence of feedback.

Equation (2) characterizes the gain of a mode with a frequency ω that is a solution of the phase equation (3) for a semiconductor laser with a composite cavity. Substituting (2) into (1) and neglecting the dependence of the gain G on the carrier density N, we obtain the signal of the autodyne system:

$$E^2=A+B\cos(\omega\tau), \tag{4}$$

where $A=J/G-N_{\rm th}(G\tau_s)^{-1}$, and $B=2k(GG_N\tau_s\tau_{\rm in})^{-1}$.

In the week feedback regime, $k(1+\alpha^2)^{1/2}(\omega_0\tau_{\rm in})^{-1}\ll 1$, the solution of Eq. (3) can be written in the form

$$\omega=\omega_0-X\sin(\omega_0\tau+\psi), \tag{5}$$

where $X=(k/\tau_{\rm in})(1+\alpha^2)^{1/2}$.

For an object vibrating in accordance with a sinusoidal law the round-trip time of the external cavity can be written as a harmonic function of the time t:

$$\tau=\tau_0+\tau_a\sin(\Omega t+\varepsilon),$$

where $\tau_a=2\xi/c$, ξ and Ω are the amplitude and frequency of the vibrations of the reflector, ε is the initial phase, and c is the speed of light.

Then expression (4) for the normalized variable component of the field amplitude can be written in the form

$$E_0^2=\cos(\omega_0\tau_0+\omega_0\tau_a\sin(\Omega t+\varepsilon)-\tau_0X\sin[\omega_0\tau_0+\psi+\omega_0\tau_a\sin(\Omega t+\varepsilon)]). \tag{6}$$

Expression (6) describes the envelope of the interference signal formed when the external mirror in an autodyne system is vibrating. In the case of low feedback, when the third term in the argument of the cosine can be neglected, expression (6) reduces to the well-known relation from the theory of homodyne measurements:

$$E_0^2=\cos[\theta+\sigma\sin(\Omega t+\varepsilon)], \tag{7}$$

where $\theta=\omega_0\tau_0$, $\sigma=4\pi\xi/\lambda$, where λ is the wavelength of the laser radiation.

The spectrum of a function of the form (7) is determined by the coefficients of the series expansion in the Bessel functions

$$E_0^2=\cos\theta J_0(\sigma)+2\cos\theta\sum_{n=1}^{\infty}J_{2n}(\sigma)\cos[2n(\Omega t+\varepsilon)]-2\sin\theta\sum_{n=1}^{\infty}J_{2n-1}(\sigma)\cos[(2n+1)(\Omega t+\varepsilon)]. \tag{8}$$

It follows from expression (8) that for $\theta=\pi n$, where $\eta=0,1,2,\ldots$, the spectrum contains only even harmonics, while for $\theta=\pi/2+\pi n$ it contains only odd harmonics.

The amplitude of the vibrations of the reflector can be reconstructed from the spectrum of the interference signal; e.g., for three even or odd harmonics it is given by the relation[6]

$$\xi^2=\frac{\lambda^2}{4\pi^2}\,\frac{n(n+1)(n+2)J_{n+1}(\sigma)}{(n+2)J_{n-1}(\sigma)+2(n+1)J_{n+1}(\sigma)+nJ_{n+3}(\sigma)}. \tag{9}$$

The choice of this method specifically is motivated by the possibility of using the even and odd harmonics separately.

A computer simulation was carried using the system of equations (1)–(3). The change of the laser frequency when the mirror undergoes harmonic vibrations was determined from the solution of the transcendental equation (3). The time dependence of the square of the field as calculated using Eq. (6) was expanded in a Fourier series, and then Eq. (9) was used to find the amplitude of the vibrations from three harmonics, both even-numbered and odd-numbered.

Figure 1 shows the results of a calculation of the amplitudes of the vibrations of the object using different sets of odd and even harmonics of the spectrum of the interference signal for different levels of feedback and with $\alpha=5$. The results of the calculation are given for the amplitudes in units of the original specified value ξ_0 of the vibration amplitude of the object. As we see from Fig. 1, at phase shifts $\theta=\omega_0\tau_0$ close to the values $\pi/2+\pi n$ for the even spectral components and to πn for the odd, the error of the calculation using expression (9) increases sharply on account of the decrease to zero of either the even or the odd components in the spectrum of the autodyne signal. For phases of the interference signal outside the region near $\theta=\pi/2+\pi n$ for the even and $\theta=\pi n$ for the odd spectral components, as can be seen by comparing Figs. 1a and 1b, one observes an increase in the error in calculating the amplitudes of the vibrations of the reflector with the use of different sets of harmonics as the level of the external feedback increases; this can be attributed to an increase in the influence of the feedback level. However, as we see from Fig. 1, there exist regions of values of the stationary phase shift for which the amplitudes of the vibrations of the object as calculated using different sets of harmonics of the spectrum of the autodyne signal agree with one another and depend comparatively weakly on the feedback level.

The result obtained follows from an analysis of expression (6). Indeed, with the notation $H=\sigma\sin(\Omega t+\varepsilon)$, expression (6) can be written in the form

$$E_0^2=\cos[\omega_0\tau_0+H-\tau_0X\sin(\omega_0\tau_0+H+\psi)]. \tag{10}$$

A mathematical description of the behavior of the function (10) can be carried out for values of the angle ψ equal to $\pi n/2$. For example, for $\psi=\pi/2$ relation (10) is written

$$E_0^2=\cos[\omega_0\tau_0+H+\tau_0X\cos(\omega_0\tau_0+H)]. \tag{11}$$

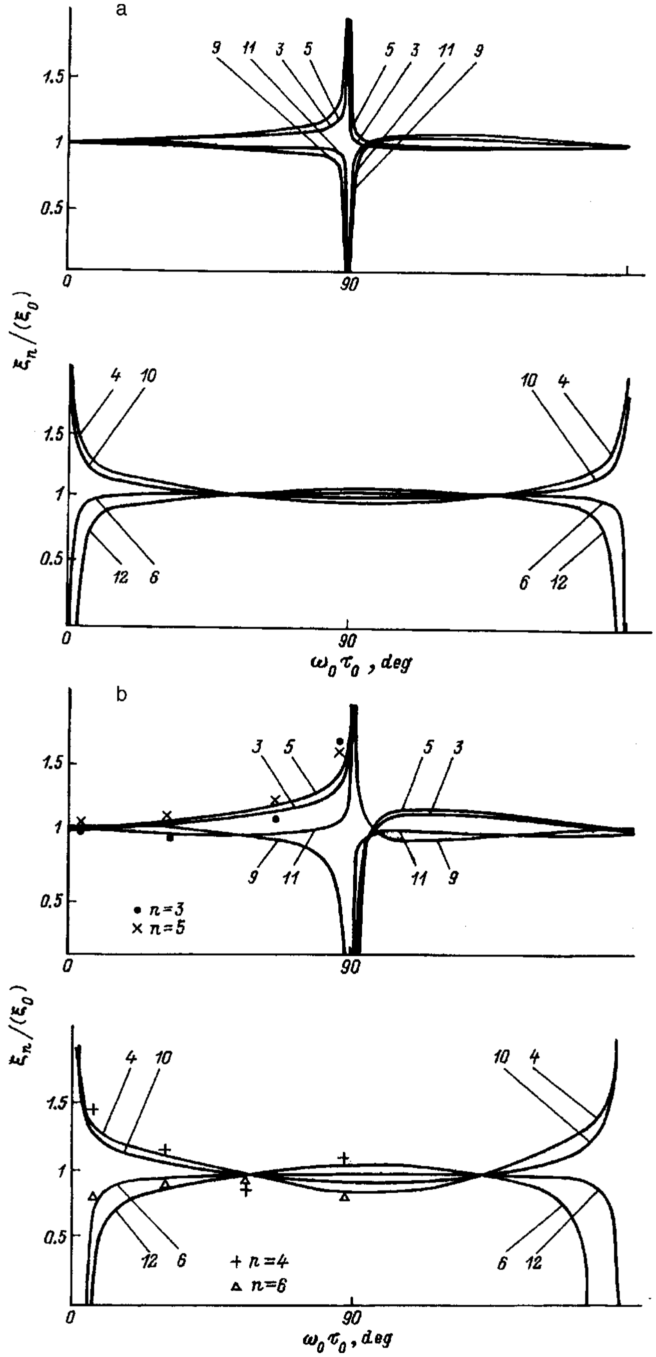

FIG. 1. Curves of the vibration amplitude calculated from a set of spectral components $(n-1,\ n+1,\ n+3)$ with numbers n versus the phase shift for different levels of feedback: $C=0.05$ (a), 0.1 (b); $n=3$ (●), 4 (+), 5 (×), 6 (△).

Let us consider the behavior of the autodyne signal function at values of the phase of the interference signal in the region near $\theta=\omega_0\tau_0=\pi n$. In this case relation (11) becomes

$$E_0^2=\cos H-(\tau_0X/2)\sin 2H, \tag{12}$$

the first and second terms of which can be represented as expansions in Bessel functions of only even and only odd order, respectively:

$$\cos H=\cos[\sigma\sin(\Omega t+\varepsilon)]=\cos\theta J_0(\sigma)$$

$$+2\cos\theta\sum_{n=1}^{\infty}J_{2n}(\sigma)\cos[2n(\Omega t+\varepsilon)], \tag{13}$$

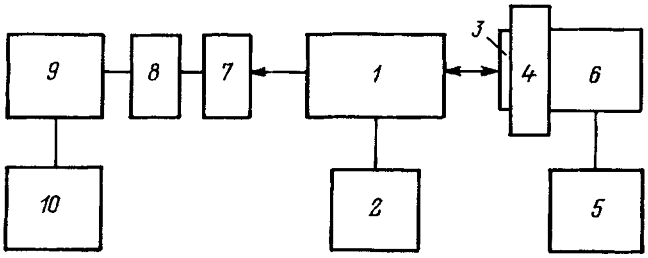

FIG. 2. Block diagram of the experimental apparatus.

$$-(\tau_0 X/2)\sin 2H = -\tau_0 X/2 \sin[2\sigma \sin(\Omega t+\varepsilon)] = \tau_0 X \sin\theta \sum_{n=1}^{\infty} J_{2n-1}(\sigma)\cos[(2n+1) \times(\Omega t+\varepsilon)]. \qquad (14)$$

The use of formula (9), which contains Bessel functions of even and odd orders separately, enables one to reconstruct the amplitude of the vibrations of the object for the region of phase values under consideration, $\theta=\omega_0\tau_0$. When the amplitude coefficients in the spectrum of even and odd harmonics are taken into account, one can establish that for the case under discussion the amplitudes of the odd harmonics described by relation (14) are significantly lower than the amplitudes of the even harmonics. Consequently, for reconstructing the amplitudes of the vibrations it is preferable to use the amplitudes of the even harmonics, the character of which, moreover, corresponds completely to the behavior of the spectrum of even harmonics in the absence of the autodyne frequency shift in the output of a semiconductor laser.

An analogous treatment of the behavior of the autodyne signal at values of the phase in the region $\omega_0\tau_0=\pi/2+\pi n$ and angle $\psi=0$ leads to the relation

$$E_0^2 = -\sin H - (\tau_0 X/2)(\cos H)^2, \qquad (15)$$

from which it follows that for reconstructing the amplitudes of the vibrations at values of the phase in the region $\theta=\omega_0\tau_0=\pi/2+\pi n$ it is preferable the use the amplitudes of the odd harmonics, which are described by the first term of relation (15). The observed character of the behavior of the signal spectrum of an autodyne system suggests that for decreasing the influence of the feedback level it is advisable to adjust the system prior to the measurements by changing the distance to the external reflector, employing for the purpose a vibrator with a calibrated vibration amplitude.

Figure 2 shows a block diagram of the experimental apparatus. The radiation from a semiconductor laser *1* (ILPN-206), stabilized by a current source *2*, was directed onto an object *3*, which was mounted on a piezoceramic *4*, the vibrations of which are excited by a sound wave generator *5*. There were provisions for translating the vibrating object by a micrometer mechanism *6*. A portion of the radiation reflected from the object was returned to the cavity of the semiconductor laser, the change in the output power of which was detected by a photodetector *7*. The signal from the photodetector was sent to an amplifier *8* and then to an analog-to-digital converter *9* and a computer *10*. After the spectrum of the detected signal was calculated, the amplitude of the vibrations of the object was determined by a fast Fourier transform according to three even and according to three odd harmonics of the signal. The results of the measurements of the vibration amplitude according to the different sets of harmonics are presented in Fig. 1. When the distance to the object and, hence, the phase of the reflected radiation was varied, the spread in values of the measured amplitudes varied from 75% to 12% of the reference value of the vibration amplitude of the control object; this indicates that there are regions of values of the phase of the interference signal which give a smaller spread in the vibration amplitudes calculated by means of reflection (9).

In summary, these investigations have shown that the autodyne detection signal formed by the motion of an external reflector in a semiconductor laser is substantially affected by the level of feedback and by the distance to the moving object. It is ordinarily assumed when using sensors based on the autodyne detection effect that at a low feedback level the vibration amplitudes of the the external reflector can be determined using formulas valid for homodyne interference systems. Decreasing the level of feedback entails a decrease in the detected signal, which leads to an increase in the error in the calculated vibration amplitudes of the object on account of the increased importance of noise in the system. We have shown that there are distances to the external reflector for which one can determine the vibration amplitudes of the object to high accuracy. At values of the stationary phase shift in the region corresponding to these preferred distances to the external reflector the spectrum of the signal of an autodyne system with a harmonically vibrating reflector separates in such a way that either the even or the odd harmonics of the spectrum convey an undistorted interference signal similar to the signal known from the theory of homodyne interference.

[1] E. M. Gershenzon, B. N. Tumanov, and B. I. Levit, Izv. Vyssh. Uchebn. Zaved. Radiofiz. **23**, 535 (1980).

[2] Van Lyk Vu, P. N. Eliseev, M. A. Man'ko, and M. V. Tsotsoriya, *Injection Lasers and Their Applications* [in Russian], Nauka, Moscow (1992), pp. 144–172.

[3] R. Lang and K. Kobayashi, IEEE J. Quantum Electron. **QE-16**, 347 (1980).

[4] B. Tromborg, J. H. Osmundsen, and H. Olesen, IEEE J. Quantum Electron. **QE-20**, 1023 (1984).

[5] H. Olesen, J. H. Osmunsen, and B. Tromborg, IEEE J. Quantum Electron. **QE-22**, 762 (1986).

[6] D. A. Usanov, A. V. Skripal', V. A. Vagarin, and M. R. Vasil'ev, Zarubezhnaya Radioélektronika, No. 6, pp. 43–48 (1995).

Translated by Steve Torstveit

TECHNICAL PHYSICS VOLUME 44, NUMBER 1 JANUARY 1999

Efficiency of an electron-beam-pumped chemical laser with an SF_6–H_2 working mixture

V. M. Orlovskiĭ, É. A. Sosnin, and V. F. Tarasenko

Institute of High-Current Electronics, Siberian Branch of the Russian Academy of Sciences, 634055 Tomsk, Russia

A. G. Ponomarenko and Yu. I. Khapov

Insitute of Laser Physics, Siberian Branch of the Russian Academy of Sciences, 634090 Novosibirsk, Russia

(Submitted July 8, 1997; resubmitted January 20, 1998)
Zh. Tekh. Fiz. **69**, 76–81 (January 1999)

Results are presented from a study of HF lasers pumped by non-chain chemical reactions initiated by a radially convergent and by a planar electron beam. The main channels of formation of vibrationally excited HF molecules are analyzed. The distribution of the energy density of the radiation in the output beam of a wide-aperture laser is measured. In 30 liters of a mixture of $SF_6:H_2=8:1$ at a pressure of 1.1 atm an output energy of ~200 J is obtained at an ~11% efficiency with respect to the energy deposition. It is shown that the admixture of a buffer gas of neon or argon improves the uniformity of the radiation energy distribution in the output beam of an HF laser pumped by a non-chain chemical reaction and initiated by an electron beam, and it also increases the output energy.
[S1063-7842(99)01201-5]

INTRODUCTION

There has recently been considerable interest in the study of HF and DF chemical lasers,[1–8] including ones which are pumped by non-chain chemical reactions.[2,6–8] This is due to the new possibilities for using lasers with high energy characteristics in the IR region of the spectrum. The chemical reactions are initiated by electron beams, discharges, optical radiation, and other means. The maximum pulse energy and specific energy of the radiation has been achieved for HF lasers (output wavelength $\lambda \approx 2.6$–$3.2\,\mu$m) with pumping by chain reactions. For many practical applications, however, it is more suitable to use HF and DF chemical lasers pumped by non-chain reactions, which, although they have substantially poorer energy characteristics, offer simplicity and safety in use. The main results of chemial laser research prior to 1982 are summarized in several monographs[9,10] and, less comprehensively, in a dissertation.[11] However, the maximum efficiency that can be achieved in HF and DF lasers pumped by non-chain chemical reactions remains an open question.

In this paper we present results of a study of the efficiency of HF lasers pumped by non-chain chemical reactions initiated by an electron beam. This study is a continuation of our previous research.[7,11]

EXPERIMENTAL DEVICES AND PROCEDURES

The experiments were done on two devices. The first (device No. 1) was an electron accelerator producing a ribbon-shaped electron beam with geometric dimensions of 3×20 cm, duration ~15 ns at half height, electron energy up to 150 keV, current up to 6.5 kA, and a laser chamber with an excited volume of 124 cm^3 (Ref. 11). By varying the charging voltage, the amount of electron beam energy deposited in the working mixture could be varied from 4 to 16 J. The voltage pulse across the vacuum diode, the current pulse in the vacuum diode, and the current pulse in the laser chamber for this device are shown in Fig. 1. The second device (device No. 2) was a compact wide-aperture laser with an active volume of ~30 liters, with which previous experiments had achieved output energies of ~100 J with XeCl* ($\lambda=308$ nm) and KrF* ($\lambda=249$ nm) molecules[12] and ~115 J in an SF_6–H_2 mixture.[7] The vacuum-insulated electron accelerator produced a radially convergent electron beam from four cathodes of a commercially produced velvet material; a similar laser is described in detail in Ref. 13. In the present study we used a modernized version of the device used in Ref. 7. A difference from Refs. 12 and 13 is that the voltage pulse generator was positioned horizontally, permitting the optical axis of the laser chamber to be set at a height of 80 cm. The main results presented in this paper were obtained at an 80 kV charging voltage of the nine-stage voltage pulse generator, a voltage of ~400 kV across the vacuum diode, a beam current of ~26 kA in the laser chamber, and a beam pulse duration of ~400 ns. The energy deposited by the electron beam in the optimal working mixture $SF_6:H_2=8:1$ at pressures equal to or above 0.7 atm was ~1.7 kJ at the 80 kV charging voltage used. The voltage pulses across the vacuum diode, the current in the vacuum diode, and the current in the laser chamber are plotted in Fig. 1. The active volume of the laser chamber had a length of ~100 cm and a diameter of 20 cm. For both electron accelerators used in these lasers the electron energy and beam current varied over the time of the voltage pulse. The working mixtures of hydrogen and SF_6 were prepared in the laser chambers. A number of experiments were done using ternary mixtures with an admixture of argon or neon. Several types of resonant cavities were used. For the ''total-reflection'' mirror we used plane mirrors and convex spherical mirrors with gold or alu-

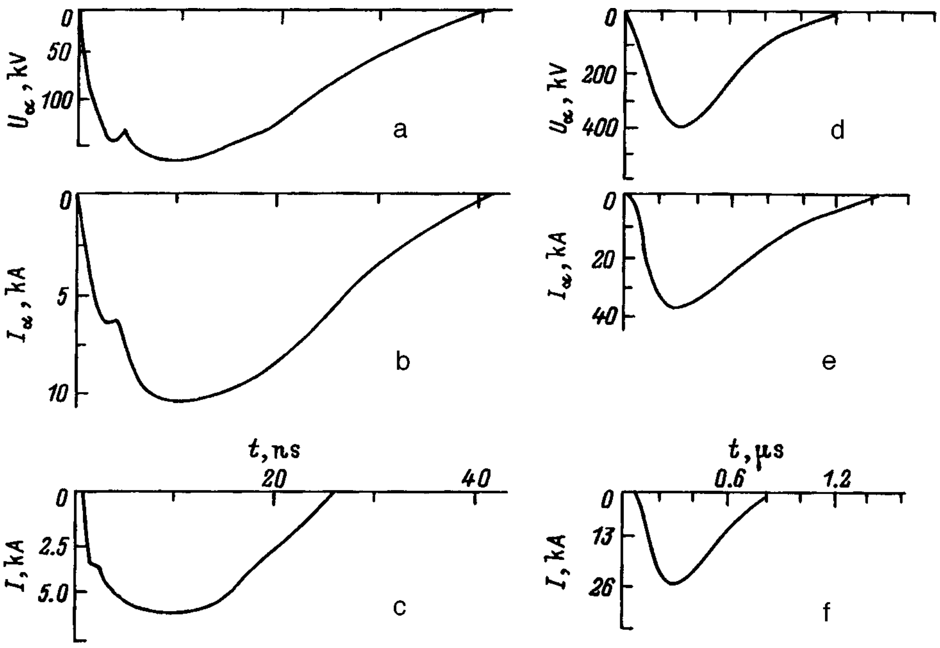

FIG. 1. Oscilloscope traces of the voltage pulses across the vacuum diode (a,d), of the current in the vacuum diode (b,e), and of the current in the laser chamber (c,g). a,b,c — Laser using a planar electron beam; d,e,g — laser using a radially convergent electron beam.

minum coatings; the output mirrors were plane-parallel slabs of BaF_2, NaCl, KRS-5, and KRS-6, with reflectivities in the $\sim 3\,\mu$m region of 7, 9, 33, and 27%, respectively.

The output energy of the lasers was measured by IMO-2 calorimeters mounted at different points in the output beam. The output energy for a mixture was ordinarily measured for the first shot of the accelerator. For the wide-aperture laser the measurements were made simultaneously in different regions by two IMO-2 calorimeters, which made it possible to rapidly determine the distribution of the energy density of the laser radiation over the cross section of the output beam. The temporal characteristics of the radiation pulse were recorded by an FP-1 receiver, the signal from which was sent to an S8-14 oscilloscope. The electron beam energy deposited in the working mixture was determined by the technique described in Refs. 6 and 11.

RESULTS AND DISCUSSION

The laser with the planar electron beam was more convenient from the standpoint of varying the experimental conditions and required less expenditure of the working gases. We therefore used device No. 1 for the detailed studies of the parameters of the laser radiation under varying conditions, and then the studies were repeated on the wide-aperture laser in the most interesting regimes found. The main results are illustrated in Figs. 2, 3, and 4. Figure 2 shows the dependence of the output energy in a pulse on the pressure of the optimum mixture at different electron beam energies. As the pressure increases, the energy of the output radiation increases to a maximum at a certain optimum pressure and then falls off. Similar curves have also been obtained in other studies.[9,10,14] The value of the optimum pressure depends on the partial compositions of the mixture and the electron energy. With increasing electron energy and increasing partial concentration of hydrogen (decreasing density of the mixture) the position of the maximum shifts to higher pressures. In addition, the energy characteristics of the output radiation depend on the composition of the working mixture. As the hydrogen partial pressure in the mixture is decreased from the optimum ratio $SF_6:H_2=8:1$ one observes a rapid decrease in the output energy and efficiency, while increasing the hydrogen content leads to a gradual decline in these output characteristics. We also note that the optimum pressure of the optimum mixture differs for different regions of the active volume, and this effect is especially noticeable in wide-aperture lasers. The pressure at which the maximum of the specific energy of the output laser radiation from a small part of the active volume (in which case one need not take into account the nonuniformity of the energy deposition over

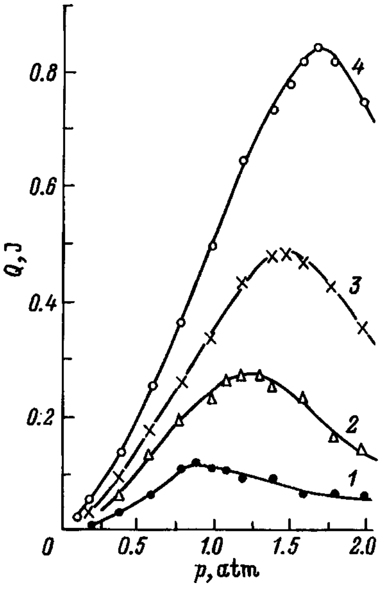

FIG. 2. Energy of the output radiation versus the pressure of the $SF_6:H_2 = 8:1$ mixture for different energy depositions. Energy of the electron beam, J: *1* — 4, *2* — 7.1, *3* — 10.3, *4* — 16.2. Device No. 1.

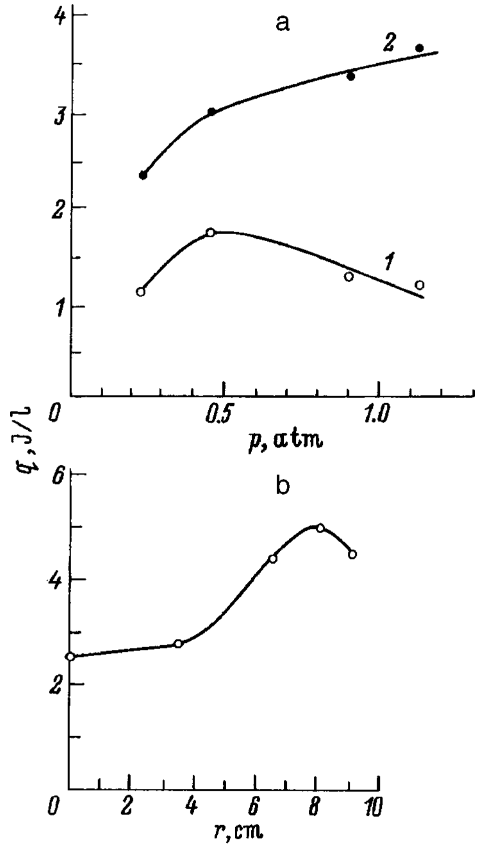

FIG. 3. Specific energy of the laser radiation on the axis of the laser chamber (*1*) and near the foil (*2*) as a function of pressure (a) and along the radius of the laser chamber (b). Device No. 2, $SF_6:H_2=8:1$ mixture.

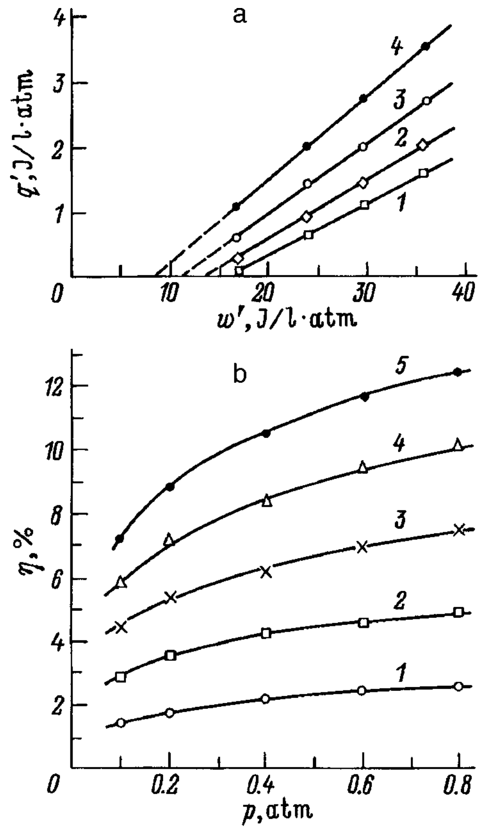

FIG. 4. Specific energy of the laser radiation as a function of the specific energy of the pump (a) and the efficiency of the laser as a function of pressure at constant values of the ratio of the threshold value of the specific pump energy to the specific energy deposition (b). Device No. 1, $SF_6:H_2=8:1$ mixture.

the cross section of the laser chamber) is attained is determined by the competition between two factors as the pressure increases in the investigated interval: a growth in the rates of the chemical reactions (which tends to increase the optimum pressure), and a growth in the rate of collisional de-excitation of the HF molecules, which first decreases the efficiency and then the output energy as well. The curves shown in Fig. 2 were obtained from measurements of the total energy of the output radiation from the entire active region encompassed by the resonant cavity. Figure 3a shows the dependence of the specific output energy on the pressure of the working mixture for device No. 2, obtained from measurements on the axis of the laser chamber and at a distance of 8 cm from the axis (2 cm from the foil). It is seen that the optimum pressure of the mixture at the center of the output beam is 0.45 atm, while at a distance of 2 cm from the foil the optimum has still not been reached at a pressure of 1.1 atm. Figure 3b shows the distribution of the specific output energy over the radius of the laser chamber of the wide-aperture laser with the optimum cavity (gold-coated mirror and plane-parallel slab of KRS-5) and a pressure of the mixture equal to 0.45 atm. The maximum and the manner in which the specific output energy on the axis of the laser chamber depended on the pressure of the mixture did not change when the cavity mirrors were changed. The specific output energy at a pressure of the mixture equal to 0.45 atm was ~5 J/l near the foil and ~2.6 J/l at the center of the laser chamber, and the total output energy was ~115 J. The lasing efficiency in terms of the electron beam energy deposited in the gas under these conditions was ~8%. As the pressure of the mixture was increased, the distribution of the energy density of the radiation over the cross section of the output beam became less uniform, but at the same time the total energy of the radiation and the efficiency increased, amounting to ~200 J and 11%, respectively, at a pressure of 1.1 atm.

Figure 4a shows the specific energy of the output radiation versus the specific energy of the pump at pressures of 0.1 (curve *1*), 0.2 (curve *2*), 0.4 (curve *3*), and 0.8 atm (curve *4*). Both the specific output energy and the specific pump energy are normalized to unit pressure. At pressures from 0.1 to 0.8 atm the specific output energy is observed to increase linearly with the specific pump energy, starting at a certain threshold value.

Figure 4b shows the pressure dependence of the lasing efficiency for various ratios of the threshold value of the specific pump energy w_{th} (at which the lasing begins to depend linearly on the energy deposition; Fig. 4a) to the specific pump energy w deposited in the working mixture: *1* — $w_{th}/w=0.8$, *2* — 0.6, *3* — 0.4, *4* — 0.2, *5* — 0. It is seen that the efficiency of the laser increases monotonically as the gas pressure increases at a constant ratio w_{th}/w. When the energy deposition is much above the threshold value (curve

TABLE I. Dependence of the integrated gain α on the composition and pressure of the mixture.

Mixture $H_2:SF_6$	P, atm	α, % / cm
1: 8	0.8	5.8
1: 8	1.0	7.5
1: 8	1.4	11.6
1: 10	1.0	6.2

5) we obtain the limiting curve for the efficiency. Thus the study of the energy characteristics of an HF laser utilizing an SF_6-H_2 mixture has shown that when the chemical reaction is initiated by a high-power electron beam the efficiency of the laser increases both with increasing pressure of the mixture (up to 1–1.5 atm) and with increasing specific energy deposited by the electron beam. The maximum efficiency obtained in our two devices was ~11%.

Measurements of the shape of the laser pulse for device No. 2 showed that under optimum conditions this pulse lags the current pulse by ~40 ns and has a duration at half maximum of ~500 ns. The power of the output radiation can exceed 200 MW. Table I gives values of the integrated gain for device No. 1. The gain was determined from the curves of the output energy versus length of the active region, which were taken with only the ''total-reflection'' mirror in place (one with 100% reflectivity at the laser wavelength was used). The highest value of the integrated gain under these conditions was 11.6%.

We also did experiments on the influence of a neon or argon admixture on the output energy of the HF laser (device No. 2). An admixture of 0.5 atm neon or argon was added to the $SF_6:H_2=8:1$ mixture at a pressure of 0.45 atm. At equal pressures of the binary and ternary mixtures (0.95 atm) the output energies for the ternary mixtures were found to be 30% higher on the axis of the laser chamber and 10% higher near the foil. This enabled us to improve the uniformity of the energy distribution in the output beam of the wide-aperture laser, which is an important consideration for producing laser beams with a low divergence of the radiation. The decrease in the output energy in the second pulse for the same portion of the working mixture was also less for the ternary mixture, ~35% instead of the ~50% drop observed in the binary mixture. Additional studies are needed to elucidate the nature of these two effects.

EFFICIENCY OF A LASER UTILIZING AN SF_6-H_2 MIXTURE

Let us analyze some of the features of the kinetic mechanism of reactions in a laser utilizing SF_6-H_2. It is ordinarily assumed that the absorption of energy from an external source leads to dissociation of the SF_6 molecules in the working mixture into SF_5 and F. We assume that there are two main processes by which vibrationally excited HF molecules can be formed as a result of chemical reactions.[11]

1. At comparatively low electron energies (~3.5 eV) atomic fluorine is formed in the dissociation reaction

$$SF_6+e\rightarrow SF_5+F-Q+e,$$

where Q is the dissociation energy, which is approximately 75 kcal/mole.

The fluorine then interacts with hydrogen and creates an inversion as a result of the endothermic reaction

$$F+H_2\rightarrow HF(v\leqslant 3)+H+Q_1,$$

where $Q_1=31.8$ kcal/mole is the energy released as a result of the chemical reaction, and v is the vibrational quantum number.

In collisional de-excitation by particles M, the decay of the excited molecules $HF(v)$ occurs by the radiationless process

$$HF(v)+M\rightarrow HF(v-1)+M.$$

Spontaneous and stimulated emission can occur in the cascade

$$HF(v)\rightarrow HF(v-1)+h\nu.$$

Let us now make the following assumptions: a) the dissociation reaction occurs over a short time, i.e., at the time $t=0$ when the chemical reaction begins, there is a certain density of atomic fluorine N_F in the active volume; b) collisional deactivation reactions can be neglected; c) the stimulated emission begins after the chemical reaction has ended, i.e., the density $N_F\approx N_{HF}$; then the limiting efficiency can be determined from the relation[11]

$$\eta=0.88\times 10^{-2}h\nu. \quad (1)$$

We note that the above assumptions are more valid for a laser pumped by an electron beam of short duration, while for pump beam durations of ~100 ns and more the chemical reactions will occur simultaneously with the stimulated emission. After substituting the numerical value $h\nu=10.2$ kcal/mole into expression (1), we find the conversion efficiency of the energy expended on dissociation of the SF_6 molecules into radiation energy: $\eta=0.09$. If we allow for the fact that the laser radiation is less than 100% of the total radiation of the HF molecules (for exciplex lasers this fraction is ordinarily ~50%), the lasing efficiency should be less than 9%. Meanwhile, in Ref. 14 an experimental efficiency of ~11% was reported, and in the present study the maximum efficiencies obtained in the two devices was also ~11%.

2. If the dissociation of the SF_6 molecules is brought about by electrons with an energy exceeding 5 eV, then the interaction can produce molecular fluorine with an energy expenditure of 105 kcal/mole (Ref. 15)

$$SF_6+e\rightarrow SF_4+F_2-Q_2+e,$$

where Q_2 is the energy released as a result of the chemical reaction.

Thus a chemically active mixture is formed in which the following reactions can occur:

$$F+H_2\rightarrow HF(v\leqslant 3)+H+Q_3(31.8\,\text{kcal/mole}), \quad (2)$$

$$F_2+H\rightarrow HF(v\leqslant 6)+F+Q_4(98\,\text{kcal/mole}). \quad (3)$$

The kinetic mechanism of reactions in this case is substantially different. A simplified description of it is as follows. HF molecules are formed in two stages. Since the specific rate of reaction (2) is significantly (5.5 times) higher than that of reaction (3) (Ref. 16), and reaction (3) occurs only after a sufficient amount of atomic hydrogen is produced, in the first stage the fluorine atoms enter into a reaction with hydrogen molecules, forming a population inversion of the molecules $HF(v \leqslant 3)$, which rapidly leads to the onset of lasing, and in the second stage a chain reaction occurs via schemes (2) and (3). However, the rate of formation of HF molecules is then governed mainly by the slower reaction (3). We note that under certain conditions in electron-beam-pumped lasers[17] one observes two lasing pulses, which also suggests the presence of two processes. If two processes participate in the formation of the HF molecules, an estimate gives the following expression for the maximum output energy:[11]

$$q_m = h\nu\{[(1-m)E/75](\Sigma v k_v - 1.5) + (mE/105)\Sigma v k_v\}, \tag{4}$$

where m is the fraction of the total energy E expended on ionization of the SF_6 molecules, k_v are the rate constants of the chemical reactions, and v is the number of the vibrational level; thus mE $(m \leqslant 1)$ goes to the formation of molecular fluorine, and the remaining energy $(1-m)E$ is expended on the formation of atomic fluorine.

Substituting the normalized values of the specific rate constants k_v of the chemical reaction,[18] we obtain

$$q_m = 10^{-2}E(9 + 12.5m). \tag{5}$$

Dividing expression (5) by the value of the energy E expended on dissociation of the SF_6 molecules, we obtain an expression for the maximum possible efficiency of a laser utilizing an SF_6-H_2 mixture: $\eta = 10^{-2}(9 + 12.5m)$. The parameter m is the fraction of the electron beam energy that is expended on dissociation of SF_6 with the formation of molecular fluorine. Thus if the conditions in the SF_6-H_2 mixture upon initiation of the chemical reaction are such that atomic and molecular fluorine are produced in the dissociation of the SF_6 molecules, one can obtain a higher output energy and higher efficiency of the laser. As we have said, in our two devices an efficiency of ~11% was achieved, and this can be explained, for example, by the conjecture that both atomic and molecular fluorine are simultaneously produced in the working mixture. To obtain such an efficiency with ~100% of the total radiation at the laser transitions the parameter m would have to be 0.2. This parameter should clearly be somewhat higher, since various types of losses were left out of the estimate. If we compare these results with the efficiency in terms of deposited energy that can be obtained in pumping by a self-sustained discharge,[8,11] the difference is at least a factor of two. It can be assumed that in pumping by a self-sustained discharge at the same energy depositions, the density of electrons with energies greater than 5 eV is substantially lower than for electron beam pumping. We plan to continue the investigation of the basic processes that influence the output efficiency of lasers utilizing SF_6-H_2 mixtures.

CONCLUSION

We have investigated HF lasers pumped by a non-chain chemical reaction initiated by radially convergent and planar electron beams. We have analyzed the main channels of formation of vibrationally excited HF molecules. We have conjectured that the high efficiencies of non-chain-reaction HF lasers is achieved on account of the simultaneous formation of atomic and molecular fluorine in the interaction of the electron beam with the working mixture. For pumping by a self-sustained discharge the production of molecular fluorine is apparently considerably less, which lowers the efficiency of electrical-discharge lasers by a factor of two or more. We have measured the distribution of the energy density of the radiation in the output beam of a wide-aperture laser. In a mixture of $SF_6:H_2 = 8:1$ at a pressure of 1.1 atm with an active volume of ~30 liters an energy of the output radiation of ~200 J was obtained at an efficiency in terms of deposited energy of ~11%. We have shown that for an HF laser pumped by a non-chain chemical reaction initiated by an electron beam, the admixture of a neon or argon buffer gas improves the uniformity of the energy distribution in the output beam and also increases the output energy.

The authors thank A. N. Panchenko, A. M. Efremov, É. N. Abdullin, and A. V. Fedenev for assistance in performing the experiments on device No. 2.

[1] I. I. Galaev, S. V. Konkin, A. D. Latyshev *et al.*, Kvantovaya Élektron. (Moscow) **23**, 217 (1996).

[2] M. Gastaud, J. Bouesc, and M. Autric, in *Proceedings of the Eleventh International Symposium on Gas Flow and Chemical Lasers and High Power Laser Conference*, Edinburgh (1996), Vol. 3092, pp. 585–588.

[3] V. P. Borisov, V. V. Burtsev, S. V. Velikanov *et al.*, Kvantovaya Élektron. (Moscow) **23**, 119 (1996).

[4] A. S. Bashkin, A. S. Boreĭko, V. V. Lebachev *et al.*, Kvantovaya Élektron. (Moscow) **23**, 428 (1996).

[5] B. P. Aleksandrov, A. A. Stepanov, and V. A. Shcheglov, Kvantovaya Élektron. (Moscow) **23**, 490 (1996).

[6] S. V. Velikanov, N. F. Zapol'skiĭ, and Yu. N. Florov, Kvantovaya Élektron. (Moscow) **24**, 11 (1997).

[7] É. N. Abdullin, A. M. Efremov, B. M. Koval'chuk *et al.*, Pis'ma Zh. Tekh. Fiz. **23**(5), 58 (1997) [Tech. Phys. Lett. **23**, 193 (1997)].

[8] M. I. Lomaev, A. N. Ponchenko, and V. F. Tarasenko, Kvantovaya Élektron. (Moscow) **24**, 499 (1997).

[9] *Handbook of Chemical Lasers*, edited by R. W. Gross and J. F. Bott [Wiley, New York (1976); Mir, Moscow (1980), 832 pp.].

[10] *Chemical Lasers* [in Russian], edited by N. G. Basova, Nauka, Moscow (1982), 400 pp.

[11] Yu. I. Khapov, Candidate's Dissertation [in Russian], Novosibirsk (1982), 187 pp.

[12] É. N. Abdullin, V. I. Gorbachev, A. M. Efremov *et al.*, Kvantovaya Élektron. (Moscow) **20**, 652 (1993).

[13] É. N. Abdullin, S. P. Bugaev, A. M. Efremov *et al.*, Prib. Tekh. Éksper., No. 5, pp. 138–141 (1993).

[14] A. S. Bashkin, A. N. Oraevskiĭ, and V. P. Tomashov, Kvantovaya Élektron. (Moscow) **4**, 169 (1977) [Sov. J. Quantum Elektron. **7**, 94 (1977)].

[15] L. V. Gurevich, G. V. Karachevtsev, V. N. Kondrat'ev *et al.*, *Breaking Energy of Chemical Bonds. Ionization Potentials and Electron Affinities* [in Russian], Nauka, Moscow (1974), 391 pp.

[16] R. L. Kerber and J. S. Whittier, Appl. Opt. **15**, 2358 (1976).

[17] R. W. F. Gross and F. Wesner, Appl. Phys. Lett. **23**, 559 (1973).

[18] R. L. J. Wilkins, J. Chem. Phys. **57**, 912 (1972).

Translated by Steve Torstveit

TECHNICAL PHYSICS VOLUME 44, NUMBER 1 JANUARY 1999

Field distribution of magnetostatic waves in a tangentially magnetized ferromagnetic slab

A. Yu. Annenkov and S. V. Gerus

Institute of Radio Engineering and Electronics, Russian Academy of Sciences, 141120 Fryazino, Moscow Region, Russia

(Submitted June 17, 1997)
Zh. Tekh. Fiz. **69**, 82–86 (January 1999)

The field distribution of magnetostatic surface and volume waves as they propagate at an arbitrary angle to a constant field in a tangentially magnetized ferromagnetic slab (Damon–Eschbach waves) is investigated. Snapshots of the magnetic field lines of the wave are constructed. The variation of the magnetic field distribution with thickness is qualitatively identified for a volume wave as it propagates at an angle equal to the cutoff angle of the surface wave, as a result of which the sinusoidal profile of the wave over thickness almost discontinuously acquires an additional phase difference. *© 1999 American Institute of Physics.* [S1063-7842(99)01301-X]

Magnetostatic modes in a tangentially magnetized ferromagnetic slab were first considered in the famous paper by Damon and Eschbach.[1] They showed that two types of magnetostatic waves can propagate in such a magnetic medium: surface waves and volume waves. They obtained dispersion relations for the indicated waves and investigated the conditions for their existence. In particular, they noted that surface waves can propagate only in a certain sector of directions whereas volume modes have no such limitation. They examined the distributions of the magnetostatic wave functions with slab thickness for two situations: a volume wave as it propagates parallel to the magnetic bias field, and the surface wave traveling in the transverse direction.

Subsequent papers dedicated to magnetostatic waves in ferromagnetic slabs investigated the influence on them of the direction of the bias field and various boundary conditions, including metallization of the surface of the ferromagnet and creation of periodic obstacles along the path of the waves.[2–4] Magnetostatic waves have also been examined in multilayer ferrite structures.[5] However, for the most part attention has been focused on such dynamic characteristics as the dispersion relation, the phase and group velocities, and the delay time of magnetostatic waves. The distribution of magnetostatic wave fields over the volume of the slab has been considered only for the particular cases of the direction of propagation mentioned above.[6]

The present study is to some extent a continuation of Ref. 1. It investigates the field distribution of surface and volume magnetostatic waves as they propagate at an arbitrary angle relative to a constant field in a tangentially magnetized ferromagnetic slab.

BASIC RELATIONS

Let the bias field H_0 be parallel to the z axis and the ferromagnetic slab lie in the yz plane (see Fig. 1). We denote by α the angle between the y axis and the direction of propagation of the wave $\mathbf{r}$. Following Ref. 1, we use the magnetostatic approximation, according to which the magnetic field of the wave is expressed in terms of the magnetostatic potential Ψ

$$\mathbf{h}=\operatorname{grad}\Psi, \tag{1}$$

for which reason it is called a magnetostatic wave. The potential Ψ satisfies the Walker equation inside the slab

$$\operatorname{div}(\hat{\mu}\times\operatorname{grad}\Psi)=0 \tag{2}$$

and the Laplace equation outside it

$$\Delta\Psi=0. \tag{3}$$

Here $\hat{\mu}$ is the permeability tensor of the ferromagnet.[6]

The conditions of continuity of the tangential component of the magnetic field of the wave and the normal component of the induction should be fulfilled on the surface of the ferromagnet.

According to Ref. 1, the solution of Eq. (2) inside the slab is expressed in terms of trigonometric functions for the volume waves and hyperbolic functions for the surface waves. For our purposes, it is convenient to represent them here in the following form:

$$\Psi_\sigma=e^{i(\omega t-\mathbf{k}_r\mathbf{r})}\times\begin{cases} S_\sigma(d/2)\times e^{-k_r(x-d/2)}, & x>d/2,\\ S_\sigma(x), & -d/2>x>d/2,\\ S_\sigma(-d/2)\times e^{k_r(x+d/2)}, & x<-d/2. \end{cases} \tag{4}$$

Here the first factor on the right-hand side describes the propagation of a wave with frequency ω in the direction of the two-dimensional wave vector $\mathbf{k}_r$; the function $S_\sigma(x)$ reflects the distribution of the wave over slab thickness

$$S_\sigma(x)=\begin{cases} \sinh(\Phi), & \sigma=+1,\\ \sin(\Phi), & \sigma=-1, \end{cases}$$

where the subscript σ determines the type of wave — it is equal to $+1$ for a magnetostatic surface wave and -1 for a

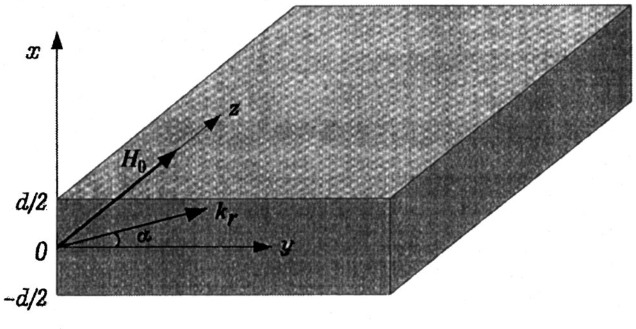

Рис. 1. Ориентации системы координат.

FIG. 1. Orientation of the coordinate system.

volume wave; the parameter $\Phi=k_x x+\Phi_0$ is the spatial phase of the periodic distribution S_σ for a magnetostatic volume wave and its generalization to the case of hyperbolic functions for a magnetostatic surface wave; Φ_0 is the initial phase controlling the symmetry of the function S_σ relative to the $x=0$ plane; k_x is a positive real number.

In formula (4) the amplitude coefficient for convenience has been set equal to 1 since we are investigating questions of the propagation of linear oscillations without regard to the conditions of their excitation. Note that although the use of the hyperbolic sine instead of the more general formula Ae^x+Be^{-x} encompasses only the case of different signs of the coefficients A and B, it is just this case that satisfies the boundary conditions.

Substituting formula (4) for the potential into the Walker equation (2), we obtain an expression linking the wave numbers k_x and k_r,

$$\left(\frac{k_r}{k_x}\right)^2=\frac{\sigma\mu}{1+(\mu-1)\cos^2\alpha}, \tag{5}$$

where $\mu=(\Omega_\perp^2-\Omega^2)/(\Omega_H^2-\Omega^2)$ is the diagonal component of the permeability tensor, $\Omega=\omega/4\pi M_0$, $\Omega_H=H_0/4\pi M_0$, $\Omega_\perp=\Omega_H(\Omega_H+1)$, H_0 is the bias field, and M_0 is the saturation magnetization of the ferromagnet.

Using expression (4) for the potential together with formula (1), we find the components of the alternating magnetic field **h** inside the ferrite slab. The ratio of the components can be represented in the following form:

$$\xi_\sigma=-i\sqrt{\frac{\sigma(\Omega^2-\Omega_\perp^2)}{\Omega^2-\Omega_H(\Omega_H+\cos\alpha)}}\,T_\sigma(\Phi), \tag{6}$$

where $\xi_\sigma=h_r/h_x$,

$$T_\sigma(\Phi)=\begin{cases}\tanh(\Phi), & \sigma=+1,\\ \tan(\Phi), & \sigma=-1.\end{cases}$$

The imaginary quantity ξ_σ describes the rotation of the magnetic field about an ellipse whose eccentricity depends on the magnitude of ξ_σ, and whose direction of rotation depends on its sign.

Let us now take the boundary conditions into account. They allow us to determine the values that the phase Φ and the quantity ξ_σ should take on the upper and lower surfaces of the slab. It follows from the Laplace equation (3) that the alternating magnetic field outside the ferrite $\mathbf{h}^e$ has circular rotation whose direction is different for the upper and lower half planes. The connection between the components of the external field can be written as follows:

$$h_r^e=i\zeta h_x^e,$$

where

$$\zeta=\begin{cases}+1, & x\geqslant d/2,\\ -1, & x\leqslant -d/2.\end{cases}$$

Since the magnetic field $\mathbf{h}^e$ and induction $\mathbf{b}^e$ outside the ferrite are equal, allowing for continuity of the tangential component of the field and the normal component of the induction at the boundary of the ferromagnet we can write down the following boundary condition:

$$h_r=h_r^e=i\zeta h_x^e=i\zeta b_x^e=i\zeta b_x. \tag{7}$$

Here **h** and **b** are the field and induction inside the ferromagnet. In turn, b_x is expressed in terms of **h** and the tensor $\hat{\mu}$

$$b_x=\mu h_x+\nu h_y, \tag{8}$$

where $\nu=i\Omega/(\Omega_H^2-\Omega^2)$ is the nondiagonal component of the tensor $\hat{\mu}$.

Hence we obtain the value that the ratio of field components should take on the upper or lower boundary of the ferromagnet

$$\eta_\zeta=\frac{h_r}{h_x}\left(x=\zeta\frac{d}{2}\right)=-i\,\frac{\Omega^2-\Omega_\perp^2}{\Omega\cos\alpha-\zeta(\Omega^2-\Omega_H^2)}. \tag{9}$$

Taking the boundary conditions into account in the given problem means equating the values returned by formulas (6) and (9),

$$\xi_\sigma(\Phi_\zeta)=\eta_\zeta, \tag{10}$$

where Φ_ζ is the value of the phase Φ on the upper and lower surfaces of the ferrite slab.

Transforming expression (10), we obtain a formula for Φ_ζ

$$T_\sigma(\Phi_\zeta)=\frac{\sigma\sqrt{\sigma(\Omega^2-\Omega_\perp^2)\times[\Omega^2-\Omega_H(\Omega_H+\cos^2\alpha)]}}{\Omega\times\cos\alpha-\zeta(\Omega^2-\Omega_H^2)}. \tag{11}$$

In turn, the values of the spatial phase on the different surfaces Φ_{+1} and Φ_{-1} allow us to find the parameter $k_x=(\Phi_{+1}-\Phi_{-1})/d$. Substituting the values of k_x into formula (5), we obtain the well-known dispersion relations for the surface and volume waves.[1]

However, we are interested in the distributions of the alternating fields of the magnetostatic waves. Note that the boundary condition in the form of formula (9) enables us to analyze the behavior of the magnetic field on the surface of the ferromagnet directly, and taking dependences (6) into account, the behavior inside it. In order to graphically represent the behavior of the field with the help of the relation $\eta=h_r/h_x$, it is convenient to introduce the following transformation:

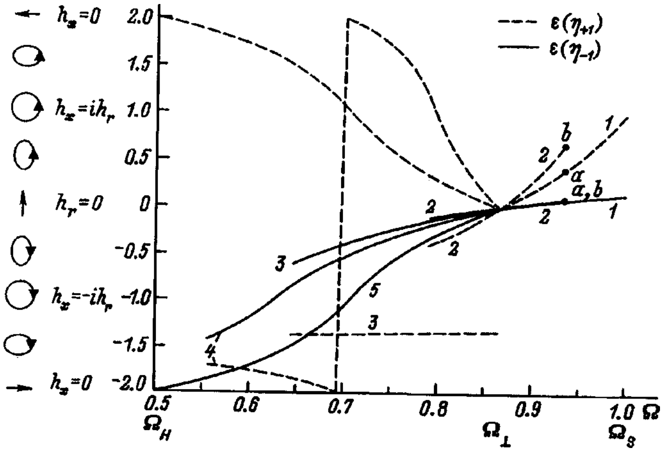

FIG. 2. Frequency dependence of the parameters $\varepsilon(\eta_{+1})$ and $\varepsilon(\eta_{-1})$, representing the shape and direction of precession of the magnetic field at the upper (dashed curves) and lower (solid curves) boundaries, respectively, of a ferromagnetic slab: $\alpha=0$ (*1*), 30° (*2*), $\alpha_c=54.7°$ (*3*), 70° (*4*), $-90°$ (*5*). The corresponding shapes of the precession ellipse are depicted to the left of the ordinate axis. $\Omega_S=\Omega_0(\alpha=0)$, $\Omega_H=0.5$.

$$\varepsilon(\eta)=\begin{cases} 2-1/i\eta, & i\eta>1, \\ i\eta, & -1<i\eta<1, \\ -2-2/i\eta, & i\eta<-1. \end{cases}$$

This transformation puts the points $h_x=0$, $ih_r/h_x=\pm1$, and $h_r=0$ into correspondence with the values $\varepsilon=2,\pm1,0$, respectively.

DISCUSSION

Figure 2 plots the frequency dependence $\varepsilon(\eta_\zeta)$ given by formula (9). Each value of ε corresponds to a definite shape and direction of the rotation ellipse of the magnetic field **h**, which is qualitatively depicted to the left of the ordinate axis. In the construction of the graphs we allowed for additional conditions of existence of the magnetostatic waves.

For magnetostatic surface waves $(\Omega>\Omega_1)$, there are two such conditions. The first one has the form

$$\Phi_{+1}>\Phi_{-1}. \tag{12}$$

It follows from the positivity of k_x and defines the known value of the cutoff angle of the surface waves $\alpha_c=\arctan\sqrt{1/\Omega_H}$. For $\alpha>\alpha_c$ surface wave do not exist. The second condition follows from the fact that the value of the hyperbolic tangent in formula (11) is bounded by unity and determines the upper frequency of existence of the surface waves propagating at a given angle α relative to the y axis

$$\Omega_0=\frac{\Omega_H(1+\cos^2\alpha)+\cos^2\alpha}{2\cos\alpha}.$$

In Fig. 2, of all the angles considered, the magnetostatic surface wave can propagate at only two. As the angle is increased, the frequency region of existence of magnetostatic surface waves narrows due to lowering of the upper frequency. In the limit $\alpha\to\alpha_c$ the upper frequency tends to $\Omega_\perp$. The parameter of the precession ellipse ε inside the ferromagnet grows from the solid curve $\varepsilon(\eta_{-1})$ to the dashed curve $\varepsilon(\eta_{+1})$. As it does, the precession of the magnetostatic wave field changes from a vertical ellipse to a circle.

For volume waves $(\Omega<\Omega_\perp)$ there are also two additional conditions. The first consists in the positivity of expression (5) and defines the lower boundary of existence of magnetostatic volume waves: $\Omega_1=\sqrt{\Omega_H(\Omega_H+\cos^2\alpha)}$. The second condition is represented by relation (12). From it, it follows that the angle α_c is also a characteristic parameter for magnetostatic volume waves. For angles $\alpha>\alpha_c$ condition (12) is valid asymptotically. For $\alpha<\alpha_c$ this condition is fulfilled only for waves for which the phase Φ_{+1} on the upper boundary, calculated according to formula (11), is increased by π. In Fig. 2 it is possible to trace out the evolution which the precession ellipse of the first mode of a magnetostatic volume wave undergoes as one goes from the lower to the upper surface of the ferrite slab. The parameter ε grows from the solid curve $\varepsilon(\eta_{-1})$ to the dashed curve $\varepsilon(\eta_{+1})$ or to the horizontal line with ordinate value 2; growth then continues from the level -2 to the dashed curve if the solid curve lies above the dashed curve. As the parameter ε varies in this way, the configuration of the ellipse passes through the phases nominally drawn to the left of the ordinate axis. Note the following circumstance: for volume modes the ratio (9), represented graphically in Fig. 2, does not depend on the mode number. Consequently, if we increase the mode number by 1, then as we rise from the lower to the upper boundary of the ferromagnet we must add an additional cyclical loop equal to four units along the ordinate axis.

Let us now consider in more detail a specific feature of magnetostatic volume waves connected with the presence of the cutoff angle α_c. Toward this end, we turn to Fig. 3, which plots the dependence of the surface phases Φ_{+1} and Φ_{-1} of the first volume mode on the wave vector $\mathbf{k}_r$. The phase inside the ferromagnetic slab is easily found since, according to formula (1), it grows linearly from Φ_{-1} on the lower boundary to Φ_{+1} on the upper boundary. Recall also that magnetostatic volume waves in a tangentially magnetized slab have negative dispersion.[1]

The dependence on wave number (or frequency) of the phase difference $\Delta\Phi=\Phi_{+1}-\Phi_{-1}$ of a volume mode turns out to be different for angles α greater and less than the critical angle α_c (Fig. 3a). For angles greater than α_c (except for $\alpha=\pi/2$) the phase Φ_{+1} grows monotonically from 0 to π as k_r increases from zero to infinity (as the frequency decreases from $\Omega_\perp$ to its lower limit). The phase Φ_{-1} has some negative minimum in the mid part of this range and is equal to 0 at its limits. The phase difference $\Delta\Phi$ grows monotonically from 0 to π.

For angles less than α_c the behavior of Φ_{+1} is different. In this case, both Φ_{-1} and Φ_{+1} have a minimum in the mid part of the range and at its boundaries are equal to 0 and π, respectively. Here the phase difference $\Delta\Phi$ turns out to be maximum and equal to π at the boundaries of the frequency range and has a minimum in its middle part.

The value $\alpha=\pi/2$ represents a special case (the wave propagates parallel to the field $\mathbf{H}_0$). In this case the curves Φ_{+1} and Φ_{-1} become symmetric relative to the abscissa (and the magnetostatic wave field relative to the center of the

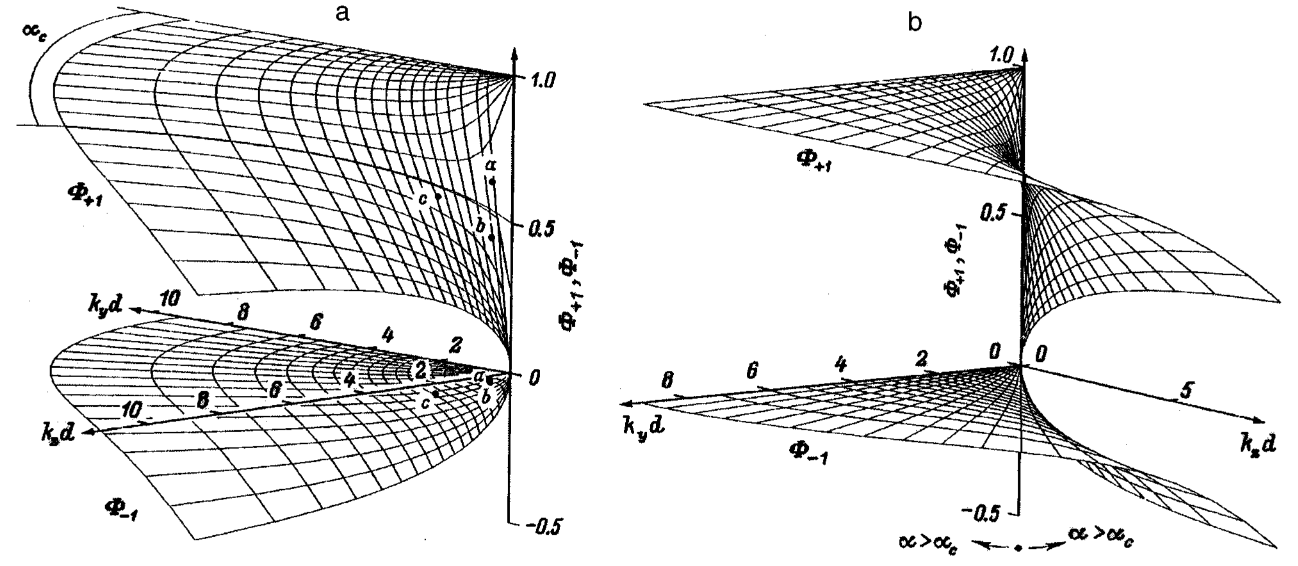

FIG. 3. Dependence of the phases Φ_{+1} and Φ_{-1} of the first mode of the magnetostatic volume waves for the upper and lower surfaces of a ferromagnet on the two-dimensional wave vector k_r (a) and view from the the critical angle $\alpha_c = 54.7°$ (b).

slab), due to the absence of nonreciprocity for this value of α.

For higher modes the behavior of Φ_{+1}, Φ_{-1}, and $\Delta\Phi$ differ from the behavior considered above by the presence of an additional term, $n\pi$, in the formulas for Φ_{+1} and $\Delta\Phi$.

Finally, let us consider how the magnetostatic wave field itself is distributed over the thickness of the magnetic slab. Figure 4 displays snapshots of the field lines of two magnetostatic surface waves propagating at one frequency but at different angles α. The tangent to the line at each of its points indicates the direction of the magnetic field of the magnetostatic wave. Unlike the lines of force of the magnetic induction, the magnetic field lines are not continuous and their density in a ferromagnet is not an indicator of the magnitude of the field. However, we have shown snapshots of the magnetic field lines because they provide the most exhaustive and convenient representation of the principal regularities of the propagation of a magnetostatic wave in the form of formulas (6), (7), and (9). For magnetostatic surface waves propagating at an angle α relative to the y axis (Fig. 4b), the structure of the field lines is similar to the case $\alpha = 0$ (Fig. 4a) examined in Ref. 6. As α is increased (for a given frequency) the wave number grows and, as follows from Fig. 2, the tangential component of the field grows relative to the normal component on the upper surface of the slab while the relative values of the components on the lower surface remain essentially unchanged.

The field distribution of the magnetostatic waves has specific features associated with the existence of the critical angle α_c. Figure 5 presents snapshots of the field lines for the first mode of the indicated waves — the ones corresponding to the states marked by points in Fig. 3. The value of the x coordinate at which the tangents to the field lines are vertical corresponds to the phase $\Phi = 0$ or π while the values of the x coordinate corresponding to the phases $\Phi = \pm\pi/2$ are those for which the field line is a horizontal line.

The field snapshots in Figs. 5a and 5b were constructed for the same wave number k_r and very similar values of the parameters Ω and α. Nevertheless, the shapes of the field lines inside the ferromagnet in this figures differ significantly. This is because the angle α is 2° less than α_c in one figure and 2° more in the other. In this case the wave vectors were chosen to be relatively small in the region where the phase Φ_{+1} (Fig. 3) has an almost jumplike singularity in its dependence on α. On the lower surface of the slab the values of Φ_{-1} are negative and small in absolute value, and almost coincide (Fig. 3). Therefore, in both figures near the lower surface there is a cross section, where the tangents to the field lines are vertical ($\Phi = 0$). But there is a horizontal field line ($\Phi = \pi/2$) only in Fig. 5a, for which $\Phi_{+1} > \pi/2$. The phase difference $\Delta\Phi$ is 120° in Fig. 5a and 87° in Fig. 5b.

For Fig. 5c the same value of $\alpha = 57°$ was chosen as in Fig. 5b, but the wave vector (frequency) was chosen such that the phase difference $\Delta\Phi$ was equal to 120°, as in Fig. 5a. In order to provide the magnetostatic volume wave with

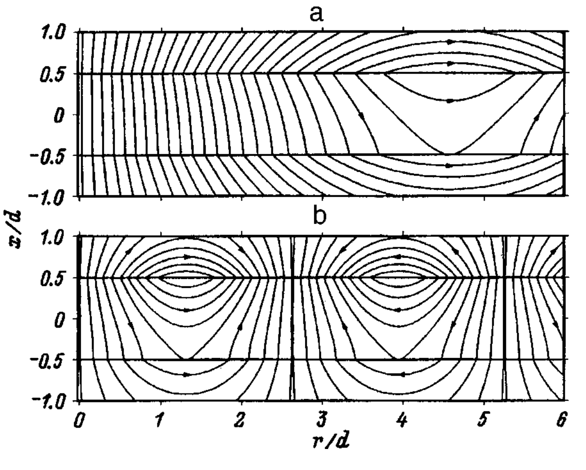

FIG. 4. Magnetic field lines of magnetostatic surface waves with frequency $\Omega = 0.935$: $\alpha = 0$ (a), 30° (b); $k_r d = 0.34$ (a), 1.2 (b); the unit of length is the thickness of the ferromagnetic slab.

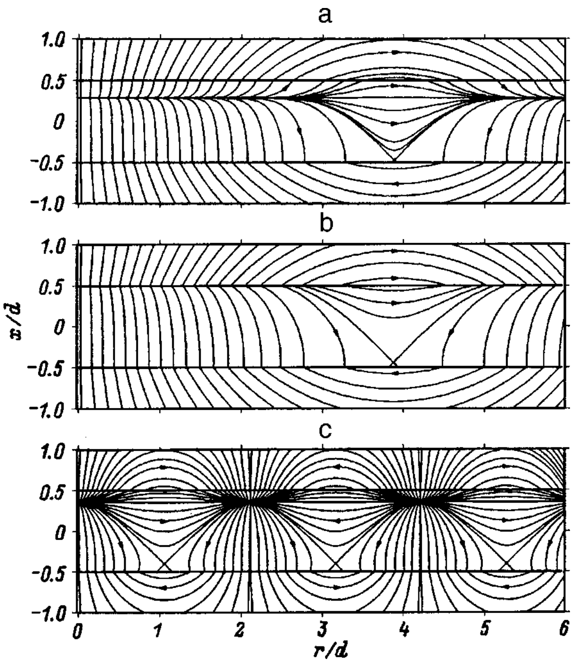

FIG. 5. Magnetic field lines of magnetostatic volume waves: $\alpha = 53°$ (a), $57°$ (b,c); $k_r d = 0.4$ (a,b), 1.49 (c); $\Omega = 0.859$ (a), 0.852 (b), 0.794 (c). These figures correspond to the points on the surfaces in Fig. 3 labeled by the same letters.

the same value of $\Delta\Phi$, as in the case of a rotation by 4° for $k_r = \text{const}$, it is necessary to increase k_r by a factor of 3.7 for $\alpha = \text{const}$. Note that in the region of small wave vectors for angles α close to but smaller than α_c, the $\Phi_{+1}(k_r)$ curves have a minimum, thanks to which the existence of identical values of Φ_{+1} is possible, which implies similar field distributions with thickness for two different values of k_r. As k_r is increased, the jumplike singularity at the surface in Φ_{+1} smooths out.

In conclusion we may note the following. The major axis of the precession ellipse of the magnetic field of the magnetostatic surface waves is oriented perpendicular to the surface of the ferromagnetic slab. The eccentricity of the ellipse takes its maximum value on the lower surface of the slab. As one moves toward the upper surface, the field amplitude grows monotonically and the eccentricity of the ellipse decreases, also monotonically. The ellipse at the upper boundary tends toward a circle with the magnetostatic waves propagating perpendicular to the bias field ($\alpha = 0°$) and the wave number tending toward infinity. As the angle α is increased, the eccentricity at the lower boundary hardly varies, the gradient of the eccentricity relative to the x coordinate (the spatial coordinate in the direction of the slab thickness) grows, but the total range of values of the eccentricity contracts to zero as the angle α approaches its critical value α_c accompanied by a simultaneous contraction of the frequency range.

The propagation of magnetostatic volume waves also has a singularity in the vicinity of angles near α_c. In the region of small wave numbers, as the angle α decreases, an almost discontinuous increase of the spatial phase takes place at the upper surface of the ferromagnet, as a result of which the picture presented by the field distribution of a magnetostatic volume wave over slab thickness is radically altered.

This work was carried out with the support of the Russian Fund for Fundamental Research (Grant No. 96-02-17283a).

[1] R. W. Damon and J. R. Eschbach, J. Phys. Chem. Solids **19**, 308 (1961).
[2] R. W. Damon and H. van der Vaart, J. Appl. Phys. **36**, 3453 (1965).
[3] W. L. Bongianni, J. Appl. Phys. **43**, 2541 (1972).
[4] A. V. Voronenko, S. V. Gerus, and V. D. Kharitonov, Izv. Vyssh. Uchebn. Zaved. Fiz. **31**(11), 76 (1988).
[5] V. I. Zubkov and V. A. Epanechnikov, Radiotekh. Elektron. **31**, 656 (1986).
[6] A. G. Gurevich and G. A. Melkov, *Magnetic Oscillations and Waves* [in Russian], Fizmatlit, Moscow, 1994.

Translated by Paul F. Schippnick

Toward a nonlinear theory of acceleration of charged particles in a linearly polarized *EH*-ubitron field

O. B. Krut'ko

Sumy State University, 244007 Sumy, Ukraine

(Submitted July 16, 1997)
Zh. Tekh. Fiz. **69**, 87–93 (January 1999)

The motion of charged particles in a linearly polarized *EH*-ubitron field with sinusoidal time dependence of the variable component of the magnetic field is investigated. It is shown that, depending on the parameters of the system and the initial conditions of entry of the particle into the *EH*-field region, three different types of motion are possible: ballistic motion, capture in the vicinity of one of the maxima of the magnetic field, and escape of particles from the *EH*-field region. An analytical expression is found for the criterion determining the type of motion of the particles, along with analytical solutions for the energy of the particles in the approximation of slow variation of the magnetic field amplitude in time. Peculiarities of the motion of the particles in *EH* fields with arbitrary rate of change of the magnetic field amplitude in time are investigated numerically. *© 1999 American Institute of Physics.* [S1063-7842(99)01401-4]

INTRODUCTION

The creation and study of new types of accelerating systems is one of the most urgent problems of contemporary physical electronics. For this reason, despite the fact that the number of accelerator models known at the present time is large,[1] newer and newer systems continue to appear. One possible direction here is the development of designs based on the acceleration of charged particles in time-varying, crossed, periodically reversed electric and magnetic (*EH*-ubitron) fields.[2] In Refs. 3–6 it was shown that such systems possess a number of unique properties such as the possibility of simultaneous codirected acceleration of oppositely charged particles,[3] nonlinear dependence of the rate of acceleration on the length of the system,[4] the possibility of accelerating quasineutral plasma bunches,[5] and the possibility of cooling and compressing charged-particle beams.[6] These efforts have opened up the possibility of using *EH*-ubitron systems to form charged-particle beams and plasma fluxes,[5,6] to develop accurate models of FEL (free-electron laser) accelerators[7] and FEL generators,[8] and also for a number of other technological purposes.

However, despite the comparatively large number of efforts dedicated to *EH*-ubitrons, a significant number of interesting physical processes taking place in systems of such type remain uninvestigated. In particular, Refs. 2–6 examined particle acceleration with the aid of the Bogolyubov averaging method,[9] where they chose the quantity

$$\varepsilon=\frac{e^2H^2}{m^2c^4k^2(\gamma_0^2-1)}\ll 1, \tag{1}$$

as the small parameter, where H is the amplitude of the magnetic component of the *EH*-field, k is the undulation frequency of the *EH*-field, e is the particle charge, m is the particle rest mass, γ_0 is the initial value of the relativistic factor of the particle, and c is the speed of light in vacuum.

Therefore, it is still unclear how the particles interact in an *EH*-ubitron field if condition (1) is violated. At the same time, analysis shows that maximal rates of acceleration can be achieved if $\varepsilon \leqslant 1$, and also that various particle capture processes are possible in the vicinity of the magnetic field maxima for $\varepsilon > 1$. In this light, in the present work I have undertaken an effort to eliminate these gaps in the nonlinear theory of particle motion in *EH*-ubitron fields.

MODEL AND BASIC EQUATIONS

Let us consider the motion of a charged particle in fields created by a periodically reversed sequence of pairs of electromagnets. We assume that the magnetic field vector **H** is oriented along the y axis, and that the sequence of pairs of electromagnets runs parallel to the z axis. In addition, we assume that a time-varying current flows through the coils of the electromagnets, as a result of which the magnetic field varies in time, inducing a solenoidal electric field. The latter is also a periodically reversed field along the z axis, and its field vector **E** is oriented along the x axis. The undulation periods of the electric and magnetic fields are equal. Such a superposition of electric and magnetic fields is known as a linearly polarized *EH*-ubitron field[2] and can be described with the aid of the vector potential

$$\mathbf{A}=A(t)\mathbf{e}_x\sin kz, \tag{2}$$

where $A(t)$ is the amplitude of the vector potential, $\mathbf{e}_x$ is the unit vector in the x direction, z is the longitudinal coordinate, t is time in the laboratory reference frame.

Thus, the electric and magnetic field strengths can be represented as

$$\mathbf{E}=-\frac{1}{c}\frac{\partial\mathbf{A}}{\partial t}=-\frac{1}{c}\frac{dA(t)}{dt}\mathbf{e}_x\sin kz,$$

$$\mathbf{H}=\operatorname{curl}\mathbf{A}=kA(t)\,\mathbf{e}_y\cos kz, \tag{3}$$

where $\mathbf{e}_y$ is the unit vector in the y direction.

Let us consider the case where the charged particle flies into the *EH*-field region with initial velocity $\mathbf{v}_0=c\beta_0\mathbf{e}_z$, where β_0 is the dimensionless velocity, and $\mathbf{e}_z$ is the unit direction in the z direction. To describe the motion of the particle we will use the Hamilton canonical equations. Thus, taking the expression for the vector potential (2) into account, the equations of motion can be represented in the form

$$\frac{d\mathcal{H}}{dt}=\frac{e^2}{\mathcal{H}}A(t)\frac{dA(t)}{dt}\sin^2 kz,\quad \frac{d\mathcal{P}_z}{dt}=-\frac{e^2}{2\mathcal{H}}kA^2(t)\sin 2kz,$$

$$\frac{dx}{dt}=-\frac{ecA(t)}{\mathcal{H}},\quad \frac{dz}{dt}=\frac{c^2\mathcal{P}_z}{\mathcal{H}}, \tag{4}$$

where $\mathcal{H}$ is the energy of the particle, $\mathcal{P}_z$ is the projection of the momentum of the particle onto the z axis, and x is the transverse coordinate.

Let us consider the case where the current in the coils of the electromagnets is a sum of a constant and a time-varying component. Then, if the variable component is described by a sine law, the amplitudes of the electric and magnetic field strengths can be represented as

$$H(t)=H_0(1+\mu\sin\omega t),$$

$$E(t)=\frac{\mu\omega H_0}{ck}\cos\omega t, \tag{5}$$

where H_0 is the amplitude of the constant component of the magnetic field, μ is a dimensionless parameter equal to the ratio of the amplitude of the variable component of the magnetic field to the amplitude of the constant component, and ω is the frequency of the variable component of the current in the coils of the electromagnets.

Here note should be made of the following: in order for the charged particle to always be found in the accelerating phase of the *EH*-field, the transit time of the particle through the *EH*-field region should be less than the period of variation of the amplitude of the magnetic field. Physically, this has to do with the fact that in this case during transit of the *EH*-field region the induced electric field performs positive work on the particle oscillating in the periodically reversed magnetic field. Thus, we will assume that the condition

$$\tau\ll\frac{2\pi}{\omega} \tag{6}$$

is satisfied,[2] where τ is the transit time of the particle through the *EH*-ubitron field region.

To study the equations of motion it is convenient in system (4) to transform to the dimensionless variables $h=\mathcal{H}/mc^2\gamma_0$, $p=\mathcal{P}_z/mc\beta_0\gamma_0$, $\xi=kz$. In addition, it can be easily seen that the right-hand sides of system (4) do not depend on the variable x. Therefore we will consider the equation for it separately. Thus, taking relations (5) into account, we obtain the basic system of equations describing the motion of a charge particle in a linearly polarized *EH*-ubitron field,

$$\frac{dh}{dt}=\alpha_1\frac{\cos\omega t(1+\mu\sin\omega t)\sin^2\xi}{h},$$

$$\frac{dp}{dt}=-\alpha_2\frac{(1+\mu\sin\omega t)^2\sin 2\xi}{h},\quad \frac{d\xi}{dt}=\alpha_3\frac{p}{h}, \tag{7}$$

where

$$\alpha_1=\frac{e^2H_0^2\mu\omega}{m^2c^4\gamma_0^2k^2},\quad \alpha_2=\frac{e^2H_0^2}{2m^2c^3\gamma_0^2\beta_0 k},\quad \alpha_3=kc\beta_0$$

are constant coefficients.

The initial conditions for system (7) can obviously be written as follows:

$$h(0)=1,\quad p(0)=1,\quad \xi(0)=0. \tag{8}$$

By virtue of the fact that the initial conditions for the particle energy and momentum enter into the definition of the coefficients $\alpha_1,\alpha_2,\alpha_3$, the nature of the motion is completely determined by the values of these coefficients. In the present work on the basis of system (7) we will investigate the charged-particle trajectories and also the dynamics of their acceleration as functions of the values of these coefficients $\alpha_1,\alpha_2,\alpha_3$.

ANALYSIS OF MOTION IN *EH*-UBITRON SYSTEMS WITH SLOW VARIATION OF THE MAGNETIC FIELD AMPLITUDE IN TIME

It is not possible to obtain analytical solutions of system (7). Therefore let us first consider approximate solutions of system (7) in the case of slow variation of the magnetic field in time. Physically this means that during transit of the particle through the *EH*-ubitron field region the amplitude of the magnetic field varies only slightly. As a criterion of slowness we adopt the condition

$$\omega\tau\ll 1. \tag{9}$$

Of course, by adopting this approximation we lower the rates of acceleration [as can be seen from relations (5), the amplitude of the induced electric field is directly proportional to the frequency ω, and if the value of the frequency is small, then the work performed by the electric field on the particle will also be small]. However, use of condition (9) allows us to simplify system (7) significantly and, as we will see below, without significantly altering the dynamics of particle motion in the *EH*-ubitron field. Thus, in the zeroth approximation in the parameter $\omega\tau$ we can rewrite system (7) in the form

$$\frac{dh}{dt}=\alpha_1\frac{\sin^2\xi}{h},\quad \frac{dp}{dt}=-\alpha_2\frac{\sin 2\xi}{h},\quad \frac{d\xi}{dt}=\alpha_3\frac{p}{h}. \tag{10}$$

In system (10) it is easy to obtain two integrals of motion

$$p=\sqrt{1-\frac{2\alpha_2}{\alpha_3}\sin^2\xi},$$

$$h=1+\frac{\alpha_1}{\alpha_3}\left(F\left(\xi,\frac{2\alpha_2}{\alpha_3}\right)-E\left(\xi,\frac{2\alpha_2}{\alpha_3}\right)\right), \tag{11}$$

where

$$F\left(\xi,\frac{2\alpha_2}{\alpha_3}\right),\quad E\left(\xi,\frac{2\alpha_2}{\alpha_3}\right)$$

are elliptical integrals respectively of the first and second kind.

Substituting relations (11) in the third equation of system (10), it is easy to see that the nature of the motion of the particle in an *EH*-ubitron field depends substantially on the value of the parameter $2\alpha_2\alpha_3^{-1}$. In other words, as the parameter $2\alpha_2\alpha_3^{-1}$ increases, bifurcation takes place, leading to a qualitative change in the form of the solutions for $\xi(t)$. Specifically, the motion of the particle in the xz plane can follow three different trajectories which are described by system (10): a) for $2\alpha_2\alpha_3^{-1}<1$ stable trajectories are realized which describe ballistic motion in the *EH*-field region; b) for $2\alpha_2\alpha_3^{-1}=1$ the particle moves along an unstable trajectory, escaping from the *EH*-field region after the first pair of electromagnets; c) for $2\alpha_2\alpha_3^{-1}>1$ stable trajectories are realized which characterize particle capture by the magnetic field of the first pair of electromagnets.

Obviously, for particle capture by the field of the first pair of electromagnets the particle undergoes further acceleration analogous to acceleration in a betatron. However, for industrial-production purposes such an operating regime of an *EH*-ubitron accelerator is obviously inefficient. This has to do, first of all, with the fact that the entire remaining part of the *EH*-field region remains unactivated. As for the unstable trajectories, the specifics of such motion are easily investigated with the aid of the following quadratures of system (10), which follow for $2\alpha_2\alpha_3^{-1}=1$:

$$p=\cos\xi,\quad h=1+\frac{\alpha_1}{\alpha_3}\left(\ln\left|\tan\left(\frac{\pi}{4}+\frac{\xi}{2}\right)\right|-\sin\xi\right),$$

$$t=\frac{1}{\alpha_3}\left(\ln\left|\tan\left(\frac{\pi}{4}+\frac{\xi}{2}\right)\right|+\frac{\alpha_1}{2\alpha_3}\ln^2\left|\tan\left(\frac{\pi}{4}+\frac{\xi}{2}\right)\right|\right.$$
$$\left.+\frac{\alpha_1}{\alpha_3}\ln|\cos\xi|\right). \tag{12}$$

It follows from these relations that at late times

$$\lim_{t\to\infty}(\xi(t))=\frac{\pi}{2},\quad \lim_{t\to\infty}(p(t))=0. \tag{13}$$

By virtue of the fact that in this case

$$\lim_{t\to\infty}(x(t))=\infty, \tag{14}$$

the particles for this type of motion are ejected from the field region in a direction parallel to the x axis, along a straight line equidistant from the first and second pairs of electromagnets.

As a numerical example, let us consider the motion of electrons in an *EH*-ubitron field. Solutions for various trajectories are shown in Figs. 1 and 2. Figure 1 plots solutions $\xi(t)$ for different values of the parameter $2\alpha_2\alpha_3^{-1}$. Figure 2 plots trajectories of electrons in the xz plane represented by the curves $kx(\xi)$ for the same values of the parameter $2\alpha_2\alpha_3^{-1}$. In both figures curves *1* correspond to capture motion for $2\alpha_2\alpha_3^{-1}=1.5$, curves *2* correspond to escape of the particle from the *EH*-field region for $2\alpha_2\alpha_3^{-1}=1$, curves *3* correspond to strongly perturbed ballistic motion for $2\alpha_2\alpha_3^{-1}=0.9$, and curve *4* describes weakly perturbed ballistic motion realized for $2\alpha_2\alpha_3^{-1}=0.01$. All of the curves were obtained for $\alpha_1\alpha_3^{-1}=10^{-4}$.

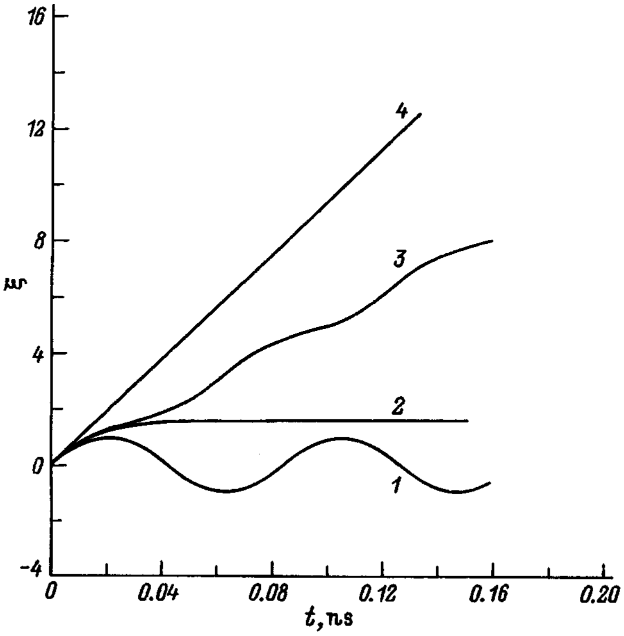

FIG. 1. Solution $\xi(t)$ for different types of motion of an electron in an *EH*-ubitron.

Analyzing the system parameters determining the value

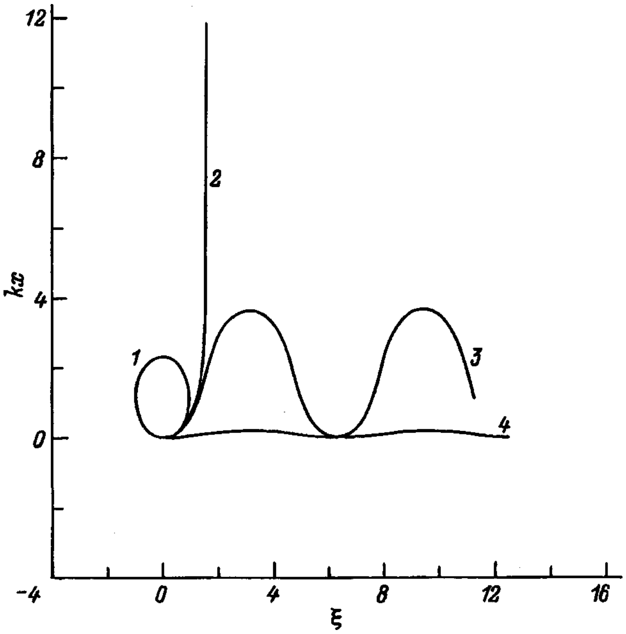

FIG. 2. Trajectories of an electron in the xz plane for different types of motion of the electron.

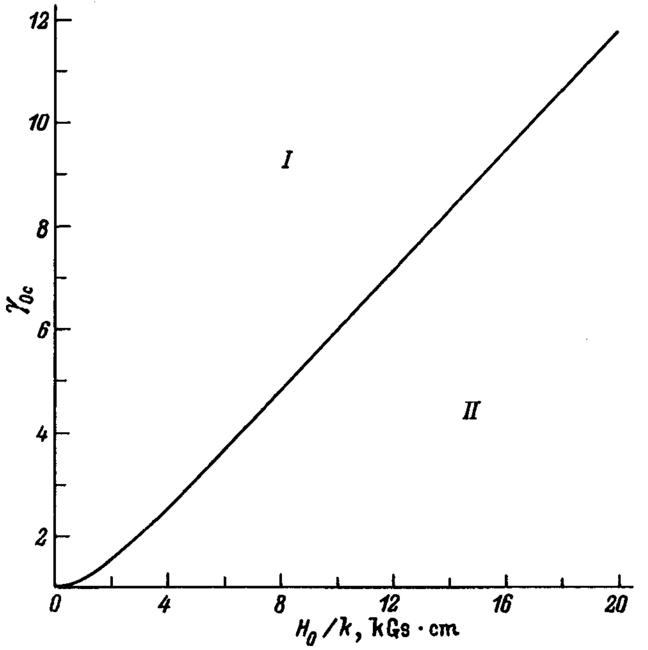

FIG. 3. Dependence of the critical value of the initial relativistic factor γ_{0c} on the parameter H_0/k for electrons.

of the parameter $2\alpha_2\alpha_3^{-1}$, it may be concluded that for a given value of H_0/k for a specific type of charged particle there exists a critical value of the initial relativistic factor, given by the expression

$$\gamma_{0c}=\sqrt{1+\left(\frac{eH_0}{mc^2k}\right)^2}. \tag{15}$$

Thus, for particle motion in an *EH*-ubitron field, capture trajectories are realized for $\gamma_0<\gamma_{0c}$, and ballistic trajectories for $\gamma_0>\gamma_{0c}$. Dependence (15) is plotted in Fig. 3 for electrons. Here region I corresponds to values of the relativistic factor for which ballistic trajectories are realized while region II corresponds to values for which capture trajectories are realized.

Obviously, particle drift along the z axis with simultaneous acceleration in the *EH*-ubitron field is possible only in the case of ballistic motion. Therefore we will obtain estimates for the variation of energy specifically for this case. By way of an example, let us consider the acceleration of a particle moving along a weakly perturbed trajectory (for $2\alpha_2\alpha_3^{-1}\ll 1$). We thus obtain the following approximate analytical solution for the dimensionless energy:

$$h=1+\frac{\alpha_1}{\alpha_3}\left(\xi-\frac{1}{2}\sin 2\xi\right). \tag{16}$$

Thus, for particle motion along a weakly perturbed trajectory the mean value of the energy grows according to a linear law. As for the rate of growth, note that the condition $2\alpha_2\alpha_3^{-1}\ll 1$, for which weakly perturbed trajectories are realized imposes the condition $\alpha_1\alpha_3^{-1}\ll 1$. Therefore, the regime of weakly perturbed trajectories is characterized by comparatively small rates of acceleration.

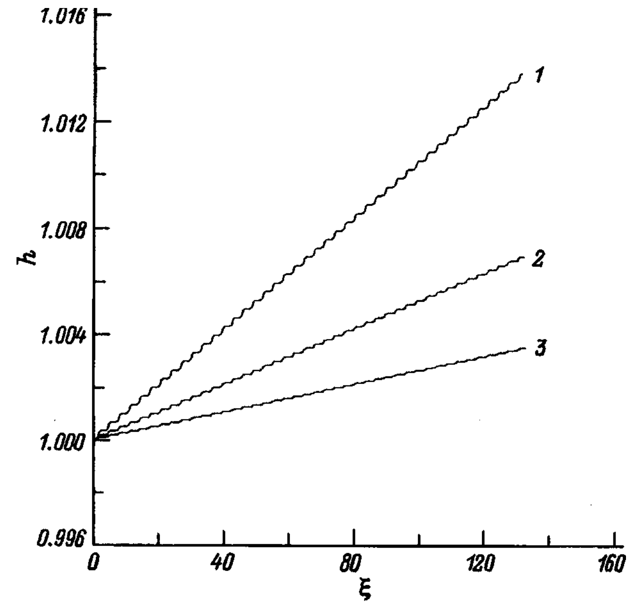

FIG. 4. Dependence of the dimensionless energy of an electron h on the longitudinal coordinate ξ for the case of ballistic motion.

The growth of energy in the case of motion along strongly perturbed trajectories can be investigated with the aid of relations (11). A plot of the corresponding dependences $h(\xi)$ is shown in Fig. 4 for electrons for different values of the parameter $\alpha_1\alpha_3^{-1}$: curve *1* corresponds to $\alpha_1\alpha_3^{-1}=6\times 10^{-5}$, curve *2* to 3×10^{-5}, and curve *3* to 1.5×10^{-5}. All three curves were calculated for $2\alpha_2\alpha_3^{-1}=0.99$.

ANALYSIS OF MOTION IN *EH*-UBITRON SYSTEMS WITH ARBITRARY RATE OF CHANGE OF THE MAGNETIC FIELD AMPLITUDE

The physics of the interaction of a particle with an *EH*-ubitron field having arbitrary rate of change of the amplitude of the magnetic field is more complex. This has to do, first of all, with the fact that processes of particle capture by the field of one of the pairs of electromagnets can take place at any point in the interaction region. In other words, even if the capture condition is not met at the first pair of magnets, it can be valid at another point in the *EH*-field region due to an increase in the magnetic field amplitude in time. In addition, in such systems the rates of acceleration will be greater due to a lifting of the restrictions on the frequency and transit time (9). However, as has already been noted, analysis of systems with arbitrary rate of change of the magnetic field is complicated by the impossibility of finding analytical solutions of system (7). Therefore, we will employ the results of numerical integration of system (7) for the case of electrons.

Analysis of system (7) allows us to identify an approximate condition for which ballistic motion is realized in systems with arbitrary rate of change of the magnetic field,

$$\frac{2\alpha_2(1+\mu\sin\omega\tau)^2}{\alpha_3}<1. \tag{17}$$

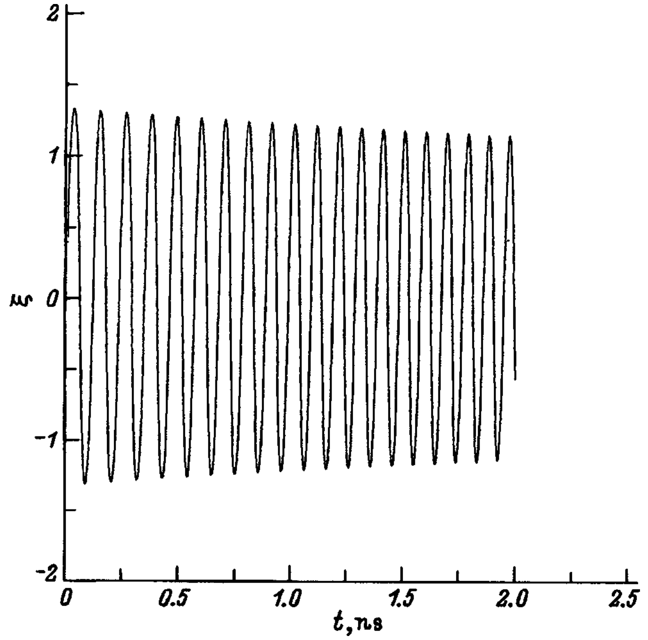

FIG. 5. Solution for $\xi(t)$, describing capture of an electron by the field of the first pair of electromagnets in the case of arbitrary rate of change of the magnetic field amplitude.

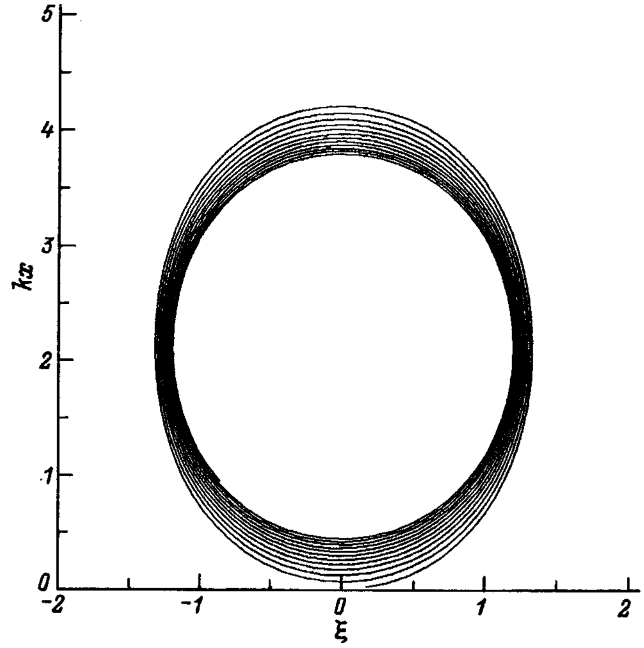

FIG. 6. Trajectories of an electron in the *xz* plane for the same conditions as in Fig. 5.

In essence, condition (17) implies that the magnetic field strength of the last pair of electromagnets is not enough for particle capture.

Let us consider numerical solutions of system (7) for different values of the parameters $\alpha_1, \alpha_2, \alpha_3$. Figure 5 plots the dependence $\xi(t)$ characterizing capture of an electron by the field of the first pair of electromagnets. The parameters of the system were taken to be the following: $\alpha_1 = 1 \times 10^8\,\mathrm{s}^{-1}$, $\alpha_2 = 4.8 \times 10^{10}\,\mathrm{s}^{-1}$, $\alpha_3 = 9.2 \times 10^{10}\,\mathrm{s}^{-1}$, $\omega = 1 \times 10^8\,\mathrm{s}^{-1}$, and $\mu = 1$. Clearly, the dependence has the character of damped oscillations. This is because with growth of the magnetic field the radius of the particle trajectory decreases. The nature of the trajectory in the *xz* plane is shown in Fig. 6 by the curve $kx(\xi)$ for the same parameter values. As follows from this figure, the particle trajectory converges upon itself as it approaches the axis between the centers of the magnets.

The transition from ballistic motion to capture motion can be investigated by considering the capture of electrons at different pairs of electromagnets. Dependences of this sort are shown in Fig. 7. This figure plots curves of the dependence $\xi(t)$ describing the transition from ballistic motion to capture motion at different pairs of electromagnets. In particular, curve *1* describes capture by the 14th pair of magnets ($\alpha_1 = 9.1 \times 10^7\,\mathrm{s}^{-1}$, $\alpha_2 = 4.28 \times 10^{10}\,\mathrm{s}^{-1}$; curve *2* describes capture by the 23rd pair ($\alpha_1 = 8.8 \times 10^7\,\mathrm{s}^{-1}$, $\alpha_2 = 4.1 \times 10^{10}\,\mathrm{s}^{-1}$); and curve *3* describes capture by the 33rd pair ($\alpha_1 = 8.4 \times 10^7\,\mathrm{s}^{-1}$, $\alpha_2 = 4 \times 10^{10}\,\mathrm{s}^{-1}$). The remaining parameters were set equal to the same values for all the curves: $\alpha_3 = 9.2 \times 10^{10}\,\mathrm{s}^{-1}$, $\omega = 1 \times 10^8\,\mathrm{s}^{-1}$, and $\mu = 1$. The trajectories in the *xz* plane are shown in Fig. 8: curve *1* is the trajectory for capture by the 14th pair of magnets (the parameters are the same as in curve *1* in Fig. 7) while curve *2* is the trajectory of a particle escaping from the *EH*-field region between the 13th and 14th pairs of electromagnets ($\alpha_1 = 9.13 \times 10^7\,\mathrm{s}^{-1}$, $\alpha_2 = 4.3 \times 10^{10}\,\mathrm{s}^{-1}$, $\alpha_3 = 9.2 \times 10^{10}\,\mathrm{s}^{-1}$, $\omega = 1 \times 10^8\,\mathrm{s}^{-1}$, and $\mu = 1$).

The acceleration processes can be investigated numerically by integrating system (7) under conditions of purely ballistic motion (17). An example of such a calculation is shown in Fig. 9, which plots the dependence of $h(\xi)$ for the following parameter values: $\alpha_1 = 1.34 \times 10^8\,\mathrm{s}^{-1}$, $\alpha_2 = 2.6 \times 10^{10}\,\mathrm{s}^{-1}$, $\alpha_3 = 9.2 \times 10^{10}\,\mathrm{s}^{-1}$, $\omega = 2.4 \times 10^8\,\mathrm{s}^{-1}$, $\mu = 1$, and $N = 100$ pairs of electromagnets. It can be seen that for these

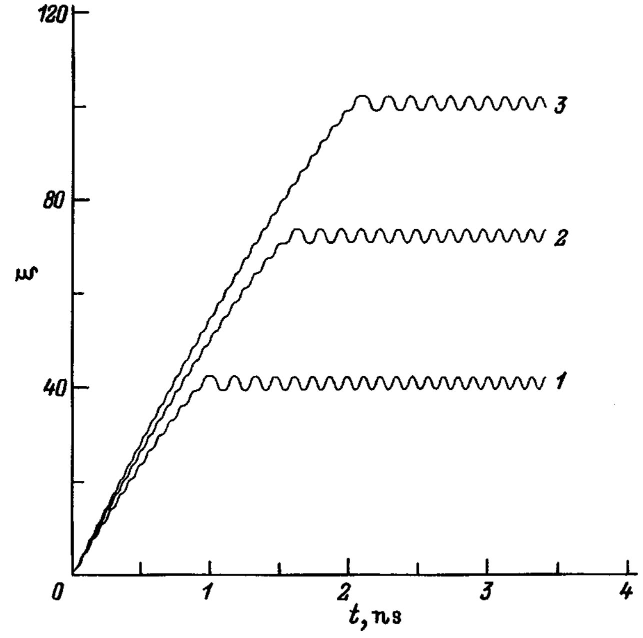

FIG. 7. Dependence $\xi(t)$ describing the transition from ballistic motion of an electron to captured motion in the vicinity of different maxima of the magnetic component of the *EH* field.

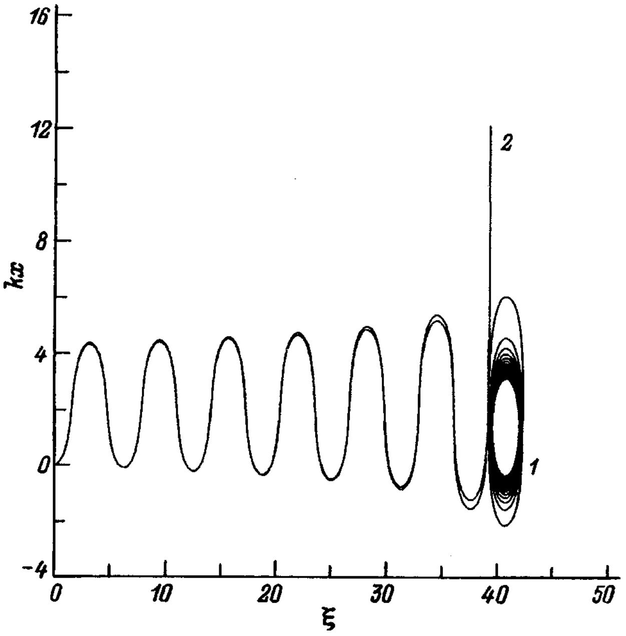

FIG. 8. Trajectories of an electron in the *xz* plane.

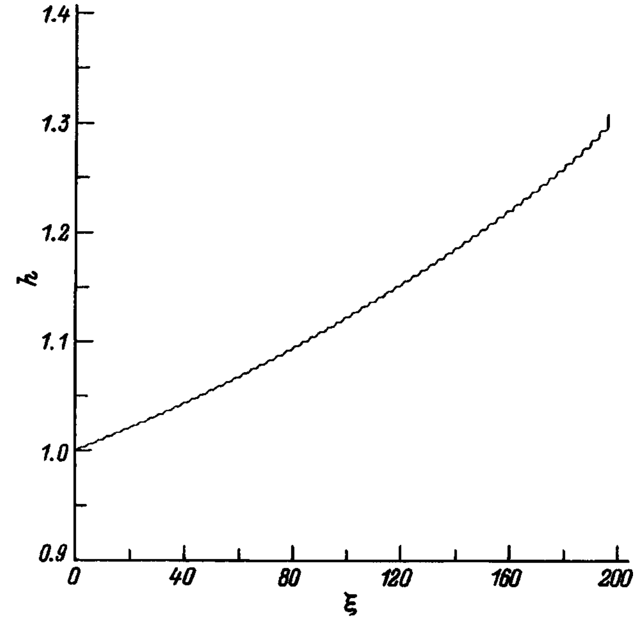

FIG. 9. Dependence of the dimensionless energy of an electron *h* on the longitudinal coordinate ξ in the case of arbitrary rate of change of the magnetic field amplitude.

values of the parameters the additional energy acquired by the electron in a linearly polarized *EH*-ubitron field is equal to roughly 30% of the total initial energy.

DISCUSSION

In the very first works dedicated to *EH*-ubitron accelerators[2] it was shown that there is an upper limit on the rates of acceleration of these systems. This upper limit is connected with the impossibility of increasing the frequency of the current ω in the coils of the electromagnets above some upper limit determined by condition (6). In the opposite case the electric field vector **E** changes sign and the particle falls into the braking phase of the *EH*-field. It also follows from the analysis presented here that for a given value of the initial relativistic factor there is an upper bound on the amplitude of the magnetic component of the *EH*-ubitron field H_0 (15). Thus, we may conclude that a second mechanism exists limiting the rates of acceleration of *EH*-ubitron accelerators, connected with the capture effects described in the present work. By virtue of the fact that the rate of growth of the particle energy in *EH*-ubitron systems is directly proportional to $H_0^2\omega$ (Ref. 2) we may conclude that the second mechanism is more important and there are fundamental limitations on the rates of acceleration of such setups. In addition, when nonmonoenergetic beams are accelerated in *EH* systems a cutoff of part of the current is possible as a result of capture of particles by the fields of different pairs of electromagnets. But the number of the magnet pair whose field captures a specific particle depends on the particle's energy. Thus the low-energy part of the beam can be delayed in the region of the accelerating section.

At the same time, as follows from the results of this work, the creation of combined schemes is possible, in which the last pair of magnets plays the role of a betatron accelerator. Such setups can be technologically advantageous if the beam-cooling effect is utilized along with the acceleration.[6] In that case an almost monoenergetic particle beam would be delivered at the entrance to the betatron section. This would eliminate the problem of accelerating particles of different energy ranges in the same working space.

In conclusion, the author wishes to thank A. I. Olemskiĭ and S. A. Kuleshov for helpful discussions.

[1] I. G. Artyukh and G. Sj. Kamal'dinova, Obzory Élektron. Tekh. Ser. I. Élektronika SVCh, No. 19, 1314 (1987).
[2] V. V. Kulish and O. B. Krut'ko, Pis'ma Zh. Tekh. Fiz. **21**(9), 52 (1995) [Tech. Phys. Lett. **21**, 339 (1995)].
[3] V. V. Kulich, P. B. Kosel, O. B. Krutko, and I. V. Gubanov, in *Proceedings of MPSL'96 Conference*, Sumy (Ukraine), 1996.
[4] V. V. Kulish, P. B. Kosel, and O. B. Krutko, *Abstracts of the 23rd European Physical Society Conference on Controlled Fusion and Plasma Physics*, Ukraine, 1996, p. 468.
[5] V. V. Kulish, P. B. Kosel, O. B. Krutko, in *Proceedings of MPSL'96 Conference*, Sumy, Ukraine, 1996.
[6] V. V. Kulish, P. B. Kozel, O. B. Krut'ko, and I. V. Gubanov, Pis'ma Zh. Tekh. Fiz. **22**(15), 68 (1996) [Tech. Phys. Lett. **22**, 630 (1996)].
[7] V. V. Kulish and O. B. Krut'ko, Pis'ma Zh. Tekh. Fiz. **21**(11), 47 (1995) [Tech. Phys. Lett. **21**, 418 (1995)].
[8] A. G. Kaĭlik, A. A. Kvak, and O. B. Krut'ko, Ukr. Fiz. Zh. **40**, 922 (1995).
[9] N. N. Moiseev, *Asymptotic Methods of Nonlinear Mechanics* [in Russian], Nauka, Moscow, 1969.

Translated by Paul F. Schippnick

Growth of $YBa_2Cu_3O_{7-x}$ thin films on sapphire with a cerium-oxide sublayer

E. K. Gol'dman, D. A. Plotkin, S. V. Razumov, and A. V. Tumarkin

St. Petersburg State Electrical-Engineering University, 196376 St. Petersburg, Russia

(Submitted July 17, 1997)
Zh. Tekh. Fiz. **69**, 94–98 (January 1999)

The possibility is demonstrated of preparing high-quality films of the high-temperature superconductor $YBa_2Cu_3C_{7-\delta}$ with thicknesses up to 2.6 μm by dc magnetron sputtering. It is found that inclusions consisting of CuO and $YBa_2Cu_3O_8$ coexist with the growing film and are ''sinks'' for defects, nonstoichiometric atoms, and mechanical stresses. Using x-ray diffraction and Rutherford backscattering, we find that the structural perfection of the films is improved by increasing the thickness when using the proposed fabrication technique.

[S1063-7842(99)01501-9]

INTRODUCTION

YBCO films of $0.6-2.6\,\mu$m thickness are quite promising materials for the construction of devices for microwave and power electronics. For microwave applications it is necessary that the film thickness exceed several London penetration depths λ_L. Otherwise the microwave signal losses grow. The London penetration depth λ_L is roughly 140–180 nm for a perfect crystal along the c axis of the unit cell[1] and is significantly greater in real films as a consequence of their structural imperfections: the presence of point defects, grain boundaries, etc. This means that it is necessary to obtain films of satisfactory quality with thickness greater than $0.5\,\mu$m. However, efforts to grow thick films run up against significant difficulties associated with deterioration of the quality of the structure with increasing thickness and a shift in the orientation of the growing film. YBCO films with the c axis of the unit cell oriented perpendicular to the substrate surface (the c orientation) are optimal from the point of view of their electrophysical properties and application in microwave devices. Starting at some critical thickness t_c, growth of grains with the c axis parallel to the surface (the a orientation) begins to prevail. In a-oriented films the critical current density is an order of magnitude lower and the London penetration depth λ_L is three times higher. Thus, the problem arises of preventing the orientation of the growing film from shifting during sputtering of films of $0.6-2.6\,\mu$m thickness.

Numerous studies of changes in the orientation during growth of YBCO films have been performed.[1–4] It can be taken as an established fact that the formation of a-oriented grains takes place at a lower temperature than formation of c-oriented grains regardless of the substrate material (studies of growth have been carried out both on substrates with well-matched lattice parameters of substrate and film (STO, $LaAlO_3$) and for mismatched substrates (MgO), and also on a presputtered thin c-oriented YBCO film). In films grown at a temperature optimal for formation of c-oriented grains, a-oriented inclusions were also observed which were detected either at the film–substrate interface[4,5] or at some depth into the film.[1,3] In either case, starting at some critical thickness t_c, growth of the a-oriented phase predominates. The authors of Ref. 4 suggest that growth along the a axis is faster as a consequence of the fact that it is easier for the unit cell to align itself with the $a-c$ and $b-c$ faces than with an $a-b$ face while the orientation of the grains forming on the substrate during the initial stages of growth depends on the temperature. This hypothesis explains the fact that the relative volume of the a phase increased with thickness in all the experiments. Computer simulations[4] showed that for a growth rate ratio of 10 : 1 the relative fraction of a-oriented phase on the surface increases from 2 to 100% as the film grows to a thickness of 300 nm. These results agree with experiment.[4] On the other hand, the authors of Ref. 6 conclude that a-oriented growth is thermodynamically favored while c-oriented growth is kinetically favored and is possible only for a high supersaturation. The other hypothesis is that cooling of its surface leads to the change in orientation of the growing film. According to the data of Refs. 1 and 2, in order for the formation of a-phase grains to prevail the temperature of the growing surface should be lowered by 120 °C. Some possible mechanisms of such cooling have been proposed; however, such a large temperature drop has not yet been confirmed by direct observations; however, the authors of Ref. 2 were able to increase the critical thickness t_c to several microns by using a linear or stepped temperature increase with growth of the film. Nevertheless, the structural perfection of these films deteriorated with thickness and the volume of the a-oriented phase increased even though it remained quite small.

It may be conjectured that both a-oriented and c-oriented grains form on the substrate surface and also on the surfaces of existing grains. Their formation rate depends on the temperature, degree of supersaturation, orientation (c- and a-) of the preceding layer, and the presence of surface defects.

Recently we examined the growth of secondary insulating phases (inclusions) during the initial stages of growth of YBCO films.[7] We found that such inclusions consist of CuO and $YBa_2Cu_3O_8$ phases and that their concentration varies with time during growth of the first layers of the film and then reaches a saturation level around $10^9\,cm^{-2}$. These inclusions can coexist with the growing film and function as ''sinks'' for defects, nonstoichiometric atoms, and mechanical stresses. Being insulators, they do not degrade the superconducting or microwave properties of the YBCO films.[8] In the present paper, working on the supposition that the secondary phases can influence the ratio of growth rates of the *a*- and *c*-oriented YBCO (123) phases, we examine $YBa_2Cu_3O_{7-x}$ films of 0.3–2.6 μm thickness whose growth conditions ensure the formation of insulating inclusions.

EXPERIMENT

The films were sputtered in a planar dc magnetron system in an atmosphere of pure oxygen at a pressure of 1 Torr. The oxygen-enriched atmosphere ensures complete oxidation of the inclusions, which determines their insulating properties and the possibility of using them in microwave devices. As the substrate we used sapphire [1102] (*r*-cut) with a sublayer of cerium oxide of thickness 200 Å and mixed (001)/(111) orientation.[9] Sputtering was performed for two values of the discharge current: 400 and 200 mA, which provided two different deposition rates.

During the first 30 min of sputtering the discharge current was increased and was thereafter kept constant. The temperature of the substrate-holder was maintained at 650 °C and was not increased during sputtering. The deposition time varied from 5 to 45 h.

The thickness of the films was measured with the help of a DEKTAK 3030 profilometer and varied from 0.1 to 2.6 μm. The deposition rate, found from the values of the film thickness, was 10.5 Å/min ($\pm 5\%$) for a current of 400 mA and 3 Å/min ($\pm 5\%$) for a current of 200 mA. It should be noted that the twofold decrease in the discharge current (and correspondingly the sputtering rate) leads to a threefold decrease in the rate of growth. This is evidence that the rate of growth is quite low and near the kinetic minimum at which all atoms arriving at the substrate re-evaporate and the film does not grow.

The structural perfection of the growing films was examined with the aid of a Rigaku-Dmax Geigerflex x-ray diffractometer. The relative fractions of the *c*- and *a*-oriented phases were calculated on the basis of the relative intensity of the YBCO peaks: (005) (*c*-orientation) and (200) (*a*-orientation). Toward this end, we compared the total peak intensities obtained from the rocking curve and normalized to the intensities for powder samples (we followed the technique described in Ref. 1). Values of the full width at half maximum (FWHM) of the (005) peak in the rocking curve were used to estimate the misorientation of the film along the *c* axis.

We also used Rutherford backscattering to analyze the structure of the films. Rutherford backscattering of ions with intermediate energies (200 keV) in conjunction with an electrostatic analyzer provides a depth resolution of around 5 Å and gives information about the structural perfection of the films along the *c* axis, allowing one to compare the structural quality of films at a fixed depth.

The surface morphology of the films was investigated with a scanning electron microscope. The concentration and mean dimensions of the surface objects were found with the help of a specially developed computer program.

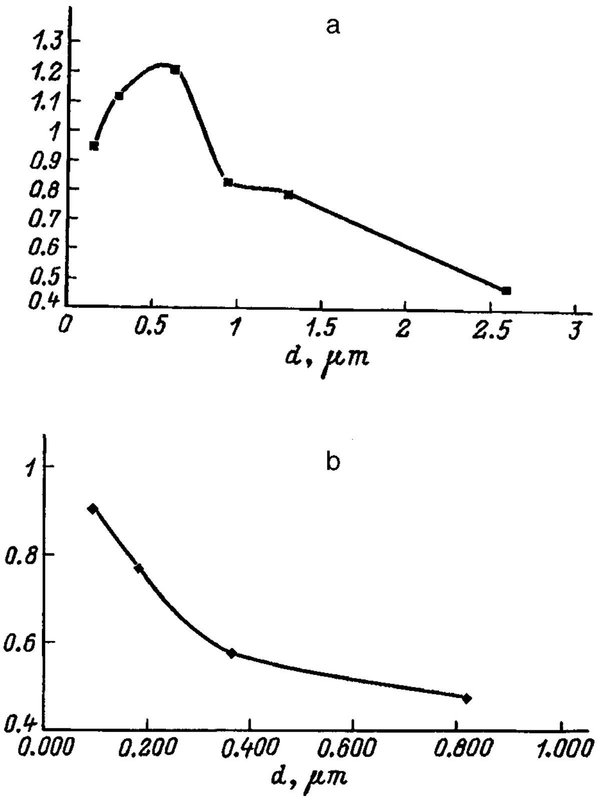

FIG. 1. Dependence of the FWHM of the (005) YBCO peak of the rocking curve on the film thickness for a current of 400 (a) and 200 mA (b).

To compare the electrical properties of the films, we chose the parameters most sensitive to the degree of structural perfection and the orientation—the critical current density j_c and the microwave surface resistance R. The critical current density was measured by a noncontact method at 77 K, and the surface resistance was measured in a copper resonator at 77 K at 60 GHz.

RESULTS

Figure 1 plots the FWHM (y) of the (005) peak of YBCO, obtained by a φ scan, as a function of thickness (d). The tendency for the misorientation of the film along the c axis to decrease is clearly visible for both deposition rates. The contribution of the broadening effect due to finite film thickness is insignificant; it can be estimated according to Ref. 10 as 0.1° for the thinnest film (0.1 μm). The instrument error was the same for all the samples and did not exceed 0.1°, i.e., the curves in Fig. 1 reflect an actual improvement in the structural perfection of the films with thickness. At the same time, the FWHM of the (005) peak for relatively thin films with thickness in the range 0.1–0.3 μm is relatively large: 1–1.1°. The range of values 0.7–0.8° reached for films 0.5 μm thick is standard for our films used in microwave devices, and the values 0.45–0.5°, observed for films 1–2 μm in thickness are close to the lowest values reported in the literature for significantly thinner films.

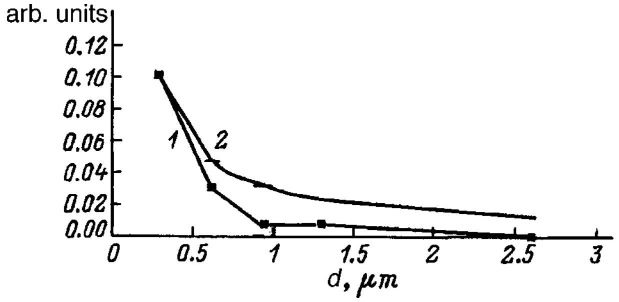

FIG. 2. Number of *a*-oriented grains: *1* — with normalization, normalization with weighting factor $R=1(200)/T(200)/(I(005)+I(200)/T(200))$, $T(200)=28.7$, $T(005)=11.2$; *2* — without anneal, current 400 mA.

Simultaneous with a decrease in the FWHM of the (005) peak, the relative fraction of *a*-oriented phase decreases with growth of the film thickness. This dependence is shown in Fig. 2 for a discharge current of 400 mA. Note that the relative volume of the *a*-phase decreases with growth of the thickness faster than if the initial number of *a*-oriented grains were kept constant (Fig. 2). This means that some recrystallization takes place: annealing in an atmosphere of pure oxygen and at a constant flux of the YBCO components onto the substrate. For all the films sputtered at the lower deposition rate (at a discharge current of 200 mA), and for the 2.6-μm thick films sputtered at a discharge current of 400 mA, no *a*-phase grains were detected in the x-ray analysis, i.e., the intensity of the (200) peak was lower than the resolution threshold of our x-ray apparatus. This suggests an upper limit on the relative volume of the *a*-phase around 5%.

Surface studies of the films using a scanning electron microscope revealed two types of macroscopic defects: holes and inclusions of secondary phases (Fig. 3). Here there were more holes in the surface of the thicker films, and more inclusions in the surface of the thinner films; slowly growing inclusions were also probably present at the bottom of the holes. The total concentration of the macroscopic defects remains at a level around $5\times10^{8}\,\mathrm{cm}^{-2}$, which is close to the saturation level in the time dependence of the concentration of islands of secondary phase in the initial stages of growth of the YBCO films.[11]

Rutherford backscattering analysis, which compares values of the dechanneling $\chi(50)$, confirmed that the orientation of the structure improves with growth of film thickness. The value of $\chi(50)$ is proportional to the ratio of the channeled to the unchanneled signal at a depth of 50 nm from the surface of the film.

The dechanneled signal χ is higher for films with a larger concentration of defects, intermediate layers, and damage in the lattice. It also grows with increase of the misorientation of the grains along the channels perpendicular to the surface. Results of a comparison for films sputtered at 200 mA are shown in Fig. 4. The dependence $\chi(t)$, where t is the distance from the film surface, also provides information about the types of defects. In our case, the indicated dependence can be approximated by a linear function $\chi=\chi(0)+Dt$. Values of $\chi(0)$, $\chi(50)$, and D are given in Table I; values of $\chi(0)$ and D, measured for a single crystal and calculated by the Monte Carlo method for a perfect crystal, are also given in the table. Note that to estimate the structural perfection we chose the quantity $\chi(50)$, which is observed directly, while both $\chi(0)$ and D are found by fitting. The quantity D reflects the presence of defects in the interior of the film such as point defects and dislocations.

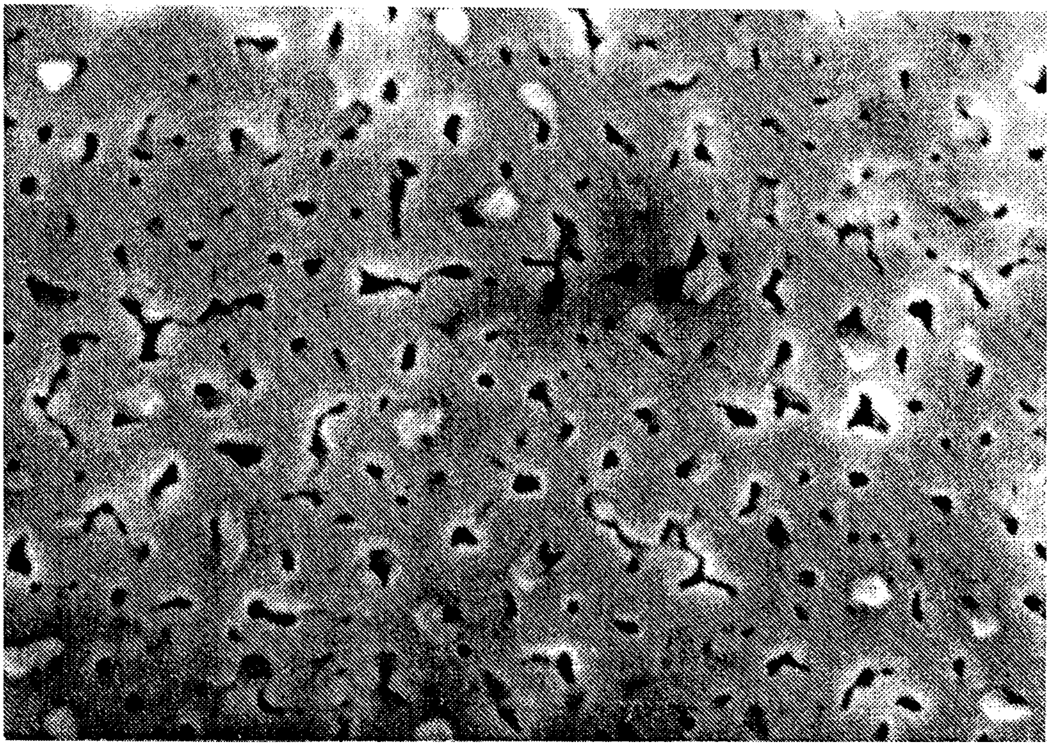

FIG. 3. Surface (scanning electron microscope).

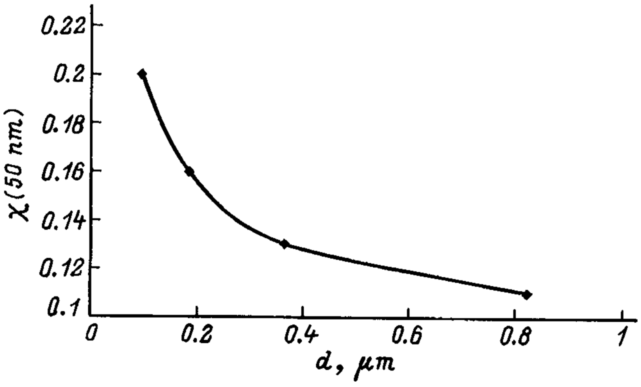

FIG. 4. Dependence on film thickness of the ratio of the channeled signal to a random signal in the Rutherford backscattering spectrum (discharge current 200 mA).

The concentration of these defects can be estimated if their type is known; assuming that the defects are dislocations, we estimate their concentration as $5\times10^{10}\,\mathrm{cm}^{-2}$. In turn, a difference between the measured and theoretical values of χ can arise due to misorientation of the grains relative to the *c* axis or the presence of a nonchanneling phase on the surface. In the first case, our films should have a misorientation on the order of $0.12-0.45°$, which is less than that observed by x-ray analysis. The second possibility seems more probable since the macroscopic defects that are visible in photomicrographs of the film surface are most likely nonchanneling. The contribution of inclusions of secondary phases on the surface to the nonchanneling signal is proportional to their concentration and average size while the contribution of the holes also depends on their depth. Taking both types of macroscopic defects into account, we should decrease the value of $\chi(0)$ for the *c*-oriented phase to 0.11 for the better films. This value is near the value measured for single crystals.

Measurements of the critical current density gave less unambiguous results. The dependence of the critical current density on film thickness had an irregular character: *j* varied between 0.9×10^6 and and 2×10^6 A/cm^2. It should be noted that both values are characteristic of good films. Better results were obtained for films of intermediate thickness. A possible explanation for this effect may be the presence of insulating macro-defects; it is unknown in what way they influence the critical current recorded by the contactless inductive method. Microwave measurements showed that the surface resistance of all the films with thickness greater than 0.2 μm is less than 50 mΩ at 60 GHz at 77 K. A study of the characteristics of microwave devices (filters) based on our films has made it possible to compare the properties of films of different thickness in more detail. The results of this study will be reported later.

We may conclude that the structural perfection of the prepared films, which was quite low for the films of thickness $0.1-0.3\,\mu$m, improved with growth of the thickness and for films of thickness $1-2\,\mu$m approached the better results obtained in processes optimized for growth of thin single-phase YBCO films. The relative fraction of *a*-phase also decreased with growth of the thickness, and recrystallization of the initially grown grains of the *a*-phase occurred. The preparation of YBCO films with thickness $1-2\,\mu$m with high structural perfection and low content of the *a*-oriented phase was reported earlier; however, the tendency of the indicated parameters to decrease with growth of the thickness is a new fact. Taking into account that growth of the *a*-oriented phase prevails at lower temperatures,[1,2] we may conclude that in our case cooling of the surface of the growing film does not take place. Since heating of the surface is improbable (there is no mechanism for such heating for 1-μm thick films with a constant temperature of the heater), the surface temperature does not vary enough to affect the orientation of the film. Thus, other factors must prevail, among which the only obvious one is the presence of macroscopic defects. The physics of their interaction with the growing film has so far not been investigated. They definitely act as sinks for defects and nonstoichiometric atoms. In addition, they can act as preferred sites for nucleation of the *a*-phase, limiting its growth and altering the volume ratio of *c*- and *a*-oriented grains in favor of the *c*-oriented phase. The results presented above suggest that the formation of secondary phases and macroscopic defects can be used to grow high-quality YBCO films of required thickness.

In summary, the results of our study of thick (up to 2.6 μm) YBCO films have shown that the relative fraction of *a*-oriented phase decreases with increasing thickness (contrary to previously published results) and amounts to less than 95% in the thickest films (2.6 μm) grown at a discharge

TABLE I.

Sample	Current, A	Thickness 10^{15} atoms/cm^2	Thickness μm	χ(50 nm)	*D*, 10^{-19} cm^2/atoms	$\chi(0)$
507	0.4	770	0.11	0.2	1.4	0.14
508	0.2	620	0.093	0.2	2	0.1
509	0.2	1250	0.183	0.16	2	0.07
513	0.2	2000	0.366	0.13	1.4	0.06
516	0.6	3100	0.4	0.17	1.4	0.1
512	0.2	>4000	0.8235	0.11	1.2	0.06
515	0.4	>8000	2.6	0.11	1.3	0.065
Theoretical					0.7	0.03
minimum					0.2	0.015

Note: The thickness was measured using Rutherford backscattering and only for films of thickness less than 0.5 μm.

current of 400 mA, and for all of the films grown at 200 mA. The orientation of the *c*-phase also improves with thickness, as confirmed by Rutherford backscattering and x-ray diffraction studies. Among the possible reasons for this, we have already remarked on the presence of macroscopic defects. Presumably these defects, detected with a scanning electron microscope, stabilize the growth of the *c*-oriented phase and hinder growth of the *a*-phase. To elucidate the mechanism of improvement of film structure and the role of macroscopic defects in the indicated process, additional studies of the growth of YBCO films in the presence of insulating inclusions are needed. In particular, the question, to what thickness can *c*-oriented films be grown, is of practical interest.

[1] F. Vassenden, G. Linker, and J. Geerk, Physica C **175**, 566 (1991).

[2] S. Sievers, F. Mattheis, and H. Krebs, J. Appl. Phys. **78**, 5545 (1995).

[3] A. H. Carin, S. N. Basu, R. E. Muenchausen, Appl. Phys. Lett. **58**, 871 (1991).

[4] C. W. Nieh, L. Anthony, J. Y. Josefowicz *et al.*, Appl. Phys. Lett. **56**, 2138 (1990).

[5] E. García-González, G. Wagner, and M. Reedyk, J. Appl. Phys. **78**, 353 (1995).

[6] S. J. Pennycook, M. F. Chisholm, D. E. Jesson *et al.*, Physica C **202**, 1 (1992).

[7] E. K. Hollmann, V. I. Goldrin, D. A. Plotkin *et al.*, Tech. Phys. Lett. **22**, 942 (1996).

[8] Y. J. Tian, L. P. Guo, L. Li *et al.*, Appl. Phys. Lett. **65**, 234 (1994).

[9] E. K. Hollmann, A. G. Zaitsev, V. E. Loginov *et al.*, J. Phys. D **26**, 504 (1993).

[10] J. P. Gong, M. Kawasaki, and K. Fujito, Phys. Rev. B **50**, 3280 (1994).

[11] E. K. Gol'man, V. I. Gol'drin, D. A. Plotkin *et al.*, Fiz. Tverd. Tela (St. Petersburg) **39**, 216 (1997) [Phys. Solid State **39**, 189 (1997)].

Translated by Paul F. Schippnick

TECHNICAL PHYSICS VOLUME 44, NUMBER 1 JANUARY 1999

The method of concentration pulses for studying hydrogen transport in solids

I. E. Gabis

Scientific-Research Institute of Physics, St. Petersburg State University, 198904 St. Petersburg, Russia

(Submitted November 19, 1996; resubmitted October 16, 1997)
Zh. Tekh. Fiz. **69**, 99–103 (January 1999)

The method of concentration pulses is designed for investigating the kinetics of hydrogen transport in complex diffusion systems and allows one to choose the most probable transport model and determine the rate constants of processes influencing the kinetics, e.g., diffusion, adsorption, and desorption, capture to traps, etc. We describe the idea of the method, its experimental realization, and a procedure for processing the results which allows one to choose the most probable model and determine the desired rate constants. © *1999 American Institute of Physics.* [S1063-7842(99)01601-3]

INTRODUCTION

In the latest studies of hydrogen transport in solids where the sphere of interest has been extended to *d* metals with filled *d* shell (Cu, Ag, Au), *s* and *p* metals, and also semiconductor materials, one of the main tasks that remains to be addressed is the determination of the mechanisms of hydrogen transport. The problem consists in the complexity of these processes, consisting of several sequential or parallel stages whose rates in one way or another influence the transport kinetics. It is of obvious interest to experimentally determine the largest number of physical parameters. Further progress in this direction without new methodological developments would be problematic.

The approach expounded here allows one to determine the most probable phenomenological transport model and obtain information about several processes influencing the kinetics. The parameters to be determined can be the hydrogen diffusion coefficients, parameters of the adsorption–desorption processes, rate constants of hydrogen capture to traps and liberation from them, etc.

The method of concentration pulses (MCP) described below was developed over the course of eight years. In particular, with its help, studies of hydrogen transport in silver have been carried out,[1,2] and also studies of hydrogen transport in thin films of nickel oxide,[3] graphite,[4] and amorphous silicon[5] deposited on a nickel membrane. The last three works illustrate the possibilities of the technique for studying semiconductors. A direct application of the method of hydrogen permeability here is problematic due to the complexity of preparing a sufficiently thin vacuum-tight membranes from semiconductor materials working under thermal loads.

In the development of a procedure allowing one to choose the most probable model from among several possible ones and to determine the kinetic parameters entering into it (the diffusion coefficient, rate constants of the interaction with the traps, desorption rate constant, etc.) a number of problems arise. One consists in setting up an experiment that is sensitive to the mechanism of hydrogen transport and will allow the recording of a dependence that is a well-based function of these parameters. Another difficulty consists in establishing a sufficient number of relations explicitly linking these parameters with the experimental data so that one can construct a calculational algorithm.

The method of concentration pulses is a complete package that includes a technique for performing the experiments, a database of possible phenomenological transport models with solutions of the corresponding boundary conditions, a set of programs for selecting the model and determining the kinetic parameters, computer-controlled experimental apparatus, and a real-time program for carrying out the experiment.

IDEA OF THE METHOD

Let us consider a flat membrane, in the near-surface region of which, adjoining one of its sides (below we will call this side the input side), sinusoidal oscillations in the hydrogen concentration are created, while the opposite side (the output side) faces a vacuum. After some time, a flux penetrating from one side to the other is set up which is also oscillating, but with a phase delay. As the frequency of the concentration oscillations ω is varied, the phase ϕ of the penetrating flux also varies. By probing the membrane with waves of different frequencies ω_j it is possible to determine the phase–frequency characteristic (PFC) of the penetrating flux.

The shape of the phase–frequency characteristic depends strongly on the mechanism of hydrogen transport. To illustrate this, Fig. 1 plots three model phase–frequency characteristics. In the classical case of Fick diffusion through a homogeneous membrane (curve *1*) the phase–frequency characteristic depends on the diffusion coefficient D and the thickness l. For diffusion accompanied by reversible capture to traps (curve *2*), it also depends on the rate constants of capture of the diffusant k_t and its liberation k_d. Curve *3* illustrates the model of penetration with a low hydrogen desorption rate on the output side of the membrane, b is the degree of influence of the surface. The boundary conditions corresponding to these models are described in the Appendix.

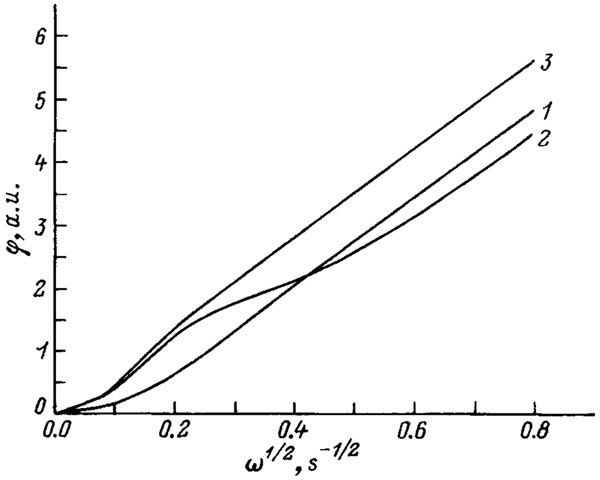

FIG. 1. Phase–frequency characteristics: *1* — $l^2/D=100\ \mathrm{s}^{-1}$; *2* — $l^2/D=100\ \mathrm{s}^{-1}$, $k_t=0.15\ \mathrm{s}^{-1}$, $k_d=0.1\ \mathrm{s}^{-1}$; *3* — $l^2/D=100\ \mathrm{s}^{-1}$, $\beta=0.1$.

The solutions of the boundary problems representing possible mechanisms of hydrogen transport constitute the model database. It consists of model phase–frequency characteristics of the form $\phi_M=f(\omega,G)$, where G is the vector of kinetic parameters. For example, for the model of diffusion with reversible capture (Fig. 1, curve *2*) $G=\{l^2/D,k_t,k_d\}$.

For each of the possible hydrogen transport models the experimental phase–frequency characteristic is approximated by a theoretical characteristic found by varying the corresponding vector of parameters G. Preference is given to the model that gives the best agreement with experiment. The measured values of the parameters to be determined are defined as the components of the vector G giving the best agreement.

PROCEDURE FOR OBTAINING EXPERIMENTAL PHASE–FREQUENCY CHARACTERISTICS

The idea of a sinusoidal hydrogen concentration wave was first published in Ref. 6, where the classical hydrogen diffusion coefficient was determined from the phase delay of the oscillations of the penetrating flux. Harmonic oscillations of the hydrogen pressure on the input side of the membrane were produced by the movement of a piston. In our first experiments[7] we also used sinusoidal pressure oscillations in the gas phase to determine the phase–frequency characteristics, but at that point we were already using a computer-controlled hydrogen feed system. However, carrying out the experiment at only one frequency allows one to obtain only effective values of the diffusion coefficient while the use of a set of frequencies makes the work unjustifiably laborious. Later, in Ref. 1 we realized a more efficient way of doing things which makes it possible to obtain the entire phase–frequency characteristic in one experiment—the pulsed method.

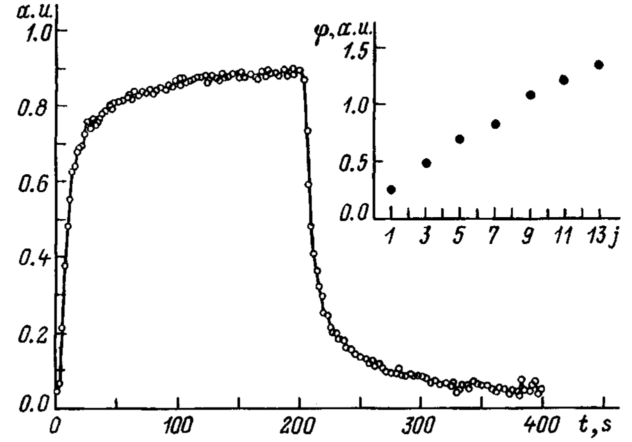

FIG. 2. Experimental curve and its phase–frequency characteristic.

The experiments were performed in an automated experimental complex, described in detail in Ref. 8. The sample consists of a flat membrane of thickness l, $x\in[0,l]$. The dissolved hydrogen concentration on its input $(x=l)$ side is varied in the form of rectangular pulses with pulse duty factor 2 (meander), which can be represented by a Fourier series of odd harmonics of the carrier frequency ω_0

$$C(t,l)=\frac{A_0}{2}+\sum_{j=1,3,\ldots,\infty}A_j\sin(j\omega_0 t)$$

$$=\sum_{j=0,\pm1,\pm3,\ \ldots,\pm\infty}\frac{A_j}{2}\exp[i(j\omega_0 t-\pi/2)],\qquad(1)$$

where i is the imaginary unit.

The real amplitudes A_j are inversely proportional to the number of the harmonic $A_j=A_1/j$. If, as happens in the majority of cases, the processes of bulk transport in the metal are linear, then concentration oscillations of different harmonics propagate through the membrane without interacting with one another and upon reaching the output side form a penetrating flux of characteristic shape. After the transients have died down, the latter also varies according to a periodic law and can be represented by the series

$$J=\sum_{j=0,\pm1,\pm3,\ \ldots,\pm\infty}B_j\exp[i(j\omega_0 t)-\pi/2].\qquad(2)$$

By way of example, Fig. 2 displays an experimental curve obtained for a silver membrane; the phase–frequency characteristic is plotted in the inset on the upper right. The periodicity of the probing signal makes it possible to accumulate information, thus reducing the noise affecting the measurement result to an acceptable level. The kinetic curve in Fig. 2 was obtained by summing information accumulated over 17 periods after die-off of transients.

Generally speaking, to realize MCP, any periodic law of variation of the hydrogen concentration would do, for example, triangular pulses. It is simpler, however, to obtain pulses with a flat top. As a rule, the probability of dissociative adsorption of a hydrogen molecule in metals is lower than for atoms or ions (see, e.g., Ref. 9). Therefore, by switching the dissociator on and off for different time intervals (by computer control; in our case, the dissociator was an incandescent tungsten filament), it is possible to obtain the necessary pulses of the adsorption flux, which corresponds, as a rule, to meander of the diffusant concentration $C(t,l)$.

At a high rate of diffusive hydrogen transport with an adsorption flux, the concentration pulses near the input side will not be rectangular; however, for an adequate boundary condition no additional problems arise.

The appearance of even harmonics in the spectrum of the penetrating flux allows us to conclude that some of the reactions constituting the process of hydrogen transport are nonlinear. Problems of even harmonics, which arise in nonlinear systems, are discussed in the section ‘‘Model database.’’

The Fourier coefficients B_j of the flux J can be represented in the form

$$B_j = A_j Z_j, \quad j = 1, \pm 3, \ldots, \pm \infty, \tag{3}$$

where Z_j are complex coefficients, the frequency dependence of whose phases $\phi_j = \arg(Z_j)$ gives the experimental phase characteristic $(j\omega_0, \phi_j)$ of the membrane; The first $N = 15-25$ harmonics are important depending on the quality of the experimental MCP curve.

MODEL SELECTION AND DETERMINATION OF RATE CONSTANTS

The obtained experimental dependence of Z_j is approximated by several models claiming to provide an adequate description of a specific experiment, where these models are represented in the form of a dependence of the phase of the model transfer coefficient Z_M on the frequency ω and vector of parameters G: $\phi_M(\omega, G) = \arg[Z_M(\omega)]$. The approximation is carried out within the framework of the standard method of least squares

$$\sum_{j=1}^{N} h_j [\phi_j - \phi_M(j\omega_0, G)]^2 \to \min, \tag{4}$$

where for each of the possible models the variable arguments are the components of the vector G.

The weight coefficients $h_j = 1/j$ take account of the decrease in accuracy in determining the ϕ_j with increase of the number of the harmonic j. After a given model has been selected, the results of the experiment are the values of the components of G that give the best agreement between the experimental and model phase–frequency characteristics.

MODEL DATABASE

In the course of development of the method of concentration pulses, a database of physically based models of hydrogen transport was formed, consisting of boundary conditions and solutions. Table I gives a picture of the considered diffusion problems. To give an illustration of the process of obtaining a solution, three simple models are derived in the Appendix (Fig. 1): classical Fick diffusion with boundary conditions of the first kind, which describes the penetration of hydrogen at high temperatures and hydrogen feed pressures through a thick membrane of some d-shell transition metal (e.g., nickel); diffusion with reversible capture to traps of unbounded capacity; and the model of penetration with a low rate of desorption on the output side of the membrane. The last model gives an example of a situation leading to the appearance of even harmonics and is the probable model if a thin layer of material is deposited on the output side of the membrane which does not offer any diffusion resistance to hydrogen but hinders its transport from solution to vacuum with association into a molecule. Examples of more complicated models arising in the analysis of concrete experimental data are described in Refs. 1–5.

TABLE I.

Diffusion	Boundary conditions
Fick’s law	Type I
With capture to traps	Low rates of adsorption and desorption
Along parallel channels In a two-layered membrane Along grain boundaries	Recombination into a molecule as the atoms move from layer to layer
In atomic and molecular form	Hindered movement from layer to layer

In order to obtain the entire spectrum of solutions corresponding to the spectrum of the input concentration (1), it is sufficient to obtain an expression for the penetrating flux for an arbitrary frequency ω. Transient processes are not considered, and all of the problems are solved for the regime of steady-state oscillations in the approximation of small hydrogen surface concentrations, which is completely justified since MCP experiments are performed at elevated temperatures. The $\wedge$ symbol denotes stationary (not time-varying) quantities, and the symbol Δ indicates the amplitudes of the oscillations.

For nonlinear boundary problems, the problem arises of the appearance of even harmonics, which are also observed in experiment. It is solved by making the amplitude of the oscillating part of the penetrating flux small in comparison with its stationary component. It is possible to vary the amplitude in an experiment by varying the incandescence current of the hydrogen dissociator or the glow-discharge current. If the condition

$$\Delta C(x) \ll \hat{C}(x), \quad x \in [0, l], \tag{5}$$

is met, quadratic terms of the order of ΔC^2 can be neglected in comparison with terms of order $\hat{C}^2$, and the boundary problem is linearized.

CONVERGENCE CRITERIA

Problems of convergence and the choice of a solution were investigated by computer construction of experimental curves and processing them with the help of working programs. The final criterion for selection of one model from among several is the discrepancy between the experimental and model kinetic curves. The latter were reconstructed using the inverse Fourier expansion after minimizing the phase discrepancy (4) for each of the candidate models.

The absence of convergence, expressed by a tendency of one or more of the parameters being varied toward unbounded growth or decrease, as a rule is evidence of inadequacy of the candidate model. A more complicated situation arises where the minimum search procedure leads to finite components of the parameter vector, but the difference between the experimental kinetic curve and the model curve obtained using the inverse Fourier expansion has a periodic character and can in turn be expanded in a Fourier series. This situation speaks of the fact that the adequacy of the model is incomplete and further refinement is needed.

Another criterion of adequacy of the model is available in the case of layers (e.g., semiconductor layers, as in Refs. 3–5) on a metallic substrate. In this case one first characterizes just the substrate without any coating. Then, for a membrane with a coating, in all of the boundary problems used to process the results the hydrogen diffusion coefficient in the substrate is taken to be an unknown quantity and also subject to determination. Non-agreement between the hydrogen diffusion coefficient in the metal obtained in this way and its true value is then an indication of inadequacy of the model.

APPENDIX

1. *The classical model.* Transport proceeds according to the Fick diffusion equation

$$\frac{\partial C}{\partial t}(x,t)=D\frac{\partial^2 C}{\partial x^2}(x,t),\quad x\in[0,l], \tag{6}$$

and boundary conditions of the first kind: on the input side of the membrane the concentration varies harmonically with frequency ω

$$C(l,t)=\hat{C}(l)+\frac{\Delta C_l}{2}\left\{\exp\left[i\left(\omega t-\frac{\pi}{2}\right)\right]\right.$$
$$\left.+\exp\left[-i\left(\omega t-\frac{\pi}{2}\right)\right]\right\}, \tag{7}$$

and on the output side is equal to zero

$$C(0,t)=0. \tag{8}$$

The concentration, written in the form

$$C(x,\,t)=\hat{C}(x)+\frac{\Delta C(x)}{2}\exp\left[i\left(\omega t-\frac{\pi}{2}\right)\right]$$
$$+\frac{\Delta\overline{C}(x)}{2}\exp\left[-i\left(\omega t-\frac{\pi}{2}\right)\right], \tag{9}$$

leads to a boundary condition for the amplitude $\Delta C(x)$

$$i\omega\Delta C=D\frac{d^2\Delta C}{dx^2},\quad x\in[0,l], \tag{10}$$

$$\Delta C(l)=\Delta C_l, \tag{11}$$

$$\Delta C(0)=0. \tag{12}$$

From its solution

$$\Delta C(x)=\frac{\Delta C_l\sinh\sqrt{i\omega x^2/D}}{\sinh\sqrt{i\omega l^2/D}} \tag{13}$$

we obtain an expression for the amplitude of the oscillations of the hydrogen flux

$$\Delta J=\frac{i\omega l\Delta C_l}{\sqrt{i\omega l^2/D}\sinh\sqrt{i\omega l^2/D}}. \tag{14}$$

In this model the vector G of the arguments of the model transfer coefficient Z_M consists of one component $g_1=l^2/D$.

2. *Diffusion with reversible capture.* The diffusion equation contains terms describing the rates of capture to traps k_tC and escape from them k_dC_t with the respective rate constants k_t and k_d

$$\frac{\partial C}{\partial t}=D\frac{\partial^2 C}{\partial x^2}-k_tC+k_dC_t,\quad x\in[0,l]. \tag{15}$$

The rate of change of the hydrogen concentration C_t in the traps is equal to

$$\frac{\partial C_t}{\partial t}=k_tC-k_dC_t,\quad x\in[0.l]. \tag{16}$$

The boundary conditions of the first kind coincide with conditions (7) and (8). Just as in the classical model, the solution is sought in the form (9). For the amplitude of the dissolved hydrogen concentration we have

$$i\omega^*\Delta C(x)=D\frac{d^2\Delta C(x)}{dx^2}, \tag{17}$$

where

$$\omega^*=\omega\frac{k_t+k_d+i\omega}{k_d+i\omega}. \tag{18}$$

Equation (17) coincides with Eq. (10); therefore its solution will be an expression similar to (13). The amplitude of the oscillations of the flux is equal to

$$\Delta J=i\omega l\Delta C_l\sqrt{\frac{k_t+k_d+i\omega}{k_d+i\omega}}\Bigg/$$
$$\left(\sqrt{\frac{i\omega l^2}{D}}\sinh\sqrt{\frac{i\omega l^2(k_t+k_d+i\omega)}{D(k_d+i\omega)}}\right). \tag{19}$$

The components of the vector G are the rate constants of hydrogen transport

$$g_1=l^2/D,\quad g_2=k_t,\quad g_3=k_d. \tag{20}$$

3. *Hindered desorption on the output side.* The diffusion equation and the boundary condition on the input side coincide with Eqs. (6) and (7) for the classical model. The boundary condition on the output side is written in the form of a balance between the fluxes of diffusion and associative transport from the dissolved state to vacuum with constant rate b^*

$$b^*C^2(0,t)=D\frac{\partial C}{\partial x}(0,t). \tag{21}$$

To solve Eq. (21) in the form (9) the procedure of taking the square reflects the appearance of the even harmonic 2ω. If condition (5) is fulfilled, then the terms of order (ΔC^2) are negligibly small in comparison with the terms of order $(\hat{C}^2)$. Taking the stationary regime

$$b^*\hat{C}^2(0)=D\frac{d\hat{C}}{dx}(0)$$

into account, we obtain a boundary condition for the concentration amplitude

$$\frac{d\Delta C}{dx}(0)=\frac{2}{l}\beta\Delta C(0). \tag{22}$$

The parameter $\beta=\hat{J}/\hat{\nu}_{rev}$ determines the degree of influence of the desorption rate on the penetrating hydrogen flux. $\hat{J}=b^*\hat{C}^2(0)$ is the constant component of the recorded penetrating flux, and $\hat{\nu}_{rev}=D\hat{C}^2(0)/l$ is the nominal reverse flux from the output side back to the input side. Taking the limit $\beta\to\infty$ leads to $\hat{C}(0)\to 0$ and, consequently, to the classical model. In the limit $\beta\to 0$ a stringent limitation of the flux by desorption (transport from the dissolved state to vacuum with association into a molecule) enters on the output side of the membrane, and the hydrogen concentration gradient across the membrane tends to zero.

Thus, the boundary problem for the concentration amplitude consists of the diffusion equation (10) and boundary conditions (11) and (22). Its solution has the form

$$\Delta C(x)=\Delta C_l\frac{\sqrt{i\omega x^2/D}\cosh\sqrt{i\omega x^2/D}+\beta\sinh\sqrt{i\omega x^2/D}}{\sqrt{i\omega l^2/D}\cosh\sqrt{i\omega l^2/D}+\beta\sinh\sqrt{i\omega l^2/D}}. \tag{23}$$

The amplitude of the penetrating flux is given by

$$\Delta J=\frac{i\omega\Delta C_l\beta}{\sqrt{i\omega l^2/D}(\sqrt{i\omega l^2/D}\cosh\sqrt{i\omega l^2/D}+\beta\sinh\sqrt{i\omega l^2/D})}. \tag{24}$$

The components of the parameter vector G are equal to

$$g_1=l^2/D,\quad g_2=\beta. \tag{25}$$

[1] I. E. Gabis and A. V. Ermakov, Fiz.-Khim. Mekh. Mater., No. 4, 64 (1989).

[2] I. E. Gabis, Pis'ma Zh. Tekh. Fiz. **21**(9), 60 (1995) [Tech. Phys. Lett. **21**, 343 (1995)].

[3] I. E. Gabis, T. N. Kompanets, A. A. Kurdyumov *et al.*, Fiz.-Khim. Mekh. Mater., No. 4, 18 (1991).

[4] I. E. Gabis, A. A. Kurdyumov, N. A. Tikhonov, A. V. Samsonov *et al.*, Pis'ma Zh. Tekh. Fiz. **20**(7), 88 (1994) [Tech. Phys. Lett. **20**, 300 (1994)].

[5] I. E. Gabis, A. A. Kurdyumov, and A. V. Samsonov, Pis'ma Zh. Tekh. Fiz. **21**(5), 1 (1995) [Tech. Phys. Lett. **21**, 165 (1995)].

[6] N. M. Morrison, D. A. Blackburn, and K. M. Chui, J. Nucl. Mater. **69–70**, 578 (1978).

[7] I. E. Gabis, T. N. Kompanets, A. A. Kurdyumov, and V. N. Lyasnikov, Fiz.-Khim. Mekh. Mater. **21**(4), 106 (1985).

[8] I. E. Gabis, A. A. Kurdyumov, and N. A. Tikhonov, Vestn. St. Peterburg. Univ., Ser. 4, Fiz.-Khim. **2**(11), 77 (1993).

[9] A. I. Livshits, Zh. Tekh. Fiz. **45**, 1915 (1975) [Sov. Phys. Tech. Phys. **20**, 1207 (1975)].

Translated by Paul F. Schippnick

Physical properties of resistive threads and structures based on them in the microwave range

B. M. Garin, O. A. D'yakonova, and Yu. N. Kazantsev

Institute of Radio Engineering and Electronics, Russian Academy of Sciences, 141120 Fryazino, Moscow Region, Russia

(Submitted September 9, 1996; resubmitted December 5, 1997)
Zh. Tekh. Fiz. **69**, 104–108 (January 1999)

The main physico-mechanical characteristics of resistive threads are investigated. The dependence of the complex dielectric constant of a resistive thread on the wavelength is measured over a wide sub-interval of the microwave range. The possibility is demonstrated of using such threads as the main element of wide-band radio-absorbing structures. © *1999 American Institute of Physics.* [S1063-7842(99)01701-8]

INTRODUCTION

Radio-absorbing materials and structures are necessary elements of many components in both radio engineering and other branches of technology.[1–3] The required electrodynamical and physico-mechanical characteristics of these materials and structures are dictated usually by the specific conditions of their application.

Radio-absorbing materials and structures based on resistive threads imbedded in insulating materials have enjoyed widespread use.[4,5] The intense interest shown in such materials and structures is due to the possibility of varying their electrodynamical and physico-mechanical characteristics in a smooth and controllable way by appropriate choice of the design thickness, geometrical dimensions of the threads, concentration of the latter in the matrix, and also the properties of the filler particles in the thread. Reference 6 gives a review of such materials produced by foreign firms. Reference 7 presents an analysis of various types of composite radio-absorbing materials based on carbon, graphite, boron, and polyethylene fibers. The experimental data presented in Ref. 8 allow one to compare materials with various fillers in terms of their ability to absorb and reflect electromagnetic energy in the microwave range, and also to analyze the influence on their electrodynamical properties of the type of filler, orientation of the fibers, and thickness of the material. It turns out in practice that the better of the given structures are either narrow-band for moderate design thickness and mass or have a larger thickness and mass working in a wide wavelength range.

It should be emphasized that it is necessary to take a critical view of information derived from some particular implementation of a radio-absorbing material. For the most part, detailed information is provided only for relatively thick, heavy (various absorbers of electromagnetic waves for anechoic chambers) and geometrically inhomogeneous (wedges, etc.) designs based on composite radio-absorbing materials.

From an analysis of the literature we can draw the following conclusions.

1. A large number of structures based on resistive films and threads have been described, varying in their electrodynamical (working range, reflection coefficient) and physico-mechanical characteristics (mass, thickness, flexibility).
2. The most typical and most often encountered absorbing fillers for structures of insulating type are soot, graphite, and carbon fibers. A wide variety of materials are used as the bonding agents.
3. Measurements of the complex dielectric constant of resistive threads in the microwave range are available at various frequencies; however, spectral studies over a wide frequency band are lacking.
4. A description of wide-band radio-absorbing structures with small reflection coefficient and good physico-mechanical properties is lacking.

Thus the problem of building new structures based on resistive threads is urgent and requires a comprehensive study of the physical properties of both the structures themselves as a whole and of the resistive threads in particular. In the present paper we present results of a study of the electrodynamical, electrical, and physico-mechanical properties of conducting glass threads, and adduce calculated characteristics of model structures based on such threads.

STRUCTURE, PHYSICO-MECHANICAL, AND ELECTRICAL PROPERTIES OF RESISTIVE THREADS

Resistive threads have been chosen as the main radio-absorbing element for new wide-band structures[9,10] A resistive thread is a multicomponent fiber, in the interior of which a conducting composite is formed. The conducting filler is soot with particle sizes in the range $300-600$ Å. These particles contain graphite crystallites. In this regard, such threads belong to a wide class of carbon–graphite structures;[11] however, they possess specific properties by virtue of the special design of the material — a fiber.

Figures 1 and 2 show photographs of a conducting thread taken with an electron microscope. Figure 1 shows part of a cross section of the thread in which the protecting polymer cladding and glass fibers with soot arrayed inside it are clearly visible. Figure 2 shows the same cross section of the thread with stronger magnification. The glass fibers in

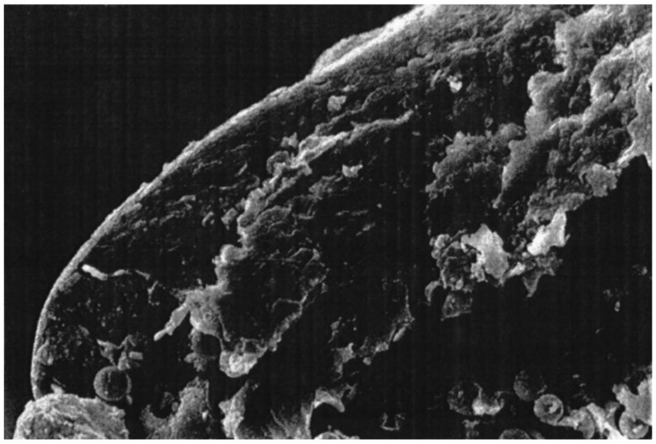

FIG. 1. Part of a transverse cut of a conducting glass thread.

such a thread are arrayed randomly with relative volume of the free interfiber space equal to 30% and form a nonuniform structure. The introduction of filler into the volume of the thread is a complicated process, and for this reason an actual resistive thread is a combination of chainlike and two-dimensional and three-dimensional structures.[12] This explains the inhomogeneity of a resistive thread and, as a consequence, the spread in its parameters. The cladding of the thread possesses good mechanical strength, is moisture-proof, and possesses good temperature characteristics.

The thread we have investigated is, taken as a whole, a conducting medium. In addition, the spatial dimensions of the inhomogeneities are much less than any of the wavelengths considered. This allows us in what follows to describe the resistive thread as a continuous medium with effective conductivity and effective complex dielectric constant. Below we will call this medium the thread material.

The thread itself is characterized by a number of other effective parameters. We will now give some of the more important effective parameters of the actual resistive thread investigated, which will be used in the calculations that follow.

The method of hydrostatic suspension[13] was used to determine the following values: the linear density 1.187×10^{-3} g/cm and volume density 1.27 g/cm^3. Important electric parameters characterizing an actual resistive thread are the average resistance of a resistive thread per unit length and the average conductivity of the thread material, both measured in direct current (dc). The average resistivity was determined from measurements of the average conductivity by the four-probe method described in Ref. 14. The measurement electrodes were attached with the help of silver paste made by Fujikura Kasel Co., Ltd. having an electrical conductivity of 10^{-4} S/cm. The experimental setup for measuring the resistivity of the various conducting materials and media used the standard digital measuring equipment: a Shch-300 volt-ammeter, a V7-27A/1 voltmeter, and a stabilized power supply. The main error in the measurement of the resistivity of the resistive thread arose in the determination of its geometrical dimensions and amounted to 5%.

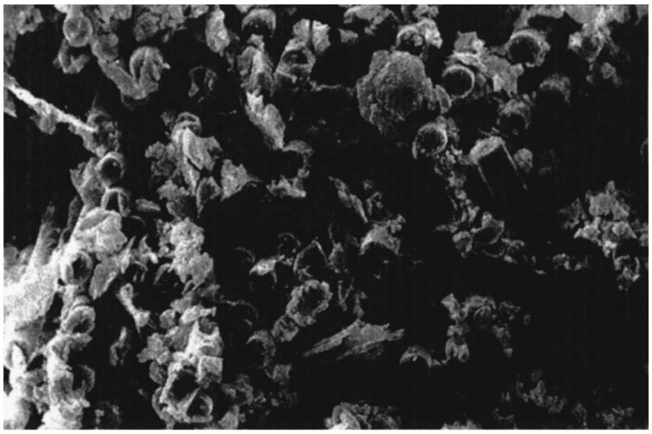

FIG. 2. Group of glass fibers with soot inside a conducting glass thread.

For the resistive thread investigated the measured average resistance per unit length was 3.7×10^3 Ω/cm, and the average conductivity of the thread material was $\sigma = 2.9 \times 10^{-1}$ S/cm.

However, the dc characteristics of the thread are not sufficient to completely determine its absorbing properties in the microwave range. A more complete characteristic of the absorbing properties of the thread is its complex dielectric constant, which is the main object of the present study.

ELECTRODYNAMICAL CHARACTERISTICS OF RESISTIVE THREADS

We examined the complex dielectric constant of the thread material in the wavelength range 0.25–15 cm. For different wavelength intervals we used one of the three following methods of measurement: resonator, waveguide, and the free space method.

In the resonator method the sample in the form of a segment of the resistive thread is placed at an antinode of the electric field.[15] A series of measurement stations was assembled, based on panoramic standing-wave coefficient meters overlapping the millimeter and centimeter wavelength ranges. Each of the measurement resonators comprised a segment of a rectangular waveguide joined to the main waveguide by a diaphragm which provided the needed connection and correspondingly high Q factor of the resonator. The investigated resistive thread was aligned with the lines of force of the electric field at a distance of $\lambda/4$ from the butt-end of the thread through a slit cut in the wide wall of the waveguide (λ is the wavelength). The complex dielectric coefficient of the thread was determined from measured values of the resonance frequencies and reflection coefficients at the resonant frequencies for the empty resonator and the resonator with the sample. The main error in the measurement of the dielectric constant was due to the error in determining the volume of the sample resistive thread and amounted to 20%.

With the aim of enhancing the reliability of the results we also determined the complex dielectric constant ε from measured values of the transmission and reflection coefficients of an electromagnetic wave from a layer consisting of densely packed resistive threads. The reflection and trans-

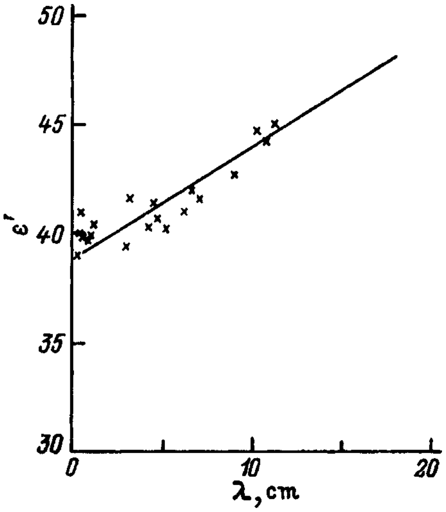

FIG. 3. Dependence of the real part of the dielectric constant of a conducting glass thread on the wavelength.

mission coefficients were measured on three types of millimeter and centimeter range setups based on panoramic standing-wave coefficient meters: the first type used a horn technique[16,17] for measuring the reflection coefficient and transmission coefficient (with two identical horns) in free space at normal incidence of the electromagnetic wave on the sample; the second type employed a technique for measuring the reflection and transmission coefficients in the waveguide,[18] i.e., for the electromagnetic wave incident on the sample at some angle; the third type used a technique for measuring the reflection and transmission coefficients in free space with the aid of a millimeter-range waveguide interferometer.[19,20]

Figures 3 and 4 plot the real and imaginary parts of the complex dielectric constant of the resistive thread as functions of wavelength. The crosses represent the experimental result of averaging numerous measurements by various techniques. The measurement results were fitted by a linear dependence. The real part ε' of the dielectric constant depends relatively weakly on the wavelength (as the wavelength is increased, ε' increases from 39 to 47); the imaginary part ε'' grows in direct proportion to the wavelength (as the wavelength is increased, ε'' increases from 5 to 310). The dependence of the imaginary part is in agreement with the theory of dielectric losses in a medium with constant (frequency-independent) conductivity for variable current σ_1 associated with the free charge carriers. According to this theory,[21] $\varepsilon'' = \sigma_1/(\varepsilon_0\omega)$ for frequencies $\omega \ll \tau^{-1}$, where ε_0 is the electric constant, and τ is the mean relaxation time of the free charge carriers per pulse ($\tau \sim 10^{-13}$ s). The observed losses correspond to the calculated effective conductivity of the thread material $\sigma_1 = 3.7\times10^{-1}$ S/cm. The given conductivity somewhat exceeds the value of σ found from the dc measurements (see above); however, it differs from them only insignificantly. Thus, the main contribution to the losses is due to the conduction of the soot with graphite crystallites that is contained in the thread. Some of the excess of σ_1 over σ may be due to the contribution to the conductivity at variable current of isolated conducting grains of graphite and soot not in electrical contact with one another, and also with the spread in the thread parameters and with measurement errors. Also note that the contribution of the free charge carriers to the real part of the dielectric constant $\varepsilon'_e \simeq -(1-\omega^2\tau^2)\tau\sigma_1/\varepsilon_0$ (Ref. 21) is independent of the wavelength to first order in the small parameter $\omega\tau$, and to second order decreases with increasing wavelength to a negligibly small value (over the entire wavelength range under consideration). Therefore it cannot explain all of the observed growth of ε' with wavelength. On the other hand, this growth of ε' corresponds to the contribution of dipole relaxation of Debye type, which, as a rule, is the main reason for the dispersion of the dielectric constant in disordered materials in the given wavelength range.[22–24] Various molecular groups in amorphous regions of the thread contribute to this relaxation.

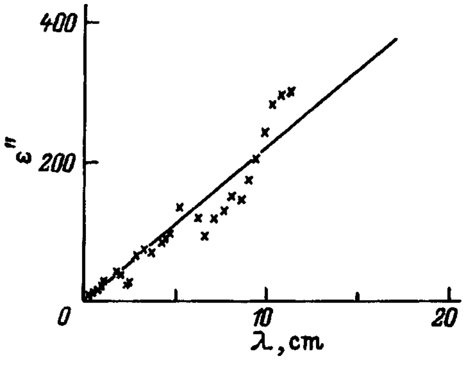

FIG. 4. Dependence of the imaginary part of the dielectric constant of a conducting glass thread on the wavelength.

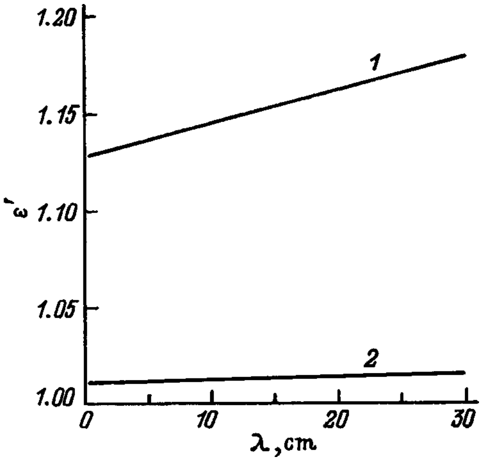

FIG. 5. Dependence of the real part of the dielectric constant of layers of the effective media on the wavelength: *1* — $d/a = 17.7$, *2* — 58.8.

STRUCTURES BASED ON RESISTIVE THREADS

On the basis of the data obtained for resistive threads, we calculated the effective complex dielectric constant of various radio-absorbing layers by the technique proposed in Ref. 25.

As a graphic illustration, Figs. 5 and 6 plot the results of such a calculation for layers of different media with effective parameters. These results then enter into the calculation for

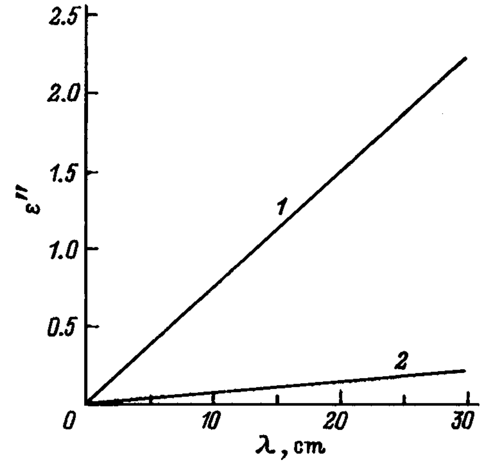

FIG. 6. Dependence of the imaginary part of the dielectric constant of layers of the effective media on the wavelength: (*1, 2* — the same as in Fig. 5).

actual single-layer and two-layer structures.[9,10] The real ε' and imaginary ε'' parts of the dielectric constant of the layers are plotted versus wavelength for different values of the ratio d/a. The parameter d/a characterizes the volume fraction of the resistive threads in the dielectric medium and is given by the formula $d/a=(3\pi V_d)^{1/2}(V_{\mathrm{th}})^{1/2}$, where d is the distance between threads, a is the radius of a thread, V_d is the volume of the dielectric, and V_{th} is the volume of the thread material. Analyzing the behavior of these dependences over the entire wavelength range, we may note that decreasing d/a, i.e., increasing the volume fraction of threads in a layer, increases the real and imaginary parts of its dielectric constant.

CONCLUSION

We have investigated the dielectric constant of a conducting glass thread in detail and measured its spectrum over a wide range of microwave wavelengths (0.25–15 cm).

[1] Ya. A. Shneĭderman, Zarubezh. Radioélektron. No. 2, 3 (1976).
[2] Ya. A. Shneĭderman, Zarubezh. Radioélektron. No. 3, 3 (1976).
[3] V. A. Torgovanov, Zarubezh. Radioélektron. No. 12, 51 (1974).
[4] B. B. Aĭzikovich, A. G. Alekseev, and V. S. Irumov, Zarubezh. Radiotekh. Elektron. No. 6, 2 (1994).
[5] B. F. Alimin, Zarubezh. Radioélektron. No. 2, 75 (1989).
[6] P. G. Filippov, V. G. Shevchenko, A. T. Ponomarenko *et al.*, *Electrical Properties of Polymer Composites with Conducting Dispersed and Fibrous Fillers* [in Russian], Ser. Interdiscipl. Questions, No. 1 (Obzornaya Informatsiya [Review Information], Moscow, 1984).
[7] F. Jefferson and I. Lindsey, in *International Symposium Digest on Antennas and Propagation*, Vol. 1, Philadelphia, 1986, p. 113.
[8] Myazakiy and S. Tominaga, *IEEE International Symposium on Electromagnetic Compatibility*, Arlington, 1983, p. 101.
[9] O. A. D'yakonova and Yu. N. Kazantsev, Russian Federation Patent No. 2037926. International Classification HO1Q 17/00.
[10] O. A. D'yakonova and Yu. N. Kazantsev, Russian Federation Patent No. 2037931. International Classification HO1Q 17/00.
[11] M. D. Mashkovich, *Electrical Properties of Inorganic Dielectrics in the Microwave Range* [in Russian], Sov. Radio, Moscow, 1969.
[12] *Electrophysical Properties of Percolation Systems* [in Russian], edited by A. N. Lagar'kova (IVTAN, Moscow, 1990).
[13] T. G. Plachenov and S. D. Kolosentsev, *Vaporimetry* [in Russian], Khimiya, Leningrad, 1988.
[14] A. R. Blythe, Polymer Testing, No. 4, 195–209 (1984).
[15] V. N. Apletalin, Yu. N. Kazantsev, G. A. Kraftmakher *et al.*, *Abstracts of the Conference ''Radio-Engineering Measurements in the High-Frequency and Superhigh-Frequency (Microwave) Ranges''* [in Russian], Novosibirsk, 1984, p. 21.
[16] V. N. Apletalin, O. A. D'yakonova, Yu. N. Kazantsev *et al.*, Izmer. Tekh. No. 7, 40 (1991).
[17] V. N. Apletalin, O. A. D'yakonova, Yu. N. Kazantsev *et al.*, *Abstracts of the Seventh All-Union Conference ''Methods and Means of Measurements of the Electromagnetic Characteristics of Materials in the High-Frequency and Superhigh-Frequency (Microwave) Ranges''* [in Russian], Novosibirsk, 1991, p. 132.
[18] V. N. Apletalin, A. S. Zubov, Yu. N. Kazantsev *et al.*, A. S. No. 1741083 SSSR.
[19] V. N. Apletalin, O. A. Dyakonova, Y. N. Kazantsev *et al.*, in *Proceedings of the Third International Conference on Electromagnetics in Aerospace Applications and the Seventh European Conference on Electromagnetic Structures*, Turin, Italy, 1993, p. 253.
[20] V. N. Apletalin, O. A. Dyakonova, Y. N. Kazantsev *et al.*, in *Proceedings of the 23rd European Microwave Conference*, Madrid, 1993, p. 308.
[21] F. J. Blatt, *Physics of Electronic Conduction in Solids* (McGraw-Hill, New York, 1968).
[22] H. Frölich, *Theory of Dielectrics: Dielectric Constant and Dielectric Loss*, 2nd ed. (Clarendon Press, Oxford, 1986).
[23] I. S. Rez and Yu. M. Poplavko, *Dielectrics. Fundamental Properties and Applications in Electronics* [in Russian] (Radio i Svyaz', Moscow, 1989).
[24] *Electric Properties of Polymers* [in Russian], edited by B. I. Sazhin (Khimiya, Leningrad, 1986).
[25] O. A. D'yakonova, *Author's Abstract of Candidate's Dissertation* [in Russian], Moscow, Institute of Radio Engineering, Russian Academy of Sciences, 1995.

Translated by Paul F. Schippnick

TECHNICAL PHYSICS VOLUME 44, NUMBER 1 JANUARY 1999

Spherical mirror analyzer as an instrument for electron coincidence spectroscopy

S. N. Davydov, M. M. Danilov, and V. V. Korablev

St. Petersburg State Technical University, 195251 St. Petersburg, Russia

(Submitted October 7, 1997)
Zh. Tekh. Fiz. **69**, 109–113 (January 1999)

The time-of-flight characteristics of a spherical-mirror electrostatic energy analyzer of charged particle fluxes are investigated under conditions of ideal solid-angle focusing for a point source located on the symmetry axis of the spectrometer. It is shown that the time it takes a particle to move from the source to the ideal focus, also located on the symmetry axis, is, to first order, independent of particle direction for directions near the normal to the axis. This time-of-flight focusing realized in this way enables efficient use of the spherical-mirror analyzer in electron spectroscopy methods in which each emission event is registered separately. *© 1999 American Institute of Physics.* [S1063-7842(99)01801-2]

INTRODUCTION

Electron spectroscopy is presently used to study the physico-chemical properties of the subsurface layers of solids. To investigate elementary processes accompanying the interaction of primary particles with the electron subsystem of a solid, it is necessary to have information about the nature of the particles emitted into the vacuum. However, the investigated interaction can be quite complex. For example, at least three electrons take part in the Auger process and, besides, Auger emission can proceed via several channels. Nevertheless, only one of all the possible processes occurs in each separate Auger event.[1] Auger electron coincidence spectroscopy is used to record each of these processes individually.[2] Isolation of each elementary Auger process from the other possible channels is effected by separating them in time as well as energy. The overall scheme of the experiment is depicted in Fig. 1. After one of the detectors detects one electron (e.g., a photoelectron), the second detector switches on for a brief time, long enough to record the second particle (the Auger electron) created in the same event. As a result, instead of the total peak shape recorded in the usual, traditional method for studying Auger processes, in the method of coincidence spectroscopy it is possible to record separately the contributions from several processes which together form the Auger spectrum. In this case not all the electrons are recorded whose energy lies within the limits of the energy window of the analyzer, only those whose creation time coincides with the creation time of the primary emitted electron leaving behind a hole in one of the energy bands of the solid.

It is not hard to show that in the absence of acceleration or retardation of the beam before it enters the analyzer, the spread in times of flight to the detector of the particles created simultaneously at the point emission source is equal to

$$\Delta t_w = t_2 - t_1 = KL\frac{\Delta W}{W_0^{3/2}}. \tag{1}$$

Here L is the characteristic length of the spectrometer, K is a size factor that depends on the geometry of the device and its operating regime, W_0 is the kinetic energy of the electrons, and ΔW is the energy spread of the beam or the absolute energy resolution of the analyzer.

Expression (1) is valid to first order in the small parameter $\Delta W/W_0$ under the condition that all the particles move along the same trajectory. It describes, so to speak, the ''energy'' contribution to the time spread of the beam associated with the nonzero energy resolution of a hypothetical analyzer possessing zero aperture ratio. Obviously, the time spread worsens as the relative energy resolution $\Delta W/W_0$ worsens (e.g., as ΔW increases) and as the tuning energy W_0 is decreased. Under conditions of a finite aperture ratio, an additional contribution to the time spread, Δt_Ω, appears, associated with different transit times of particles from the source to the detector along different trajectories.

In comparison with the usual methods of Auger spectroscopy, the speed of recording the spectra in coincidence spectroscopy is several orders of magnitude lower and is equal to about $0.1-1$ pulse per second.[3] Different methods are applied to increase the intensity of the recorded flux: position-sensitive detectors (PSD) are used, or the PSD is tilted in order to partially compensate for the difference in the time of flight corresponding to different trajectories.[2]

It is obvious, however, that the best results can be obtained by using an electron-optical system with a large aper-

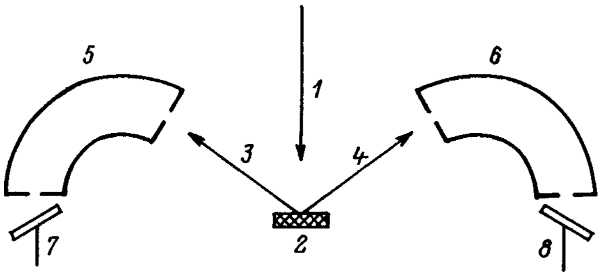

FIG. 1. Auger electron coincidence spectroscopy. Scheme of the experiment: *1* — ionizing radiation (electrons, photons); *2* — sample; *3* — emission of secondary or photoelectron from an inner level; *4* — Auger electron; *5, 6* — energy analyzers; *7, 8* — PSD-based collectors.

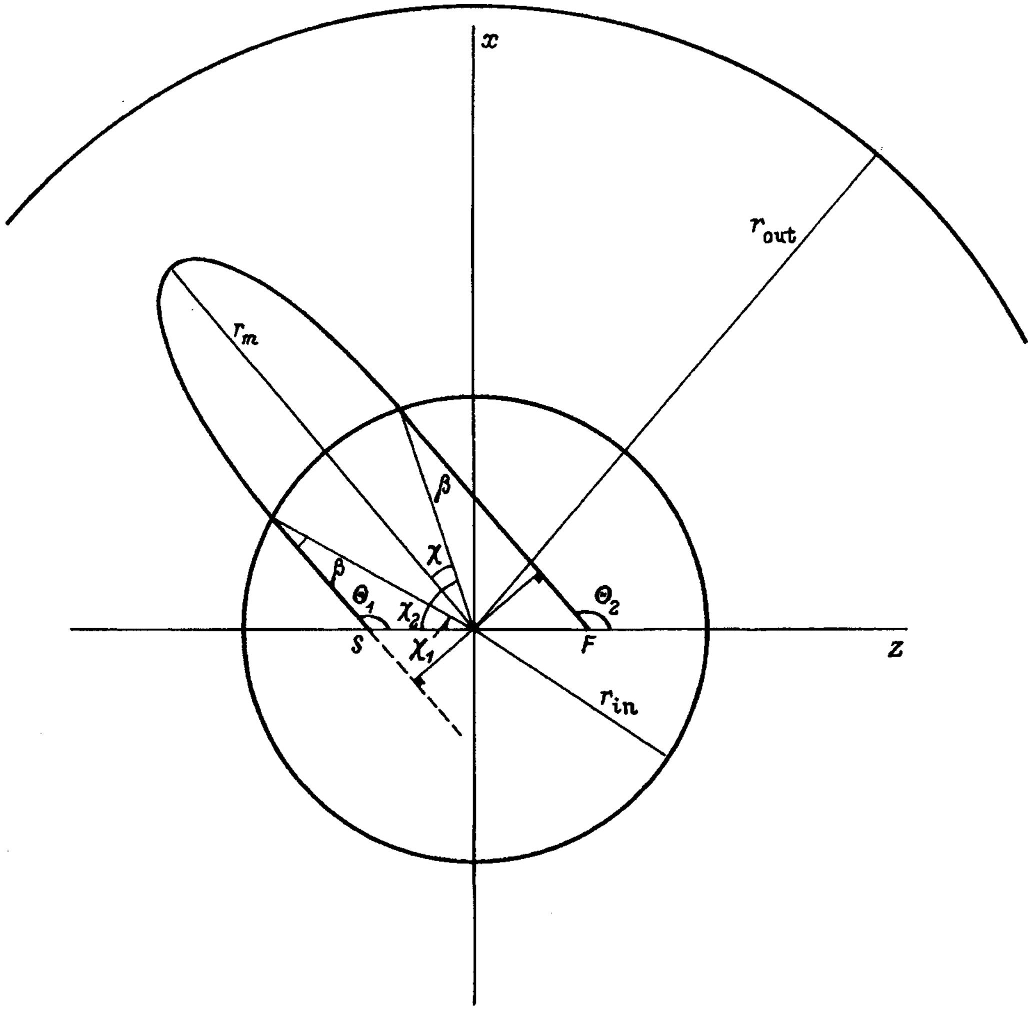

FIG. 2. Trajectory of charged particle in a spherical capacitor.

ture ratio, the conditions of angular (and, one hopes, spatial) focusing in which coincide with the conditions of focusing in time. In this case it becomes possible without any deterioration of the time resolution to use the entire particle flux emitted into the investigated solid angle.

TIME OF FLIGHT OF AN ELECTRON IN A CENTRAL FIELD

Let us consider an electrostatic system of ''spherical capacitor'' type (Fig. 2). Let a point source of particles S and an entrance slit F onto which the electrons should be focused be located on the axis of the system, i.e., let an axis-to-axis focusing regime of the spherical mirror be realized.[4] In this case, each electron will move in some fixed axial plane passing through the symmetry axis z, and the azimuthal position of this plane will be determined by the azimuthal emission angle. The intersection points of the trajectory of the particles with the surface of the inner electrode are prescribed by the coordinates χ, χ_1, χ_2, Θ_1, Θ_2.

We take as our unit of electric charge the charge of the electron, and its mass as our unit of mass: $e=1$, $m=1$. Let the electrostatic potential U between two spherical plates of a capacitor with radii r_{in} and r_{out} vary according to the law $U=-1/r$, and the potential of the inner sphere and the field-free region inside it be equal to -1. The latter condition is equivalent to expressing all linear dimensions in units of the radius of the inner electrode: $r_{\mathrm{in}}=1$.

The angular momentum of the electron relative to the center of the field is equal to

$$M=|\mathbf{r}\times\mathbf{p}|=|\mathbf{r}\times\mathbf{v}|=\sqrt{2W}|z_1|\sin\Theta_1=\mathrm{const.} \tag{2}$$

Here $\mathbf{r}$ is the current radius vector of the particle; $\mathbf{p}$, $\mathbf{v}$, W are its initial momentum, velocity, and kinetic energy; the position of the source S is given by z_1.

The total energy of the particle[5]

$$E=\frac{v_r^2}{2}+\frac{M^2}{2r^2}+U(r), \tag{3}$$

where v_r is the radial velocity.

Let $r=1$

$$E=U(1)+W=W-1. \tag{4}$$

The total time of flight of the particle from the source to the entrance slit t_{1f} is equal to the sum of three components

$$t_{1f}=t_{1b}+t_{be}+t_{\mathrm{eff}}. \tag{5}$$

Here t_{1b} is the time of flight from the source to the field boundary $r=1$ in the field-free space, t_{be} is the time of flight in the field, t_{eff} is the time when the particle is back in the field-free space and it moves from the point of escape from the field to the focus. By virtue of the symmetry of the elliptical trajectory in the potential $U=-1/r$, the time t_{be} can be represented as the sum of two equal terms t_{bt} and t_{te}, characterizing the rising and falling branches of the trajectory (the trajectory of the particle in the field is symmetric relative to the radius vector drawn to the turning point).

The time t_{1b} is found from elementary geometrical considerations

$$t_{1b}=\left[\frac{-z_1\cos\Theta_1+\sqrt{1+\cos^2\Theta_1-z_1^2}}{\sqrt{1+\cos^2\Theta_1}}\right]\bigg/\sqrt{2W}. \tag{6}$$

To calculate t_{be}, we first find the largest separation of the particle from the center of the system r_m. Since $v_r=0$ at the turning point of the trajectory, equating expressions (3) and (4) we obtain the equation

$$W-1=-\frac{1}{r_m}+\frac{M^2}{2r_m^2}, \tag{7}$$

and by solving this equation we find the value of $r_m>0$

$$r_m=\frac{1+\sqrt{1-4Wz_1^2\sin^2\Theta_1(1-W)}}{2(1-W)}. \tag{8}$$

Employing expression (1), (4), and (6) from Ref. 5 for the time of flight of the particle in the central field, we have

$$t_{bt}=\int_1^{r_m}\frac{dr}{\sqrt{2(W-1)+(2/r)-(M/r)^2}}. \tag{9}$$

Taking relations (2) and (8) into account along with the relation $t_{be}=2t_{bt}$, after integrating we obtain

$$t_{be}=\frac{\sqrt{2W}\cos\beta}{1-W}+\frac{2}{[2(1-W)]^{3/2}}\times\left\{\frac{\pi}{2}+\arcsin\left[\frac{2W-1}{\sqrt{1-4W(1-W)\sin^2\beta}}\right]\right\}. \tag{10}$$

Here $\beta=\pi-\Theta_1-\chi_1$ and $\sin\beta=|z_1|\sin\Theta_1$. To find the time from the time of escape of the particle from the field to the time when it falls upon the entrance slit t_{ef}, it is necessary to know the point of escape of the trajectory from the field, defined by the angle χ (Fig. 2). According to formula 14.7 from Ref. 5,

$$\frac{\chi}{2}=\int_1^{r_m}\frac{M\cdot dr}{r\sqrt{-2(1-W)r^2+2r-M^2}}=\arcsin\left[\frac{r-M^2}{r\sqrt{1-2M^2(1-W)}}\right]\Bigg|_1^{r_m}. \tag{11}$$

Employing relations (2) and (8) and the formula for expanding the sine of the difference of two angles, we finally obtain

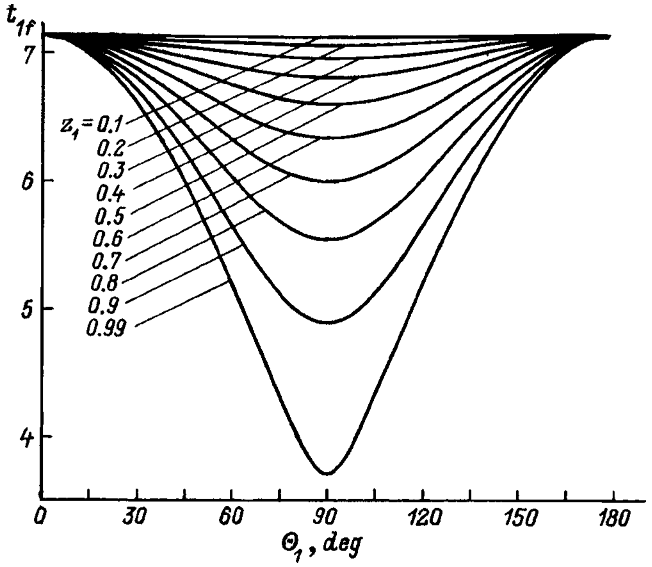

FIG. 3. Dependence of time it takes the particle to move from the source to the focus with both located on the symmetry axis of the spectrometer (z_1 is coordinate of the point source).

$$\sin\frac{\chi}{2}=\frac{W\sin 2\beta}{\sqrt{1-4W(1-W)\sin^2\beta}}. \tag{12}$$

The above expression is equivalent to formula (2) derived in Ref. 4. Now, knowing the initial angles Θ_1 and χ_1, the angle χ, and the kinetic energy W, it is easy to calculate the time of flight of the particle from the moment it leaves the field until it reaches the focal point, t_{eff}

$$t_{\mathrm{eff}}=\frac{\sqrt{[z_f-\cos(\pi-\chi-\chi_1)]^2+\sin^2(\pi-\chi-\chi_1)}}{\sqrt{2W}}. \tag{13}$$

Here z_f is the coordinate of the focus F. Adding expressions (6), (10), and (13), according to Eq. (5) we have the total time of flight of the particle from the source to the entrance slit t_{1f}.

FOCUSING IN TIME AND THE DISPERSION UNDER CONDITIONS OF IDEAL SPATIAL FOCUSING

Focusing in time is the condition that t_{1f} does not depend, at least to first order, on the angle Θ_1. Let us restrict the discussion to the regime of ideal angular focusing in Θ_1. According to Ref. 4, this regime is realized for $W=0.5$ and the point source located at any point on the z axis. In this case the coordinate of ideal focus is $z_f=z_1$.

Calculation of the dependence of the total time t_{1f} on the polar emission angle Θ_1 for different positions of the source z_1 revealed the presence of focusing in time for $\Theta_1=90°$. This is illustrated in Fig. 3, which plots the time t_{1f} as a function of the polar emission angle Θ_1 for different positions of the source. It can be seen from the figure that for any value of z_1 and $Q_1=90°$ the time t_{1f} is, to first order, independent of Θ_1, i.e., the desired conditions of focusing to first order in time are realized. As the source is moved away from from the center of the system, first of all, the absolute value of the time t_{1f} decreases and, second, the absolute change in

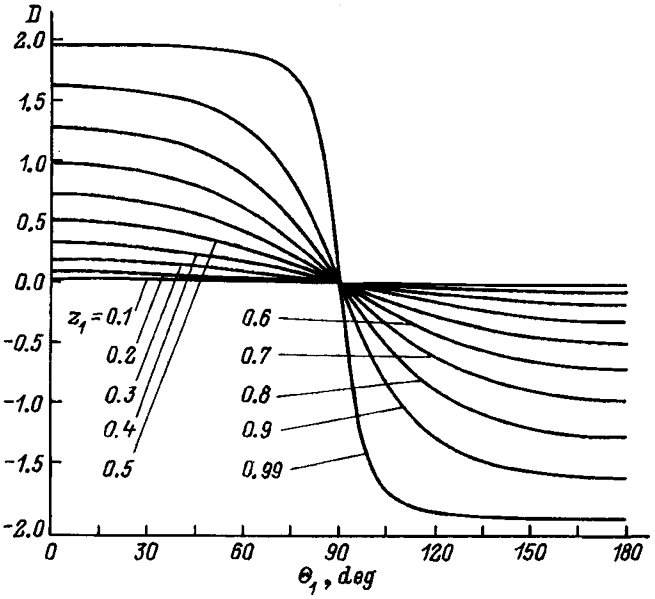

FIG. 4. Dependence of energy dispersion D on direction of flight of particle for different positions of point source z_1.

this quantity Δt_{1f} increases due to variation of Θ_1. As a result, the relative spread in the total time of flight of the particle $\Delta t_{1f}/t_{1f}$ corresponding to any fixed range of emission angles $\Delta\Theta_1$ increases still more strongly. It is obvious that if one builds an electron spectrometer for coincidence spectroscopy based on a spherical mirror analyzer, then from the point of view of the aperture ratio of the device the source, and along with it the detector, should be located as close as possible to the origin. In the limit in which z_1 tends to zero, the time of flight of the electron from the source to the focus is constant and equal approximately to 7.1416 relative units. This corresponds, however, to the case in which the source and image coalesce at the origin, the trajectory degenerates to a line segment, and the linear dispersion in energy is equal to zero. According to Ref. 4, it depends on z_1 and Θ_1 in the following way:

$$D=2z_1^2\frac{\cos\Theta_1}{\sqrt{1-z_1^2\sin^2\Theta_1}}. \tag{14}$$

Figure 4 plots a family of variants of the dependence $D(\Theta_1)$ corresponding different values of z_1. For any fixed angle the dispersion increases with z_1. It follows that as the resolving power of the hypothetical analyzer is increased, the source and detector should be located as far as possible from the center of the system, near the very boundary of the field.

The contradiction between the desire to increase the resolving power and preserve the aperture ratio without sacrificing the temporal resolution must, apparently, be solved in each concrete case on the basis of the conditions of the specific physical experiment. The source can in practice be located at any point of the field-free space for $r<1$ in the presence of ideal spatial focusing. Indeed, even for $z_1=0.99$, when the dispersion almost reaches its maximum value $D=2$, temporal focusing conditions exists in the vicinity of $\Theta_1=90°$.

TABLE I.

$Z1$	Δt, ns	R, %
-0.5	1.5	1
-0.6	2.25	0.7
-0.7	3.45	0.4
-0.8	5.25	0.3
-0.9	8.1	0.2

POSSIBLE SCHEMES OF ENERGY AND ANGLE ANALYSIS

The best application of the given system can be achieved if the diameter of the probe beam ΔS is reduced to its limiting value, which is entirely realizable, for example, in the case of Auger electron spectroscopy. In this case the central trajectory of the analyzed beam can have the angle value $\Theta_1=90°$ (Fig. 2), corresponding to zero energy dispersion. In this case the analyzer operates as follows. According to the conditions of ideal spatial focusing described above, at the exit diaphragm only electrons emitted with energy $W=0.5$ relative units in any direction within the limits of the entire hemisphere visible from a test point on a flat target. Even minimum variation of the emission energy, ΔW, radically weakens focusing since the conditions of ideal focusing are absolutely destroyed by any deviation from the tuning energy of the analyzer. The resolution in this scheme deteriorates abruptly with increase of the size of the source. Thus, in a spectrometer[6] with source diameter $\Delta S=1$ mm and $r_{\text{in}}=75$ mm a relative resolution $R\approx4\%$ was achieved for $z_1=-0.65$. The temporal resolution in such a regime for

$$W=100\,\text{eV},\quad r_{\text{in}}=75\,\text{mm},\quad \Delta S=1\,\text{mm} \tag{15}$$

and the implemented range of angles $\Theta_1=60-120°$ (aperture ratio $L=0.27\pi$) can be made equal to $\Delta t\approx9.3$ ns for $z_1=-0.9$ or $\Delta t\approx4.05$ ns for $z_1=-0.7$. It is possible to ''shadow'' the center of the angular aperture and exclude from the analysis part of the flux in the vicinity of $\Theta_1=\pi/2$, where the energy dispersion is small. In such a case, a screen is added to the usual scheme, which holds back part of the particle flux passing through the diaphragm at angles near 90°. Calculation for the same values (15) using the above range of angles with shadowing of the angular aperture from 80 to 100° ($L=0.24\,\pi$) gives the results tabulated in Table I.

It is possible to add a planar PSD, locating it on the other side of the output diaphragm parallel to the z axis. It follows from geometrical considerations that this improves the temporal resolution. On the other hand, an additional possibility arises (apparently not used anywhere earlier) of fixing the direction of emission of the particle in addition to its time of creation and energy. Calculated values of the main characteristics of the analyzer for the same parameter values (15), for the distance from the z axis to the PSD plane equal to 10 mm and the aperture ratio $L=0.24\pi$ are listed in Table II.

CONCLUSION

On the basis of the above calculations we may draw the following conclusions: 1) all of the proposed electron-optical

TABLE II.

$Z1$	Δt, ns	R, %
−0.5	1.95	1
−0.6	2.7	0.7
−0.7	3.9	0.4
−0.8	5.7	0.3

schemes will work well in the region of Auger coincidence spectroscopy with electron excitation since the diameter of the probe beam in Auger spectrometers is usually very small (0.1 mm and smaller); 2) for photon or other excitation with large ΔS it is necessary either to screen the central part of the analyzed flux or make the spectrometer sufficiently large ($r_{\text{in}} \approx 300$ mm), which is justified for such a complicated experiment; 3) the electron-optical scheme developed here not only delivers an enhanced recorded electron flux but also makes it possible when using position-sensitive detectors to simultaneously perform an energy analysis together with an angle analysis of the Auger electron emission.

The authors express their deep gratitude to Prof. Thurgate of the School of Mathematical and Physical Sciences of Murdoch University, Perth, Western Australia for the idea of developing electron-optical systems with coincident focusing in the particle emission angles and their time of flight to the detector.

[1] D. E. Ramaker, Phys. Scr. **41**, 77 (1992).
[2] S. M. Thurgate and C. P. Lund, J. Electron Spectrosc. Relat. Phenom. **72**, 289 (1995).
[3] R. A. Bartynski, Phys. Scr. **41**, 168 (1992).
[4] V. V. Zashkvara, L. S. Yurchak, and A. F. Bylinkin, Zh. Tekh. Fiz. **58**, 2010 (1988) [Sov. Phys. Tech. Phys. **33**, 1218 (1988)].
[5] L. D. Landau and E. M. Lifshitz, Mechanics, 3rd ed. (Pergamon Press, Oxford, 1976; Nauka, Moscow, 1988, 208 pp.).
[6] Daimon Hiroshi, Rev. Sci. Instrum. **59**, 545 (1988).

Translated by Paul F. Schippnick